Technische Universität München

Institut für Luft-und Raumfahrt

A Method for the Comparison of Transport Aircraft with Blown Flaps

Corin Gologan

Vollständiger Abdruck der von der Fakultät für Maschinenwesen der Technischen Universität München zur Erlangung des akademischen Grades eines

Doktor-Ingenieurs (Dr.-Ing.)

genehmigten Dissertation.

Vorsitzender: Univ.-Prof. Dr.-Ing. Mirko Hornung

Prüfer der Dissertation: 1. Hon.-Prof. Dr.-Ing. Dr. h.c. Dieter Schmitt

2. Univ.-Prof. Dr.-Ing. Horst Baier

Die Dissertation wurde am 10.12.2009 bei der Technischen Universität München eingereicht und durch die Fakultät für Maschinenwesen am 07.09.2010 angenommen.

Für Alina, Daniela und Stefan

Vorwort

Diese Arbeit entstand während meiner Zeit als wissenschaftlicher Mitarbeiter am Bauhaus Luftfahrt. Die ausgezeichneten Rahmenbedingungen am Bauhaus Luftfahrt waren eine wesentliche Grundlage für den Erfolg dieser Arbeit. Besonders bedanke ich mich bei Herrn Hon.-Prof. Dr.-Ing. Dieter Schmitt, der mir als Doktorvater mit stets kompetenten und hilfreichen Ratschlägen zur Seite stand. Ebenso danke ich Frau Dr. Anita Linseisen für ihre Unterstützung in sämtlichen nicht-technischen Angelegenheiten. Bei Herrn Prof. Dr.-Ing. Klaus Broichhausen bedanke ich mich dafür, dass er mich davon überzeugt hat, am Bauhaus Luftfahrt anzufangen und für die Unterstützung bei der anfänglichen Themenfindung. Herrn Univ.-Prof. Dr.-Ing. Horst Baier, sei gedankt für die freundliche Übernahme der zweiten Begutachtung dieser Arbeit und Herrn Univ.-Prof. Dr.-Ing. Mirko Hornung für die freundliche Übernahme des Prüfungsvorsitzes.

Am Bauhaus Luftfahrt war es mir möglich, mit sehr erfahrenen Experten aus der Industrie und Wissenschaft zusammenzukommen. Ich danke Herrn Jan van Toor von der EADS dafür, dass er sich regelmäßig an Reviews beteiligt hat und mit seiner Expertise wichtige Impulse für diese Arbeit gegeben hat. Ebenso danke ich Prof. Dr. Max Platzer für wertvolle Literaturhinweise und das Einbringen seiner Erfahrungen aus dem Bereich „powered lift“.

Ich danke allen Kollegen am Bauhaus Luftfahrt für viele interessante Diskussionen, durch die ich nicht nur im Bereich der Luftfahrtsysteme, sondern auch in der Informatik und der Ökonomie an Erfahrung gewonnen habe. Insbesondere sei Dr. Andreas Sizmann, Dr. Jost Seifert und Dr. Roland Schneider für hilfreiche Diskussionen und Ratschläge bei der Themenfindung und Vorgehensweise für diese Arbeit sowie zum wissenschaftlichen Arbeiten im Allgemeinen gedankt. Das besondere Engagement von Dr. Sizmann und Dr. Schneider weit über ihre Arbeitszeit hinaus möchte ich dabei hervorheben. Dr. Christian Kelders und Dr. Andreas Kuhlmann danke ich für die Zusammenarbeit bei mehreren interdisziplinären Publikationen, die für die Motivation der Arbeit aus ökonomischer Sicht wichtig waren. Bei Arne Seitz und Hans-Jörg Steiner bedanke ich mich für stets fruchtbare Diskussionen in sämtlichen Disziplinen der Flugzeugmodellierung. Florian Stagliano danke ich dafür, dass er mir auch an den Wochenenden und in den späten Abendstunden als stets kompetenter und kritischer Diskussionspartner zur Verfügung stand.

Mara Cole und Cyrilla Maelicke danke ich für hilfreiche Ratschläge zu sprachlichen Formulierungen.

Nicht zuletzt danke ich meiner Frau Daniela und meiner Tochter Alina. Daniela, Du hast mich stets liebevoll motiviert und mir während des Endspurts dieser Arbeit bedingungslos und geduldig den Rücken frei gehalten. Dein und Alina‘s Lächeln haben mir die Kraft zum Durchhalten gegeben.

München, im Dezember 2009 Corin Gologan

Summary

A method for the conceptual design and the comparison of short take-off and landing transport aircraft with blown flaps is developed. Key aspect for blown flaps is the interdependence of thrust, forward speed, and the aerodynamic forces during take-off and landing. Therefore, the focus of the thesis is on the modeling of the low-speed engine characteristics and the determination of the aerodynamic coefficients. Based on the low-speed engine characteristics and aerodynamic coefficients, methods for the calculation of the balanced field length and landing field length as well as the low-speed control characteristics are developed. The methods are integrated into a parametric aircraft model to determine the impact of the short take-off and landing capability on the aircraft design and the overall mission performance. In an application example, regional aircraft with different blown-flaps systems are compared to a conventional take-off and landing reference aircraft.

Zusammenfassung

Es wird eine Methode für den Konzeptentwurf und den Vergleich von kurzstartfähigen Transportflugzeugen mit angeblasenen Hochauftriebssystemen entwickelt. Kernaspekt bei solchen Systemen ist die Modellierung der Abhängigkeit zwischen Auftrieb, Geschwindigkeit und Schub während Start und Landung. Schwerpunkte der Arbeit sind somit die Modellierung der Triebwerkseigenschaften im Langsamflug und die Bestimmung der aerodynamischen Beiwerte. Darauf aufbauend werden Methoden für die Berechnung der Start- und Landebahnlänge sowie der Langsamflugeigenschaften entwickelt. Die dafür entwickelten Methoden werden in ein parametrisches Flugzeugmodell integriert, um die Auswirkung der Kurzstartfähigkeit auf die Flugzeugauslegung und die Gesamtmission zu bestimmen. In einem Anwendungsbeispiel wird die Gesamtmission von Regionalflugzeugen mit verschiedenen angeblasenen Hochauftriebssystemen mit einem konventionell startenden Referenzflugzeug verglichen.

Table of Contents

List of Figures

List of Tables

Nomenclature

a	Acceleration
AR	Aspect ratio
Alt	Altitude
b	Wing span
BFL	Balanced field length
BPR	Engine bypass ratio
c	Chord length
c_{d0}	2-dimensional minimum drag coefficient
c_f	Chord length of flap
c_h	Horizontal tail volume coefficient
c_v	Vertical tail volume coefficient
c_y	2-dimensional side-force coefficient
C_D	Drag coefficient
C_D^*	Drag coefficient (including engine jet momentum)
C_{D0}	Minimum drag coefficient
C_{Di}	Induced drag coefficient
C_{L_α}	Lift curve slope
C_l	Aileron rolling moment coefficient
C_L	Lift coefficient
$C_{L\max}$	Maximum lift coefficient
C_m	Pitching moment coefficient
C_{m_α}	Pitching moment derivative with respect to the angle of attack
C_μ	Jet momentum coefficient
C_{Y_v}	VT side force coefficient
d	Cruise drag calibration factor
D	Drag
e	Oswald efficiency factor
F_{AX}	Axial force of wind-tunnel model / aircraft at zero airspeed
F_N	Normal force of wind-tunnel model / aircraft at zero airspeed
F_x	Resultant force in x-direction
g	Average gravitational acceleration, g = 9.81 m/s²

h_F	Flare height
h_{obstacle}	Obstacle clearance height
k	Lift coefficient safety margin
K	Relative excess thrust available in the case of engine failure
K_b	Span factor
l_h	HT lever arm (distance between AC of HT and aircraft CG)
L	Lift
LFL	Landing field length
m	Mass
$\overline{m}$	Relative mass
M_x, M_y, M_z	Moment around x-, y-, z-axis of aircraft
Ma	Mach number
MAC	Mean aerodynamic chord
MLW	Maximum landing weight
$MTOW$	Maximum take-off weight
$MTOW_i$	Initial maximum take-off weight
$\dot{m}_{\text{des}}^{*}$	Mass flow of reference engine in design condition
$\dot{m}_{\text{RSTD}}$	Standard day corrected mass flow (mass flow at sea level static condition)
$\dot{m}_{\text{RSTD}}^{*}$	Standard day corrected mass flow of reference engine
$\dot{m}_j$	Jet mass flow
$\dot{m}_j \cdot v_j$	Jet momentum
$\left(\dot{m}_j \cdot v_j\right)_{\text{BypassOfftake}}$	Jet momentum of air taken off the bypass of the engine
$\left(\dot{m}_j \cdot v_j\right)_{\text{CoreOfftake}}$	Jet momentum of air taken off the core of the engine
$\left(\dot{m}_j \cdot v_j\right)_{\text{Exhaust}}$	Jet momentum of the entire engine exhaust
$\left(\dot{m}_j \cdot v_j\right)_{\text{ExhaustOfftake}}$	Jet momentum of air taken off the exhaust of the engine
$\left(\dot{m}_j \cdot v_j\right)_{\text{Offtake}}$	Jet momentum of air taken off the engine
N	Number of engines
OEW	Operating empty weight
OPR	Overall pressure ratio
p_t	Total pressure

p_{t13}	Bypass total pressure
p_{t16}	Total pressure of the bypass air in the mixing plane of a mixed-flow turbofan engine
p_{t6}	Total pressure of the core air in the mixing plane of a mixed-flow turbofan engine
q	Dynamic pressure, $\rho/2 \cdot v^2$
R	Radius
RD	Ram drag
s	Distance
S	Reference area of lifting surface (Wing reference area, if no index)
S_{cf}	Area of lifting surface affected by control flap
SFC	Specific fuel consumption
t	Profile thickness
T	Actual thrust
T_0	Sea level static thrust
T_0^*	Sea level static thrust of reference engine
T_{des}^*	Design thrust of reference engine
T_{SP}^*	Specific thrust of reference engine
T_{res}	Residual thrust of engine when air is taken off
T/W	Ratio of total installed thrust T_0 to $MTOW$
$TOFL$	Take-off field length
v	Velocity
v_j	Jet velocity
v_{mc}	Minimum control speed
v_{min}	Minimum velocity, where aerodynamic data is available
v_{ST}	Stall speed
v_1	Decision speed
v_2	Speed at end of 2nd climb segment
v_{18}	Velocity at the bypass nozzle of a separate flow turbofan engine
v_8	Velocity at the core nozzle of a separate flow turbofan engine
V_{MAOEI}	Velocity during missed approach with one engine inoperative relative to v_{APP}
W/S	Ratio of $MTOW$ to S
x	X-position measured from aircraft nose

$\bar{x}$	X-coordinate relative to *MAC*
y	Spanwise position measured from aircraft symmetry plane
Y	Side force
z	Z-position measured from aircraft nose
α	Angle of attack
γ	Climb/approach angle
δ_f	Flap deflection angle
δ_j	Jet turning angle
ε	Downwash angle
η_{Fan}	Isentropic efficiency of the fan
η_{LPT}	Isentropic efficiency of the low-pressure turbine
η_t	Thrust recovery factor
θ	Ratio of approach thrust to available OEI thrust
λ	Taper ratio
μ	Runway friction coefficient
ξ	Ratio of mass flow taken off the core engine to total core mass flow
ρ	Density
σ	Relative duct pressure loss: ratio of Δp_t to p_t at the offtake position
τ	Ratio of mass flow taken off the exhaust of engine to total mass flow
φ_{25}	Sweep of quarter chord
Δ	Increment
Δp_t	Duct pressure loss
Δz_v	Z-distance between VT aerodynamic center and CG
Π_{13}	Outer fan pressure ratio

Subscripts

ail	Aileron
av	Available
AC	Aerodynamic center
AEO	All engines operative condition
APP	Approach
ATO	Aborted take-off
B	Breaking
BF	Block fuel

cf	Control flap
clean	Clean configuration without flaps or control surfaces extended
CE	Critical Engine
CG	Center of gravity
CL	Climb segment
Cr	Cruise
f	Flaps
fs	Flapped section
F	Flare
FR	Free roll
fus	Fuselage
GR	Ground-roll segment
h	Horizontal Tail
L	Landing
MA	Missed approach
MAOEI	Missed approach with OEI
N	Neutral point of aircraft
OEI	One engine inoperative condition
reac	Pilot reaction in the case of aborted take-off
ref	Reference point of wind-tunnel wing-fuselage configuration
req	Required
RD	Ram drag
RDC	Ram drag corrected
Sp	Spoilers
TD	Touch down
TO	Take-off
TR	Transition segment
v	Vertical tail
USB	Upper Surface Blowing
WF	Wing-fuselage configuration
wm	Wind milling
WT	Wind-tunnel model

Abbreviations

AC	Aerodynamic center
AEO	All engines operative
AIBF	Advanced Internally Blown Flaps
APP	Approach
AW	Augmentor Wing
BFL	Balanced field length
BPR	Bypass ratio
CE	Critical engine
CFD	Computational Fluid Dynamics
CG	Center of gravity
CL	Climb
CTOL	Conventional take-off and landing
EBF	Externally Blown Flaps
ES	Engine simulator
FAA	Federal Aviation Administration
HT	Horizontal Tail
LD	Landing
LFL	Landing field length
MA	Missed approach
n.a.	Not available
IBF	Internally Blown Flaps
OEI	One engine inoperative
OEW	Operating empty weight
QSRA	Quiet Short-Haul Research Aircraft
SFC	Specific fuel consumption
SLST	Sea level static thrust
STOL	Short take-off and landing
TOC	Top of climb
TOFL	Take-off field length
USB	Upper Surface Blowing
VT	Vertical Tail

1 Introduction

A predominant problem in the USA as well as in Europe is the imminent capacity shortage of major hub airports. Air traffic is assumed to increase worldwide by around 5% per year (Boeing 2009b), while further runway extensions of airports are often difficult because of local residents stress acceptance level and limited real estate availability. According to the Federal Aviation Administration (FAA 2007), 22 major US airports will suffer from capacity shortages in the next two decades, even after the implementation of the respectively planned improvements. Eurocontrol's most recent study on the challenges of growth (Eurocontrol 2008) predicts that 11% of the European demand (around 2.3 million flights) will not be able to be accommodated in 2030 due to capacity shortage and that 19 airports will be saturated for 8 hours a day. Furthermore, several communities are constrained from building new runways or implementing other airfield projects to enhance capacity.

In the literature, various studies discuss solving this problem on the aircraft side. With these approaches, short take-off and landing (STOL) regional jets use existing airport infrastructure for take-off and landing to increase capacity. The solutions discussed are

- the opening of small satellite airports (Zuk and Wardwell 2005), (Kehse 2008)
- operation on underutilized turbo-prop runways (Couluris, Hange et al. 2007) or unused crossing runways (Hange 2003) and
- operation on other unused areas at hub airports (Gologan, Kelders et al. 2009).

A potential capacity increase has been demonstrated for the use of the turbo-prop runway at Newark Airport (Couluris, Hange et al. 2007) and for a generic airport, where STOL aircraft take-off and land from an extended taxi-way (Böck and Kelders 2009). For all solutions discussed, STOL field lengths between 600 m and 1000 m are required. Typical field length requirements for conventional take-off and landing (CTOL) regional jets are in the order of 1,500 to 2,000 m.

Several studies have shown the potential benefits for airlines and the community that could result from STOL operations: One benefit could be reduced noise levels through new approach trajectories enabled by low minimum flight speeds of STOL aircraft. The different aspects related to that option are being intensively studied in NASA's subsonic fixed-wing project (Hange 2008). Additional research is conducted at the German Aerospace Center (DLR) (Bertsch, Looye et al. 2009) and the German Air-Traffic Control (Schwanke 2009) in

the German Aeronautical Research Program (LuFo IV). Economic studies have estimated slot values, which were worth up to $43,800 per day (Gologan, Kelders et al. 2009) in the past. This indicates the high value of additional slots for an airline. According to Peperak a potential prevention of delay through STOL aircraft would allow for up to 17% higher fuel burn and 17% higher mass and maintenance cost for regional aircraft with 110 passengers (Peperak 2008). This gives an indication of the upper limit for the penalties that an aircraft can have due to STOL capability and powered lift system integration.

For the overall assessment of different STOL conceptual design solutions, a comparison of these penalties with respect to overall mission performance (fuel burn, maximum take-off weight, component weights, etc.) is required and presents one important open issue (Gologan, Kelders et al. 2009) in powered lift research.

1.1 Motivation

A large number of wind-tunnel experiments for cantilever high-wing aircraft configurations with different powered lift systems were conducted in the 1970s at NASA. Thereby most powered lift systems considered for STOL turbo-fan aircraft applications were blown-flaps systems. The results of the wind-tunnel experiments are publicly available and include detailed low-speed aerodynamic performance data.

Based on these wind-tunnel data, several studies compared the climb performance or the take-off and landing performance of different blown-flaps aircraft. Neither certification aspects such as, for example, the one engine inoperative condition or missed approach climb performance, nor the impact of the STOL capability on the overall mission performance were considered. (Hoad 1972), (Margason 2002), (Bobbitt and Margason 2007)

Several conceptual studies and comparisons of aircraft with blown flaps that were designed based on the wind-tunnel data have been published, but the design methodology, the calculation of the field length as well as the overall mission performance were not documented. (Cochrane, Riddle et al. 1982), (Chin, Aiken et al. 1975), (Braden, Hancock et al. 1980a), (Galloway 1972)

Some blown-flaps aircraft have been built and flown in the past. Well known examples of prototype aircraft with Upper Surface Blown Flaps are the YC-14 (Wimpress and Newberry 1998), the Quiet Short Haul Research Aircraft of NASA (Riddle, Innis et al. 1981). Other aircraft are the McDonnell Douglas YC-15 (Jane's 1977) with Externally Blown Flaps, the de Havilland of Canada C8-A Buffalo with the Augmentor Wing system

(Farbridge 1987) and the Hunting H.126 (Hunting 1963) with Internally Blown Flaps. The C-17 Globemaster of Boeing with Externally Blown Flaps and the Antonov An-72/74 with Upper Surface Blowing are blown-flaps aircraft that reached serial production (Jane's 2000) and are both still in operation. These concepts were designed for different missions, restrictions and performance requirements. Mission fuel burn and cruise performance data were rarely published. Furthermore, too few blown-flaps aircraft have been built to generate an empirical database that can be used for a comparison.

For the reasons mentioned above, it is impossible to conduct a coherent comparison of the different blown-flaps systems for current applications based on the previous work. The purpose of this thesis is to fill this need with the research objective detailed below.

1.2 Research Objective

The objective of this thesis is to develop a method that enables the conceptual design and comparison of STOL turbo-fan aircraft with different blown-flaps systems considering certification requirements as far as applicable to blown flaps as well as the implications on the overall mission performance. The method should be able to make use of publicly available low-speed wind-tunnel data, but should also be applicable to low-speed aerodynamic data from other origins such as for example Computational Fluid Dynamics.

The method should be able to model turbo-fan aircraft with the following blown flaps systems:

- Externally Blown Flaps
- Upper Surface Blown Flaps
- Internally Blown Flaps and Augmentor Wing
- Advanced Internally Blown Flaps

Not considered are other powered lift systems such as direct lift (e. g. lift-fans, cross-flow fans), turbo-prop powered systems (e. g. deflected slipstream, tilt-wing), or circulation control (e. g. rotating cylinders). The method can be adapted to also include such systems, but this is beyond the scope of this work.

The result of the method is the overall mission performance of STOL blown-flaps aircraft designed for a certain field length requirement. The overall mission performance can then be compared to a CTOL aircraft with mechanical high-lift devices. Thus, the thesis contributes to answering the question of whether STOL transport aircraft are an economically feasible solution to increase capacity and to reduce delays.

1.3 Methodical Approach

The methodical approach to reach the objectives is shown in Figure 1, and also reflects the main chapters of the thesis.

First, an overview of the current state in blown-flaps research and development is given. In an introduction the main characteristics of blown flaps are summarized. Subsequently, the functionality of the blown-flaps systems investigated is summarized and an overview of publicly available wind-tunnel data is given. Furthermore, previous comparison studies are reviewed and an overview of realized blown-flaps aircraft is given. Based on this literature survey, the research needs and the research task is discussed in more detail.

Subsequently, the methodical approach for the conceptual design is discussed. Based on a handbook approach for the conceptual design of conventional aircraft, the approach adapted for the conceptual design of blown-flaps aircraft is presented and discussed.

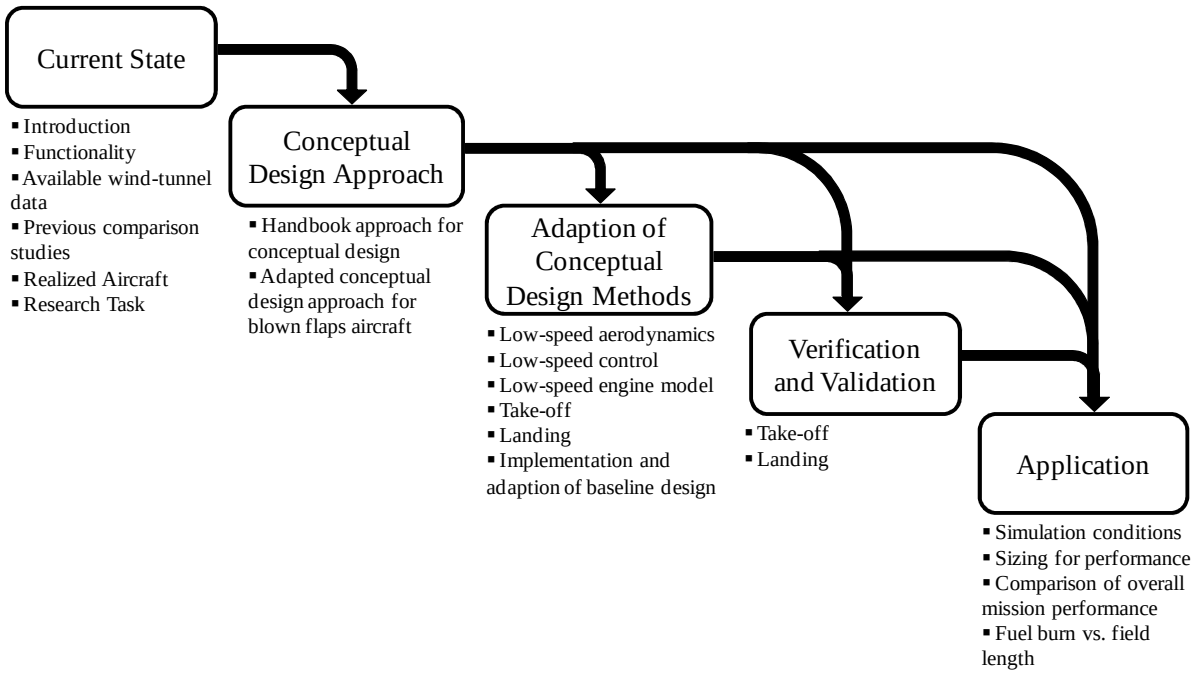

Figure 1. Methodical Approach

In the next chapter, the specific methods that were developed or adapted for the modeling of the physics of blown-flaps aircraft are documented. First is discussed how available wind-tunnel data can be used for the modeling of the low-speed aerodynamic performance. As blown-flaps aircraft take-off and land at significantly lower speeds than conventional aircraft, the low-speed control characteristics and the related tail and aileron sizing is discussed. For the determination of the coupling of engine thrust and low-speed

aerodynamic performance, a scalable low-speed engine model is developed with a gas-turbine performance simulation tool. Numerical methods for the calculation of balanced field length as well as landing field length are developed based on the above low-speed models and certification requirements as far as applicable for blown-flaps aircraft.

Next, the parametric aircraft model for the baseline design is documented, which includes handbook methods for the main disciplines required to model the overall mission performance of a conventional aircraft. By adoption of these methods and by the integration of the developed blown-flaps methods into the parametric aircraft model, the impact of STOL performance requirements on the overall mission performance and the related sizing effects are modeled.

In the following chapter, the methods developed for the take-off and landing of blown-flaps aircraft are validated by a comparison with flight-test data and verified by plausibility studies.

In the next chapter, the application of the methods is shown by the conceptual design and the comparison of STOL regional jets with different blown-flaps systems. First, the requirements, the assumptions as well as the design parameters and their design space are presented. Next, it is shown, which trade-studies have to be performed to size the blown-flaps aircraft for the required take-off and landing performance. Subsequently, the overall mission performance of the different blown-flaps aircraft is compared to each other and to a CTOL regional jet. Finally, a tradeoff between fuel burn penalty and field length required is given for the investigated blown-flaps aircraft.

In the end, the results of the thesis are summarized and an outlook for further research is given.

2 Current State and Needs in Blown-Flaps Research

This chapter first gives a general introduction to blown flaps. This is followed by an overview of the functionality of the different blown-flaps systems investigated and of publicly available wind-tunnel data. Next, previous comparison studies are reviewed and an overview of several realized blown-flaps aircraft is shown. As a conclusion, the research questions of this thesis are summarized.

2.1 Introduction to Blown Flaps

Today's transport aircraft use mechanical high-lift devices to increase the maximum lift coefficient during take-off and landing. Thereby, flaps at the trailing edge of the wing are extended to increase the wing circulation and lifting surface area. Additionally, slats at the leading edge increase the maximum angle of attack. Due to these measures the take-off and landing speed is reduced, and thus also the take-off and landing field length. Figure 2 shows a comparison of maximum lift coefficients achieved with mechanical flaps and with powered lift. Maximum lift coefficients of mechanical flaps have converged around 3.5, which at a given thrust-to-weight ratio and wing loading limits the take-off and landing field length. To further improve take-off and landing performance and to achieve lift coefficients significantly higher than the values for mechanical flaps, powered lift systems are required, as they can achieve maximum lift coefficients of more than 10. In this thesis, powered lift refers to blown flaps for short take-off and landing (STOL) aircraft with turbo-fan engines. Not considered is powered lift as a means of vertical flight (e. g. tilt-wing), direct lift (e. g. lift-fans, cross-flow fans), turbo-prop powered systems (e. g. deflected slipstream), or circulation control (e. g. rotating cylinders).

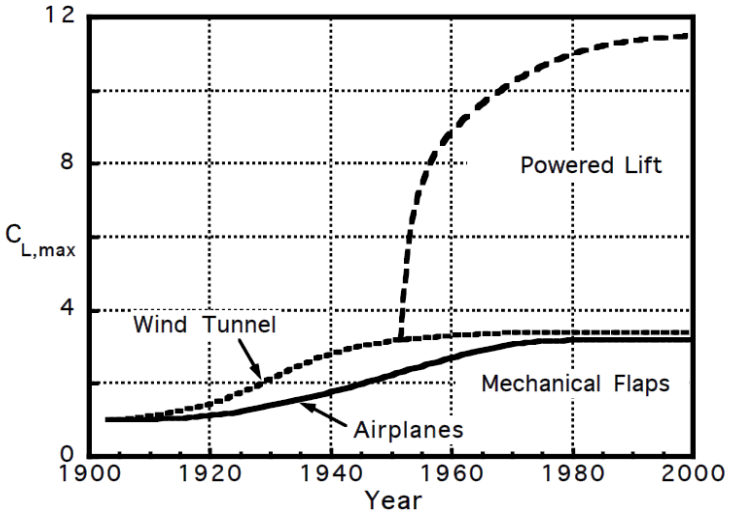

Figure 2. Evolution of maximum lift coefficient in the 20th century (Margason 2002)

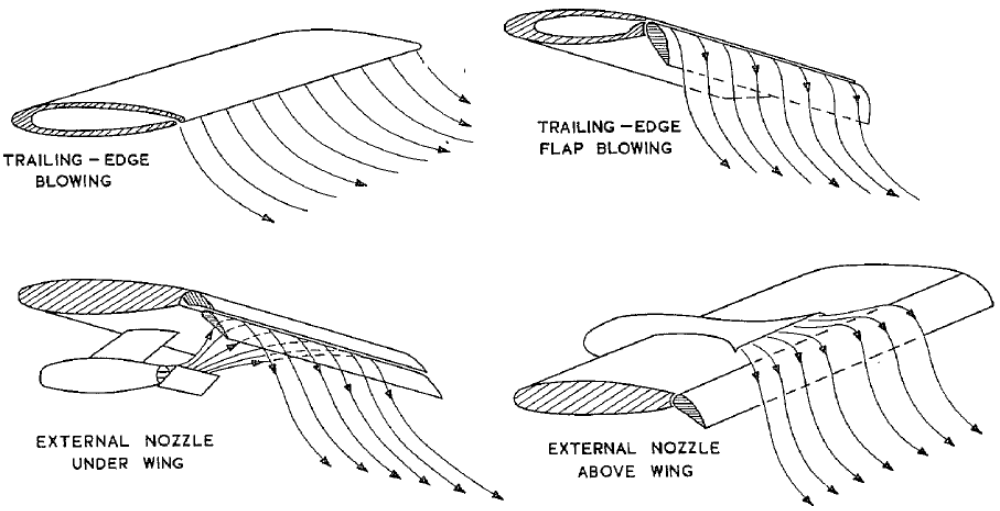

Figure 3. General options for blown-flaps devices (Williams, Butler et al. 1963)

Aircraft with blown-flaps devices use the blowing of high momentum air to induce power in the wing's flow field. Depending on the device, high momentum air is blown

- out of the wing's trailing edge, either with or without an additional flap,
- externally onto the flaps from the wing's lower side,
- above the wing, or
- out of the trailing edge of an extended flap.

Due to the extended flap, the trailing edge jet is vectored downward and increases the effective flap chord. The consequence is an increase in lift compared to the unpowered wing due to super-circulation (also known as powered circulation) and the vectored thrust. The magnitude of the increase in lift is characterized by the jet momentum coefficient[*] C_μ, which is defined as the ratio of the jet momentum $\dot{m}_j \cdot v_j$ that affects the blown-flaps device to the wing area and the dynamic pressure:

$$C_\mu = \frac{\dot{m}_j \cdot v_j}{\frac{\rho}{2} \cdot v^2 \cdot S} \tag{1}$$

Figure 4 illustrates qualitatively the lift increase over the jet momentum coefficient for an EBF system at a constant angle of attack. The characteristics of the effects are also valid for the other blown-flaps devices investigated. One can see that the total lift of the aircraft is significantly higher than the sum of the unpowered lift and the thrust component that is

[*] The jet momentum coefficient is sometimes also named "thrust coefficient" or "blowing coefficient"

vectored downward, which explains the denotation “super-circulation” or “powered circulation”.

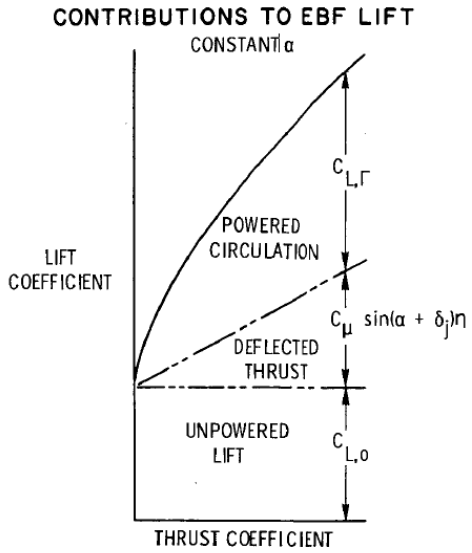

Figure 4. Contributions to lift of Externally Blown Flaps (Johnson 1972)

The jet momentum coefficient is an additional degree of freedom in the aerodynamic polar of a blown-flaps aircraft. Figure 5 shows a typical tail-off aerodynamic polar of an IBF wind-tunnel model with a flap deflection of 15° taken from wind-tunnel experimental data (Vogler 1976). The characteristics for other blown-flaps systems are similar. The polar includes lift coefficient of the wind-tunnel model $C_{L_{WT}}$ as a function of angle of attack α and C_μ as well as drag coefficient $C^*_{D_{WT}}$ and pitching moment coefficient $C_{m_{WT}}$ as a function of $C_{L_{WT}}$ and C_μ. The drag coefficient $C^*_{D_{WT}}$ represents the resultant force in aircraft x-direction and includes the engine jet momentum. For this reason it can reach negative values.

The higher the jet momentum coefficient, the higher is the lift coefficient (see Figure 4 and Figure 5). Equation (1) shows that for blown-flaps aircraft the lift coefficient is a function of engine thrust, speed and reference area. This coupling of thrust and lift is the main difference compared with conventional aircraft. It makes the calculation of the take-off and landing more complex than for conventional aircraft, where the maximum lift coefficient $C_{L\max}$ is constant during take-off. With increasing speed, C_μ decreases for a given jet momentum and reference area (see equation (1)). With decreasing C_μ, $C_{L\max}$ decreases and C^*_D and C_m increase. Consequently, for the calculation of take-off and approach speeds the following has to be considered: These speeds are a function of the lift coefficient; lift

coefficient is a function of C_μ, which is a function of speed. Therefore, take-off and approach speed are a function of the speed itself and have to be calculated iteratively, if no approximate analytical closed-form solution is possible.

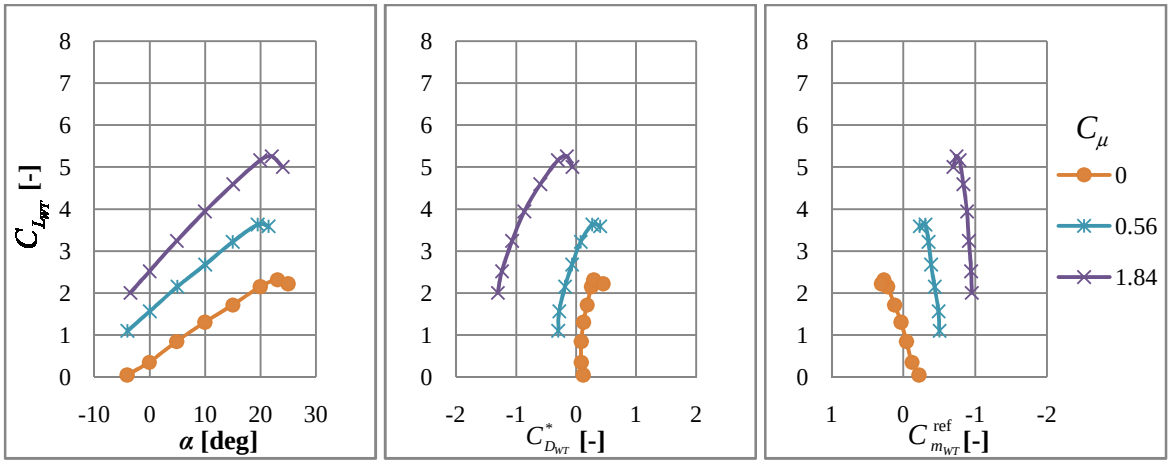

Figure 5. Low-speed polar of wing-fuselage wind-tunnel model with Internally Blown Flaps, δ_f=15° (Vogler 1976)

At a higher flap deflection (see Figure 6), the circulation increases and more thrust is vectored downward. Therefore, the lift coefficient increases. At the same time the drag increases, as less thrust acts in forward direction. The nose-down pitching moment coefficient of the wing-fuselage configuration increases with increasing C_μ and increasing flap deflection (Figure 5 and Figure 6).

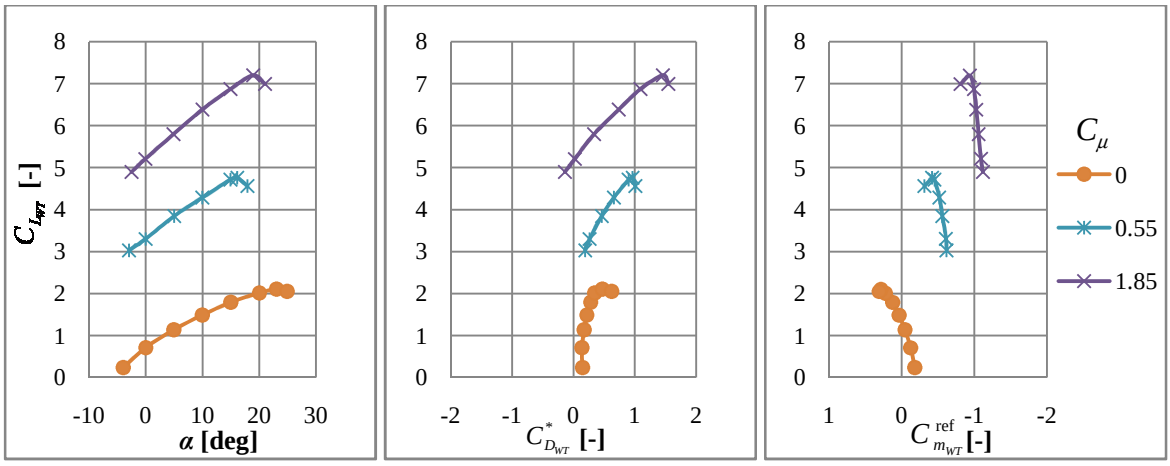

Figure 6. Low- speed polar of wing-fuselage wind-tunnel model with Internally Blown Flaps, δ_f=45° (Vogler 1976)

For a given jet momentum $\dot{m}_j \cdot v_j$ and reference area the jet momentum coefficient varies with airspeed. Wind-tunnel data are limited by the available maximum jet momentum coefficient, which is limited by wind-tunnel constraints or testing procedures. For the

example given in Figure 6 the aerodynamic data is available only between C_μ=0 and C_μ=1.85. This maximum available jet momentum coefficient corresponds to a minimum velocity v_{min}, where aerodynamic data are available; for a more detailed discussion on this topic see Bobbitt and Margason (Bobbitt and Margason 2007, p. 4). Below v_{min}, the aerodynamic characteristics are unknown. For the determination of the forces at zero airspeed, the thrust recovery factor η_t and jet turning angle δ_j at zero airspeed (static turning) are given in experimental results for different flap angles:

$$\eta_t = \frac{\sqrt{F_{Ax}^2 + F_N^2}}{T_0} \tag{2}$$

$$\delta_j = \arcsin\left(\frac{F_N}{\eta_t \cdot T_0}\right) \tag{3}$$

With the values for η_t and δ_j and the static thrust of the engine T_0, the lift (F_N) and thrust (F_{Ax}) at zero speed can be calculated. For airspeeds between v=0 and v=v_{min} the forces can then be determined by interpolation.

2.2 Functionality of Different Blown-Flaps Systems

This section explains the functionality of different blown-flaps systems, gives an overview about their general characteristics, and shows examples of aircraft built.

2.2.1 Upper Surface Blowing

Aircraft with Upper Surface Blowing (USB) systems (Figure 7) have their engines installed on the upper side of the wing. The entire engine exhaust is blown over the upper side. Due to the Coandă effect (Mentral and Zerner 1948) the exhaust follows the extended flap and is vectored downwards. Due to the resulting jet flap effect, the circulation is increased. The flaps for USB can be conventional multi-slotted flaps or continuous radius flaps. Wind-tunnel investigation have shown that USB aircraft with radius flaps have a better aerodynamic performance than with multi-slotted flaps (Sleeman, Hohlweg et al. 1975).

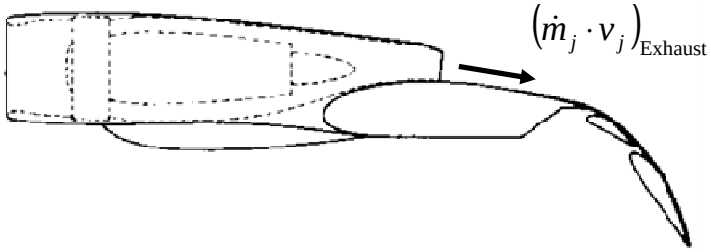

Figure 7. Sketch of Upper Surface Blowing Flap System (Phelps 1972)

The jet momentum of the entire engine exhaust $\left(\dot{m}_j \cdot v_j\right)_{\text{Exhaust}}$ influences the wing circulation (see Figure 7). Therefore the jet momentum that is used to calculate the jet momentum coefficient C_μ is equivalent to the engine gross thrust.

Advantages of the USB system are better low-speed turning performance compared to the Externally Blown Flaps system and good noise characteristics due to the upper engine installation (Dorsch and Reshotko 1972). One major disadvantage is the high drag in cruise condition due to the unique engine installation (see section 4.6.1). The USB system has been realized in several prototypes and research aircraft (see Table 2, p. 23). The only aircraft that has been certified for civil application is the Antonov AN-72/74 (Figure 8).

Figure 8. Antonov AN-72/74 transport aircraft with USB (Antonov 2004)

2.2.2 Externally Blown Flaps

The Externally Blown Flaps (EBF) system has the engines installed conventionally, on the lower side of the wing. The entire engine exhaust is blown on the multi-slotted flaps. The exhaust follows the extended flap, and a part of the exhaust flows through the flap slots and entrains the wings upper flow (Figure 9). In this way, the jet is vectored downwards creating a jet flap effect, which increases the circulation and the lift.

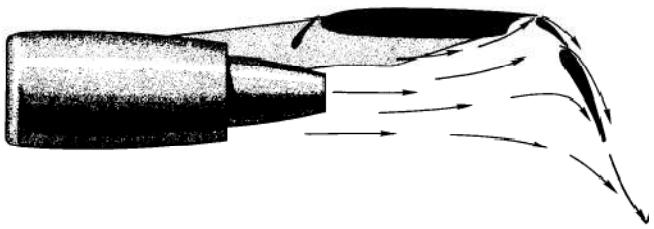

Figure 9. Sketch of Externally Blown Flap System (Johnson 1972)

Similar to USB, the entire engine exhaust $\left(\dot{m}_j \cdot v_j\right)_{\text{Exhaust}}$ affects the blown-flaps system and the jet momentum coefficient C_μ is also calculated from the entire engine gross thrust.

Advantages are the comparably simple and well known engine installation that has good drag characteristics in cruise and the conventional mechanical flap system. Disadvantages

compared to USB are higher noise (Dorsch and Reshotko 1972) and slightly lower low-speed aerodynamic performance (Hoad 1972), (Margason 2002), (Nicolai 1975).

The YC-15 was a successful research aircraft with EBF. The only certified aircraft with EBF is the McDonnell Douglas (now Boeing) C-17 military transport aircraft (Figure 10).

Figure 10. Boeing C-17 military transport aircraft with EBF (Boeing 2009a)

2.2.3 Internally Blown Flaps

For Internally Blown Flaps (IBF), different alternatives have been developed in the past (see Figure 11 for some examples documented). All IBFs blow their air out of the inside of the wing and, therefore, require an air ducting system.

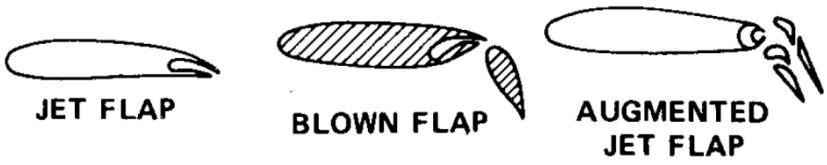

Figure 11. Examples for Internally Blown Flaps (Englar and Hemmerly 1981)

The jet flap blows high momentum air out of the wing trailing edge, which increases the effective wing chord and in this way produces super-circulation. Depending on the outlet angle, the jet is vectored downwards which increases the lift.

The blown flap blows high momentum air out of the trailing edge of the wing over an extended flap. Due to the Conadă effect, the jet follows the extended flap and increases the effective flap chord, which produces super-circulation. The increase in lift can be controlled by the flap angle, depending on the required ratio of lift-to-drag. The augmented jet flap (also named Augmentor Wing) has an additional flap installed over the basic flap forming a channel to create an ejector system that augments the thrust of the nozzle by entraining additional air. (Chambers 2005)

The aerodynamic characteristics of all IBF systems depend on the jet momentum coefficient. In contrast to the USB and EBF systems, the relevant jet momentum is not the

jet momentum of the total engine gross thrust. It is only the jet momentum of the bleed air that is taken off the core, bypass or exhaust of the engine:

$$C_\mu = \frac{\left(\dot{m}_j \cdot v_j\right)_{\text{Offtake}}}{\frac{\rho}{2} \cdot v^2 \cdot S} \tag{4}$$

If only a part of the engine mass flow is taken off, the residual gross thrust component T_{res} remains, which acts conventionally in the forward direction (see Figure 12).

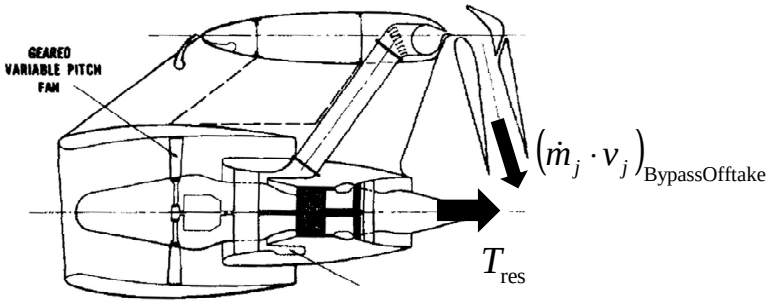

Figure 12. Rolls-Royce RB 419: Proposed engine installation and air offtake for Augmentor Wing aircraft (Whittley 1971)

Two research aircraft with IBF systems have been built and flown in the past. The Hunting H.126 (Figure 13) had blown flaps and a fuselage-mounted Bristol Siddeley “Orpheus” turbojet engine. More than half of the engine exhaust was transmitted to the blown flaps through ducts that had to withstand temperatures of 600°C to 640°C. Heat insulation was the major challenge and caused the major problems during this project. Around 10% of the exhaust was ducted to the nozzles at the wing tips and the tail to provide control power at very low speeds. (Hunting 1963)

The H.126 performed over 100 experimental flights between 1963 and 1967. However, this solution for the IBF system was not developed further due to the impracticalities of the nozzle system’s complex ducting. (Chambers 2005, p. 166)

Figure 13. Hunting H.126 IBF research aircraft (RAF-Museum 2009a)

The Buffalo C-8A Augmentor Wing (AW) research aircraft (Figure 14) of de Havilland of Canada used the bypass air of two Rolls-Royce Mk.801 Split-Flow Spey Engines for internally blowing and was able to vector the residual thrust downwards (Farbridge 1987).

Figure 14. de Havilland C-8A Augmentor Wing research aircraft (NASA 2009)

The different solutions that were realized for providing high pressure air to the flaps show two different air offtake options for IBF systems, the exhaust offtake and the bypass air offtake. The nozzle pressure ratio is an important parameter in the different options of providing high pressure air from the engines to the internally blown flaps. The nozzle pressure ratio determines the duct area and has an impact on the duct pressure losses. Figure 15 shows pressure losses measured in a large scale wind-tunnel model. One can see that with increasing pressure ratio, the duct losses increase. Decreasing total pressure ratios reduce the pressure loss, but necessitate larger ducts and thicker airfoils.

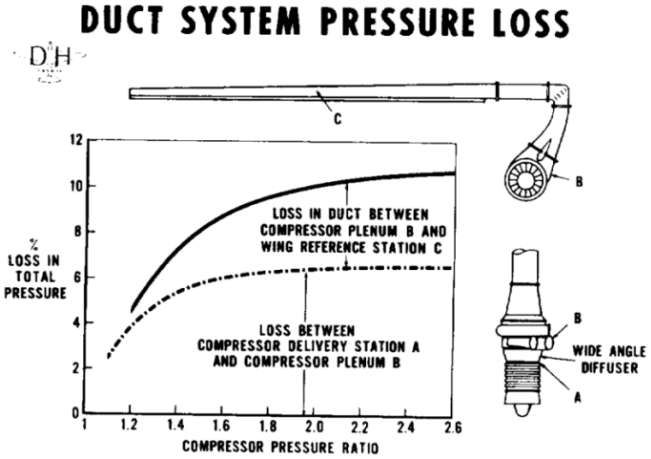

Figure 15. Duct pressure losses for Augmentor Wing system (Whittley 1971)

Exact values for duct pressure ratios are not available, neither for the aircraft built nor for the wind-tunnel models. However, the ducts and nozzle areas are very small and it can be assumed that the pressure ratios are close to the pressure ratio that provides very high exit velocities near Mach 1, which keeps the duct areas as small as possible. For bypass air, the pressure ratio that results in an exit velocity of Mach 1 equals 1.9 (Waters, Anthony et al. 2009).

2.2.4 Advanced Internally Blown Flaps

The Advanced Internally Blown Flap (AIBF) (Figure 16) has been developed and investigated in wind-tunnel experiments in the 1970's with the intention of benefiting from spanwise distribution and to minimize the disadvantages of the IBF system. The IBF system uses hot high-pressure air from the engine exhaust, separate devices or high pressure bypass air and, therefore, suffers from high pressure losses. In contrast, the AIBF system uses low-pressure air from the engine's bypass that is brought through an expandable duct to the trailing edge where it creates a jet flap effect. While the aerodynamic performance is similar, it has several advantages compared to an IBF system. As low-pressure bypass air is used, no heat insulation for the ducting is required and the core engine performance is almost not affected. Pressure losses in the duct are minimized as the area of the air duct is variable. Compared to IBF systems, low pressure ratios of around 1.3 have been realized in wind-tunnel experiments (Aiken, Aoyagi et al. 1973), which cause comparably low pressure losses (see Figure 15). However, the AIBF is mechanically more complex than an IBF due to the expandable duct. (Chin, Aiken et al. 1975)

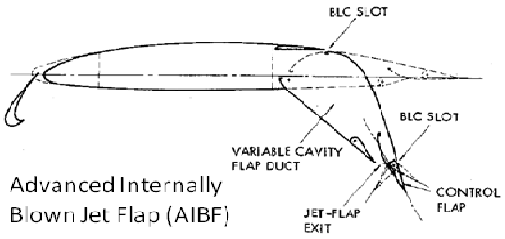

Figure 16. Advanced Internally Blown Flap airfoil section (Chin, Aiken et al. 1975)

The jet momentum coefficient for AIBF is defined based on the bypass jet momentum, as only this component of the gross thrust affects the AIBF system (see Figure 17):

$$C_\mu = \frac{\left(\dot{m}_j \cdot v_j\right)_{\text{BypassOfftake}}}{\frac{\rho}{2} \cdot v^2 \cdot S} \tag{5}$$

The general aerodynamic characteristics are similar to the other blown-flaps systems. The core gross thrust acts conventionally in the forward direction (see Figure 17).

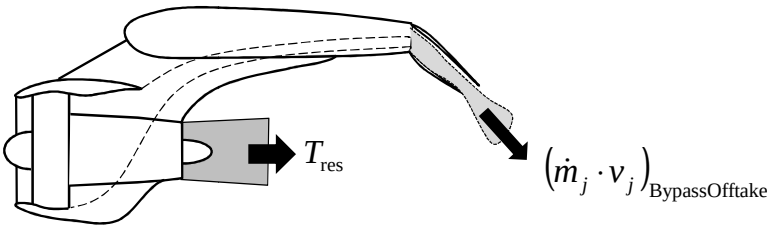

Figure 17. Sketch of the jet momentum components of the AIBF system

Figure 18 shows the bypass air offtake system that was proposed for a STOL transport concept. All the bypass air is collected via a transition duct and blown out above and slightly aft of the primary-exhaust exit during take-off and landing. For cruise, all bypass-air is exhaust in forward direction. (Chin, Aiken et al. 1975)

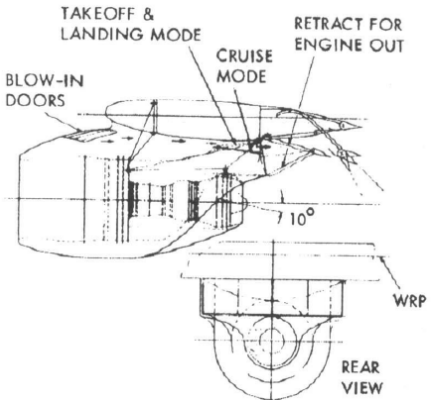

Figure 18. Engine installation for AIBF system (Chin, Aiken et al. 1975)

The advantages of the AIBF system are low pressure losses due to the usage of low pressure air. The expandable ducts enable large duct areas for low speed operation and thin airfoils for good transonic cruise efficiency. A disadvantage of the AIBF system is the higher mechanical complexity. Considering that the general trend of turbofan engines is towards engines with higher bypass ratios that have higher bypass gross thrust and low fan pressure ratios, the AIBF system could be a promising solution for modern blown-flaps aircraft.

2.3 Publicly Available Wind-Tunnel Data

Aerodynamic data of several wind-tunnel experiments for the USB, EBF, IBF and AIBF systems are publicly available. Almost all wind-tunnel models that were built at NASA are high-wing configurations with T-tails (see Figure 19). The aerodynamic coefficients were measured for a large range of angles of attack, jet momentum coefficients, and flap angles. Data from other test series, as, for example, Boeing studies are in the literature limited to only few data showing principal trends only (see Figure 20).

Table 1 gives an overview of several the wind-tunnel experiments that were performed for different blown flaps systems in the 1970's. The table is not complete, as not all wind-tunnel experiments that have been conducted in the past are publicly available. The experiments at NASA Langley used a small basic model with a wing area of 0.483m² and an aspect ratio of 7.48 and a wing sweep of 30°. A slightly different model for USB had a wing area of 0.458m² and an aspect ratio of 7.0. One large scale half-model has been investigated at NASA Langley with an unswept wing and one USB engine over the wing.

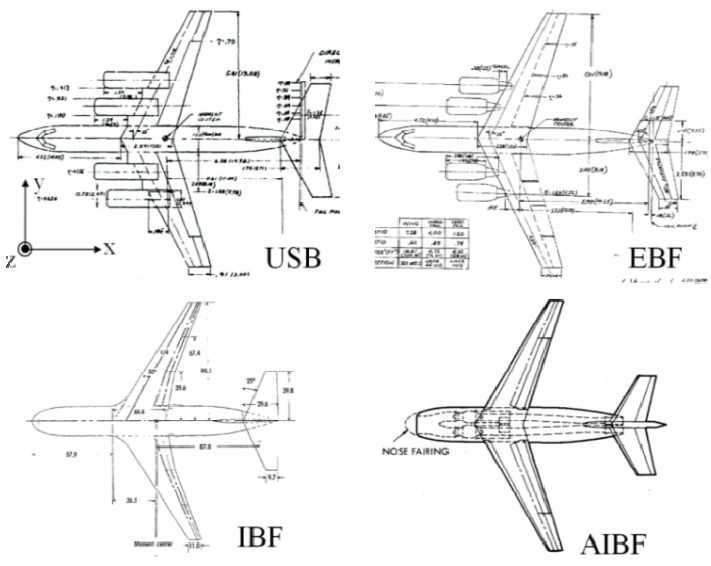

Figure 19. Top-view of several wind-tunnel models (Aoyagi, Falarski et al. 1975), (Aoyagi, Falarski et al. 1973), (Vogler 1976), (Chin, Aiken et al. 1975)

At NASA Ames, two almost similar basic wind-tunnel models were investigated. The model for USB and EBF had a wing area of 19.61m², an aspect ratio of 7.28 and a sweep of 25°. The basic model for AIBF and AW had a reference area of 21.37m², an aspect ratio of 8 and a sweep of 27.5°. Most experiments for EBF and USB were performed with four engines, while for USB also data for a two-engine configuration are available. For the IBF AW and AIBF systems, the engines were installed in the fuselage, as in the wind-tunnel they served as high-pressure air generators only. For transport aircraft applications the engines have to be installed under the wing, similar to the de Havilland C-8 AW aircraft (Figure 14) or the AIBF concept study (Figure 18), as the payload has to be stored in the fuselage.

Table 1. Overview of selected blown-flaps wind-tunnel experiments

	NASA Report Number	Year	Institution	Engine Installation	φ_{25}	S	AR
USB	TN D-7399	1973	Langley	4 over wing	30°	0.458	7.0
	TN D-8061	1975	Langley	4 over wing	30°	0.4833	7.48
	TN D-7526 (semi-span)	1974	Langley	1 over wing	0°	16.3	7.8
	TM X-62419	1975	Ames	4 over wing	25°	19.61	7.28
	TM X-62296	1973	Ames	2 over wing	25°	19.61	7.28
IBF and AW	TN D-8309	1976	Langley	pressure generators	30°	0.483	7.48
	TM X-62145		Langley	in fuselage	27.5°	21.36	8.0
	TM X-62029		Langley	in fuselage	27.5°	21.37	8.0
AIBF	TM X-62281	1973	Ames	in fuselage	27.5°	21.37	8.0
EBF	TN D-8057	1975	Langley	4 under wing	30°	0.4833	7.48
		1975	Langley	4 under wing	30°	0.4833	7.48
	TM X-62197	1973	Ames	4 under wing	25°	19.61	7.28

2.4 Previous Comparisons of Blown-Flaps Systems and Performance

This section is intended to review previous studies on the comparison of different blown-flaps systems or conceptual design studies, with the goal of a better understanding of the need for more research in the investigated field.

2.4.1 Comparison of Wind-Tunnel Data

Probably the most prominent comparison of blown flaps aerodynamic data (Figure 20) is based on Boeing wind-tunnel experiments and is available in various textbooks (Nicolai 1975), (Wimpress and Newberry 1998). The drag polars of IBF, AW, USB, EBF and Vectored Thrust* systems in take-off configuration at C_μ=2.0 are compared with each other and with the theoretical upper limit. One can see that the IBF system has the highest maximum lift coefficient (nearly 9.0), followed by the AW system (8.5) and the USB system (8.0). The EBF system has a maximum lift coefficient of 7.2 and the Vectored Thrust system has the lowest maximum lift coefficient (5.4). Generally the same trends apply to the drag characteristics, with the only exception, that the Vectored Thrust system has relatively good drag characteristics compared to its low maximum lift performance.

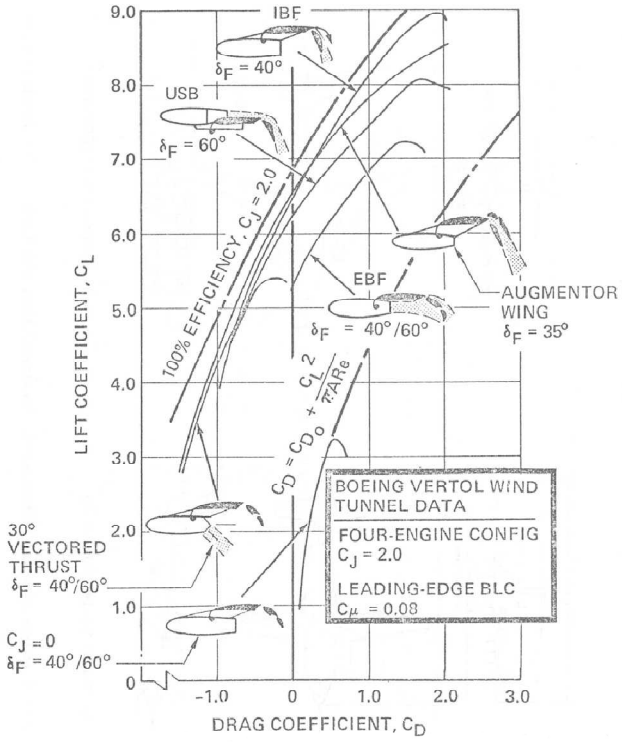

Figure 20. Drag polars of different blown flaps in take-off configuration (Wimpress and Newberry 1998)

* Vectored thrust systems have the engines installed under the wing. The entire engine exhaust is vectored downwards, which increases the lift. Although the flaps are not blown, the low-speed aerodynamic characteristics of the Vectored Thrust system are similar to USB and EBF, while the lift is significantly lower. The methodology worked out within this thesis is also applies to Vectored Thrust systems

A direct comparison of the aerodynamic performance of USB, EBF and Vectored Thrust is possible, as these aircraft have the same total installed thrust for the same jet momentum coefficient (all systems use the entire engine exhaust). A comparison of the IBF and the AW systems with the USB and the EBF systems at the same C_μ is misleading, as C_μ for IBF aircraft represents the jet momentum of the bleed-air only and does not include any information about the total installed thrust. A comparison of the blown-flaps system including the main engine (which is of main interest for a comparison at the aircraft system level) is only possible if an appropriate engine model that considers bleed air offtake is included.

2.4.2 Comparisons of Climb and Approach Performance

Hoad compared the aerodynamic performance of the blown-flaps systems USB, EBF, Vectored Thrust, IBF and AW based on data from NASA Langley wind-tunnel experiments (Hoad 1972). The results show that at the same jet momentum coefficients, the IBF and AW systems have higher lift coefficients than the USB, EBF and Vectored Thrust systems, which underlines the results of the Boeing wind-tunnel experiments. Based on the wind-tunnel data with the flaps in landing configuration, Hoad calculated the required thrust-to-weight ratio over the wing loading for a -6° approach at 75 kts (Figure 21). The Vectored Thrust system needs the highest thrust-to-weight ratio for a given wing loading followed by the EBF and USB systems, while the USB system performs slightly better than the EBF system due to the better aerodynamic performance. The IBF and AW systems have the lowest thrust-to-weight ratio required, but again, only the thrust of the bleed air was considered. No considerations were made about the total installed thrust required to provide the bleed air.

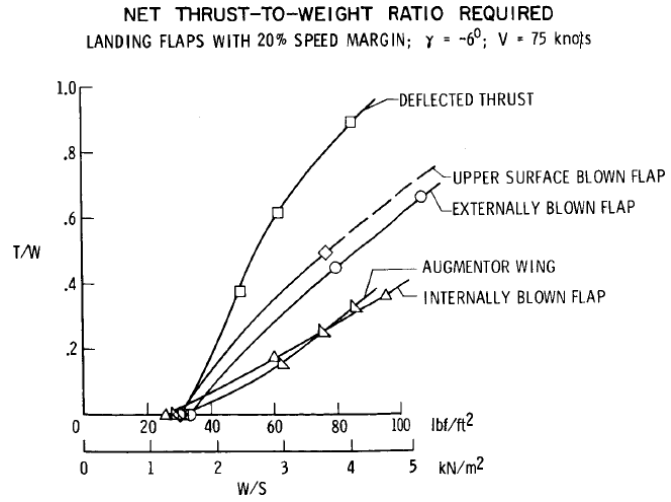

Figure 21. Thrust required for different blown-flaps systems in landing configuration (Hoad 1972)

As a further step to Hoad's study, Margason compared STOL concepts with USB, EBF and IBF based on All Engines Operative (AEO) longitudinally trimmed NASA Langley

wind-tunnel data (Margason 2002). For a velocity of 75 kts, he calculated the thrust-to-weight ratio required to climb along a 6° path (or to descent along a -6° path) as a function of wing loading. The results showed that the same trends also apply to climb performance and, in this way, Margason underlined the trends found by the previously mentioned studies. While the studies of Hoad and Margason show general trends of the aerodynamic performance and go one step further than a simple comparison of the wind-tunnel data, following issues are still to be addressed:

- The calculations consider climb and descent performance at a fixed velocity. Usually a certain take-off and landing field length performance is required. For this reason the blown-flaps systems have to be compared for the same take-off and landing performance that does not necessarily result in the same speed. The iterations related to take-off and approach speed discussed in section 2.2.1 have to be considered thereby.
- Data for AEO condition are used in the above studies, which for civil as well as for military transport application are not sufficient. The one engine inoperative (OEI) take-off and landing has to be considered.
- For the IBF and AIBF systems, engine models that consider bleed-air offtake and the residual gross thrust are required for a significant comparison of the IBF and AIBF systems to USB or EBF.

2.4.3 Comparison of Take-Off and Landing Performance

Bobbitt and Margason compared the take-off and landing performance of USB and IBF aircraft based on AEO wind-tunnel data (Bobbitt and Margason 2007). They developed an analytical method for the determination of TOFL considering the segments ground roll, transition, and climb to obstacle clearance, as well as LFL considering approach, flare, and deceleration. At the same thrust-to-weight ratio and wing loading, the results show a better take-off performance for the IBF aircraft compared with the USB aircraft.

In this study, the safety margin to stall speed is considered according to the safety margins defined for CTOL aircraft. In the engine model for the IBF system, it is assumed that the engine thrust can be spread variably into a component that affects the IBF system and a component that produces the residual thrust of the engine (without consideration of the interaction of the two thrust components to each other and duct pressure losses).

The following shortcomings of this method may be improved:

- The method considers AEO take-off and landing only, it does not account for engine failure and calculation of balanced field length (including consideration of decision speed).
- The engine model for the IBF system does not consider the effect of bleed air offtake on the residual engine thrust and does not discuss bleed air offtake limitations.
- The impact of the take-off and landing performance on the overall mission performance is not discussed.

2.4.4 Comparison of Blown-Flaps Concepts

Galloway presented the results of NASA designed STOL aircraft concepts with the blown-flaps systems USB, EBF, IBF and AW compared to aircraft with mechanical flaps (MF) (Galloway 1972). Figure 22 shows the thrust requirements and the gross weight trends for a 600-m field performance requirement and 100 passengers and 500 nm design mission. The trends found in the previously mentioned studies for climb and descent performance also apply to field performance. The AW concept has the lowest thrust requirement and the highest wing loading. The wing loading required for MF systems for the 600-m field is far beyond wing loadings that are suitable for turbo-fan aircraft. The gross weight trends show that for a required field length of less than around 900 m the gross weight rises reciprocally with decreasing field length.

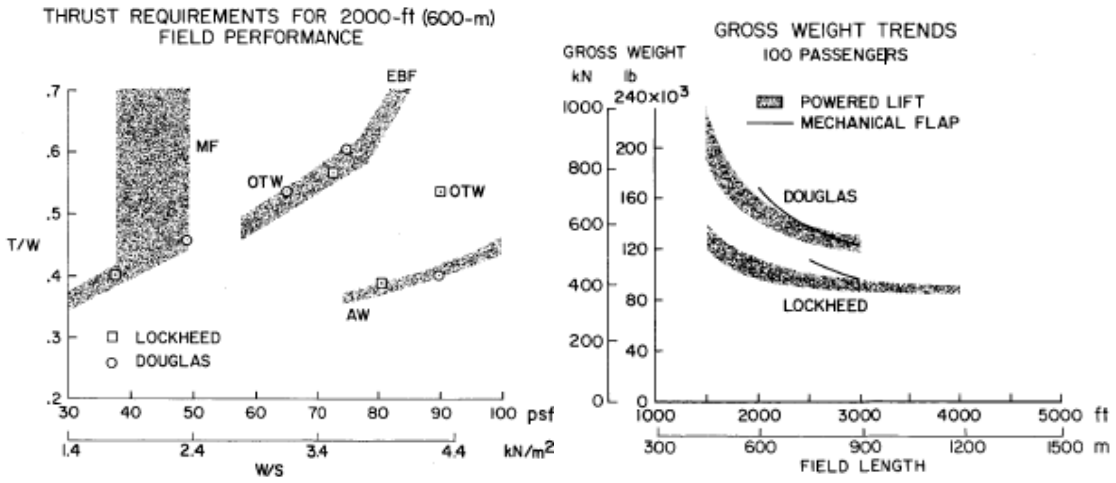

Figure 22. Comparison of thrust requirements and gross weight trends (Galloway 1972)

This study shows the results of a comparison for one set of requirements. The methods used for the calculation of the field length performance including the application of FAR-25 requirements as well as mission performance or engine modeling are not documented. Therefore, the results of these studies cannot be used for the conceptual design of aircraft with other mission requirements.

2.5 Comparison of Realized Blown-Flaps Aircraft

After World War II, enhanced propulsion systems enabled the development of blown-flaps systems. Several blown-flaps aircraft were built and flown in the second half of the last century. Very high lift coefficients up to 10 were demonstrated in wind-tunnel as well as in flight. Table 2 gives a comparison of the main data of several realized aircraft with blown-flaps systems. Most work was spent on EBF and USB systems. These systems achieved serial production with the C-17 (EBF) and the Antonov An-72/74 (USB).

Table 2. Overview of built aircraft with blown flaps

	Boeing C-17 A	An-72/74 TK-200	YC-14	YC-15	QSRA	ASUKA	C8-A Buffalo	Hunting H.126
Blown-Flaps System	EBF	USB	USB	EBF	USB	USB	AW	IBF
First Flight	1991	1977	1976	1975	1978	1985	1972	1963
Entry into Service	1993	1985	-	-	-	-	-	-
Application Type	Military	Military Civil	Research	Research	Research	Research	Research	Research
MTOW [kg]	265,350	36,500	107,500	98,284	27,215	45,000	20,412	4,872
OEW/*MTOW*	0.47	0.6	0.5	0.48	0.61	0.75	0.71	0.77
Payload [kg]	72,575	10,000	n.a.	28,122[*]	n.a.	n.a.	n.a.	n.a.
Range [nm]	2,400	430	2770x[†]	2,600[†]	315[†]	650[†]	300[†]	n.a.
T/W [-]	0.28	0.36	0.47	0.3	0.68	0.43	0.4	0.37
W/S [kg/m²]	752	370	593	502[‡]	488.2	373	254	238
Alt_{Cr} [ft]	28,000	33,135	n.a.	n.a.	n.a.	28,000	10,000	3,000
Ma_{Cr} [-]	0.74-0.77	0.66[§]	438 kts	434 kts	160 kts	0.55	160 kts	n.a.
N [-]	4	2	2	4	4	4	2	1
References	(Jane's 2000)	(Jane's 2000)	(Jane's 1977)	(Jane's 1977)	(Jane's 1979)	(Jane's 1989)	(Jane's 1977)	(RAF-Museum 2009b)

Looking at the main aircraft data, one can see that the aircraft are very different in terms of transport mission, weight, and main design parameters (*T/W* and *W/S*). Mission fuel burn and cruise performance is not available in many cases. Too few blown-flaps aircraft have been built to generate an empirical database that covers all performance data of interest. For these reasons the different blown-flaps aircraft are not sufficient to be used in a comparison for current applications.

[*] Maximum payload

[†] Ferry range

[‡] Prototype No. 1 (Prototype No. 2 had a smaller wing area)

[§] Maximum cruise Mach number

2.6 Current Research Needs and Research Task

The following conclusions can be drawn from the literature survey in this chapter:

- Current data of realized blown-flaps aircraft is insufficient for the comparison of different blown-flaps systems at the aircraft system level.
- Many wind-tunnel data from numerous experiments on entire aircraft models with different blown-flaps systems are available.
- A comparison of the low-speed aerodynamic performance of blown-flaps systems only is not sufficient for the conceptual design of STOL aircraft.
- Wind-tunnel data have been used for the comparison and conceptual design of STOL transport aircraft in various studies.
- The methodology used for previous comparisons of blown-flaps systems at the aircraft system level and the implication on overall mission performance is irreproducible because of lack of documentation.

For a comparison of aircraft with different blown-flaps systems at a conceptual design level, the calculation of take-off and landing performance have to be discussed in more detail, considering certification requirements as far as applicable to blown-flaps aircraft (for example operation with OEI). The implications of the required take-off and landing performance on the aircraft design and mission performance have to be modeled to enable a comparison of different blown-flaps systems at the aircraft system level including overall mission performance. Therefore, the main research task is the development of a method that enables the comparison of aircraft with different blown-flaps systems for the same design mission and same performance requirements at a conceptual design level.

To accomplish the research task a number of related research questions have to be addressed:

- How can wind-tunnel data be used for conceptual design?
- How can the coupling of engine thrust with the aerodynamic performance be modeled for different blown-flaps systems within a conceptual design?
- What are suitable methods for calculation of take-off and landing performance of blown-flaps aircraft and how do certification requirements affect these methods?
- What aspects at aircraft system level have to be modeled to capture the impact of STOL capability at the aircraft system level and the overall mission performance?

3 Conceptual Design Approach

First, a handbook approach for the conceptual design of conventional aircraft is presented including the general approach of sizing for performance and the determination of a baseline design. Subsequently is discussed, how this approach has been adapted for the conceptual design of blown-flaps aircraft.

3.1 Handbook Approach for Conceptual Design of Conventional Aircraft

In conceptual design, different aircraft alternatives are competitively compared with each other to find a small number of baseline designs that are subsequently considered for further preliminary design. Every aircraft alternative is first sized for the required performance with simple empirical methods. Subsequently, a baseline design is generated for every alternative with more detailed methods and finally compared to the other baseline designs. (Schmitt 2009)

3.1.1 Sizing for Performance

The sizing for performance means to determine a combination of thrust-to-weight ratio (*T/W*) and wing loading (*W/S*), which best satisfies all mission segment requirements. This combination is often also referred as the "design point". For each of the relevant mission segments, the combinations of *T/W* and *W/S* that satisfy the respective performance requirement are calculated and plotted in one chart. The following requirements and mission segments are, thereby, relevant for civil transport aircraft:

- Balanced field length (BFL) and landing field length (LFL) required
- Minimum climb rate for take-off with one engine inoperative (CL TO OEI)
- Minimum climb rate for missed approach with all engines operative (CL MA)
- Minimum climb rate for missed approach with OEI (CL MA OEI)
- Minimum climb rate at top of climb (TOC)

This chart, which is often referred to as "matching chart" or "performance constraint chart", includes all constraints for *T/W* and *W/S* that result from the above mission segment requirements. In this way it gives the feasible region for these parameters, where all performance constraints are fulfilled (see Figure 23 for example). Within this feasible region a minimization of *T/W* and a maximization of *W/S* are attempted, which leads to the aircraft design point.

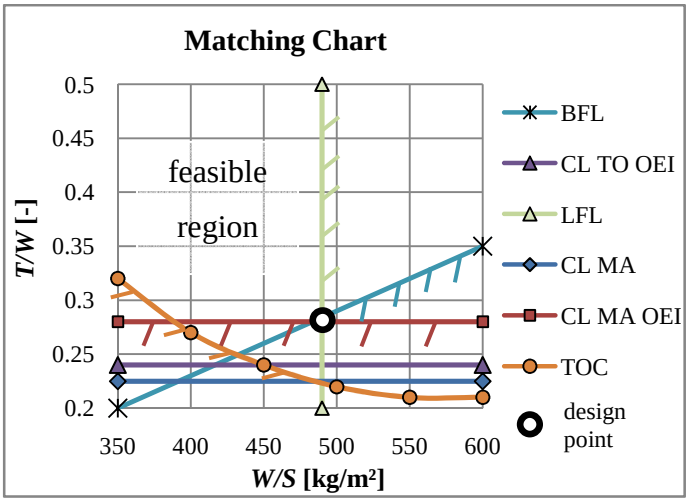

Figure 23. Example for matching chart of a generic aircraft with mechanical high-lift devices

For conventional aircraft with mechanical high-lift devices simple handbook methods based on empirical data are used for the calculation of the constraints, e. g. (Loftin 1980) or (Raymer 2006). The minimum climb rates required are defined in FAR-25 (FAA 2009) as a function of the number of the installed engines. The take-off and landing field length required is usually specified by the manufacturer or customer but, for their calculation, certification requirements also have to be considered.

For the design point, a first mission performance calculation is performed with the fuel fraction method based on empirical data and experience to determine an initial maximum take-off weight *(MTOW)*. *MTOW*, *T/W* and *W/S* give the absolute values for sea level static thrust T_0 and wing reference area *S*.

3.1.2 Baseline Design

Subsequently, a baseline design is modeled with more detailed component-based methods for the calculation of mass and drag and a more detailed mission simulation. Several design cycles have to be performed to determine a converged baseline design, as the calculated *MTOW* usually differs from the initial *MTOW*.

Finally, the different baseline designs for the aircraft alternatives are compared with each other to select the alternatives that are considered for detailed design.

3.2 Adaption of Conceptual Design Approach for Blown-Flaps Aircraft

For conventional aircraft, the simple methods for conceptual design that are based on empirical data and experience of previous designs give a good approximation to the aircraft size. For new aircraft types or configurations, the available methods give rough

approximations only. New assessment methods have to be developed in this case. (Jenkinson, Simpkin et al. 1999, p. 14)

Most unconventional for blown-flaps aircraft is the coupling of thrust and lift during take-off and landing, which causes different physical effects compared with aircraft with mechanical high-lift devices. For this reason, empirical handbook methods developed for conventional aircraft with mechanical high-lift devices do not apply to the calculation of the take-off and landing performance of blown-flaps aircraft. Empirical methods for the take-off and landing of blown-flaps aircraft are not available in the literature. Therefore, the focus and main effort of this thesis lies in the development of methods that model the interaction of thrust and lift of blown-flaps aircraft during take-off and landing. Thereby, the take-off and landing field length calculation as well as the low-speed control characteristics have to be considered. The development of these methods is the first step in the proposed conceptual design approach for blown-flaps aircraft (Figure 24).

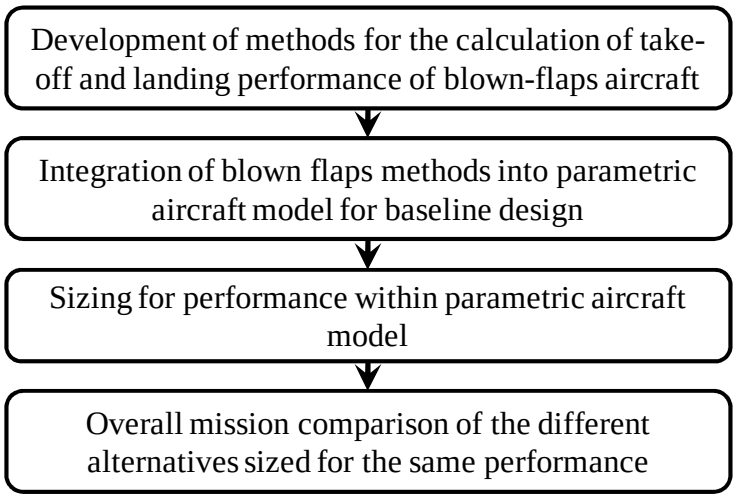

Figure 24. Conceptual design approach for blown-flaps aircraft

The general layout and the characteristics of blown-flaps aircraft during cruise are similar to conventional aircraft. Therefore, a parametric model for the baseline design of conventional aircraft is used as an integration platform for the blown flaps specific methods. This model includes a detailed mission simulation and uses detailed component-based handbook methods for the calculation of the aircraft weights and aerodynamics. Specific characteristics of the blown-flaps aircraft, e. g. higher cruise drag due to engine installation, are modeled by the use of penalty factors (based on wind-tunnel data) that are applied to the component-based methods. In this parametric aircraft model, the different aircraft alternatives are sized for the required performance, considering the relevant

mission segments presented above. With the methods for take-off and landing integrated in the baseline model, the interdependence between the take-off and landing performance and the overall mission performance as well as the scaling effects can be determined in one model.

3.2.1 Method Development for Take-Off and Landing of Blown-Flaps Aircraft

The coupling of thrust and lift has implications for different aspects connected to take-off and landing calculations. The dependence of the aerodynamic coefficients on thrust gives an additional degree of freedom, which is not represented in empirical handbook methods for the calculation of the low-speed aerodynamic coefficients. A low-speed engine model that provides the jet momentums required for the calculation of the aerodynamic coefficients has to be developed. The different low-speed aerodynamic and engine characteristics have implications for balanced field length and landing field length calculations, which are not captured by empirical take-off and landing methods.

Figure 25 illustrates how the main models, which are developed and documented in the sections 4.1 to 4.5, are connected to each other and to the main aircraft parameters *T/W*, *W/S* and *MTOW*.

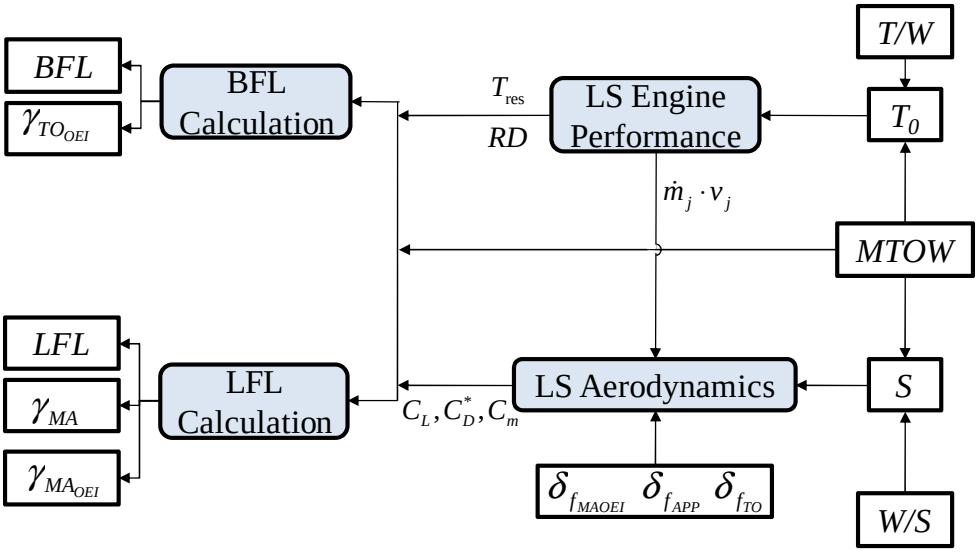

Figure 25. Methods developed for take-off and landing

Based on T_0, the low-speed (LS) engine performance model calculates the jet momentum $\dot{m}_j \cdot v_j$ that is required for the calculation of the LS aerodynamic coefficients. The low-speed (LS) aerodynamic model calculates the aircraft's aerodynamic coefficients (C_L, C_D^*, C_m) as a function of the jet momentum coefficient C_μ, which is a function of the engine jet momentum $\dot{m}_j \cdot v_j$, reference area *S* and airspeed.

The balanced field length and landing field length including the related climb and approach angles are calculated with the aerodynamic coefficients (C_L, C_D^*, C_m) for the respective flap angle, the residual gross thrust and the ram drag of the engine. For the design mission, *MTOW* is used for *BFL* calculation and maximum landing weight (*MLW*) for *LFL* calculation. In the *BFL* and *LFL* calculations, the control surface aerodynamic coefficients required to trim the aircraft in different flight stages are calculated from the aerodynamic coefficients and the engine characteristics.

To sum up, the outcome of these methods is the performance of the blown-flaps aircraft for the mission segments that have to be considered for the determination of the aircraft design point within the matching chart (Figure 23):

- *BFL* and *LFL*
- $\gamma_{TO_{OEI}}$
- γ_{MA}
- $\gamma_{MA_{OEI}}$

3.2.2 Integration of Blown-Flaps Methods into Parametric Aircraft Model

A parametric aircraft model, which includes component-based methods, is used for the modeling of the baseline design. The main disciplines included are discussed with the help of a simplified representation of this model (Figure 26). With an initial maximum take-off weight $MTOW_i$ and the main sizing parameters, *T/W* and *W/S*, the sea level static thrust T_0 and the wing reference area *S* are determined. The operating empty weight (*OEW*) includes the structure weight, propulsion weight, operational items weight and equipment weight, which are calculated based on the aircraft geometry. While operational items are constant for a given payload, the structure, propulsion and equipment weights scale with $MTOW_i$, T_0 and *S*. Based on the aircraft geometry, the high-speed drag polar is calculated and provided to the mission module. The engine deck includes the part load characteristic of the specific fuel consumption (*SFC*). The mission module requires the mission profile, *OEW*, drag polar, and *SFC* to calculate the mission fuel burn. The sum of mission fuel burn, *OEW* and payload is the calculated *MTOW*. $MTOW_i$ has to be iterated until it matches the calculated *MTOW*, which is a standard procedure within conceptual design. These applied handbook methods and their adoptions for blown-flaps aircraft are documented in section 4.6.

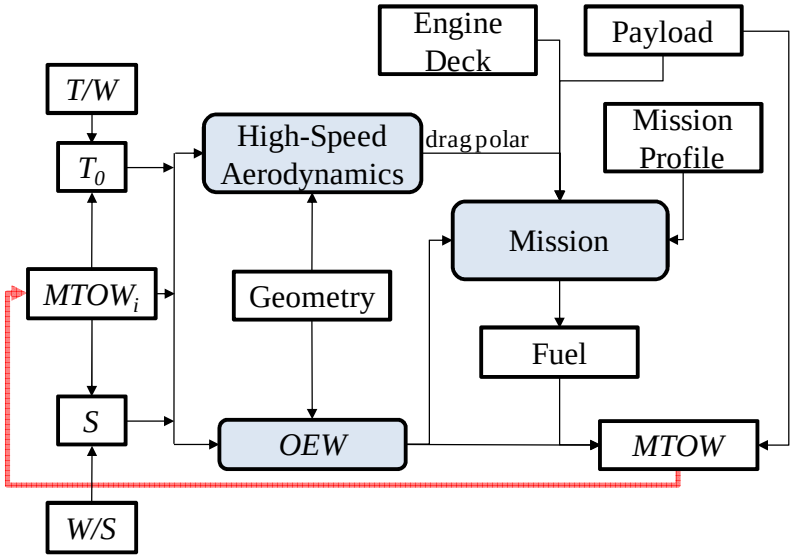

Figure 26. Parametric aircraft model for baseline design

The methods developed for the take-off and landing are integrated into the parametric aircraft model of the baseline design, giving the parametric aircraft model for the blown-flaps aircraft (see Figure 27). Therein, the interactions between blown flaps take-off performance and overall mission performance can be determined: when *T/W* and *W/S* are sized to meet a certain take-off, landing and climb performance, the baseline design model automatically scales and determines the overall mission performance. In this way the impact of the STOL capability on the aircraft components and overall mission performance including the related scaling effects is modeled.

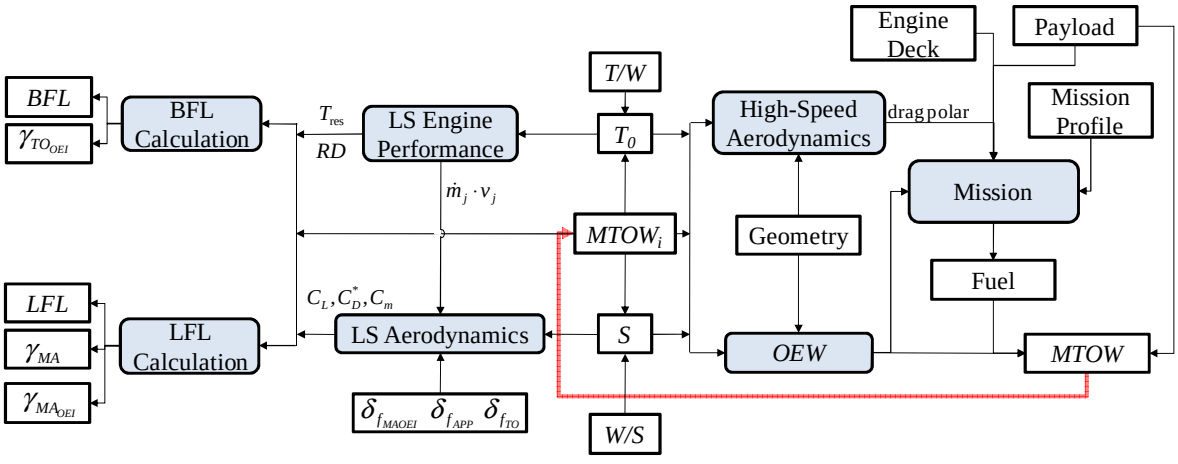

Figure 27. Parametric aircraft model for blown flaps baseline design

By the integration of the low-speed aerodynamic data and low-speed engine models for the various blown-flaps systems investigated, models for the different aircraft alternatives are generated. The overall mission performance of the different aircraft alternatives that are all sized for the same mission requirements can be compared with each other.

3.2.3 Sizing for Performance

The main design parameters for transport aircraft that have to be sized for the required performance are *T/W* and *W/S*. For blown-flaps aircraft additional parameters that are strongly coupled to the take-off and landing performance have to be considered for the determination of the design point. The flap angles for take-off $\delta_{f_{TO}}$ and landing $\delta_{f_{APP}}$ that result in the best take-off and landing performance and meet the required climb angles for take-off with OEI and missed approach (MA) have to be determined. A flap setting for MA with OEI as well as a thrust rating during approach have to be found to meet the climb requirement for this critical segment at a minimum installed thrust.

For conventional aircraft the constraints for the matching chart can be calculated analytically with the simple handbook methods (see section 3.1.1). For unconventional configurations, the constraints for the matching chart can be calculated analytically, if the specific methods developed are given in an analytical closed form solution, as for example documented in a previous study for vertical/short take-off and landing aircraft with direct lift (Gologan, Broichhausen et al. 2009).

For the methods developed in this thesis, the constraints for the different mission segments that have to be considered in the matching chart cannot be calculated analytically. The methods developed for the take-off and landing are not given in analytical form and include several iterations. Therefore the approach chosen for the sizing to performance is to explore all combinations of the design parameters within a feasible design space. For every combination, the performance for all relevant mission segments is calculated and compared with the respective mission segment performance required. In this way the combinations of *T/W, W/S* and the other design parameters are identified, which satisfy all performance requirements and the best combination of *T/W* and *W/S* can be selected as the design point.

The sizing for performance is a typical multidimensional optimization problem with the design parameters of the aircraft as design variables, the mission segment requirements as optimization constraints and the objective to minimize *T/W* and maximize *W/S*. Such an optimization can be performed with the parametric aircraft model implemented with different optimization algorithms. However, the gain of knowledge of the system is thereby low. For this reason, an example, how this multidimensional design space can subsequently be analyzed by the help of relevant trade studies and the matching chart is given in chapter 6.

4 Adaption of Conceptual Design Methods for Blown Flaps

In the following, the methods adapted and developed for the representation of the blown-flaps aircraft are documented. First, an approach to modeling the low-speed aerodynamic characteristics based on available wind-tunnel data is presented. Secondly, low-speed control aspects and the approach for tail and aileron sizing are discussed, since these aspects are very important for blown-flaps aircraft flying at low speeds. Subsequently, the low-speed engine model that has been worked out for the coupling of engine and aerodynamic performance is documented. Afterwards, the methods for the calculation of the take-off and landing performance are described. The handbook methods implemented in the baseline design model are finally documented and how they model the impact of short take-off and landing capability on overall mission performance is discussed.

4.1 Low-Speed Aerodynamics

This section presents the approach that has been developed to determine the low-speed aerodynamic coefficients (lift coefficient C_L, drag coefficient C_D^*, and pitching moment coefficient C_m) of blown-flaps aircraft based on available wind-tunnel data. Many previous studies have used wind-tunnel data to model the low-speed aerodynamic performance (see section 2.4). The advantage of using wind-tunnel data is that first comparisons can be performed very quickly, as the wind-tunnel data are already available. Additionally, realistic efficiency losses and non-linear effects are represented, which cannot be modeled by analytical methods that use linear approximations. The disadvantage of wind-tunnel data is that they represent the wind-tunnel configurations and similar ones, only. An aircraft that differs from the wind-tunnel configuration may have different aerodynamic characteristics. However, the wind-tunnel models presented in section 2.3 are very similar to transport aircraft configurations (see Figure 19, p. 18). If similar values for the main parameters (aspect ratio, taper ratio, sweep, etc.) are used for the modeled aircraft, the wind-tunnel data serve as a good baseline. However, the methods developed for the calculation of the low-speed control, low-speed engine performance and take-off and landing apply to any blown flaps low-speed aerodynamic data. A replacement of the wind-tunnel data by data from other origins such as for example Computational Fluid Dynamics (CFD) is possible.

In the following, some aspects are discussed that can support the decision, as to which of the available wind-tunnel data to use. How the aerodynamic coefficients are extracted from the wind-tunnel data is then presented. Subsequently, which corrections have to be

performed to assure comparability are shown. Missing aerodynamic data at zero airspeed for Internally Blown Flaps (IBF) and Advanced Internally Blown Flaps (AIBF) are derived from other blown-flaps systems. An approach for the modeling of the one engine inoperative (OEI) characteristics of the IBF and AIBF systems is presented as, for these systems, OEI experimental data are not available. The impact of the engine bypass ratio (BPR) on the blown flaps aerodynamic coefficients is finally discussed.

4.1.1 Selection of Wind-Tunnel Data

This section is intended to discuss aspects that are important to evaluate the applicability of available wind-tunnel data. While for AIBF systems the results of only one wind-tunnel experiment are available, for the other technologies several different experiments have been published. The availability of different operational conditions drives the decision as to which data to use. For civil application, All Engines Operative (AEO), as well as, OEI, data have to be available, as the OEI condition has to be analyzed for certification and safety reasons. Tail-off data enable the calculation of the trim condition for different tail sizes and, in this way, allow the adaption of the tail size for the specific requirements. A larger variety of flap angles measured for the AEO, as well as for the OEI condition allow for a brighter flap angle variation. Static turning data is required for the calculation of lift and thrust at zero airspeed, where C_μ is not defined (section 2.1). Table 28 (appendix D) gives an overview about important operational conditions available from the experiments discussed in chapter 2.3 and can be used as an aid for the decision which data to use.

4.1.2 Determination of Aerodynamic Coefficients from Wind-Tunnel Data

For all wind-tunnel experiments, the lift coefficient of the wing fuselage configuration $C_{L_{WF_{WT}}}$, the drag coefficient $C^*_{D_{WT}}$ and the pitching moment coefficient $C_{m_{WT}}$ are available as a function of C_μ and α for different flap angles δ_f. Additionally, the static turning characteristics are given for different flap angles. An example of a low speed polar is presented in Figure 28 for a flap angle of δ_f=30°. From this low-speed polar, for any C_μ, α, δ_f available, the aerodynamic coefficients $C_{L_{WF_{WT}}}$, $C^*_{D_{WT}}$ and $C_{m_{WT}}$ can be determined. For values for C_μ, α, δ_f that are between the measured points, the aerodynamic coefficients are retrieved by linear interpolation. The angle of attack for the example presented in Figure 28 is α=10° and the jet momentum coefficient C_μ=1.5. The according values for the aerodynamic coefficients are $C_{L_{WF_{WT}}}$=3.9, $C^*_{D_{WT}}$=-0.9 and $C^{ref}_{m_{WT}}$=0.1.

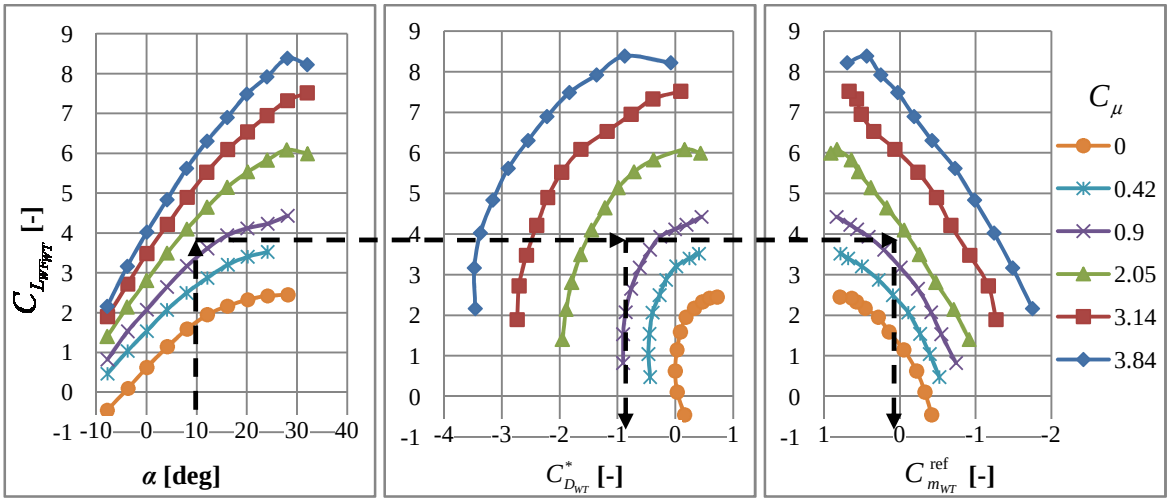

Figure 28. Interpolation in low-speed aerodynamic polar, USB with AEO, δ_f=30°

For the integration of this data into a modeling environment, the experimental data is stored in multidimensional look-up tables. The parameters that are varied in the experiments are the flap angle δ_f, the jet momentum coefficient C_μ and the angle of attack α. These variables are the input dimensions of the look-up table. The results of the wind-tunnel experiments are the lift, drag, and pitching moment coefficients as well as the static turning characteristics which represent the output dimensions of the look-up table. For the usage of this data for numerical calculations or trade-studies, interpolation between the available data points is required. Modern software environments allow for a simple integration of such multidimensional look-up tables and provide different methods for interpolation. Linear interpolation is the simplest method and gives sufficient fidelity, if enough data points are available. For C_μ it is important to remember that this parameter is a function of the speed and engine jet momentum for a given reference area, which causes a permanent change of the aerodynamic coefficients with the speed.

Table 3 summarizes the input and output dimensions for a look-up table generated from blown flaps wind-tunnel data. If data from other origins such as for example CFD is organized in the same way, they can be applied to the methods for the calculation of take-off and landing performance presented in the sections.

Table 3. Input and output dimensions for the calculation of the low-speed aerodynamic coefficients

Input Dimensions	Output Dimensions
δ_f	$C_{L_{WF_{WT}}}$
C_μ	$C^*_{D_{WT}}$
α	$C^{ref}_{m_{WT}}$
	η_t
	δ_f

The lift coefficient of the wing-fuselage configuration either with AEO or with OEI is retrieved directly from the respective tail-off low-speed polar:

$$C_{L_{WF}} = C_{L_{WF_{WT}}} \tag{6}$$

The aircraft lift coefficient is retrieved from the lift coefficient of the wing fuselage configuration and the HT lift coefficient that is required to trim the aircraft longitudinally:

$$C_L = C_{L_{WF}} + C_{L_h} \cdot \frac{S_h}{S} \tag{7}$$

The pitching moment of the wing fuselage configuration C_m is calculated directly from the respective low-speed polar:

$$C_m^{\text{ref}} = C_{m_{WT}}^{\text{ref}} \tag{8}$$

The pitching moment coefficient of the wind-tunnel model is referred to the respective reference point, given in the wind-tunnel data relative to the mean aerodynamic chord (*MAC*).

For the calculation of the aircraft drag coefficient C_D^*, some corrections and additional considerations which are documented in the next section are proposed.

4.1.3 Corrections of Wind-Tunnel Data

The drag coefficient provided with the wind-tunnel data represents the respective wind-tunnel model. Corrections are required to assure comparability and to account for differences between the modeled aircraft and the wind-tunnel models. Ram drag correction is carried out to ensure comparability between the different wind-tunnel models. Minimum drag coefficient correction is suggested to allow for a specific modeling of the minimum drag coefficients and a detailed drag breakdown is proposed to allow for the calculation of the drag for different flap, slat and control surface deflections.

A. Ram Drag

Engine ram drag (or intake momentum drag) is caused by scooping up the air and accelerating it relative to the undistributed condition (Stinton 1988, p. 152). Ram drag is equals the engine mass flow multiplied with the free stream velocity:

$$RD = \dot{m} \cdot v \tag{9}$$

Especially for high BPR engines, the ram drag has a significant contribution to the forces acting on the aircraft.

The problem with the wind-tunnel data and the ram drag is that some wind-tunnel data have the ram drag of the wind-tunnel engine included in $C^*_{D_{WT}}$, for example the data of NASA TM X-62419 (Aoyagi, Falarski et al. 1975). Using $C^*_{D_{WT}}$ including the ram drag of the wind-tunnel for aircraft design would scale the ram drag of the wind-tunnel engine with the wing reference area, as $C^*_{D_{WT}}$ is defined relative to the wing area. This would not represent the engine's physical behavior, as the ram drag scales with the engine mass flow.

Therefore, the drag coefficient of the wind-tunnel models $C^*_{D_{WT}}$ has to be corrected for the ram drag coefficient of the wind-tunnel engines $C_{D_{RD_{WT}}}$ giving the ram-drag corrected drag coefficient $C^*_{D_{RDC}}$:

$$C^*_{D_{RDC}} = C^*_{D_{WT}} - C_{D_{RD_{WT}}} \tag{10}$$

The ram drag coefficient of the wind-tunnel engines $C_{D_{RD_{WT}}}$ is given with the experimental data. The correction of the wind-tunnel data for ram drag has the advantage that it allows for the investigation of different engines that have different ram drag characteristics, for example due to different BPRs. The modeling of the ram drag in this method is described in section 4.3.

B. Minimum Drag Coefficient

Table 4 shows the minimum drag coefficients $C_{D0_{WT}}$ of selected wind-tunnel models in take-off and landing configuration for C_μ=0 (no blown flaps effects). The USB and the EBF model have the same minimum drag coefficient for take-off configuration. The EBF model has a higher minimum drag coefficient in the landing configuration and has the spoilers deflected, while the USB model has no deflected spoilers.

Table 4. Minimum drag coefficients of selected wind-tunnel models (Aoyagi, Falarski et al. 1975), (Aoyagi, Falarski et al. 1973), (Vogler 1976), (Chin, Aiken et al. 1975)

	take-off	landing	spoiler
USB	0.18	0.3	no
EBF	0.18	0.4	yes
AIBF	0.15	0.2	no
IBF	0.1	0.15	no

The AIBF and IBF models have a significantly lower minimum drag coefficient in take-off configuration as well as in landing configuration as they have no engines installed. The

minimum drag coefficients of the models are very high compared to typical data for commercial aircraft in take-off configuration. Typical values for minimum drag are approximately C_{D0}=0.06 in take-off configuration including landing gear, and approximately C_{D0}=0.1 in landing configuration including landing gear (Roskam 1985a, p. 127). Additionally, the fact that the models are measured for different spoiler deflections and that the AIBF and IBF model do not have engines installed makes a comparison of the different models based on the original data difficult.

For this reason the ram-drag-corrected drag coefficient $C^*_{D_{RDC}}$ is corrected for the minimum drag coefficient of the respective wind-tunnel model $C_{D0_{WT}}$ giving the corrected drag coefficient $C^*_{D_{corr}}$ (see also Figure 29):

$$C^*_{D_{corr}} = C^*_{D_{RDC}} - C_{D0_{WT}} \tag{11}$$

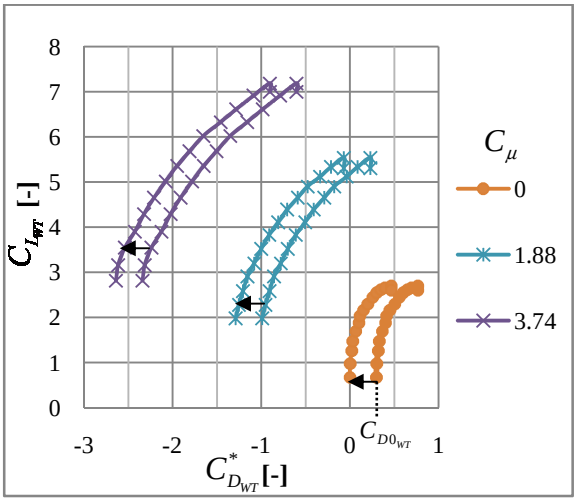

Figure 29. Minimum drag coefficient correction

Minimum drag coefficients that account for the minimum drag of the clean aircraft $C_{D0_{clean}}$, drag due to flaps ΔC_{D0_f}, landing gear $\Delta C_{D0_{LG}}$, spoilers $\Delta C_{D0_{Sp}}$ and the additional drag due to control flaps deflection (vertical tail VT, horizontal tail HT, and aileron) are then added to the corrected drag coefficient $C^*_{D_{corr}}$ of equation (11) giving the blown flaps drag coefficient of the aircraft C^*_D:

$$C^*_D = C^*_{D_{corr}} + C_{D0_{clean}} + \Delta C_{D0_f} + \Delta C_{D0_{LG}} + \Delta C_{D0_{Sp}} + \Delta C_{D_v} + \Delta C_{D_h} + \Delta C_{D_{ail}} \tag{12}$$

This approach allows for a consistent modeling of the minimum drag for different blown-flaps systems. Additionally, it allows for the study of different flap and spoiler deflections,

which is important for the conceptual design of blown-flaps aircraft because of the low speed operation. Minimum drag coefficients of the clean configuration can be for example calculated according to Torenbeek (Torenbeek 1982, Appendix F), which are documented in section 4.6.1. The contributions of the extended flap and landing gear are calculated according to Torenbeek (Torenbeek 1982, Appendix G).

The aileron, rudder and elevator are considered as plain flaps. Their minimum drag contributions can be calculated for example according to Roskam (Roskam 1985c, p. 82):

$$\Delta C_{D0_{cf}} = \Delta c_{d0_{\varphi_{25}=0}} \cdot \cos(\varphi_{25}) \cdot \frac{S_{cf}}{S} \tag{13}$$

Hereby, $\Delta c_{d0_{\varphi_{25}=0}}$ is the two-dimensional minimum drag increment of the flap section as a function of the relative flap chord c_{cf}/c and the control flap deflection δ_{cf} (see appendix Figure 101). For ailerons the ratio of the flapped area to the reference area is the span factor K_b (see Figure 102, appendix A), for example taken from US DATCOM (Finck 1978, p. 6.1.4.1-15).

The lift induced drag increment due to rudder or elevator deflection is:

$$\Delta C_{Di_{cf}} = \frac{1}{\Pi \cdot AR \cdot e} \cdot C_{L_{cf}}^2 \cdot \frac{S_{cf}}{S} \tag{14}$$

For the VT the effective aspect ratio has to be used (Torenbeek 1982, p. 53). The effective aspect ratio (*AR*) accounts for the better induced drag characteristics of T-tails. The impact of the aileron deflection on the aircraft lift is neglected, as it is assumed that the assymetric lift contributions of the aileron compensate each other. With respect to the comparison of the overall mission performance of aircraft with different blown-flaps systems this effect is considered as secondary. However, this effect has to be considered for detailed design.

Usually the function of spoilers is to generate rolling moments and drag during landing. For wing-integrated spoilers these effects are strongly coupled with lift loss. On the one hand, drag generation during landing can be advantageous for blown-flaps aircraft, as the thrust during landing can be increased which increases the lift (Gologan, Stagliano et al. 2009). On the other hand, wing spoiler deflection decreases the lift which is unfavorable. For this reason, fuselage-installed split spoilers that generate drag but do not decrease the lift are proposed. The additional drag of the spoilers can be treated as a free variable. However, the drag and lift loss of wing-installed spoilers could also be calculated according to US DATCOM (Finck 1978).

4.1.4 Static Turning

Static turning measurements are important for the calculation of the forces acting on the aircraft between v=0 and v=v_{min} (see section 2.1). While for EBF and USB the static turning characteristics (η_t and δ_j) are given for different flap angles (see Table 5), these data are not available for AIBF and IBF systems. Static turning is especially important for the take-off flap settings. Static turning data is not required for landing, as the engines are in idle during landing deceleration and the aerodynamic forces at zero airspeed are not required for landing field length calculation.

Johnson shows with the help of wind-tunnel data that the static turning characteristics are also representative for the aerodynamic characteristics under forward speed conditions (Johnson 1972). To determine the static turning characteristics, it is assumed that the aerodynamic characteristics under forward speed conditions also give an indication of the static turning characteristics at zero airspeed.

Table 5. Static turning characteristics of wind-tunnel models with EBF (Aoyagi, Falarski et al. 1973) and USB (Aoyagi, Falarski et al. 1975)

	EBF		USB	
δ_f	20°	30°	30°	75°
δ_j	12°	20°	26°	59°
η_t	80 %	79 %	98 %	97 %

Figure 20 (page 19) or Chin (Chin, Aiken et al. 1975) show that IBF and AIBF systems have better aerodynamic characteristics than EBF systems or USB systems at the same jet momentum coefficients. Therefore, it is very likely that the static turning characteristics of AIBF and IBF systems are also better. For this reason, the conservative assumption is made that the IBF and AIBF systems have the same thrust recovery factor as the USB system (η_t=98 % for δ_f =30°) and similar jet turning angle δ_j characteristics relative to the respective flap deflection angle.

4.1.5 OEI Characteristics

OEI aerodynamic coefficients are available for EBF and USB systems from the wind-tunnel experiments, while the aerodynamic coefficients for OEI are not available for IBF and AIBF systems. Nevertheless, the aerodynamic coefficients for this critical flight condition can be calculated by the use of a lower jet momentum for the calculation of the aerodynamic coefficients. This assumes that in the case of engine failure, uniform distribution of the remaining jet can be realized. The magnitude of the remaining jet

momentum on each side of the wing is dependent on the OEI cross ducting system. A cross ducting system is required for aircraft with AIBF or IBF to assure uniform distribution of the remaining jet and to reduce the rolling moment. The following two cross-ducting options are discussed within this thesis for four-engine aircraft, as example, while the general idea also applies to aircraft with two engines.

Option 1:

For an aircraft with four engines, cross-ducting of the two engines on each side means that the half-wing where the engine fails has only 25 % of the total AEO jet momentum $\dot{m}_j \cdot v_j$ available, while the other half-wing has 50 % of the total AEO jet momentum available (see Figure 30). In total, the aircraft has 75 % of the AEO jet momentum available. A rolling moment has to be compensated for by the ailerons and a yawing moment has to be compensated for by the vertical tail due to the asymmetric lift and thrust production.

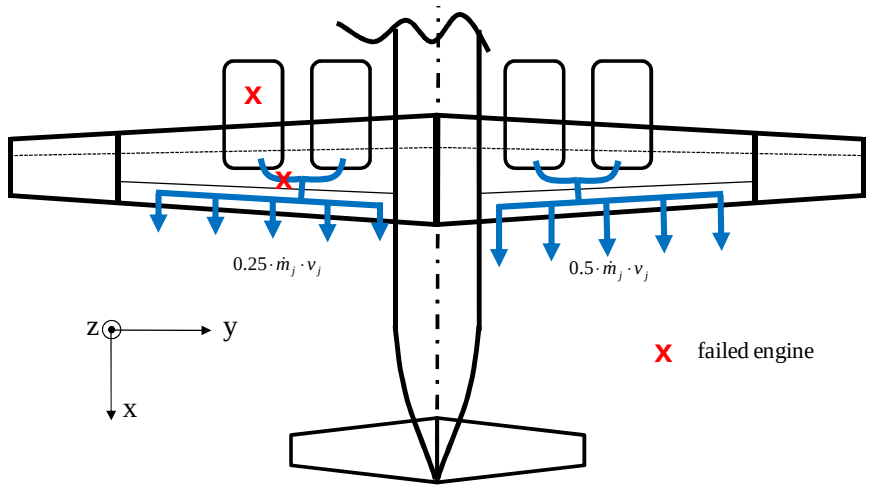

Figure 30. Cross-ducting for AIBF and IBF four-engine aircraft, option 1

For this asymmetric flight condition, lift, drag and pitching moment are calculated separately for each half-wing from the wind-tunnel data for the respective jet momentum coefficient. The sum of the half-wing data gives the total lift, drag and pitching moment coefficient at OEI condition.

Option 2:

Cross-ducting of all engines means that, under OEI conditions, the aircraft has 75 % of the jet momentum available with AEO (see Figure 31), while neither a rolling moment nor a yawing moment occur. The disadvantages are higher weight and higher pressure losses due to longer ducts.

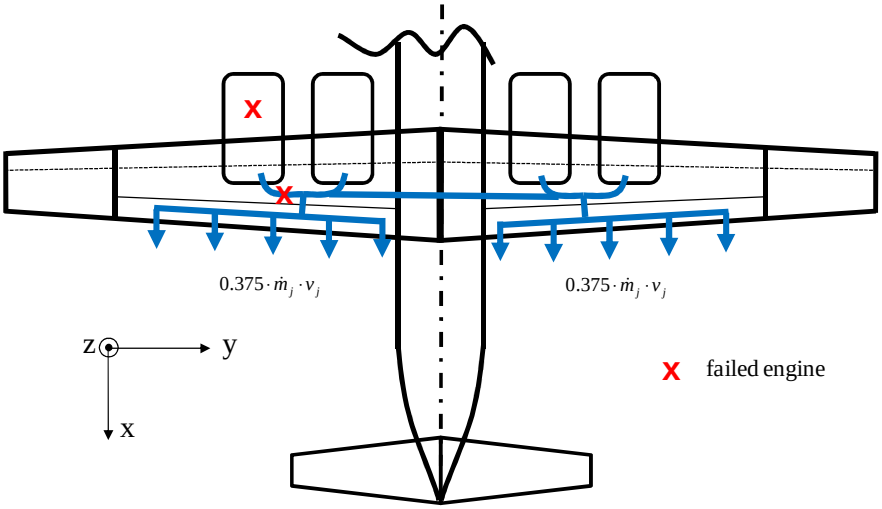

Figure 31. Cross-ducting for AIBF and IBF four-engine aircraft, option 2

For this symmetric flight condition the jet momentum is reduced as documented above. The aerodynamic coefficients are then calculated from equations (7), (8) and (12), for the reduced jet momentum.

4.1.6 Effect of Bypass Ratio and Engine Size

The effect of the BPR, which is strongly coupled to the size of the engine, is of special interest, as the general trend is towards turbofan engines with increased BPR for cruise efficiency reasons. The BPR has different effects on the low-speed performance of the investigated blown-flaps systems. Therefore its effect has to be considered in the conceptual design to some degree.

For EBF systems, increasing BPR means that less jet air affects the flap due to higher jet area. Therefore, less engine exhaust is turned downwards. As a consequence, the lift is lower for higher BPR, while the thrust available in the forward direction is slightly higher. (Johnson 1972, p. 46)

This effect was measured in a wind-tunnel experiment for the BPRs 6.2 and 10 (Johnson 1975). In Figure 32 one can see that the wind-tunnel model with a BPR of 10 produces always less lift but more thrust than the model with BPR=6.2 for the same jet momentum coefficient and the same angle of attack. By the use of these data for the above BPRs and by interpolation, the effect of the BPR ratio will be modeled to determine its impact on the overall mission performance.

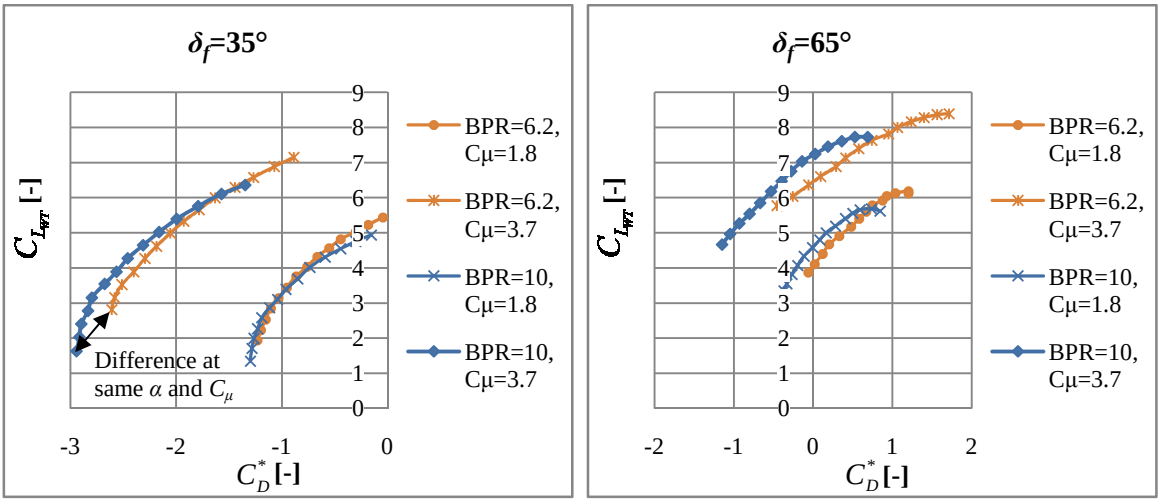

Figure 32. Comparison of drag polar of EBF wind-tunnel model with different BPRs

For AIBF and IBF systems, the BPR mainly impacts the jet momentum available for the jet flaps. A higher BPR for an IBF system that uses bypass air or the AIBF system means a higher jet momentum available for the jet flap, as more jet momentum is available in the bypass of the engine. For these systems the impact of BPR is represented in the engine model that provides the jet momentums required for the calculation of the aerodynamic coefficients (see section 4.3). For these systems, however, limitations for BPR result from the fan pressure ratio, which will also be discussed there.

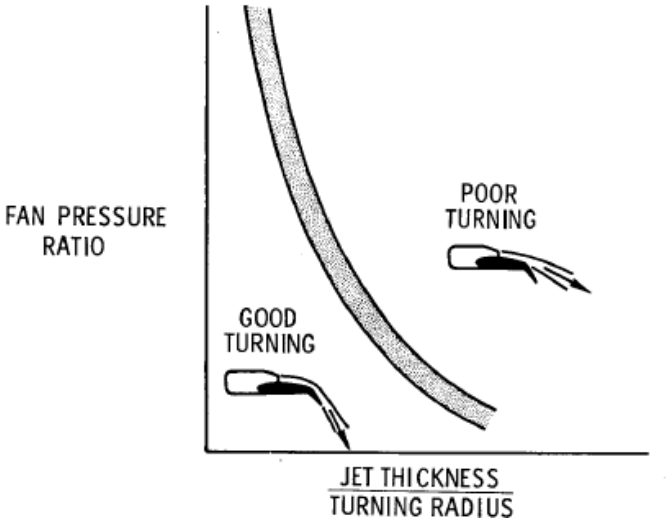

Figure 33. Turning characteristics of USB jet flap (Phelps 1972, p. 105)

The effect of BPR on the aerodynamic performance of USB aircraft is described only qualitatively in the literature. Figure 33 schematically shows how the turning characteristics of USB aircraft depend on the fan pressure ratio (which is strongly coupled with BPR) and the ratio of the jet thickness to the turning radius. This figure indicates that

good turning can be obtained with the use of engines with lower pressure ratios (higher BPRs) and thicker exhaust jets. Consequently, the use of high BPR engines does not require the very thin jet sheet and the related flow distributing nozzles that are required for turbojet installations with low BPRs. (Phelps 1972, p. 99)

However, as Figure 33 shows quantitative correlations only and no other information is available in the literature, the impact of the BPR on the low-speed aerodynamic coefficients of USB aircraft is not considered in this work. The data of the wind-tunnel experiment are used “as is”, which is a conservative approach for engines with high BPRs, as a higher BPR (lower fan pressure ratio) could even improve the turning characteristics. For a detailed design the BPR and the jet thickness is a parameter combination that should be optimized. However, the impact of the BPR on the engine gross thrust is modeled (see section 4.3) thus providing a certain impact of the BPR on the aerodynamic performance.

4.2 Low-Speed Control

Blown-flaps aircraft operate at lower speeds compared to conventional take-off and landing (CTOL) aircraft, which leads to lower effectiveness of the control surfaces due to the associated lower dynamic pressure. In the case of the OEI condition, blown-flaps aircraft as well as conventional aircraft suffer from thrust loss, which causes a yawing moment. Additionally, blown-flaps aircraft suffer from a loss in lift, which causes a rolling moment. The nose-down pitching moment of the wing-fuselage configuration of a blown-flaps aircraft is higher than for conventional aircraft, which requires a larger horizontal tail (HT). Longitudinal static stability required also impacts the HT size. For these reasons the low-speed control has to be considered already in the conceptual design.

This section documents how the rolling and yawing moments as well as the pitching moments are calculated from the low-speed aerodynamic data. Subsequently how the control surface coefficients required and the longitudinal static stability margin are calculated from the resulting moments is documented. Finally, an approach for the sizing of the tail and the different conditions considered therefor are documented.

4.2.1 Rolling and Yawing Moments with One Engine Inoperative

A. USB and EBF

The USB and EBF systems have similar OEI characteristics. In the case of critical engine (CE) failure, lift is lost on the corresponding side of the wing (see Figure 34). A rolling moment results due to the loss in lift, depending on the position of the engine.

Additionally, the vertical tail (VT) side-force that compensates the yawing moment increases the rolling moment. The rolling moment has to be compensated for by aileron deflection.

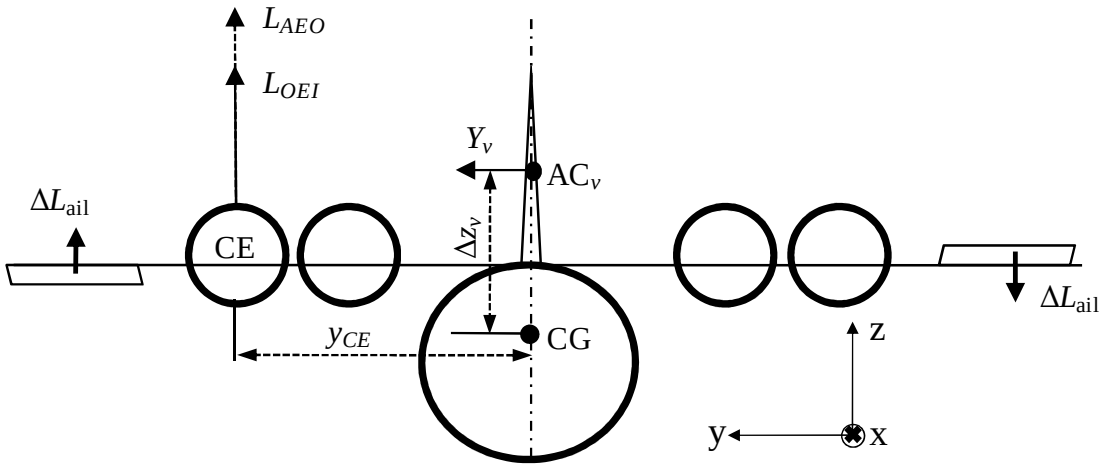

Figure 34. Lift-loss and rolling moment in the case of engine failure for USB and EBF

The rolling moment that results from the lift loss is calculated from the difference in lift coefficients of the experimental data with AEO and OEI under the respective flight condition and the contribution of the VT side force:

$$M_{x_{OEI}}^{CG} = (C_{L_{OEI}} - C_{L_{AEO}}) \cdot q \cdot S \cdot y_{CE} - C_{Y_v} \cdot q \cdot S_v \cdot (z_{AC_v} - z_{CG}) \tag{15}$$

Thereby, it is assumed that the lift loss acts at the position of the critical engine y_{CE} which, according to wind-tunnel data, is a conservative estimation for USB (Phelps 1972, p. 110) as well as for EBF (Parlett 1972, p. 67). In both cases, the actual rolling moments measured in the wind-tunnel were slightly lower than the rolling moments calculated from the lift loss. $C_{L_{AEO}}$ and $C_{L_{OEI}}$ are calculated from the respective wind-tunnel polar with equation (7).

Additionally to the rolling moment, engine failure causes a yawing moment due to asymmetric thrust loss, which is calculated from the difference between the drag forces and the wind-tunnel data for AEO and OEI condition. Thereby, the fact that the failed engine causes additional wind-milling drag D_{wm} has to be considered:

$$M_{z_{OEI}}^{CG} = \left(\left(C_{D_{AEO}}^{*} - C_{D_{OEI}}^{*} \right) \cdot q \cdot S - D_{wm} \right) \cdot y_{CE} \tag{16}$$

$C_{D_{AEO}}^{*}$ and $C_{D_{OEI}}^{*}$ are calculated with equation (12) for the respective flap deflection and angle of attack.

B. AIBF and IBF

For the asymmetric flight condition that can occur for AIBF and IBF, the lift, drag and pitching moment are calculated separately for each side of the wing from the wind-tunnel data for the respective jet momentum coefficient according to section 4.1.5. The resulting rolling moment and the yawing moment are calculated from the differences of lift respectively drag of the OEI flight condition and the AEO flight condition in analogy to equations (15) and (16).

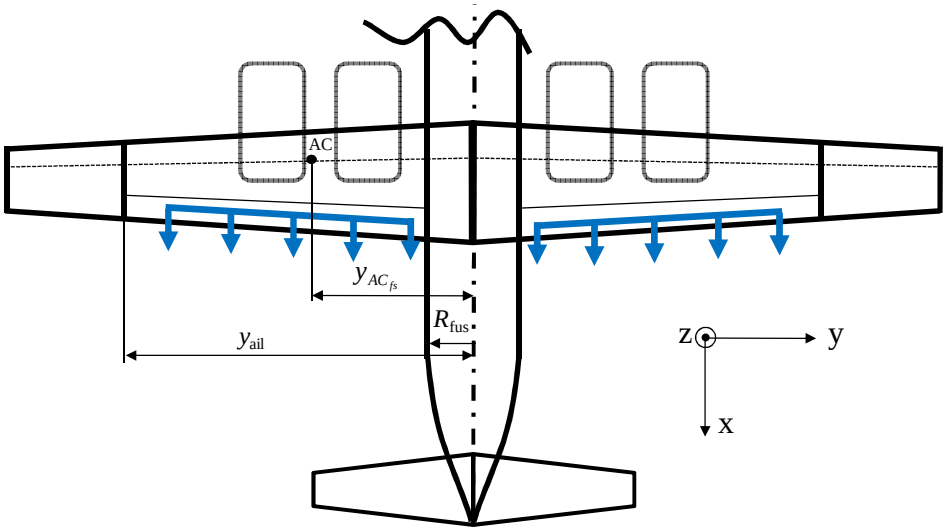

Figure 35. Definitions for the calculation of the AC of flapped section for IBF and AIBF aircraft

Thereby the fact that the lever arm of the forces is the aerodynamic center (AC) of the AIBF/IBF flapped section has to be considered (Figure 35). The spanwise position of the AC of the flapped section calculated for example with the following modified approximation based on a method taken from Schmitt (Schmitt 2005):

$$y_{AC_{fs}} = R_{fus} + \frac{\left(y_{ail} - R_{fus}\right)}{6} \cdot \left(\frac{1+2\cdot\lambda}{1+\lambda}\right) \tag{17}$$

4.2.2 Pitching Moment

The pitching moment of the wing-fuselage configuration is

$$M_{y_{WF}}^{CG} = q \cdot S \cdot C_m^{ref} \cdot MAC + q \cdot S \cdot C_{L_{WF}} \cdot \left(\bar{x}_{CG} - \bar{x}_{ref}\right) \cdot MAC \tag{18}$$

where the center of gravity of the aircraft $\bar{x}_{CG}$ and the pitching moment reference point $\bar{x}_{ref}$ are given relative to *MAC*. The pitching moment coefficient C_m^{ref} and the lift coefficient of the wing-fuselage configuration $C_{L_{WF}}$ are taken directly from the tail-off wind-tunnel polar (equations (6) and (8)). The calculation of the pitching moment of the

wing-fuselage configuration is important for tail sizing, as the tail has to be large enough to trim the pitching moment (see equation (22)). The critical flight stages considered are discussed in section 4.2.5.

4.2.3 Control Surface Coefficients Required

In this section the control surface coefficients required to trim the moments documented in the previous section are discussed.

A. Ailerons

The function of the ailerons is to generate the rolling moment that compensates the rolling moment due to the OEI condition. The rolling moment due to aileron deflection is:

$$M_{x_{\text{ail}}}^{CG} = q \cdot S \cdot b \cdot C_{l_{\text{ail}}} \tag{19}$$

The aileron rolling moment coefficient $C_{l_{\text{ail}_{\text{req}}}}$ required to trim the aircraft is calculated with equations (15) and (19):

$$C_{l_{\text{ail}_{\text{req}}}} = (C_{L_{OEI}} - C_{L_{AEO}}) \cdot \frac{y_{CE}}{b} - C_{Y_v} \cdot \frac{S_v \cdot (z_{AC_v} - z_{CG})}{S \cdot b} \tag{20}$$

Various methods are available for the calculation of the maximum rolling moment coefficient available $C_{l\,\max_{\text{ail}}}$ based on the area of the aileron section and the aileron layout, for example according to US DATCOM (Finck 1978, p. 6.2.1.1-4) or Schlichting and Truckenbrodt (Schlichting and Truckenbrodt 2001, p. 453-454).

B. Horizontal Tail

The function of the HT is to trim the aircraft longitudinally. The HT pitching moment is:

$$M_{y_h}^{CG} = q \cdot S_h \cdot C_{L_h} \cdot l_h \tag{21}$$

Thereby the HT lever arm l_h is the distance between the HT aerodynamic center and the actual position of the center of gravity x_{CG}. The HT lift coefficient $C_{L_{h_{\text{req}}}}$ required to trim the aircraft longitudinally is calculated from the equations (18) and (21):

$$C_{L_{h_{\text{req}}}} = \frac{S}{S_h} \cdot \frac{MAC}{l_h} \cdot \left[C_m^{\text{ref}} + C_{L_{WF}} \cdot \left(\bar{x}_{CG} - \bar{x}_{\text{ref}} \right) \right] \tag{22}$$

The maximum lift coefficient of the HT $C_{L\max_h}$ that is available for the trimming of the aircraft is depending on the selected elevator layout.

C. Vertical Tail

The VT compensates the yawing moment in the case of the OEI condition. The yawing moment generated by the VT is:

$$M_{z_{Fin}} = C_{Y_v} \cdot q \cdot S_v \cdot \left(x_{AC_v} - x_{CG}\right) \tag{23}$$

The VT side force coefficient required to trim the aircraft is calculated from equations (16) and (23):

$$C_{Y_{v\,\mathrm{req}}} = \left[\left(C^*_{D_{AEO}} - C^*_{D_{OEI}}\right) \cdot q \cdot S - D_{wm}\right] \cdot \frac{y_{CE}}{q \cdot S_v \cdot \left(x_{AC_v} - x_{CG}\right)} \tag{24}$$

For the IBF and AIBF aircraft, y_{CE} has to be replaced by $y_{AC_{fs}}$. The maximum side force coefficient available $\Delta C_{Y_{v\max}}$ of the VT can be calculated with handbook methods, for example according to US DATCOM (Finck 1978, p. 6.1.1.3-4).

4.2.4 Longitudinal Static Stability

The longitudinal stability has to be considered for the sizing of the HT. The longitudinal stability margin is defined as:

$$\frac{x_N - x_{CG}}{MAC} = -\frac{C^{CG}_{m_\alpha}}{C_{L_\alpha}} \tag{25}$$

The aircraft lift-curve slope is (Torenbeek 1982, equation 9-6):

$$C_{L_\alpha} = C_{L_{\alpha_{WF}}} + C_{L_{\alpha_h}} \cdot \frac{S_h}{S} \cdot \left(1 - \frac{\partial \varepsilon}{\partial \alpha}\right) \cdot \frac{q_h}{q} \tag{26}$$

The lift-curve slope of the wing-fuselage configuration $C_{L_{\alpha_{WF}}}$ can be calculated directly from the lift-curve slope of the low-speed polar by the evaluation of the lift coefficient at two angles of attack in the linear region. The lift-curve slope of the HT can be calculated according to Torenbeek (Torenbeek 1982, Eq. E-8). A typical value for $\partial\varepsilon/\partial\alpha$ is 0.3; the ratio of the dynamic pressures is often assumed to be one.

The pitching moment derivative $C^{CG}_{m_\alpha}$ is calculated from the pitching moment derivative of the wing-fuselage configuration and the contribution of the HT:

$$C^{CG}_{m_\alpha} = C^{CG}_{m_{\alpha_{WF}}} + C_{L_{\alpha_h}} \cdot \left(1 - \frac{\partial \varepsilon}{\partial \alpha}\right) \cdot \frac{S_h \cdot l_h}{S \cdot MAC} \tag{27}$$

Thereby $C_{m_{\alpha_{WF}}}^{CG}$ can be calculated directly from the low-speed polar by the evaluation of the pitching moment coefficient and the lift coefficient at two different angles of attack:

$$C_{m_{\alpha_{WF}}}^{CG} = C_{m_{\alpha_{WF}}}^{\text{ref}} + C_{L_{\alpha_{WF}}} \cdot \left(\bar{x}_{CG} - \bar{x}_{\text{ref}}\right) \tag{28}$$

4.2.5 Tail and Aileron Sizing Approach

The size of the tail depends on the take-off and landing field length (or the take-off and approach speed) required. The lower the field length, the larger the tail has to be. Tail sizing is an iterative process, as its size is a function of the speeds related to take-off and landing, which are again a function of tail size. Therefore, the following approach is proposed for tail and aileron sizing (Figure 36):

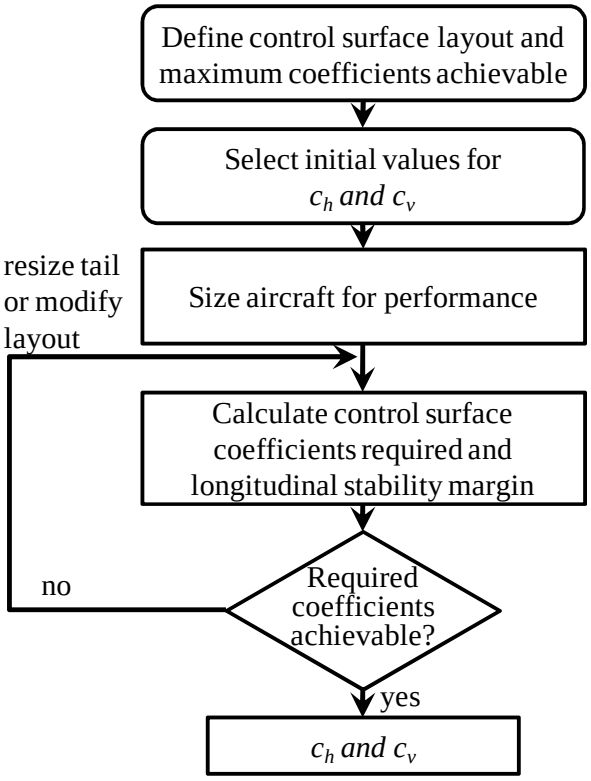

Figure 36. Flow chart for tail sizing approach

The layout of the control surfaces (c_f/c, maximum control flap deflection, t/c) and the related maximum coefficient achievable (according to the technology available) are defined first. Initial tail volume coefficients according to the data of a blown-flaps aircraft or a blown flaps conceptual study with similar take-off and landing requirements are selected. The aircraft is then sized for performance and the control surface coefficients required to trim the aircraft during the different flight stages and the longitudinal stability margin are calculated. The tail volume or aileron layout is then adapted until the required

coefficients and the longitudinal stability margin are achieved. If the resulting tail volumes differ from the initial values such that it impacts the take-off and landing performance significantly, the aircraft sizing for performance may be repeated.

The following flight conditions are considered for the sizing of the HT:

- HT lift coefficient required
  - to rotate the aircraft at v_{mc} and α=0° with AEO
  - to rotate the aircraft at v_{mc} and α=0° with OEI
  - for take-off with AEO at v_{mc}
  - for take-off with OEI v_{mc}
  - for take-off with AEO v_{TO}
  - for take-off with OEI v_{TO}
  - for MAwith AEO at v_{APP}
- Minimum longitudinal stability margin required for aft CG position at v_{TO} and v_{APP}

Minimum control speed v_{mc} and take-off speed v_{TO} are calculated in the balanced field length module. All flight stages that calculate the HT lift coefficient required are calculated for forward CG position as in this case the nose-down pitching moment of the wing-fuselage configuration is the highest.

For the sizing of the VT, the following flight stages are considered:

- VT side force coefficient required for trim of OEI condition at v_1 and α=0° (roll on runway)
- VT side force coefficient required for trim of OEI flight condition at v_{mc} and the corresponding angle of attack

The decision speed v_1 is determined in the balanced field length calculation.

For the sizing of the ailerons, the area of the aileron section is limited by the blown flaps section. For the aileron, its layout can be adapted if the required rolling moment coefficient cannot be provided by the actual layout. Options for aileron adaption can be for example a larger c_f/c, higher maximum deflection or even the introduction of blown ailerons to increase their effectiveness for very low take-off speeds.

Although additional cases may have to be considered for FAR-25 requirements, these cases already give an approximation of the tail size that is more sophisticated than the simple approach of sizing by historical data for tail volume coefficients.

4.3 Low-Speed Engine Models

For the take-off calculation of conventional turbofan aircraft, the engine net thrust as a function of Mach number (net thrust lapse) is required. An important parameter influencing the thrust-lapse is the bypass ratio (BPR). For conceptual design purposes, generic scalable net thrust lapse data are available as a function of the BPR in textbooks, e. g. (Jenkinson, Simpkin et al. 1999, pp. 203-217). Therein, the net thrust lapse characteristics are given relative to sea level static thrust T_0 to allow for engine scaling. Engine sizing effects on thrust lapse behavior are neglected in the first instance.

The net thrust lapse is not sufficient for blown-flaps aircraft. The engine gross thrust or the jet momentum of the bleed air which is taken off the engine have to be determined as a function of the Mach number. These parameters are required for the calculation of the jet momentum coefficient C_μ, which is needed for the calculation of the aerodynamic coefficients C_L, C_D^*, and C_m.

In this section, scalable low-speed engine characteristics are developed for different BPRs which provide the jet momentum characteristics required.

4.3.1 Basic Engine Models

Generic separate-flow as well as mixed-flow turbofan engines are modeled with the gas-turbine simulation software GasTurb 11 (Kurzke 2007a) to determine the jet momentums available for different BPRs and Mach numbers. Thereby, a burner exit temperature of 1,620 K, an overall pressure ratio of 30, and state of the art component efficiencies are assumed for the design condition. The engines are designed for a cruise condition of Ma=0.74 at an altitude of 31,000 ft. BPRs of 5.0, 7.5 and 10 are investigated to cover the large range of today's turbofan engines up to tomorrow's higher BPR engines.

The outer fan pressure ratio for the separate-flow engines is iterated to meet the ideal jet velocity ratio in design condition. This is a common approach in turbofan engine design (Kurzke 2007b):

$$\left(\frac{v_{18}}{v_8}\right)_{\text{ideal}} = \eta_{\text{Fan}} \cdot \eta_{\text{LPT}} \tag{29}$$

The ideal fan pressure ratio for the mixed-flow engines is iterated such that the ratio of bypass total pressure p_{t16} to core exit total pressure p_{t6} in the mixing plane equals one, which yields minimum mixing losses (Kurzke 2007b):

$$\left(\frac{p_{t16}}{p_{t6}}\right)_{\text{ideal}} = 1 \tag{30}$$

Table 6 shows the main data of the separate-flow engines and Table 7 for the mixed-flow engines simulated, including reference design thrust T_{des}^{*} and reference mass flow $\dot{m}_{\text{des}}^{*}$, reference sea level static thrust T_0^{*}, standard day corrected mass flow $\dot{m}_{\text{RSTD}}^{*}$, reference sea level specific thrust T_{SP}^{*} and the outer fan pressure ratio in design condition Π_{13}.

Table 6. Main data of the simulated separate-flow engines

BPR [-]	$\dot{m}_{\text{des}}^{*}$ [kg/s]	T_{des}^{*} [kN]	T_0^{*} [kN]	$\dot{m}_{\text{RSTD}}^{*}$ [kg/s]	T_{SP}^{*} [kN]	Π_{13} [-]
5	150	13.3	51.8	145	357	2.08
7.5	200	13.2	55.5	188	295	1.71
10	250	13.1	58.0	225	258	1.53

Table 7. Main data of the simulated mixed-flow engines

BPR [-]	$\dot{m}_{\text{des}}^{*}$ [kg/s]	T_{des}^{*} [kN]	T_0^{*} [kN]	$\dot{m}_{\text{RSTD}}^{*}$ [kg/s]	T_{SP}^{*} [kN]	Π_{13} [-]
5	150	13.9	54.5	148	368	1.81
7.5	200	13.8	58.8	192	306	1.59
10	250	13.6	61.2	229	267	1.45

For the same mass flow, the mixed-flow engines have slightly higher thrust and mass flow, while the fan pressure ratios are slightly lower.

Engine thrust scales with mass flow, which means that the specific thrust of an engine remains constant if an engine is scaled. Hence, the standard day corrected mass flow that is needed to generate a required static thrust T_0 can be scaled with constant specific thrust:

$$\dot{m}_{\text{RSTD}} = \frac{T_0}{T_{SP}^{*}} \tag{31}$$

This thrust-scaling approach neglects changes in component efficiencies due to Reynolds number effects that, in fact, occur when sizing an engine. For a detailed design of an aircraft, these effects are important with respect to *SFC* in cruise. For the determination of the general trends of the jet momentums relative to T_0, several simulations have shown that a potential change of component efficiencies can be neglected in the first instance.

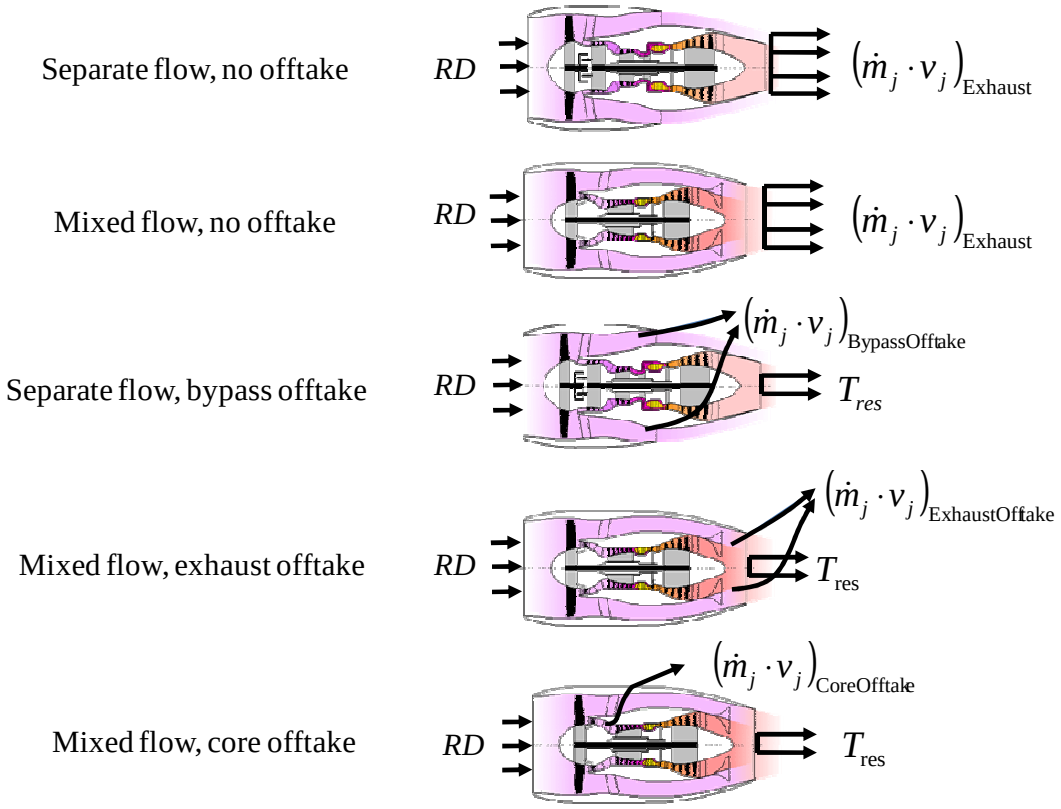

Figure 37. Jet momentums and ram drag during low-speed operation; figure based on GasTurb sketches (Kurzke 2007a)

Figure 37 schematically shows the different offtake options considered and the related jet momentums:

- The separate-flow and mixed-flow engines without bleed offtake represent the engines for the EBF and USB systems. The jet momentum of the entire exhaust $(\dot{m}_j \cdot v_j)_{Exhaust}$, which equals the engine gross thrust, affects the blown flaps and has to be determined.
- The separate-flow engine with the bypass offtake represents the AIBF system and the IBF system that uses bypass air. The jet momentum of the air that is taken off the bypass $(\dot{m}_j \cdot v_j)_{BypassOfftake}$ affects the blown flaps, the residual gross thrust of the engine T_{res} acts conventionally in a forward direction.

Additional options for the IBF system are:

- The exhaust offtake, where a certain amount of exhaust air is taken off the exhaust and ducted to the jet flaps. The jet momentum of the air taken off the exhaust $(\dot{m}_j \cdot v_j)_{ExhaustOfftake}$ affects the blown flap.

- The core offtake, where a certain amount of bleed air is taken off the core of the engine and ducted to the jet flaps. The jet momentum of the air taken off the core $\left(\dot{m}_j \cdot v_j\right)_{\text{CoreOfftake}}$ affects the blown flap.

For both last options, the residual gross thrust of the engine T_{res} acts conventionally in forward direction. For all systems the ram drag characteristics are additionally required, as ram drag is an important parameter for take-off and landing calculation.

Parametric studies for Mach number at sea level were performed with GasTurb 11 to determine these relevant jet momentums. The standard component maps that are provided with GasTurb 11 were used to model the off-design characteristics of the engines. The results are then normalized for the respective reference sea level static thrust T_0^* to generate thrust-scalable low-speed performance engine decks.

4.3.2 Separate-Flow and Mixed-Flow Engines without Offtake

Figure 38 shows the relative ram drag RD^*/T_0^* and the relative exhaust jet momentum $\left(\dot{m}_j \cdot v_j\right)^*_{\text{Exhaust}} / T_0^*$ characteristics for the separate-flow engines (no power-offtake) over Mach number. As expected, the ram drag of the engine increases with higher BPRs due to the increased engine frontal area. The engines with the higher BPRs show the stronger increase in gross thrust with increasing Mach number. The values of relative gross thrust and relative ram drag for the mixed-flow and separate-flow engines are very similar (see appendix B, Figure 103). The difference can be neglected in the first order for conceptual design. Therefore, the same characteristics can be used for the two different engine types.

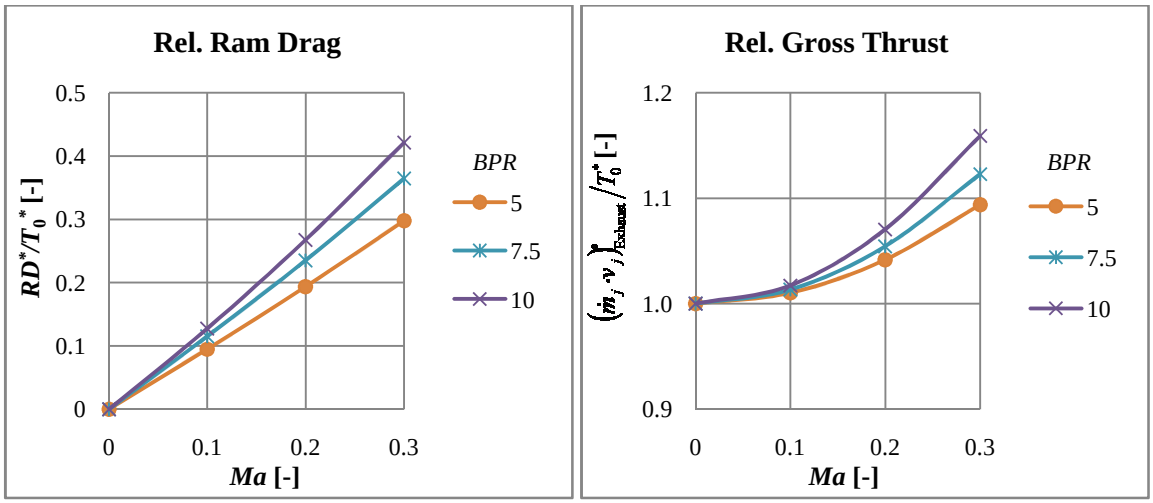

Figure 38. Relative ram drag and relative gross thrust over Mach number, separate-flow engines without offtake

With the characteristics of the reference engines given in Figure 38, the exhaust jet momentum and the ram drag of the engine can be scaled for any engine sea level static thrust:

$$\left(\dot{m}_j \cdot v_j\right)_{\text{Exhaust}} = T_0 \cdot \frac{\left(\dot{m}_j \cdot v_j\right)^*_{\text{Exhaust}}}{T_0^*} \tag{32}$$

$$RD = T_0 \cdot \frac{RD^*}{T_0^*} \tag{33}$$

The engine exhaust jet momentum $\left(\dot{m}_j \cdot v_j\right)_{\text{Exhaust}}$ calculated with equation (32) is used for the calculation of the jet momentum coefficient C_μ (equation (1)), which can be made for any speed during take-off and landing using the above characteristics. The residual gross thrust T_{res} for the EBF and USB engine is zero, as the entire engine gross thrust is used for the blown flaps.

4.3.3 Separate-Flow Engine with Bypass Offtake

For the AIBF system and the IBF system with bypass offtake, the entire bypass mass flow is taken off the engine and ducted to the jet flaps. Thereby, duct pressure losses have to be considered for the bypass. The residual gross thrust of the engine T_{res} and the jet momentum of the bypass offtake $\left(\dot{m}_j \cdot v_j\right)_{\text{BypassOfftake}}$ have to be determined. For the calculation of the bypass jet momentum, duct pressure losses have to be considered. Figure 39 shows the relative residual gross thrust of the engine T^*_{res} / T_0^* and the relative jet momentum of the bypass air taken off $\left(\dot{m}_j \cdot v_j\right)^*_{\text{BypassOfftake}} / T_0^*$ for the reference engines, simulated with GasTurb 11 for a bypass duct pressure loss of σ =-6 %.

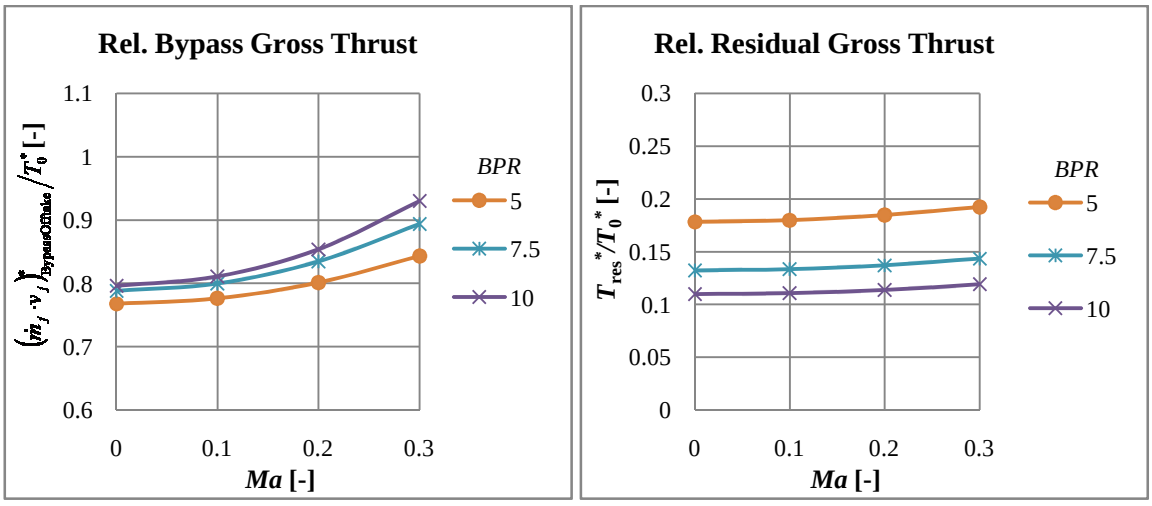

Figure 39. Relative bypass and residual gross thrust, separate-flow engines with bypass offtake, σ =-6 %

The sum of the relative bypass gross thrust and the relative core gross thrust equals the total relative gross thrust, which equals 1 for zero Mach number and zero pressure loss. For σ =-6 %, around 5.3 % of the thrust are lost for the BPR 5 engine, while for the BPR 7.5 engine the thrust loss is around 8 %, and 9.4 % respectively for the BPR 10 engine.

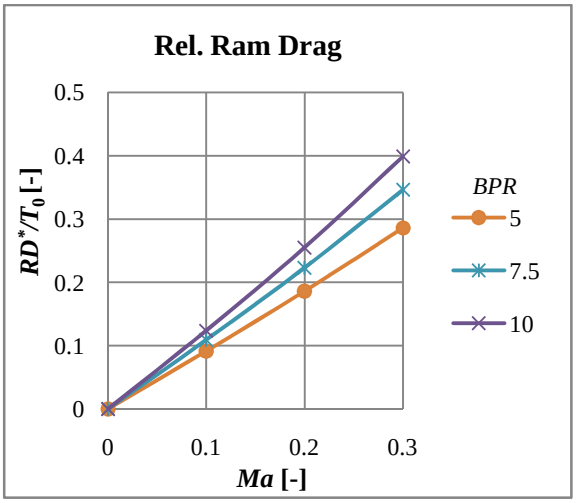

Figure 40. Relative ram drag, separate-flow engines with bypass offtake, σ =-6 %

The general characteristics of the relative ram drag are similar to the ram drag characteristic of the engine without offtake, while the absolute values are slightly lower due to lower total mass flow.

The jet momentum of the bypass offtake $\left(\dot{m}_j \cdot v_j\right)_{\text{BypassOfftake}}$ and the ram drag are calculated analogically to equations (32) and (33). The residual gross thrust of the engine T_{res} is calculated from Figure 39 with:

$$T_{\text{res}} = T_0 \cdot \frac{T_{\text{res}}^*}{T_0^*} \tag{34}$$

As documented in section 2.2.3, IBF systems use high-pressure air to achieve nearly Mach 1 at the nozzle, which corresponds to a pressure ratio of approximately 1.9 for bypass air (Waters, Anthony et al. 2009). Table 8 gives the outer fan pressure ratios of the separate-flow engine without pressure loss for different BPRs. One can see that the general trend to higher BPRs leads to lower outer fan pressure ratios, which is undesirable for IBF, as this leads to larger duct areas required.

Considering that even higher duct pressure losses than -6 % may have to be expected for an IBF system, the turbofan engine with the BPR 5.0 is the only engine that can achieve nearly Mach 1 at the nozzle of an IBF. The engine model with the high BPR is better

suited for the AIBF system, as the fan pressure ratio is low and lies in the region of the pressure ratios that were realized in the investigated wind-tunnel model (see section 2.2.4).

Table 8. Outer fan pressure ratio at sea level for separate-flow engines, σ =-6 %

BPR [-]	Π_{13} [-]
5	1.87
7.5	1.54
10	1.39

Duct pressure losses are a function of detailed duct design, which goes beyond the scope of conceptual design comparative studies. To allow for sensitivity studies of this parameter in conceptual design, the jet momentum characteristics are given for additional pressure losses in appendix B (Figure 104 to Figure 113).

4.3.4 Mixed-Flow Engine with Exhaust Offtake

For the IBF system, different bleed air offtake solutions have been realized. As presented in section 2.2.3, the Buffalo C-8A used the cold bypass air of a turbofan engine for the augmented jet flaps, as discussed in the previous section. The H.126 used the hot exhaust of a turbojet engine for the blown flaps. An offtake of the core exhaust only of the separate-flow engines is not favorable, since the core gross thrust contribution is very low (see Figure 39) for the engines investigated. This would result in very low jet momentum coefficients. Therefore, the mixed-flow engine is selected for the analysis of the exhaust offtake option. Table 9 shows the Mach numbers calculated with GasTurb for the exhaust offtake for an ideal offtake as well as for σ =-6 % and σ =-12 %. One can see that velocities approaching *Ma*=1 are only achievable with the BPR 5 engine.

Table 9. Mach number of exhaust offtake, mixed-flow engine

		Pressure loss σ		
		0 %	-6 %	-12 %
BPR [-]	5	0.93	0.88	0.81
	7.5	0.81	0.74	0.67
	10	0.72	0.65	0.56

An additional variable for exhaust offtake is the ratio of the mass flow that is taken off to the total engine mass flow τ. Figure 41 shows the relative gross thrust of the engine T_{res}^{*} / T_{0}^{*} and the relative jet momentum of the exhaust offtake $\left(\dot{m}_j \cdot v_j\right)_{\text{ExhaustOfftake}}^{*} / T_{0}^{*}$ that is taken off the engine with *BPR*=5 with the array parameter τ. The pressure loss for these characteristics is

σ =-6 %. The jet momentum of the exhaust offtake and residual gross thrust are calculated analogically to equations (32) and (34). Ram drag is calculated with the characteristics given in Figure 38.

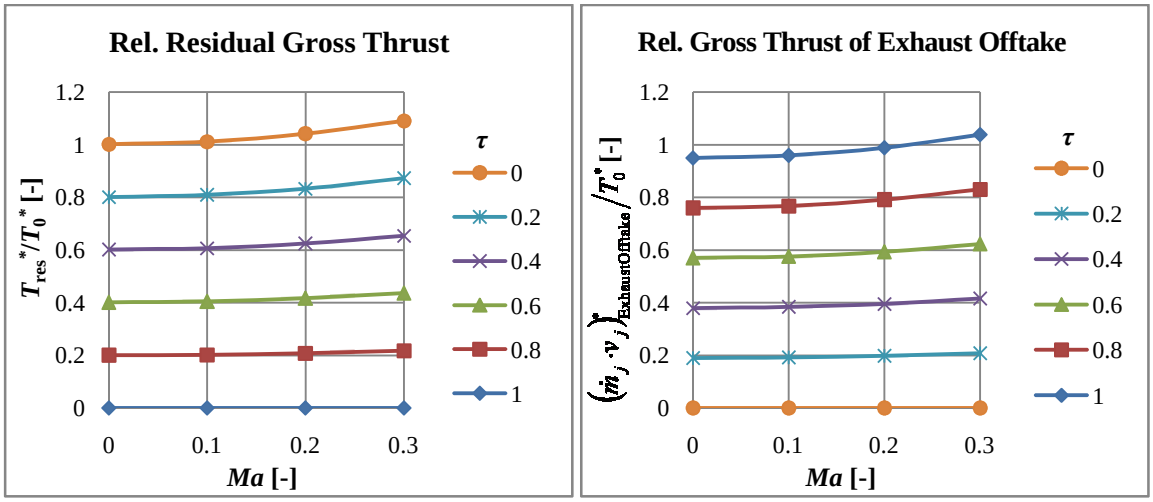

Figure 41. Relative residual and exhaust offtake gross thrust, mixed-flow engine, σ =-6 %

The sum of both thrust contributions is the total gross thrust, which at zero Mach number is lower than 1 due to the duct pressure losses. Around 5 % of the total gross thrust is lost for σ =-6 % compared to the engine reference gross thrust due to pressure losses if the entire exhaust is taken off the engine. Again, to enable sensitivity studies for the duct pressure losses, these engine decks are given for different pressure losses in appendix B (Figure 114 to Figure 116).

4.3.5 Mixed-Flow Engine with Core Bleed Offtake

The core engine offtake is analyzed as a possible additional solution. Figure 42 shows the relative residual gross thrust of the engine T_{res}^* / T_0^* and the relative jet momentum of the core bleed $\left(\dot{m}_j \cdot v_j\right)^*_{\text{CoreOfftake}} / T_0^*$ that is taken off the engine. The array parameter ξ is the ratio of the core mass flow that is taken off to the total core mass flow. The pressure loss of the air taken off is σ =10 %. One can see that this offtake option significantly reduces the residual thrust of the engine, while the jet momentum of the bleed air is very low (between 1.2 % and 4 % of T_0). At an offtake of 40 % of the core mass flow and static condition, only approximately 30% of the reference thrust is available, only. This is well in line with the general understanding that core air offtake in the compressor significantly decreases the engine thrust. Core offtake may be feasible for circulation control applications, where only very low offtake is required. For blown flaps applications it is not considered further.

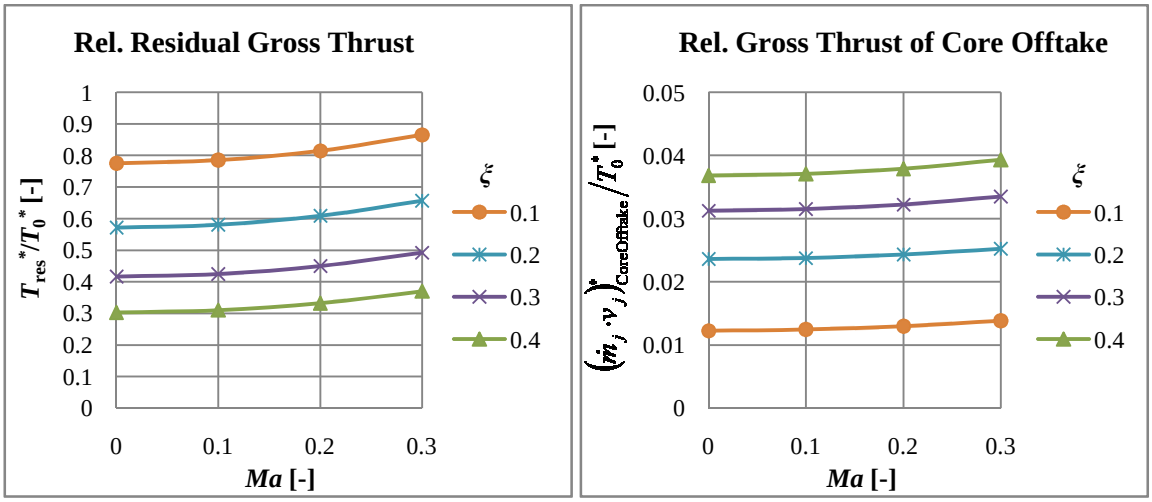

Figure 42. Relative residual gross thrust and core offtake gross thrust, separate-flow engine, *BPR*=10 engine, σ =-10 %

4.3.6 Conclusion

With respect to the blown-flaps systems investigated, the following conclusions for the engines investigated can be drawn from the parametric studies documented in this section:

- For USB and EBF systems the same characteristics can be used for conceptual design.
- For the AIBF system, the BPR 10 engine is best suited with respect to the required fan pressure ratios.
- For the IBF system with bypass air offtake as well as with exhaust offtake, the BPR 5 engine is best suited with respect to the required fan pressure ratios and nozzle Mach numbers.
- Core engine offtake makes no sense for the high jet momentums required.

4.4 Balanced Field Length and Climb Performance

For conventional take-off and landing (CTOL) aircraft the balanced field length (BFL) can be determined with simple handbook methods based on empirical data. As already stated in section 2.2.1, in contrast to a conventional aircraft, lift and thrust of blown-flaps aircraft are interdependent. Therefore, simple handbook methods based on empirical data of CTOL aircraft cannot be applied to blown-flaps aircraft (for further discussions on this topic see Ball et al. (Ball, Turner et al. 2008). Consequently, a physics-based approach is chosen for the calculation of the BFL. The following three cases according to FAR-25 are considered for the BFL calculation (Figure 43):

1) Take-off with all engines operative (AEO): Acceleration with AEO, rotation, and climb to 35 ft plus a 15 % margin
2) Take-off with one engine inoperative (OEI): Acceleration with AEO to decision speed v_1, acceleration to v_{TO} with OEI, rotation, and climb to 35 ft
3) Acceleration with AEO to v_1, 2 seconds reaction time, and deceleration to full stop

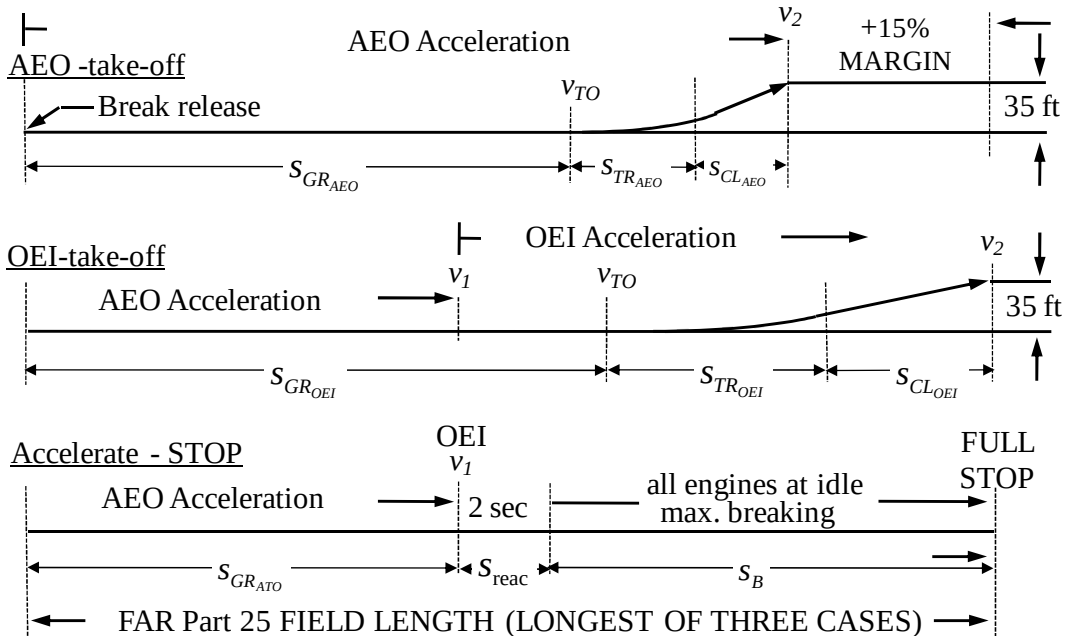

Figure 43. Considered cases for BFL calculation (Riddle, Innis et al. 1981)

Accordingly, the three take-off distances are calculated as follows:

$$s_{TO_{AEO}} = 1.15 \cdot \left(s_{GR_{AEO}} + s_{TR_{AEO}} + s_{CL_{AEO}} \right) \tag{35}$$

The take-off distance with OEI $s_{TO_{OEI}}$ is:

$$s_{TO_{OEI}} = s_{GR_{OEI}} + s_{TR_{OEI}} + s_{CL_{OEI}} \tag{36}$$

The distance traveled for aborted take-off is:

$$s_{TO_{ATO}} = s_{GR_{ATO}} + s_{reac} + s_B \tag{37}$$

Thereby, decision speed v_1 has to be iterated such that $s_{TO_{OEI}}$ equals $s_{TO_{ATO}}$. The longest distance of the three cases is the FAR-25 BFL.

First, the take-off speed is defined and its calculation documented, as it is an important parameter for BFL calculation. Subsequently, the methods for the calculation of the distance traveled during the above segments and the climb performance with AEO and OEI are documented.

4.4.1 Calculation of Take-Off Speed

In FAR-25, the speeds related to take-off speed, for example v_{TO} or the speed at the end of the second climb segment v_2, are defined as the stall speed v_S multiplied with a certain safety-factor k:

$$v = k \cdot v_{ST} \tag{38}$$

The stall speed is calculated based on the maximum lift coefficient $C_{L\max}$:

$$v_{ST} = \sqrt{\frac{W}{\frac{\rho}{2} \cdot S \cdot C_{L\max}}} \tag{39}$$

For CTOL aircraft $C_{L\max}$ is constant during take-off. Stall speed v_S is calculated analytically with equation (39). The speed at the end of the 2nd climb segment v_2 is subsequently calculated with equation (38) for k=1.2 according to FAR-25.

When applying this approach to blown-flaps aircraft, the following problems arise:

1) Stall speed cannot be calculated analytically, as $C_{L\max}$ is a function of speed and not given in analytical form.
2) Take-off speed has to be defined for OEI operation, as the aircraft has to generate enough lift, even if one engine fails. In a documentation of Quiet Short-Haul Research Aircraft (QSRA) take-off flight tests (Riddle, Innis et al. 1981), defining stall speed and the dependent speeds at OEI condition to account for this critical operational mode was proposed.
3) v_2 cannot be calculated with equation (38) and the common safety factor k=1.2, since $C_{L\max}$ at v_2 is lower than $C_{L\max}$ at v_S due to lower C_μ at v_2 (see equation (1)). Therefore, applying the definition above, the safety margin to stall at v_2 for a blown-flaps aircraft would be lower than the safety margin for a CTOL aircraft.

The third problem is illustrated based on experimental data gained from (Aoyagi, Falarski et al. 1975) for a USB wind-tunnel model in take-off configuration. Table 10 shows the evolution of jet momentum coefficient, lift coefficient, maximum lift coefficient, and the ratio of $C_L/C_{L\max}$ with increasing airspeed. Stall speed is 38.6 m/s, at this point the jet momentum C_μ is 2.63 and C_L equals $C_{L\max}$ (6.58). If the take-off speed v_{TO} was defined as $1.2 \cdot v_{ST}$, the jet momentum coefficient would be reduced to 1.83 at $1.2 \cdot v_{ST}$. Therefore $C_{L\max}$ would be reduced to 5.5 at $1.2 \cdot v_{ST}$. The lift coefficient required at $1.2 \cdot v_{ST}$ is 4.57, which is 83% of $C_{L\max}$. The lift coefficient at $1.2 \cdot v_{ST}$ of an aircraft with constant $C_{L\max}$ is 69 %

(1/1.2²) of C_{Lmax}. Thus, the blown-flaps aircraft would operate closer to stall than a conventional aircraft.

Table 10. Evolution of jet and lift coefficients with increasing speed for USB wind-tunnel model

v/v_{ST} [-]	v [m/s]	C_μ [-]	C_L [-]	C_{Lmax} [-]	C_L/C_{Lmax} [-]
1	38.6	2.63	6.58	6.58	1.00
1.05	40.5	2.39	5.97	6.20	0.96
1.1	42.4	2.18	5.44	6.00	0.91
1.2	46.3	1.83	4.57	5.50	0.83
1.3	50.2	1.56	3.89	5.00	0.78

This example shows that if the safety margin was defined relative to stall speed, the safety margin with respect to lift coefficient would be smaller for blown-flaps aircraft compared to aircraft with mechanical high-lift devices. The safety margin defined in FAR-25 is, therefore, interpreted as a safety margin for the lift coefficient compared to the maximum lift coefficient at the respective speed (see also Figure 44):

$$C_L = \frac{1}{k^2} \cdot C_{L\,max} \tag{40}$$

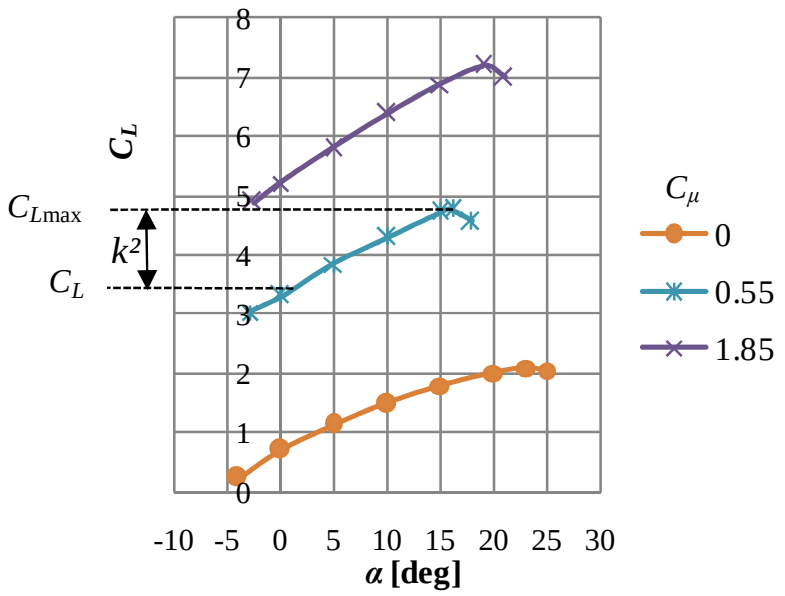

Figure 44. Safety margin defined for lift coefficient

In this study, it is assumed that v_{TO} equals v_2, which is a common approach in conceptual design (Torenbeek 1982, p. 167). Take-off speed is calculated iteratively, as C_{Lmax} is changing with speed. The algorithm developed is given in Figure 45.

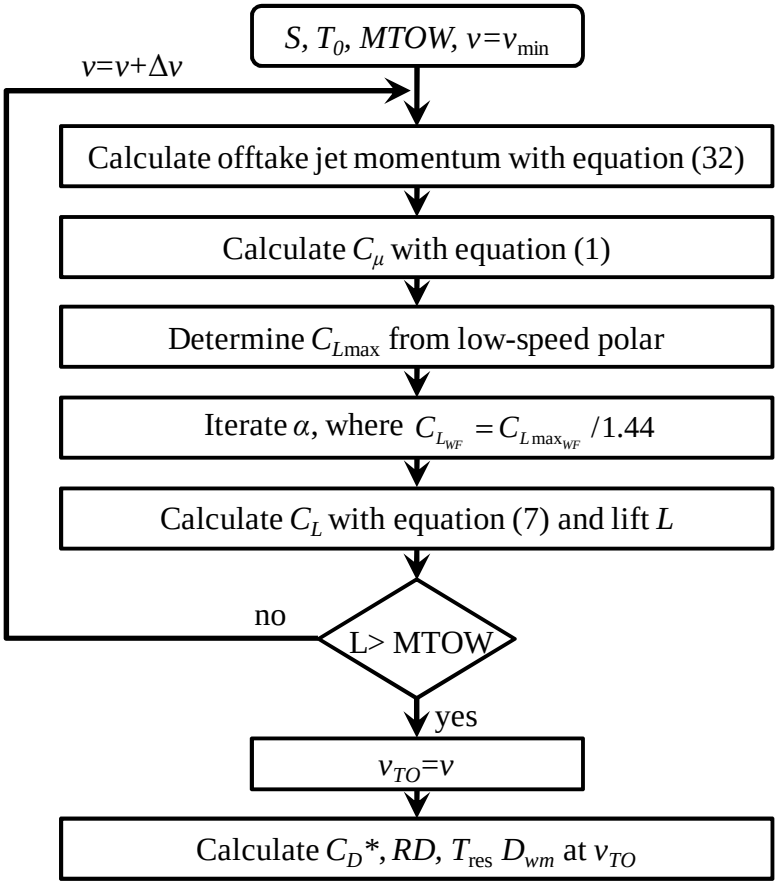

Figure 45. Flow chart for take-off speed iteration

Starting with a low speed $v=v_{\min}$, the speed v is incrementally increased by Δv. At every evaluated speed, the respective offtake jet momentum is calculated with equation (32). Thereby the total reference OEI thrust $T_{0_{OEI}}$ is used to assure that take-off can also be performed if one engine fails:

$$T_{0_{OEI}} = \frac{(N-1)}{N} \cdot (1+K) \cdot T_0 \tag{41}$$

K accounts for a potential increase in thrust of the remaining engines in the case of engine failure due to higher burner exit temperature. With the offtake jet momentum the jet momentum coefficient is calculated with equation (1). For this jet momentum the maximum lift coefficient $C_{L\max}$ of the wing-fuselage configuration is interpolated from the low-speed polar at OEI condition. From $C_{L\max}$, the lift coefficient of the wing-fuselage configuration $C_{L_{WF}}$ that satisfies the safety margin required is calculated:

$$C_{L_{WF}} = \frac{1}{1.2^2} \cdot C_{L\max} \tag{42}$$

The corresponding angle of attack α for $C_{L_{WF}}$ is subsequently determined from the low-speed polar. In the following, the lift coefficient of the aircraft C_L is calculated with equation (7) considering the horizontal tail (HT) lift coefficient required to trim the aircraft longitudinally at the forward CG position (see equation (22)). If the lift L at v is high enough to lift the aircraft weight, then v_{TO}=v; otherwise v is increased by Δv.

In the following step, the total force in flight direction at the iterated take-off condition with OEI $F_{x_{TO}}$ is:

$$F_{x_{TO}} = T_{\text{res}} - q \cdot S \cdot C_D^* - RD - D_{wm} \tag{43}$$

The ram drag RD and the residual thrust are calculated with equations (33) and (34) and the respective engine characteristics depending of the engine type. According to Roskam, D_{wm} is 15 % (used for BPR=5) of T_0 for low BPR engines and 25 % (used for BPR=10) of T_0 for high BPR engines (Roskam 1985b, p. 267-268). Wind-milling drag is zero for the AEO case. C_D^* is calculated from equation (12).

A feasible value for minimum control speed is:

$$v_{mc} = 1.1 \cdot v_{ST} \tag{44}$$

Stall speed is not calculated, as v_{TO} is iterated directly. Therefore, a definition of v_{mc} relative to v_{TO} is better suited for blown-flaps aircraft. With

$$v_{TO} = 1.2 \cdot v_{ST} \tag{45}$$

and equation (44) v_{mc} can be calculated directly from take-off speed for the above definition:

$$v_{mc} = \frac{1.1}{1.2} \cdot v_{TO} \tag{46}$$

This approach is conservative as, at speeds lower than v_{TO}, the safety margin to stall is even higher compared to aircraft with mechanical high-lift devices due to higher corresponding $C_{L\max}$.

4.4.2 Calculation of Ground Roll

The ground roll distance traveled to accelerate the aircraft to take-off speed is:

$$s_{GR} = \int_0^{v_{TO}} \frac{v}{a} dv \tag{47}$$

with

$$a = \frac{F_{x_{GR}}}{m} \tag{48}$$

Where $F_{x_{GR}}$ is the resultant force accelerating the aircraft. According to handbooks, for a CTOL aircraft, this velocity-dependent resultant force is averaged and evaluated at 70.7 % of v_{TO} (Torenbeek 1982, p. 167) which provides an analytical solution for s_{GR}.

Due to the interdependence of thrust and forward speed, the aerodynamic forces acting on blown-flaps aircraft (see equation (49)) have different characteristics during take-off compared to a CTOL aircraft. For this reason the resultant force cannot be averaged for the calculation of the ground roll distance.

$$F_{x_{GR}} = T_{\text{res}} - q \cdot S \cdot C_D^* - \mu \cdot (m_{TO} \cdot g - q \cdot S \cdot C_L) - RD - D_{wm} \tag{49}$$

Ground effect is thereby neglected. Ram drag RD, residual thrust T_{res}, C_D^* and C_L are velocity-dependent and not available in analytical form (look-up tables). The wind-milling drag occurs in the case of engine failure only. A closed analytical solution of equation (47) is consequently not available. Therefore, the ground roll distance has to be calculated numerically. Small segments of distance travelled Δs are calculated for small increments of speed Δv, for which constant acceleration is assumed. The discretization of equation (47) in combination with equations (48) and (49) gives:

$$\Delta s = \frac{m_{TO} \cdot v \cdot \Delta v}{T_{\text{res}} - q \cdot S \cdot C_D^* - \mu \cdot (m_{TO} \cdot g - q \cdot S \cdot C_L) - \dot{m} \cdot v - D_{wm}} \tag{50}$$

Starting with v=0m/s, the speed is increased by Δv, until v_{TO} is reached. For every evaluated speed v, C_μ is calculated. Based on C_μ, C_D^* (equation (12)) and C_L (equation (7)) are determined from the respective low-speed polar for α=0°. Ram drag is calculated with equation (33). For the AEO take-off, full engine thrust can be used for the calculation of C_D^*, C_L and RD, while for the OEI segment the thrust available at OEI condition from equation (41) is used. Wind-milling drag is zero for the AEO case.

For OEI take-off, the ground roll distance is calculated with AEO until v_1 is reached. Beyond v_1, the available thrust with OEI and the OEI low-speed polar have to be used for the calculation of C_D^* and C_L. Wind-milling drag has to be considered.

For speeds below v_{min}, the forces are interpolated linearly from the forces calculated from the low-speed polar at v_{min} and the forces calculated from the static turning characteristics at v=0 m/s (see equations (2) and (3)). A typical friction coefficient for take-off is μ=0.03 (Torenbeek 1982, p. 168). The total ground roll distance s_{GR} is the sum of the small distance segments Δs.

4.4.3 Calculation of Transition and Climb Segment

For the calculation of the transition distance s_{TR} it is assumed that transition time is 3 seconds at v_{TO}, which is a common approach (Bobbitt and Margason 2007). The climb angle is calculated from the ratio of total force in forward direction to the lift at v_{TO}

$$\tan\gamma = -\frac{F_{x_{TO}}}{L} \tag{51}$$

where $F_{x_{TO}}$ is calculated with equation (43) at v_{TO} and the corresponding angle of attack (see section 4.4.1); the lift equals the aircraft weight. Based on the climb angle, the distance traveled over ground during transition s_{TR}, the height after transition segment h_{TR} and the distance needed to climb to 35ft (s_{CL}) is calculated according to Bobbit and Margason (Bobbitt and Margason 2007, pp. 11-12). This is carried out for AEO as well as for OEI. For AEO the wind-milling drag in equation (43) is zero. The climb angle with OEI is one of the constraints that have to be considered for the matching chart.

4.4.4 Calculation of Reaction and Breaking Segment

For aborted take-off, a reaction time after engine failure of 2s at v_1 has to be considered first, which gives the distance traveled s_{reac}. Deceleration from v_1 to zero is calculated with a handbook method of Brandt where the forces are averaged at 70 % of v_1 (Brandt 2004, p. 223). Averaging the forces is feasible in this case, as the engines run in idle mode (for the calculation of C_D^* and C_L it is assumed that idle thrust is 8 % of T_0), hence almost no blown flaps effects occur:

$$s_B = \frac{0.5 \cdot m_{TO} \cdot v_1^2}{(q \cdot S \cdot C_D^* + \mu \cdot (m_{TO} \cdot g - q \cdot S \cdot C_L))_{@0,7 \cdot v_1}} \tag{52}$$

Typical values for breaking coefficient are between μ=0.3 (Jenkinson, Simpkin et al. 1999, p. 243) and μ=0.5 (Raymer 2006, p. 552).

4.5 Landing Field Length and Missed Approach Climb Performance

For the calculation of landing field length, the approach speed v_{APP} has to be calculated first. Based on the approach speed, the climb performance for missed approach (MA) with AEO as well as with OEI and the landing field length have to be determined.

4.5.1 Approach Speed

FAR-25 regulations specify a safety factor of k=1.3 for v_{APP} (FAA 2009). For approach speed calculation, the same problem as for the take-off speed calculation occurs: $C_{L\max}$ is a function of speed, which requires the iteration of v_{APP}. The speed has to be found, where $C_{L\max}$ at v_{APP} is 1.3² times higher than $C_{L_{APP}}$ and the lift equals the weight. In addition to v_{APP}, the thrust rating has to be iterated for landing to find the jet momentum coefficient C_μ where the required approach angle is met.

Figure 46 illustrates with the help of the aircraft drag polar, why v_{APP} and C_μ (the thrust rating) have to be iterated. For this example a -5° approach angle is required. A combination of lift coefficient and jet momentum coefficient on the line of constant ratios of lift-to-drag that correspond to a -5° approach angle has to be found. Thereby, the lift has to equal the weight and the lift coefficient safety margin has to be satisfied. The minimum speed, where all these conditions are fulfilled is the approach speed that has to be iterated.

A point with a higher jet momentum coefficient (see Figure 46)

a) may provide enough lift, but could cause an approach angle that is above the required one
b) may provide enough lift and meet the required approach angle, but would have a safety margin that is too low

A point with a lower jet momentum coefficient (see Figure 46)

c) may provide enough lift, but could cause an approach angle that is below the required one, or
d) may provide enough lift, but could cause an approach angle that is below the required one and would have a safety margin that is too low.

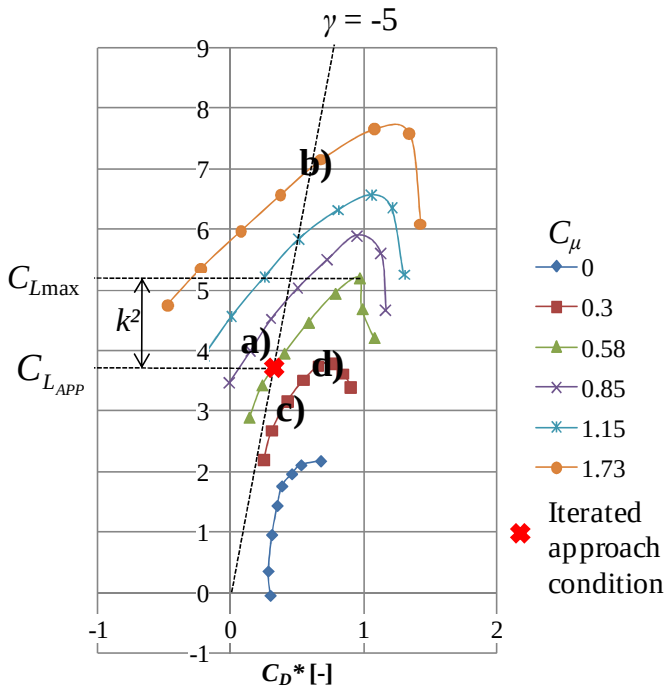

Figure 46. Illustration of different approach conditions

To ensure that enough lift is available if one engine fails, the approach speed is defined for the OEI condition. Therefore, the low-speed polar for the OEI condition is used for the calculation of the aerodynamic coefficients during landing.

The algorithm illustrated in Figure 47 was developed to find the combination of v_{APP} and thrust rating that meets the approach angle and safety margin requirements. The input parameters are the reference area S, the maximum allowable approach thrust $T_{APP\max}$, the approach flap angle $\delta_{f_{APP}}$ and the maximum landing weight MLW. The algorithm starts with a low speed v=$v_{\min}$ and sets the actual thrust T equal to zero. The jet momentum is calculated with the procedure documented in section 4.3 for the respective engine type. The jet momentum coefficient is calculated with equation (1) using the respective jet momentum. For the jet momentum coefficient calculated, the maximum lift coefficient $C_{L\max}$ of the wing-fuselage configuration is interpolated from the low-speed polar at OEI condition. From $C_{L\max}$, the lift coefficient of the wing-fuselage configuration $C_{L_{WF}}$ is calculated which satisfies the safety margin required:

$$C_{L_{WF}} = \frac{1}{1.3^2} \cdot C_{L\max} \tag{53}$$

The corresponding angle of attack α is subsequently determined. In the following, the lift coefficient of the aircraft C_L is calculated with equation (7) considering the horizontal

tail (HT) lift coefficient required to trim the aircraft longitudinally at forward CG position (see equation (22)). The total force in the forward direction during approach is calculated analog to equation (43). Subsequently the flight path angle γ is determined with equation (51). If γ is not within a specified range $\Delta\gamma$, the thrust is increased and the procedure from the calculation of the jet momentum is repeated. If γ is within the specified range or the actual thrust reaches $T_{APP\max}$, whether the lift is greater than the weight is checked. If not, the speed is increased by Δv. The speed is increased until the lift is greater than the weight. At this point, the v_{APP} equals v.

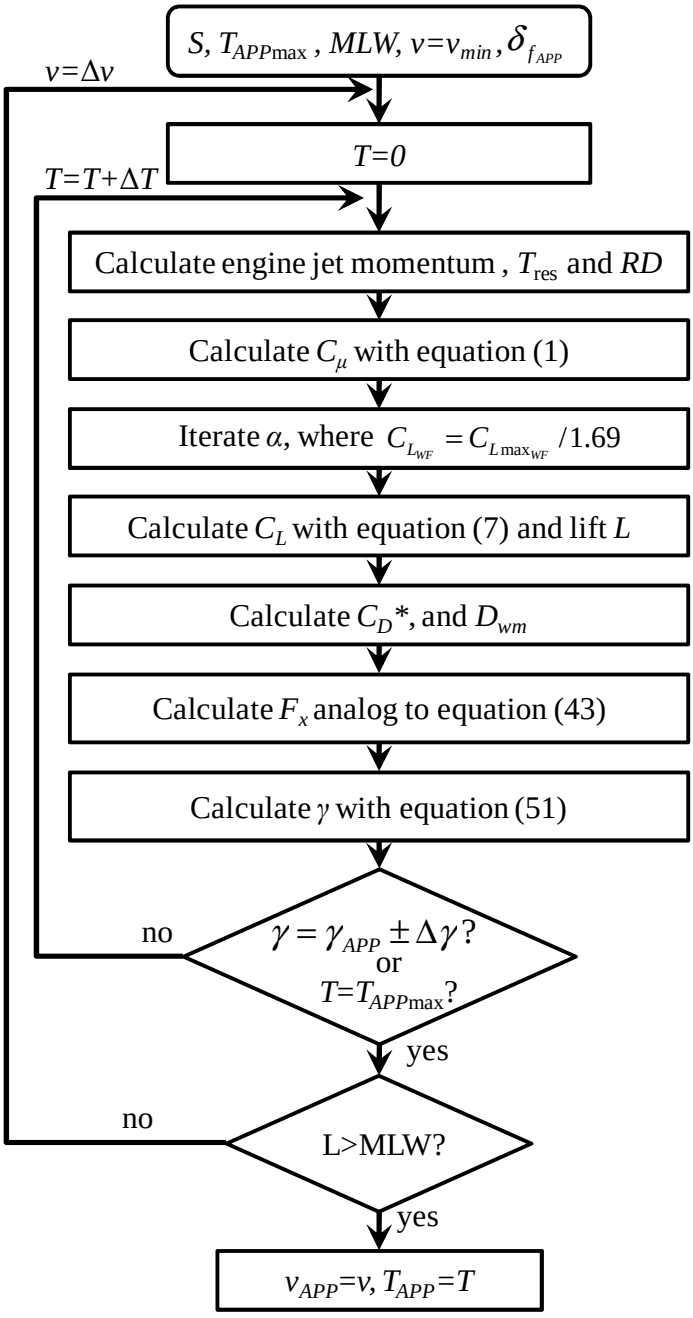

Figure 47. Algorithm for approach speed iteration

The maximum approach thrust $T_{APP\max}$ is introduced as an upper limit for the allowed thrust during approach to provide a thrust reserve that can be used for the missed approach. In the following, $T_{APP\max}$ will be given relative to the available OEI thrust:

$$\theta_{\max} = \frac{T_{APP\max}}{T_{0_{OEI}}} \tag{54}$$

The iterated relative thrust θ for the approach condition may be below $\theta_{\max}$, as the maximum available thrust may result in a greater approach angle γ_{APP} than the required one. On the other hand, $\theta_{\max}$ may not be enough to meet the required γ_{APP}. In this case, the algorithm would give an approach angle that is smaller than the required one. A further increase in speed could be an alternative solution to try to meet the required approach angle, but can lead to infinite loops. The approach path required has, therefore, to be considered as an additional constraint in the matching chart.

4.5.2 Missed Approach Climb Performance

Once v_{APP} is iterated, the climb performance for missed approach (MA) with AEO as well as with OEI must be determined, as minimum climb rates are required for certification. These performance constraints have a special importance for blown-flaps aircraft, as a certain amount of thrust is already used for lift generation during landing and is not available for forward thrust generation.

A. Missed Approach with AEO

For the MA with AEO, the minimum climb rate required has to be demonstrated at v_{APP} with the flaps in landing configuration. In Figure 48, this operational flight condition is illustrated for an approach angle of -6° and a required MA climb rate of 0.032 (FAA 2009) (which is equivalent to a climb angle of 1.83°). In the case of a missed approach, full all engines operative (AEO) engine thrust is available, which increases the jet momentum coefficient. The lift coefficient remains constant, while the increased jet momentum coefficient moves the operational point in the region of the drag polar, where a positive climb angle can be achieved (Figure 48 right). The aircraft has to reduce the angle of attack to maintain the lift coefficient (Figure 48 left), as the speed does not change.

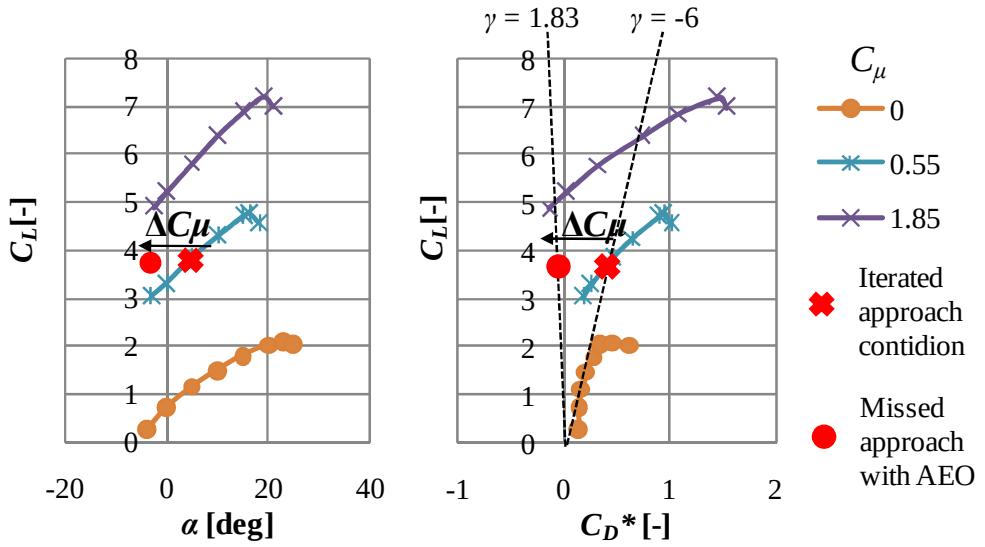

Figure 48. Illustration of additional jet momentum required for MA with AEO, δ_f=45°

The available climb rate for MA with AEO is calculated in the following way:

1) Calculate C_μ with equation (1) and ram drag with equation (33) for v_{APP} and full AEO thrust
2) Iterate the angle of attack, where the calculated C_μ corresponds to $C_{L_{APP}}$
3) Calculate C_D^* with equation (12) for this angle of attack
4) Calculate F_x with equation (43)
5) Determine the climb rate from the ratio of F_x to lift with equation (51)

The approach angle $\delta_{f_{APP}}$ and the engine thrust T_0 are the parameters that have a main impact on the climb rate for MA with AEO and have to be selected such that the required climb rate is satisfied.

B. Missed Approach with OEI

The minimum climb performance required for MA with OEI has to be demonstrated for a MA with OEI speed v_{MAOEI} between $1.3 \cdot v_{ST}$ and $1.5 \cdot v_{ST}$ and the flaps in the setting for MA with OEI $\delta_{f_{MAOEI}}$ according to FAR-25 requirements (FAA 2009). This means that, for conventional aircraft, the MA with OEI may be demonstrated for a higher speed than the approach speed, which enables a lower lift coefficient and, therefore, a lower flap angle. As a consequence, drag is reduced which improves the climb performance respectively reduces the thrust required for MA with OEI.

In analogy to the missed approach with AEO, the climb performance for MA with OEI is calculated for v_{MAOEI} using the low-speed polar for $\delta_{f_{MAOEI}}$:

1) Calculate C_μ with equation (1) and ram drag with equation (33) for v_{MAOEI} and full OEI thrust and the wind-milling drag D_{wm}
2) Iterate the angle of attack, where C_L at the calculated C_μ corresponds to the aircraft weight
3) Iterate the maximum lift coefficient for the calculated C_μ
4) Calculate C_D^* with equation (12) for this angle of attack
5) Calculate F_x with equation (43)
6) Determine the climb rate from the ratio of drag to lift with equation (51)
7) Calculate the safety margin $C_L/C_{L\max}$

For blown-flaps aircraft, a high amount of thrust may be used for lift generation during landing, as approach speed reduction is of primary interest. The result is that only a small amount of thrust is available for climb with OEI during landing, which means that the additional thrust available to increase C_μ may not be enough to meet the required climb angle (see Figure 49). Additionally, at high flap deflections, an increase in C_μ means an increase in lift, not in thrust, as the jet momentum is turned downwards.

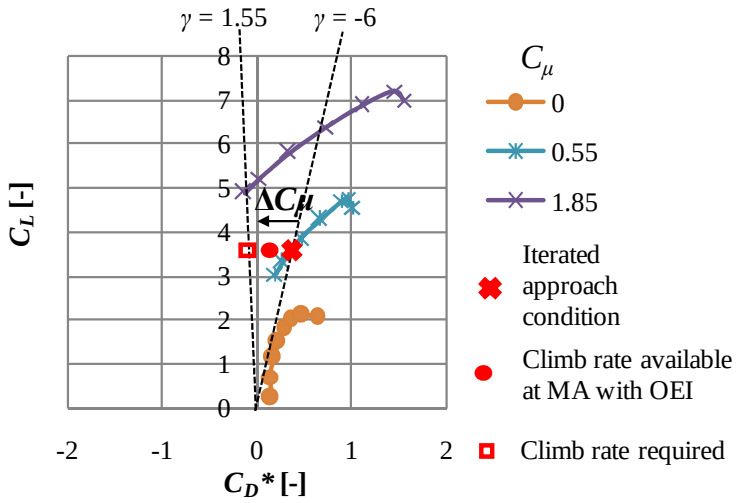

Figure 49. Change in operational condition for MA with OEI, δ_f=45°

Now, different strategies for the improvement of the climb performance during MA with OEI can theoretically be developed for blown-flaps aircraft:

a) A limitation in thrust that is used for approach T_{APP} to a certain value $\theta_{\max}$ increases the thrust reserve that is available for climb in the case of the MA with OEI and can lead to

an increase in C_μ that is sufficient to achieve the required approach angle. The consequence is a decrease in the approach lift coefficient, as less thrust is used for lift production during approach. This leads to an undesired increase in approach speed. This strategy is illustrated with the help of a drag polar in Figure 50.

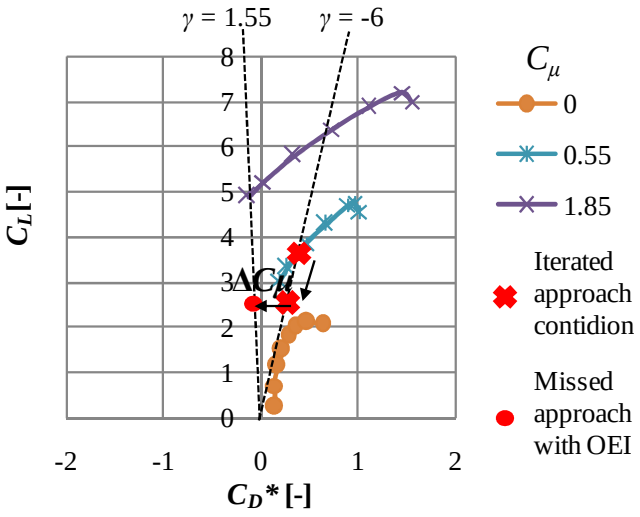

Figure 50. Reduction of the thrust rating during approach as a strategy to improve climb performance during MA with OEI, δ_f=45°

b) A reduction in the flap angle for MA with OEI $\delta_{f_{MAOEI}}$ at v_{APP} results in a better climb performance as less thrust is turned downwards. However, at the same time the safety margin decreases, as the angle of attack has to be increased to maintain the lift coefficient required (see Figure 51).

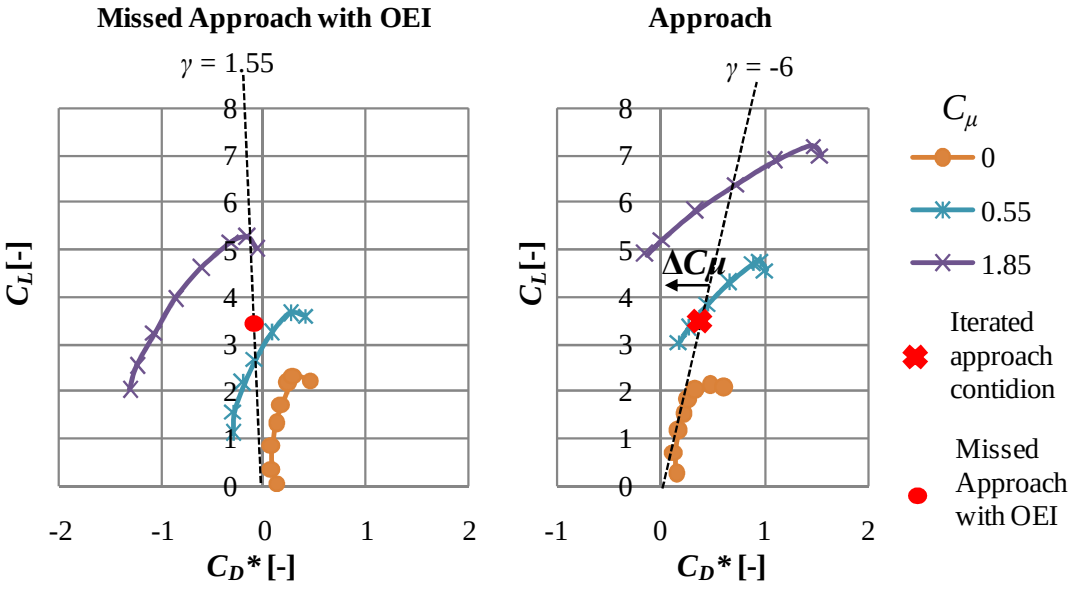

Figure 51. Reduction of flap angle for MA with OEI as a strategy to improve climb performance during MA with OEI, δ_f=15° (left) and δ_f=45° (right)

c) A reduction in the flap angle for MA with OEI $\delta_{f_{MAOEI}}$ and a simultaneous increase in the speed v_{MAOEI} reduce the lift coefficient required, but also reduce the jet momentum coefficient which results in lower aerodynamic performance and a lower maximum lift coefficient, which again decreases the safety margin. (see Figure 52)

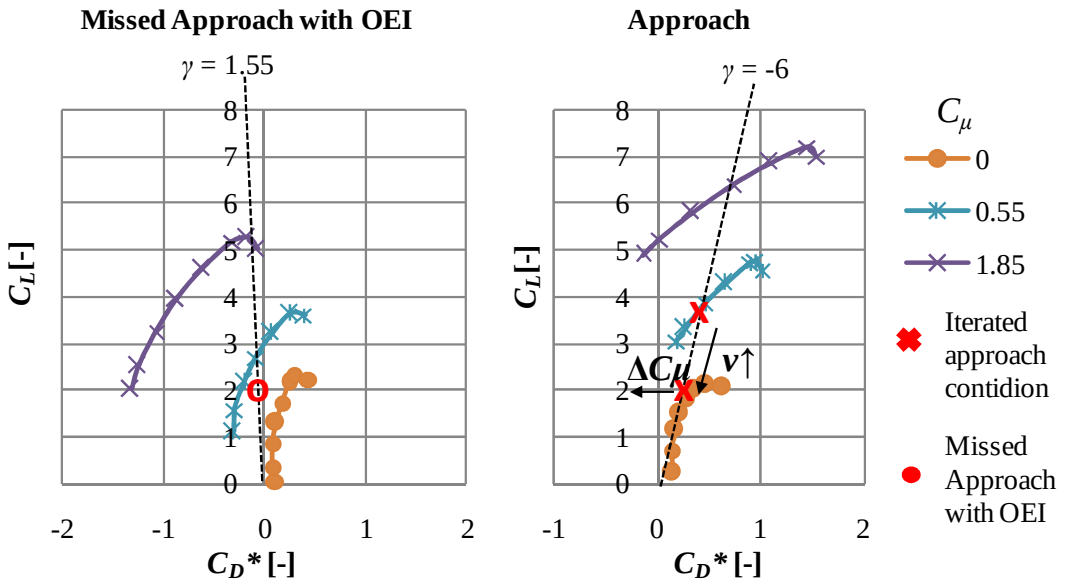

Figure 52. Reduction of $\delta_{f_{MAOEI}}$ and increase in speed (lower C_μ) as a strategy to improve climb performance during MA with OEI, δ_f=15° (left) and δ_f=45° (right)

d) A reduction in the approach flap angle $\delta_{f_{APP}}$ reduces the drag during approach and, therefore, can improve the climb performance during MA with OEI, but consequently increases the approach speed.

These general considerations show the complexity of the landing of blown-flaps aircraft. The need to achieve the required climb performance for MA with OEI always conflicts with the goal of reducing the approach speed. A combination of the above strategies can lead to a feasible point that satisfies all requirements at a minimum v_{APP} by variation of the following parameters:

- Ratio of maximum allowed thrust during approach to available thrust with OEI $\theta_{\max}$
- Flap angle for MA with OEI $\delta_{f_{MAOEI}}$
- Ratio of speed during MA with OEI to stall speed V_{MAOEI}
- Flap angle for approach $\delta_{f_{APP}}$

For every parameter combination, the approach speed has to be iterated, as these parameters all impact the approach speed.

4.5.3 Landing Field Length

Based on v_{APP}, LFL is calculated according to Raymer (Raymer 2006, p. 551-552). The method considers the segments approach, flare, free roll and deceleration (Figure 53).

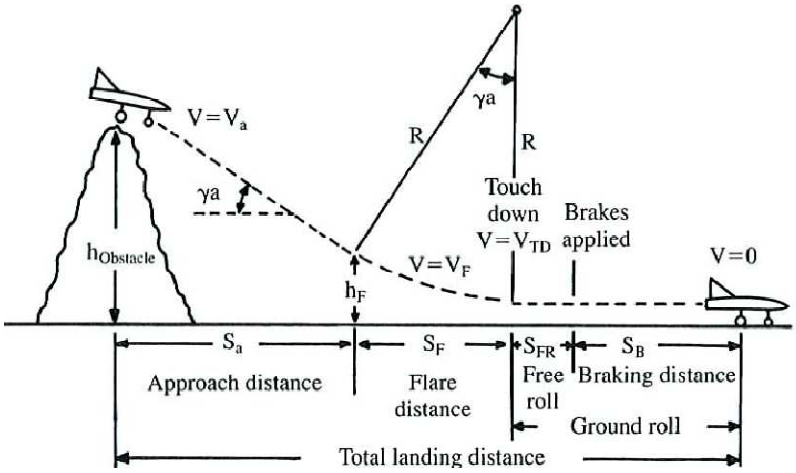

Figure 53. Relevant segments for LFL calculation, (Raymer 2006, p. 552)

Accordingly, the flare radius is:

$$R_F = \frac{v_{TR}^2}{0.2 \cdot g} \tag{55}$$

Transition speed is the average between v_{APP} and touch down speed v_{TD}, which is

$$v_{TD} = \frac{1.15}{1.3} \cdot v_{APP} \tag{56}$$

based on the usual definition, which says that v_{TD}=1.15·v_{ST}. Flare height is:

$$h_F = R_F \cdot \left(1 - \cos\gamma_{APP}\right) \tag{57}$$

The distance over ground during flare is:

$$s_F = R_F \cdot \sin\gamma_{APP} \tag{58}$$

The distance traveled during approach is:

$$s_{APP} = \frac{h_{\text{obstacle}} - h_F}{\tan\gamma_{APP}} \tag{59}$$

For the calculation of the free roll distance s_{FR} a typical value of 2s at v_{TD} is used. Obstacle clearance height h_{obstacle} is 50 ft for transport aircraft. The breaking distance s_B is calculated with equation (52) at landing weight. Typical breaking coefficients thereby are between μ=0.3 according to (Jenkinson, Simpkin et al. 1999, p. 243) or μ=0.5 according to (Raymer 2006, p. 552). The total landing distance is multiplied by 1.67 to account for FAR-25 requirements.

4.6 Implementation and Adaption of Baseline Design

How handbook methods are able to capture the impact of the blown-flaps systems and STOL capability on overall mission performance is discussed in this section. It is dealt with, how component-based handbook methods for the determination of the high-speed drag polar can be used and adapted to model the installation effects of the engines. Further on, the type of high-speed engine model has to be used is documented, to account for the fact that the engines of blown-flaps aircraft may run in part load during cruise. The component-based methods for mass estimation are summarized and how they can be used for sensitivity studies of mass penalties for blown-flaps aircraft is discussed. Finally, the implemented mission module is introduced. For the methods of Torenbeek documented in this section, parts of the commercial aircraft conceptual design software Pacelab APD (PACE 2007) are used.

4.6.1 High-Speed Aerodynamics

The trimmed high-speed drag polar (clean configuration, no flaps, no gear) is calculated component-based according to Torenbeek from the aircraft geometric parameters (Torenbeek 1982, appendix F). Thereby, lift-dependent profile drag of the components wing, fuselage, horizontal tail (HT), vertical tail and engines are calculated from the wetted areas. Wing wave drag is calculated as a function of sweep, airfoil type and airfoil relative thickness. Induced drag of wing, HT, and fuselage are calculated from the component dimensions. Using this detailed approach for cruise drag estimation, one can model the differences between the different aircraft sizes that result for the different blown-flaps aircraft designs, for example:

- For a given payload the fuselage dimension remains constant. The wing and tail areas are determined from the take-off and landing field length required and may vary for aircraft different blown-flaps systems due to differences in the take-off and landing performance.
- Engine size may differ for the different blown-flaps aircraft for the same reasons, resulting in differences in the nacelle drag.

These differences impact the aircraft drag polar, which is modeled by the above component-based methods. A simple approach for the calculation of the drag polar based on empirical data (for example with a constant profile drag and k-factor) would not account for these geometrical differences that result from the take-off and landing requirements.

Another advantage of this approach is that drag penalties can be introduced for the aircraft components to model the impact of engine installation effects on the aircraft drag. Previous studies (Birckelbaw 1992) or (Braden, Hancock et al. 1980b) have indicated that USB configurations suffer from a severe drag penalty compared to a conventional aircraft due to its unique over-the-wing engine installation and the resulting interferences and wave drag, which have to be considered for the overall mission performance calculation. Birckelbaw performed wind-tunnel experiments to determine the cruise drag penalty $\Delta C_{D0_{USB}}$ due to USB engine installation (Birckelbaw 1992). He determined the cruise drag penalty for different engine installation configurations with 2 or 4 engines which are given in appendix C, Figure 117. One can see that the USB drag penalty generally increases with Mach number, which confirms the wave drag increment that is associated with engines installed on the upper side of the wing (Fujino 2003). The configurations with two engines have lower drag penalties than the configurations with four engines. One can also see that higher clearance from the fuselage and between the engines reduces the drag.

The profile drag of the wing alone of the wind-tunnel model $C_{D0_{wing}}$ was 0.01 in Birckelbaw's experiments. The ratio of the USB cruise drag penalty plus the wing drag to the wing drag can be used as a wing drag calibration factor d_{USB}:

$$d_{USB} = \frac{C_{D0_{wing}} + \Delta C_{D0_{USB}}}{C_{D0_{wing}}} \tag{60}$$

This calibration factor can be applied to the wing drag calculated with the methods above to account for the USB engine installation penalties.

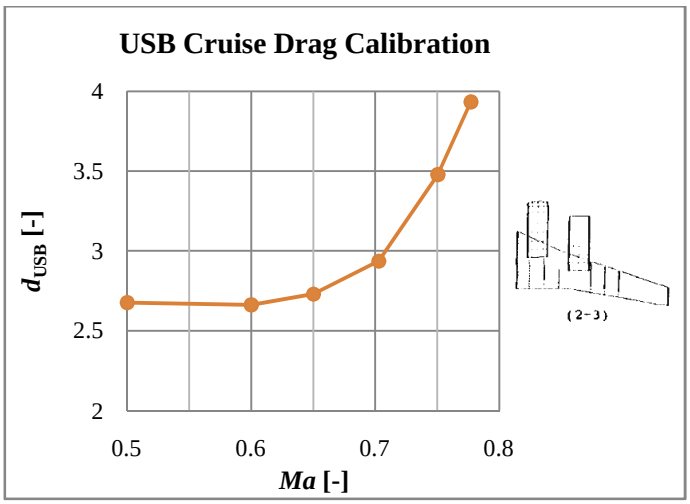

Figure 54. Cruise drag penalty due to USB engine installation based on data from (Birckelbaw 1992)

Figure 54 shows d_{USB} over the Mach number calculated from Birckelbaws experiments for the USB engine installation that is chosen for the application example in chapter 6 (Figure 117, configuration 2-3). The USB cruise drag penalty is very high, especially at high Mach numbers. For a Mach number of 0.75 the drag of the wing plus the USB drag penalty is 3.5 times higher than the drag of the wing alone.

The engines for EBF systems are installed conventionally under the wing. Therefore, it can be assumed that there are no installation effects of the EBF system compared to a conventional under-wing engine installation that is represented by the methods of Torenbeek above. The integration of the engines for IBF and AIBF systems is similar to conventional aircraft under wing but features ducts for the offtake of the bypass air. However, as the effect of the engine installation on cruise performance is not available in the literature, a sensitivity studies for a potential drag penalty can be performed with the documented methods.

4.6.2 High-Speed Engine Performance and Engine Geometry

STOL aircraft with blown flaps may have a higher thrust installed than required for cruise due to short field requirements. Depending on the blown flaps technology used and its low-speed performance, the different solutions may have different thrust installed. Therefore, when comparing such aircraft with each other, the model for the engine performance has to represent these differences. An engine deck is required that accounts for the dependence of SFC on the thrust rating in cruise. Such engine decks are available in textbooks, for example (Jenkinson, Simpkin et al. 1999, pp. 203-214), or can be generated with engine performance simulation tools, such as GasTurb.

In this section a cruise SFC-loop is given for the separate-flow BPR 10 engine modeled in section 4.3. Parametric studies were performed within GasTurb (Kurzke 2007a) to determine the *SFC* for different altitudes, Mach numbers and thrust lapse values (see Figure 55 left). The consideration of the impact of the thrust lapse on *SFC* allows for the modeling of the impact of an oversized engine on cruise *SFC*. The maximum available climb thrust as a function of Mach number and altitude is required for the calculation of the climb performance at top of climb altitude.

The SFC-loops for the engines with BPR 7.5 and BPR 5, show that the BPR 7.5 engine has around 2.5 % higher SFC and the BPR 5 engine has 7.9 % higher SFC at 31,000 ft and *Ma*=0.74. The maximum climb thrust available is 5.5 % higher for the BPR 7.5 and 14 %

higher for the BPR 5 engine. These data represent the engine designed in section 4.3. However, for other requirements customized engine decks have to be generated or taken from the literature.

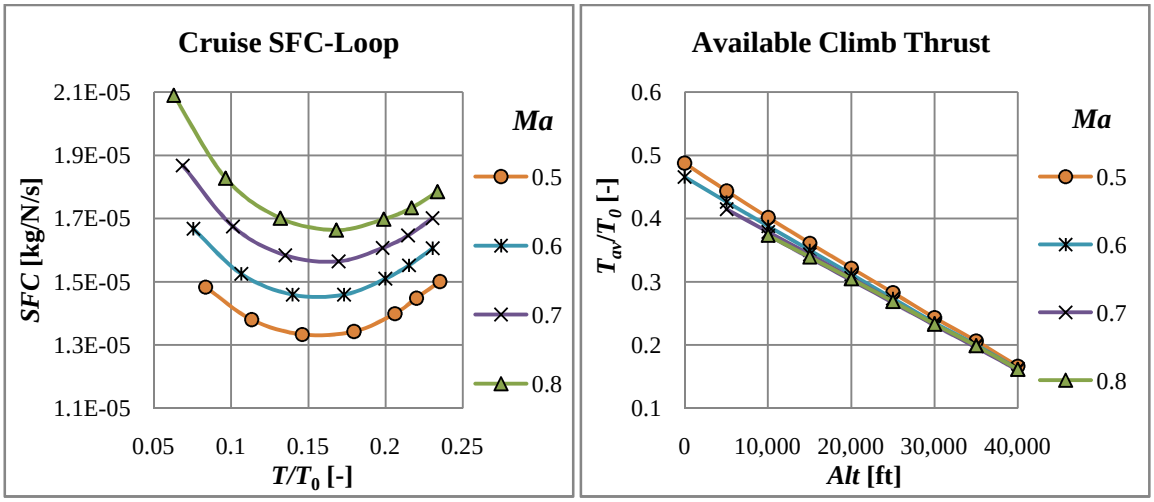

Figure 55. SFC-loop at 31,000ft (left) and available climb thrust (right), separate-flow turbofan engine, *BPR*=10

Engine geometry has to be scaled with SLST to account for the impact of larger engines on the aircraft drag. In the model implemented, the fan diameter is calculated according to Jenkinson (Jenkinson, Simpkin et al. 1999, p. 199) as a function of mass flow, which is determined from equation (31). Thus, the influence of engine size on the nacelle drag can be considered. An alternative approach is to scale the engine dimensions with static thrust according to Raymer based on the dimensions of a reference engine (Raymer 2006, p. 226).

4.6.3 Operating Empty Weight Estimation

Simple mass estimation methods use a constant fraction of operating empty weight *OEW* to maximum take-off weight *MTOW* for the calculation of *OEW*. This approach is sufficient, if empirical data is available. For the comparison of aircraft with different blown-flaps systems, this approach is not sufficient, as differences in thrust-to-weight ratio and wing loading cause different component weights and thus different fractions of *OEW* to *MTOW*.

For the calculation of *OEW*, the structure weights, propulsion system weight, operational items weights, and equipment weight according to the mass breakdown of Torenbeek are implemented (Torenbeek 1982, Table 8-3). The structural components fuselage, wing (including surface controls), HT, VT and engine nacelles, as well as operational items and equipment weight, are calculated according to Torenbeek (Torenbeek 1982, chapter 8).

Landing gear weight is calculated according to Raymer (Raymer 2006). Dry engine weight is calculated as a function of T_0, T_{SP}, *OPR* and *BPR* according to Torenbeek (Torenbeek 1982, Eq.4-36).

These component-based methods account for the scaling effects that occur

- due to the sizing of the main parameters *T/W* and *W/S* for the required performance.
- due to scaling effects over the entire mission, for example that the iterated *MTOW* increases due to higher engine weight, which increases the wing weight, landing gear weight, etc.

Another advantage is that weight penalties can be introduced for the different components, for example for penalties due to wing ducting or higher control surface weights.

The center of gravity (CG) is calculated component based with methods of Torenbeek (Torenbeek 1982, chapter 8). The wing is positioned such that the CG of the empty aircraft is positioned at 40 % of *MAC*.

4.6.4 Mission Performance

The mission performance simulation module of the commercial aircraft conceptual design software Pacelab APD (PACE 2007) is used. The mission performance module calculates the mission fuel burn, block time, climb and decent angles for the user-specified mission profile by the evaluation of mass, lift, drag, thrust and SFC for small mission segment. Thus, the change in *SFC* and drag during the mission are modeled.

5 Verification and Validation of Methods

The main focus of this thesis is the development of methods for the calculation of the take-off and landing performance of blown-flaps aircraft. Results for take-off and for landing gained with the methods developed are validated by the comparison with flight test data and with handbook methods and are checked for plausibility, where flight test data is not available.

5.1 Take-Off

The numerical method developed and implemented for the calculation of balanced field length (see section 4.4) is first applied to a conventional aircraft with mechanical flaps by setting C_μ=0 and by the use of a conventional net thrust lapse derived from the separate-flow engine model (section 4.3.2). The results are compared to a handbook method of Torenbeek (Torenbeek 1982, p. 167-169). Figure 56 shows good agreement for a large range of wing loading and thrust-to-weight ratio. The maximum deviation of the BFL is 5 % for a thrust-to-weight ratio of *T/W*=0.4. This shows that the calculation with the algorithms implemented agrees with results gained from a well established method.

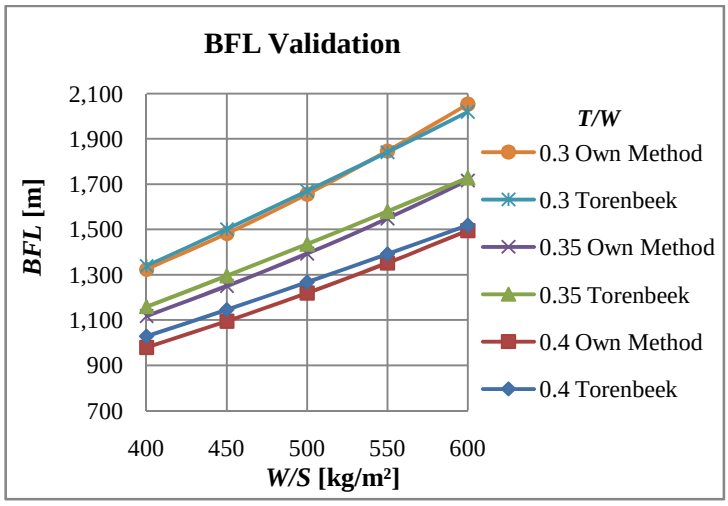

Figure 56. Comparison of BFL calculated with the implemented numerical method with BFL calculation according to Torenbeek (Torenbeek 1982, p. 167-169)

For the Quiet Short-Haul Research Aircraft (QSRA) with USB, flight test results for take-off have been published (Riddle, Innis et al. 1981). The take-off field length with one engine inoperative (OEI) including transition and climb to clearance height (35 ft) is given for different values of *W/S* at *T/W*=0.3. NASA all engines operative (AEO) and OEI wind-tunnel data from TM X-62419 (Aoyagi, Falarski et al. 1975) for the flaps in take-off condition (Figure 124 and Figure 127) is used to determine the blown-flaps aerodynamic

coefficients. The engine characteristics developed in section 4.3 for *BPR*=5 are used. These data are applied to the methods implemented for the calculation of the take-off distance with one engine inoperative $s_{TO_{OEI}}$ (section 4.4). The comparison of the calculated take-off field length with OEI with the flight test data shows good agreement (see Figure 57); the average deviation (5 %) is smaller than the spread of empirical data (8 %). In all cases the method is conservative and therefore provides safe results. This demonstrates the applicability of the methods developed and the usefulness of wind-tunnel data for the modeling of blown-flaps aircraft.

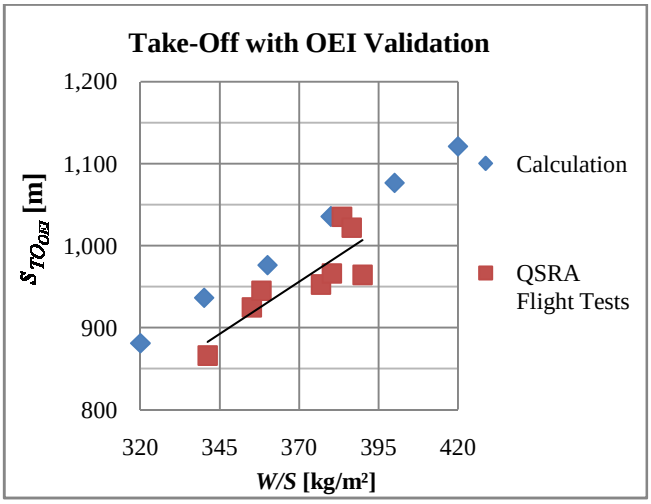

Figure 57. Comparison of calculated OEI take-off field length with QSRA flight test results, *T/W*=0.3

5.2 Landing

For the landing phase, the approach speed iteration as well as the calculation of the landing field length have to be verified.

5.2.1 Approach Speed

The Boeing C-17 is modeled with publicly available data (Jane's 2000) in the parametric aircraft model to verify the calculation of approach speed. A safety factor of k^2=1.44 is used, as military transport aircraft required lower safety margins than civil aircraft, where k^2=1.69 (Raymer 2006, p. 550). The EBF data of NASA TN-D 8057 with *BPR*=6.2 (Johnson 1975) is used to model the low-speed aerodynamic coefficients (see Figure 129 to Figure 132). The approach speed of the C-17 is 115 kts at maximum payload (Jane's 2000), which corresponds to a weight of 202,300 kg. Information about the flap angle and the approach angle are not available, therefore an exact verification is not possible. Figure 58 gives the approach speed calculated with the methods documented in section 4.5.1 for

the C-17 at different approach flap angles and γ_{APP}=-6°. In the investigated range for $\delta_{f_{APP}}$, the calculated approach speeds show a good agreement with the approach speed of the Boeing C-17, especially for $\delta_{f_{APP}}$=45°, where positive climb angles during missed approach can be achieved.

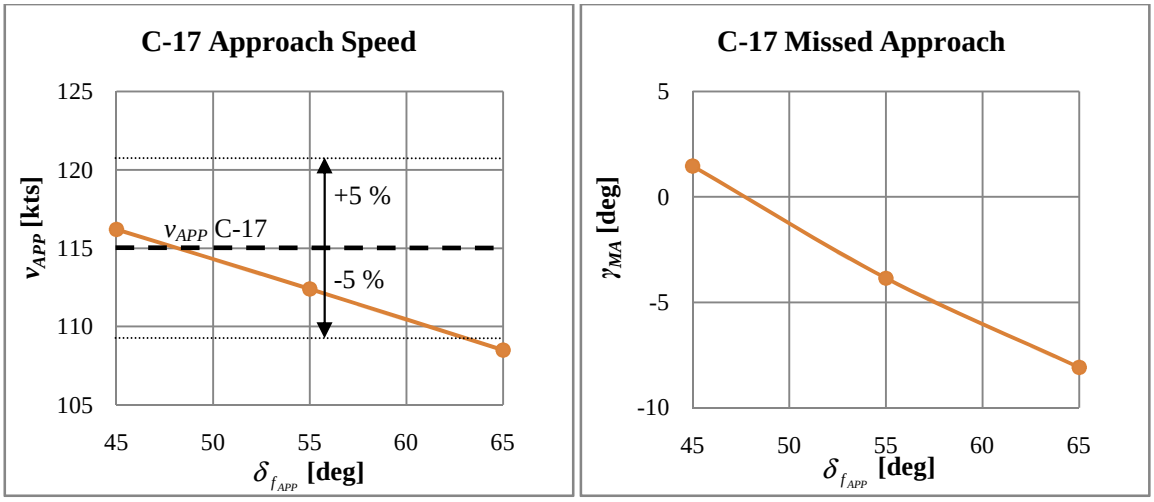

Figure 58. Calculated approach speed (left) and MA climb angle (right) for Boeing C-17

Further on, the approach speed calculation is checked for plausibility by a variation of the parameters that mainly impact the approach speed. Figure 59 shows the approach speed iterated with the algorithm documented in section 4.5.1 over wing loading for different thrust-to-weight ratios compared with aircraft with mechanical high-lift devices. The aircraft with mechanical high-lift devices are calculated with the algorithm developed by setting C_μ=0. A landing weight of 90% of MTOW is assumed. Wind-tunnel data for the EBF system (Johnson 1975) and the low-speed engine model without bleed offtake (*BPR*=6.2) are used.

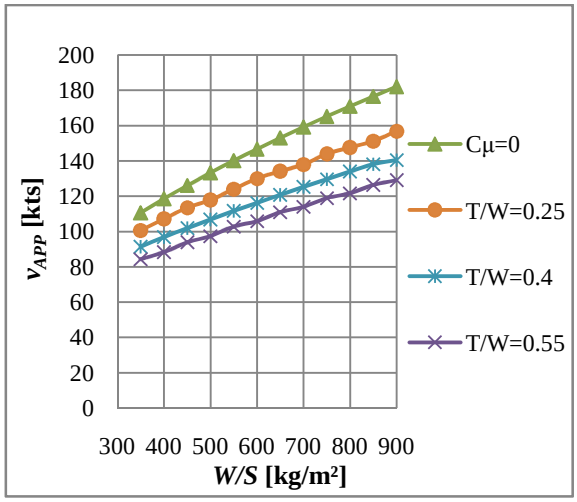

Figure 59. Verification of approach speed characteristics, EBF, δ_f=50°

The results show plausible characteristics: The approach speed decreases with decreasing wing loading and with increasing thrust-to-weight ratio. The approach speeds for the EBF aircraft are below the approach speed for the unpowered approach (C_μ=0).

5.2.2 Landing Field Length

The method implemented for the calculation of landing field length is compared with aircraft data taken from Jenkinson et al. (Jenkinson, Simpkin et al. 1999, Data A: Aircraft Data File). Around 50 turbo-fan aircraft types of the manufacturers Boeing, Airbus, Embraer, Bombardier, Fokker, BAe, McDonnell Douglas, Tupolev and Ilyushin are included. Figure 60 shows the FAR-25 landing field length over the square of approach speed. Included are the aircraft data and the results of the method implemented for runway friction coefficients of μ=0.3, μ=0.4 and μ=0.5 at a -3° approach angle.

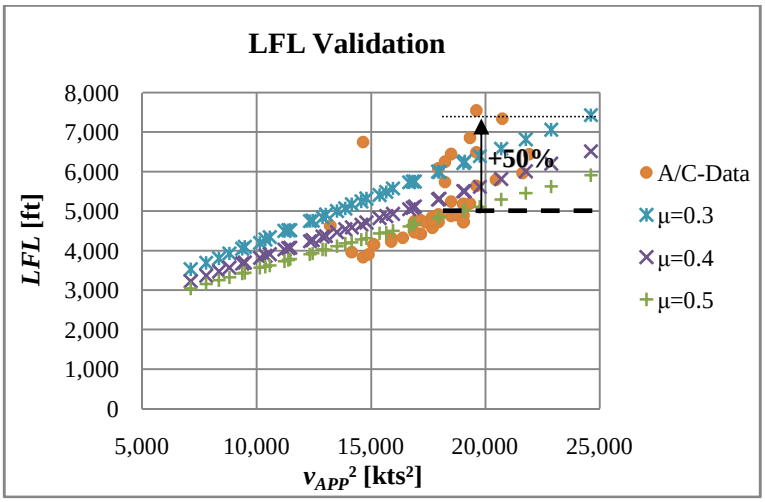

Figure 60. Comparison of calculated LFL for different runway friction coefficients with aircraft data from (Jenkinson, Simpkin et al. 1999)

The data for aircraft with lower approach speeds between v_{APP}^2=14,000 m²/s² and v_{APP}^2=18,000 m²/s² fits best with the friction coefficient of μ=0.5. The aircraft with higher approach speeds are better represented using the friction coefficients μ=0.3 or μ=0.4. However, for the higher approach speeds, the variation of the aircraft data is in the range of 50 %. Within the typical range for the friction coefficient, the implemented method matches the performance of most of the available aircraft data very well.

While most aircraft use an approach angle of γ_{APP}=-3°, a steeper approach is discussed for STOL aircraft (Hange 2003), (Hange 2008), (Schwanke 2009). Figure 61 shows the landing field length over the square of approach speed for a γ_{APP}=-3° and a γ_{APP}=-6° approach angle at μ=0.5 to check the plausibility of the method implemented. A decrease

in the approach angle from γ_{APP}=-3° to γ_{APP}=-6° improves the landing field length by around 500 ft due to the shorter approach and flare segment.

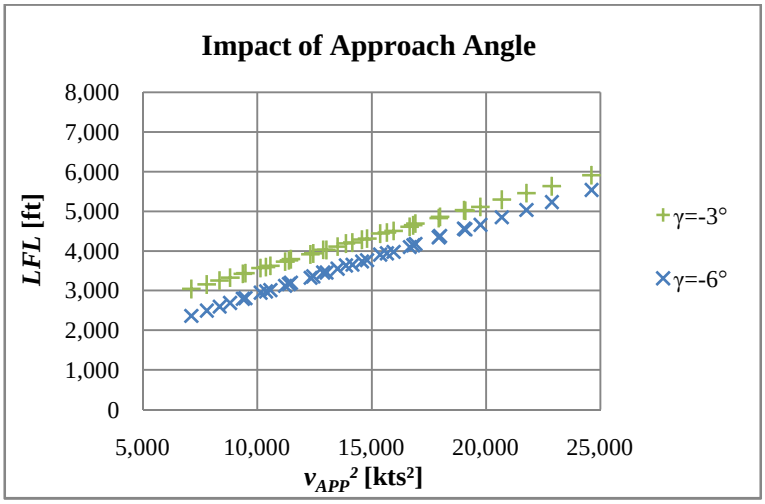

Figure 61. Landing field length over the square of approach speed for different approach angles

Depending on the values chosen for the friction coefficient and the design approach angle, significant differences result for the LFL. Important for a comparison study is a consistent selection of these design parameters. The characteristics given in Figure 61 are used for the application example in the next chapter.

6 Application of Method: Comparison of STOL Aircraft with Blown Flaps

In this chapter, the method developed is applied to the conceptual design and the comparison of short take-off and landing (STOL) regional aircraft. Aircraft with the following blown-flaps systems are designed and compared to a conventional take-off and landing (CTOL) reference aircraft with mechanical high-lift devices:

- Upper Surface Blown Flaps (USB)
- Externally Blown Flaps (EBF)
- Advanced Internally Blown Flaps (AIBF)
- Internally Blown Flaps with bypass air offtake (IBF-by)
- Internally Blown Flaps with exhaust air offtake (IBF-ex)

The aircraft alternatives with the different blown-flaps systems are generated by integration of the corresponding corrected low-speed wind-tunnel data (Figure 118 to Figure 136, appendix D) and the corresponding low-speed engine model (see section 4.3) into the parametric aircraft model, which includes the methods developed for take-off and landing (see Figure 27, p. 30).

In the first section, the simulation conditions are documented. Included are the reference mission requirements, the reference aircraft dimensions, the wind-tunnel data selected and the assumptions made, as well as the aircraft design parameters, mission segment constraints and the objective. Subsequently, the trade studies performed and the matching charts generated for the sizing for the required performance are documented. Based on the derived design points, the overall mission performance of the designed aircraft is compared with a CTOL reference aircraft with mechanical high-lift devices. Finally a tradeoff for the mission fuel burn penalty vs. the field length is given.

6.1 Simulation Conditions

This section presents the simulation conditions including the reference design mission, the dimensions of the basic configuration including the assumptions made and the wind-tunnel data selected. Further on, the aircraft design parameters as well as the mission segment constraints and the objective for this application example are introduced.

6.1.1 Design Mission

The top-level requirements for the reference mission of the regional aircraft are based on the research documented in a previous publication (Gologan, Kelders et al. 2009). The design range is 1,200 nm with a payload of 110 passengers; the design cruise condition is *Ma*=0.74 at 31,000 ft. The field length requirement is 1,000 m for take-off as well as for landing (see Table 11). The design approach angle required is γ_{APP}=-6° as previous investigations have shown that this approach angle results in the minimum landing field length (Gologan, Stagliano et al. 2009).

Table 11. Top-level requirements for design mission

Parameter	Unit	Value
Payload	PAX	110
Range	nm	1,200
Ma_{Cr}	-	0.74
Alt_{Cr}	ft	31,000
BFL	m	1,000
LFL	m	1,000

The field length requirements for the conventional take-off and landing aircraft with mechanical high-lift devices are a BFL of 1,900 m and a LFL of 1,450 m taken from Bombardier's next generation regional aircraft CS 100 (Bombardier 2009), while the other mission requirements are the same as for the STOL aircraft. A diversion of 200 nm to an alternative airport and a 30-min hold are considered for the calculation of the total design mission fuel weight.

6.1.2 Basic Configuration and Assumptions

The basic configuration investigated in this application example is a high-wing arrangement with a T-tail and four engines. However, with the methodology developed, USB, IBF and AIBF systems with two engines can also be investigated with respect to the available wind-tunnel data. For EBF systems, wind-tunnel data for two engine configurations have not been published in the literature, but the method developed also allows for the investigation of such configurations, if such data become available. The engines are positioned at 25 % of the half span (inner engine) and 45 % of the half span (outer engine) on the basis of the selected EBF and USB wind-tunnel models. For the maximum landing weight a value of 90 % of *MTOW* is selected, which is a common value for regional aircraft (Roskam 1985a, p. 107).

The fuselage dimensions are taken from the Bombardier CS 100, with an overall length of 35 m and a fuselage diameter of 3.6 m (Bombardier 2009). Reasonable values are selected for the wing and tail main geometric parameters (see Table 12), which are kept constant during the sizing process. Initial values for tail volume coefficients given for an USB STOL transport aircraft concept are used. The corresponding values were 1.47 for the horizontal tail (HT) and 0.124 for the vertical tail (VT) (Cochrane, Riddle et al. 1982), which are higher compared to typical data for conventional aircraft (0.09 for VT and 1.0 for HT) according to Raymer (Raymer 2006, p. 122).

Table 12. Main wing and tail parameters

Parameter	Unit	Wing	VT	HT
S	m²	80.9	12	13.9
AR	-	9	1	5
λ	-	0.3	0.8	0.3
t/c	%	12	9	9
φ_{25}	deg	20	40	28
Volume coefficient	-		0.124	1.47

This basic configuration with the values given in Table 12 serves as the baseline for the blown-flaps aircraft. With the tail volume values for conventional aircraft it represents the reference aircraft with mechanical high-lift devices.

For all blown-flaps aircraft it is assumed that they have 25 % higher control surface mass and the excess thrust during take-off and landing with OEI is set to K=0.1 (10 % of T_0). For the tail, a relative thickness of 9 % is selected. The choice of this common value for conventional aircraft allows the resulting tail volume to be compared with typical values of conventional aircraft. However, a higher relative thickness would allow for smaller tails, as the maximum lift coefficient due to rudder deflection is increased (Figure 97, appendix A). For the rudder, full span plain flaps with a relative chord of 30 % are selected. The maximum flap deflection is assumed to be 20°. If these values are applied to a methods of US DATCOM (Finck 1978, p. 6.1.1.3-12) and Roskam (Roskam 1985c, p. 83) using the data given in Figure 97 to Figure 101 (appendix A), a maximum rudder side force coefficient of $\Delta c_{y\,\max_{\text{rudder}}}$=0.5 and a profile drag increment due to rudder deflection of $\Delta c_{d0_{\varphi_{25}=0}}$=0.038 result. It is assumed that these 2-dimensional values can be used for the 3-dimensional VT, as full span flaps are chosen.

For the determination of $C_{L\max}$ of the HT, a plain flap is selected giving a maximum lift coefficient of 2.2 (Scholz 1999, p. 62). For the determination of the maximum lift

coefficient that can be used to trim the aircraft, a safety margin is considered, chosen to be k^2=1.69 (according to the landing lift coefficient safety margin) resulting in a maximum lift coefficient available for the HT of $C_{L\max_h}$ =1.3. The profile drag increment due to elevator deflection is assumed to have the same value as for the rudder.

The position of the aileron section extends from 70 % to 100 % of the span, according to the flap extension of the wind-tunnel models. The maximum rolling moment coefficient of the aileron $C_{l\max_{ail}}$ is determined according to (Schlichting and Truckenbrodt 2001, p. 453-454) for an aspect ratio of *AR*=9 and the according spanwise extension of the aileron. The resulting rolling moment derivative $\partial C_l / \partial \delta_{f_{ail}}$ is 0.3/rad, giving a maximum value of $C_{l\max_{ail}}$ =0.13 for a maximum aileron deflection of $\delta_{f_{ail}}$ =25°. For this deflection a value of $\Delta c_{d0_{\varphi_{25}=0}}$=0.04 for the 2-dimensional profile drag increment due to aileron deflection is determined according to Figure 101.

The maximum forward center of gravity (CG) position, which is important for the HT size, is selected at 10 % of the mean aerodynamic chord *MAC*; the maximum aft CG position, which is important for the longitudinal stability is set at 60 % *MAC*.

Duct pressure losses of 5 % are assumed for the AIBF aircraft and 10 % for the IBF aircraft, according to Figure 15, p. 15). The AIBF aircraft uses an engine with a high BPR and low fan pressure ratio (approximately 1.3), while the IBF aircraft uses an engine with a lower BPR of 5 and, therefore, has duct pressure ratios of around 2 (see section 4.3).

6.1.3 Selected Wind-Tunnel Data

The wind-tunnel data for the representation of the investigated blown-flaps systems are selected based on the considerations discussed in section 4.1.1, and the data summarized in Table 28 (appendix D). From the four engine USB models, NASA TM X-62419 (Aoyagi, Falarski et al. 1975) is preferred compared with NASA TN D-8061 (Sleeman, Hohlweg et al. 1975), as NASA TN D-8061 has only limited OEI data available. The engines of NASA TM X-62419 have a low BPR of 3, which does not represent state of the art engine technology. Using this data is conservative as a higher BPR improves the low-speed turning characteristics or allows for simpler nozzle design (see section 4.1.6). For EBF, the data of NASA TM X-62197 (Aoyagi, Falarski et al. 1973) represent engines with a BPR of 3. Increasing BPR decreases the effectiveness of EBF systems as discussed in section 4.1.6. The data of NASA TN D-8057 (Johnson 1975) is selected, as BPRs of 6.2 and 10 are

available, which lie in the range of current and future high BPR engines. Additionally, tail-off data for OEI and AEO are available. For the IBF system, the data of NASA TN D-8309 (Vogler 1976) are selected as they have the highest number of flap angles available. For the AIBF aircraft, the only wind-tunnel data available (NASA TM X-62281) are used (Aiken, Aoyagi et al. 1973). The disadvantage of the AIBF data is that only two flap deflections were measured and aerodynamic data a flap deflection of δ_f=0° are not available. All the corrected wind-tunnel data used are given in appendix C (Figure 118 to Figure 136).

6.1.4 Design Parameters

The main design parameters that impact all mission segments are the thrust-to-weight ratio *T/W* and the wing loading *W/S*. Secondary design parameters are the flap angles for take-off $\delta_{f_{TO}}$ and landing (final approach) $\delta_{f_{APP}}$ as they impact the take-off and landing performance. Additional design parameters result from the problems related to the missed approach (MA) with AEO and OEI (see section 4.5), which are the flap angle for MA with OEI $\delta_{f_{MAOEI}}$, the maximum ratio of approach thrust to available OEI thrust $\theta_{\max}$, and the ratio of the speed selected for MA with OEI to the approach speed V_{MAOEI}.

Table 13. Design parameters and design space

Design Parameter	Unit	Design Space
T/W	-	0.2 – 0.6
W/S	kg/m²	350 - 600
$\delta_{f_{TO}}$	deg	Depending on available wind-tunnel data
$\delta_{f_{APP}}$	deg	Depending on available wind-tunnel data
$\delta_{f_{MAOEI}}$	deg	Depending on available wind-tunnel data
$\theta_{\max}$	-	0.4 – 1.0
V_{MAOEI}	-	1.0 – 1.15

For *T/W* and *W/S* a relatively large design space is selected to be able to determine design points for even more challenging field length requirements than 1,000 m. The design space for the flap angles is dependent on the available wind-tunnel data (see Table 28, appendix D). Linear interpolation between flap angles is performed, while extrapolation is not allowed. The maximum relative approach thrust $\theta_{\max}$ explored ranges from 40 % of the available OEI thrust to full OEI thrust during approach, where $\theta_{\max}$ equals 1. The design space for the speed for MA with OEI is defined by FAR-25 requirements (FAA 2009).

An additional design parameter for the IBF system with the mixed-flow engine is the ratio of mass flow that is taken off the engine to the engine's total mass flow τ. An additional

design parameter for the EBF and USB aircraft is the BPR, as it has an impact on the take-off and landing performance as well as on the overall mission performance. For the USB aircraft, a design space for BPR between *BPR*=5 and *BPR*=10 is selected, which is in the range of the engine models developed. For the EBF aircraft, the design space is between *BPR*=6.2 and *BPR*=10, determined by the wind-tunnel data available.

6.1.5 Constraints

The FAR-25 balanced field length and landing field length required for this application example is 1,000 m. Thereby, FAR-25 requirements are applied as documented in sections 4.4 and 4.5. The climb rates required for the relevant mission segment are taken from the FAR-25 requirements for transport aircraft with four engines (FAA 2009). An additional constraint for the approach angle has to be considered, since the algorithm implemented can also give approach angles that are smaller than the one required (see section 4.5.1). These mission segment requirements are summarized in Table 14. The requirements reflect the constraints that are used in the matching chart to determine the design point.

Table 14. Performance requirements

Parameter	Constraint
BFL	< 1000 m
LFL	< 1000 m
$\gamma_{TO_{OEI}}$	> 1.72°
γ_{TOC}	> 300 fpm
$\gamma_{MA_{OEI}}$	> 1.55°
$\gamma_{MA_{AEO}}$	> 1.83°
γ_{APP}	=-6°

6.1.6 Objective

The determination of the design point is a classical optimization problem. In the matching chart, the optimization problem is solved geometrically. The objective function is a combination of *T/W* and *W/S*, where one tries to minimize *T/W* and maximize *W/S* at the same time, based on the experience that these measures minimize fuel burn and *MTOW*. The constraints documented in the previous section determine the feasible design space for *T/W* and *W/S*.

6.2 Sizing for Performance

In this section, the sizing for the required performance is documented for the aircraft with blown flaps. As discussed in section 3.2.3, the complexity of the methods for the take-off

and landing of blown-flaps aircraft requires a design space exploration for the determination of the aircraft design point. For every combination of the design parameters given in Table 13, the performance for every mission segment is calculated and compared to the respective mission segment requirement (see Table 14). In this way the mission segment constraints are determined numerically.

The determination of the design point in this design space is a classical multidimensional optimization problem with the design parameters and constraints presented above. Such optimizations can be performed with different available optimization algorithms. However, the gain in knowledge of the system behavior is, thereby, low. Therefore, for this example, the design space is subsequently analyzed with the help of trade studies and the matching chart. In this stepwise approach, the design parameters related to the missed approach (MA) are first determined by the help of trade studies. Subsequently, the constraints determined for the different mission segments are plotted in the matching chart to find the best combination of *T/W* and *W/S*. In this way the main findings are discussed to better understand the effects that occur for blown-flaps aircraft.

The way to find the final design point within the explored design space has to be an iterative one, as all design dimensions cannot be displayed at the same time. Therefore, a sequential approach for its determination is presented in the following (Figure 62).

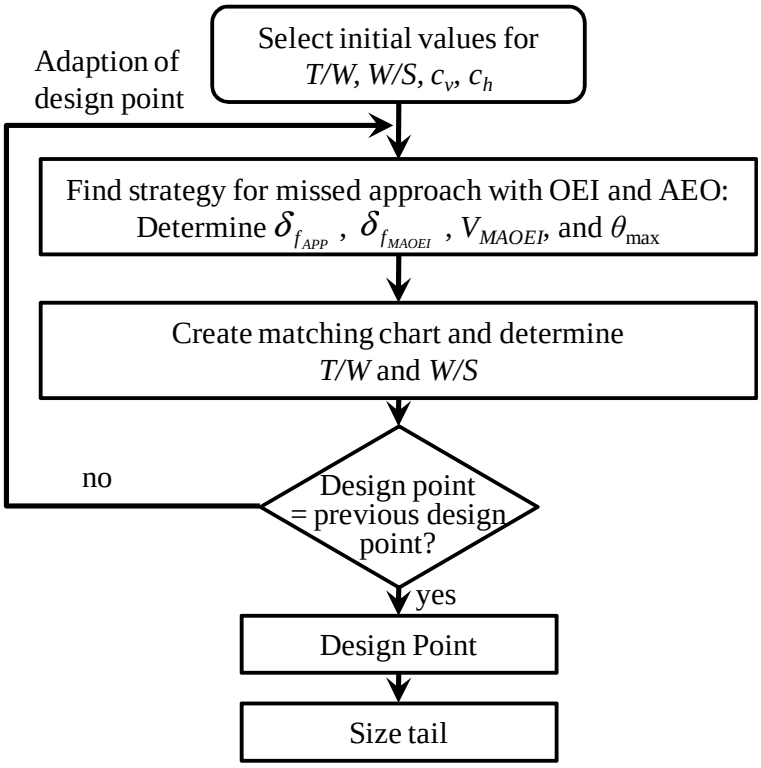

Figure 62. Approach for sizing for performance

A reasonable initial combination of *T/W* and *W/S* (design point) is selected first. As discussed in section 4.5.2, a MA strategy has to be found that satisfies all climb requirements related to the approach segment. This includes finding a combination of approach flap angle $\delta_{f_{APP}}$, ratio of approach thrust to available OEI thrust $\theta_{\max}$, MA flap angle $\delta_{f_{MA}}$, and relative MA speed V_{MAOEI} (see section 4.5.2). With the parameter combination selected, the matching chart is created to find a design point (*T/W, W/S*) that satisfies all requirements. If the design point differs from the initial one, new trade studies are performed, to adapt the parameter setting for the MA with OEI, until the final design point is found. Finally, the tail of the aircraft is resized according to the approach presented in section 4.2.4. If the tail size required differs from the initial one, such that it impacts the take-off, landing and climb performance, the sizing approach has to be repeated. This procedure is performed for different BPRs to find the different design points for the different BPR engines.

In the following, for the EBF aircraft, the trade-studies required to determine the approach parameters and the tail size is presented, as example. Thereby the final design point is anticipated. The final matching charts for the different aircraft alternatives are presented and compared to each other. Subsequently, examples for the trade studies performed to size the tails of the aircraft are presented and the take-off and landing is discussed for the design points determined.

6.2.1 Trade Studies for Missed Approach

The trade studies required to find the main parameters for the MA with AEO and OEI are presented for the EBF concept with a BPR of 6.2. The design point chosen, thereby, is *T/W*=0.5 and *W/S*=600 kg/m², which is very close to the final design point.

The scope of this section is to show the main interrelations between the design parameters and the MA climb performance and to discuss the potential strategies that were derived in section 4.5.2. Consequently, the parameters varied are:

- $\delta_{f_{APP}}$
- $\delta_{f_{MAOEI}}$
- V_{MAOEI}
- $\theta_{\max}$

The relevant constraints that have to be satisfied for approach and MA are:

- γ_{MAOEI} > 1.55°
- γ_{MA} > 1.83°
- γ_{APP} = -6°
- $k^2_{MAOEI} > 1.69$

For the MA with OEI, the same lift coefficient safety margin as for the final approach is assumed. In a 2-dimensional chart, two input dimensions are visualized by the help of one array parameter. This is done systematically for different values for γ_{MA} and γ_{MAOEI} to account for the third and fourth input dimension. The flap angles investigated are the flap angles available (δ_f=35° and δ_f=65°) and δ_f=50°, where the aerodynamic coefficients are determined by linear interpolation. The relevant mission segment constraints are visualized in the charts to find the combination of the design parameters that satisfies all requirements best.

A. Approach Flap Angle $\delta_{f_{APP}}$=35°

Figure 63 shows the climb angle during MA with OEI for an approach flap angle of $\delta_{f_{APP}}$ = 35° and different values for V_{MAOEI}, θ_{max}, and $\delta_{f_{MAOEI}}$. Only $\delta_{f_{MAOEI}}$=35° gives reasonable values for γ_{MAOEI} (see Figure 63) up to V_{MAOEI} =1.1. The higher flap angle of $\delta_{f_{MAOEI}}$=50° has negative values for γ_{MAOEI}, which means that the aircraft cannot climb and does not meet the minimum climb angle required (γ_{MAOEI}>1.55°). For $\delta_{f_{MAOEI}}$=65°, γ_{MAOEI} has even lower values. This flap angle is therefore not displayed here.

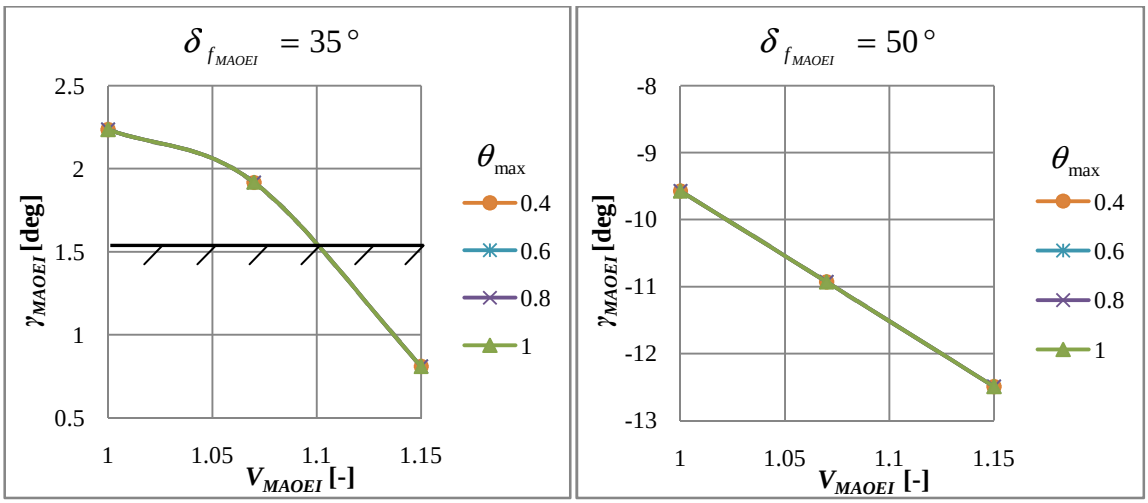

Figure 63. Climb angle for MA with OEI over V_{MAOEI} and θ_{max} ($\delta_{f_{APP}}$ = 35°)

Due to the very low approach flap angle of $\delta_{f_{APP}}$=35°, the iterated approach speed is relatively high for a blown-flaps aircraft (v_{APP}=137 kts). At such a low value for $\delta_{f_{APP}}$, only a small amount of thrust can be used for landing (θ=0.3). A higher amount of thrust during approach cannot be used as it would result in a higher approach angle than the one required. The thrust used during landing is therefore always below all values for the maximum limit θ_{max} displayed in Figure 63, which is the reason why the characteristics collapse. The climb angle for MA with OEI γ_{MAOEI} decreases with increasing V_{MAOEI}, as the jet momentum coefficient decreases with increasing speed (see Figure 64, right), which results in lower climb performance.

Additionally, the safety margin for MA with OEI has to be considered, which for $\delta_{f_{MAOEI}}=35°$ is higher than the required value (k^2_{MAOEI}=1.69) for all values of V_{MAOEI} (see Figure 64 left). The safety margin decreases with increasing V_{MAOEI}, as the jet momentum coefficient decreases with increasing speed (see Figure 64 right), which results in a lower maximum lift coefficient.

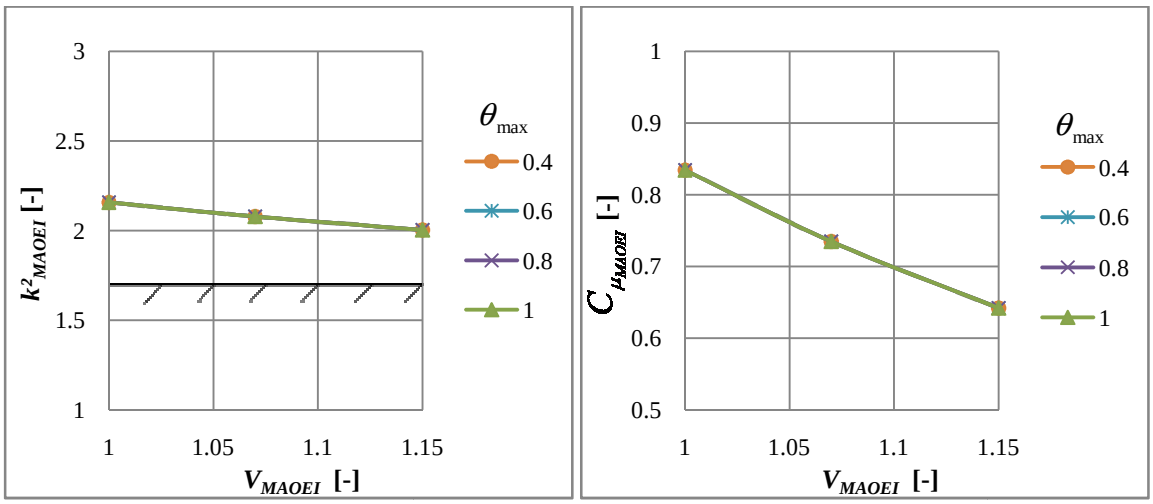

Figure 64. Lift coefficient safety margin (left) and C_μ (right) for MA with OEI ($\delta_{f_{APP}}$=35°, $\delta_{f_{MAOEI}}$=35°)

The climb angle for MA with AEO is γ_{MA}=12.1° and exceeds the minimum climb angle required, as there is a large amount of thrust available that can be used during MA and as the approach flap angle is low, which results in low drag.

The solutions for the approach parameters summarized in Table 15 all satisfy the climb constraints for MA with OEI and AEO. However, at $\delta_{f_{APP}}$=35° the EBF aircraft has a relatively high approach speed and makes only limited use of blown flaps effects during

approach (C_μ=0.23). This is an option to land in an almost conventional way with a low flap extension and a low jet momentum coefficient.

Table 15. Approach parameter values that satisfy the MA and MA with OEI requirements at $\delta_{f_{APP}}$ =35°

Parameter	Unit	Design Space
$\delta_{f_{MAOEI}}$	deg	35
θ_{max}	-	0.4 - 1.0
V_{MAOEI}	-	1.0 - 1.1
v_{APP}	kts	137

B. Approach Flap Angle $\delta_{f_{APP}}$ =50°

Due to the higher approach flap angle, more thrust is turned downward which allows for a higher thrust rating during approach. Therefore, the upper limit for the approach thrust θ_{max} is reached and impacts the approach speed and climb performance at $\delta_{f_{APP}}$ =50° in contrast to $\delta_{f_{APP}}$ =35°, where all characteristics for the different values for θ_{max} collapsed.

Figure 65 shows the climb angle during MA with OEI for $\delta_{f_{APP}}$ =50°. Again, the required climb angle during MA with OEI can only be achieved with the flap deflection of $\delta_{f_{MAOEI}}$ = 35° (see Figure 65 left). With a flap deflection of $\delta_{f_{MAOEI}}$ =50° during MA with OEI, positive climb rates cannot be achieved (see Figure 65 right).

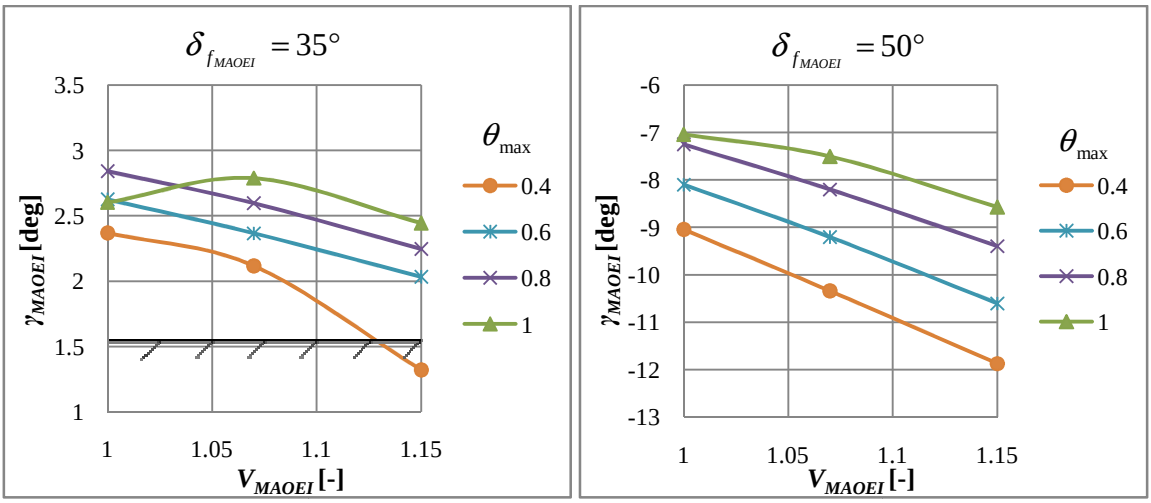

Figure 65. Climb angle for MA with OEI over V_{MAOEI} and θ_{max} ($\delta_{f_{APP}}$ =50°)

Surprisingly, a limitation of the approach thrust, which means that more thrust reserves are available for missed approach, decreases the climb angle during MA with OEI. The reason is that if the approach thrust is limited, the jet momentum coefficient for approach decreases

(Figure 66, right), which increases the approach speed (Figure 66, left). Increased approach speed again decreases the jet momentum coefficient. As a consequence, the climb performance decreases. For θ_{max} =0.4 the approach speed is 134 kts at $C_{\mu_{APP}}$ =0.31. For maximum available OEI thrust, where θ_{max} equals 1, the approach speed is 112 kts at $C_{\mu_{APP}}$ =1.1.

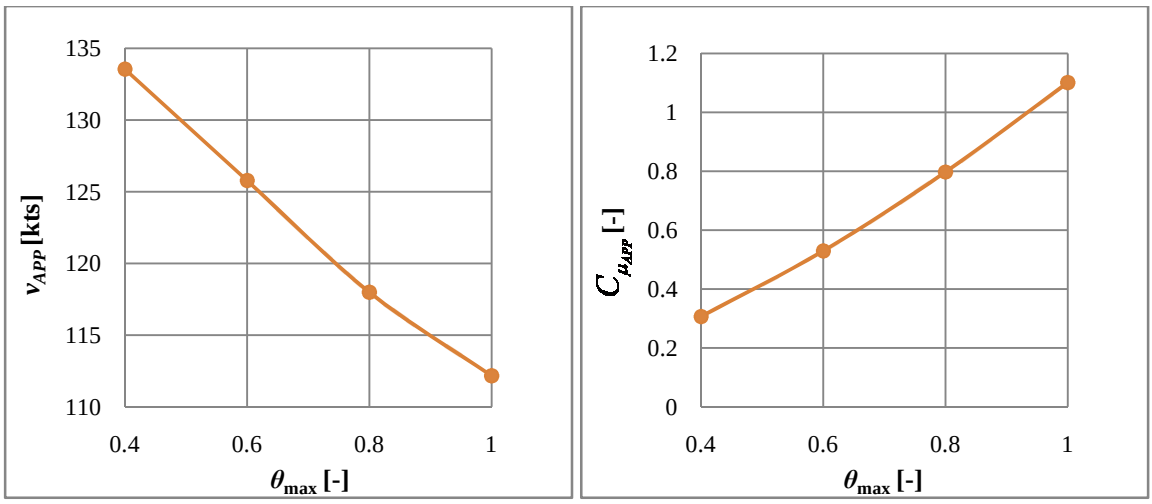

Figure 66. v_{APP} (left) and jet momentum coefficient (right) over θ_{max} ($\delta_{f_{APP}} = 50°$, $\delta_{f_{MAOEI}} = 35°$)

The jet momentum coefficient during MA with OEI decreases with decreasing θ_{max}, due to the increasing approach speed (Figure 67), although more thrust is available: The jet momentum coefficient decreases with the square of v_{APP}, and increases only linearly with the jet momentum (see equation (1)). For the same reason, the jet momentum coefficient decreases with decreasing MA speed (Figure 67). Due to the lower jet momentum coefficients, the climb performance during MA with OEI is decreasing with decreasing θ_{max} and increasing V_{MAOEI} (see Figure 65).

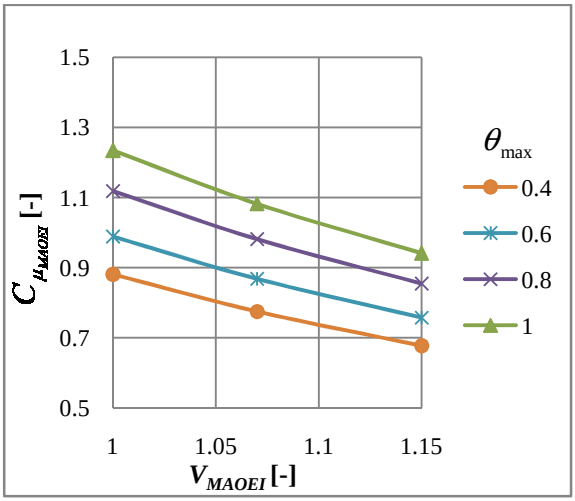

Figure 67. Jet momentum coefficient for MA with OEI over V_{MAOEI} and θ_{max} ($\delta_{f_{APP}}$ =50°, $\delta_{f_{MAOEI}}$ =35°)

The additional constraints that have to be considered are the approach angle during MA with AEO γ_{MA} and the lift coefficient safety margin during MA with OEI k^2_{MAOEI}.

Figure 68 shows γ_{MA} over θ_{max}. Due to the decreasing jet momentum coefficient during approach with decreasing θ_{max} (Figure 66 right), the climb angle during MA decreases with decreasing θ_{max}. Beyond θ_{max}=0.78 the required climb angle during MA is achieved.

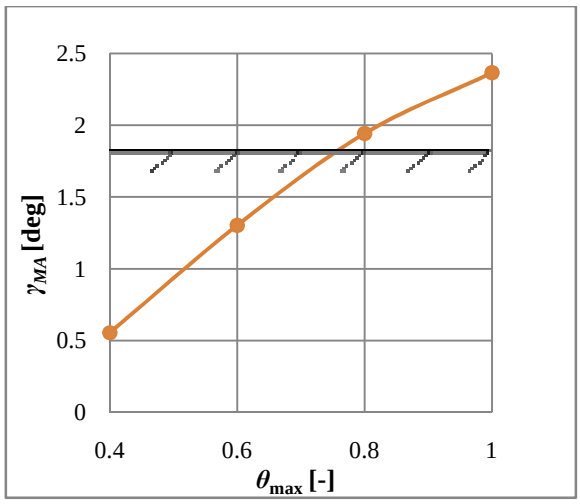

Figure 68. Climb angle for MA with AEO over V_{MAOEI} and θ_{max} ($\delta_{f_{APP}}$ =50°, $\delta_{f_{MAOEI}}$ =35°)

Figure 69 shows the lift coefficient safety margin k^2_{MAOEI} over V_{MAOEI} and θ_{max}. The minimum safety margin required is 1.69, which at V_{MAOEI} =1 is satisfied for all values for θ_{max}. For higher MA speeds, the safety margin is only satisfied for lower values for θ_{max}, which are not desirable, as they have higher approach speeds (Figure 66 left).

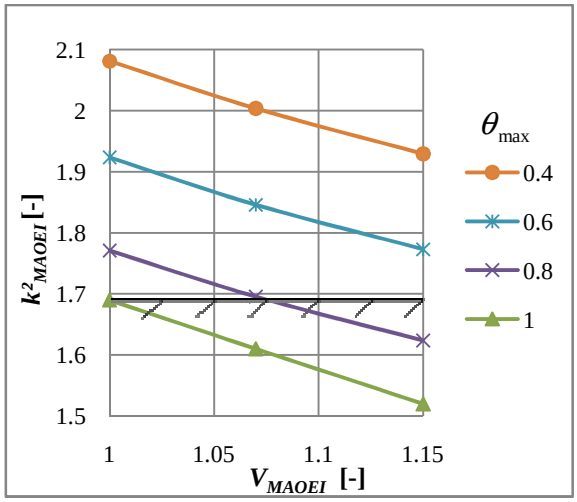

Figure 69. Lift coefficient safety margin for MA with OEI, ($\delta_{f_{APP}}$ =50°, $\delta_{f_{MAOEI}}$ =35°)

The combination of the design parameters that satisfies all requirements and has the lowest approach speed is summarized in Table 16. Only a flap angle during MA with OEI of $\delta_{f_{MAOEI}}$ =35° meets the required climb angle (Figure 65). Values for θ_{max} between θ_{max} =0.78 and θ_{max}=1.0 meet the required climb angle during MA with OEI and MA (Figure 65 and Figure 68), but θ_{max}=1.0 has the lowest approach speed (see Figure 66, right). At θ_{max}=1.0, the required lift coefficient safety margin is only satisfied at V_{MAOEI} =1.0. The approach speed for this parameter combination is 112 kts and significantly lower than for $\delta_{f_{APP}}$ =35° (137 kts, see Table 15).

Table 16. Approach parameter values that satisfiy the MA and MA with OEI requirements at $\delta_{f_{APP}}$ = 50°

Parameter	Unit	Design Space
$\delta_{f_{MAOEI}}$	deg	35
θ_{max}	-	1.0
V_{MAOEI}	-	1.0
v_{APP}	kts	112

C. Approach Flap Angle $\delta_{f_{APP}}$ =65°

For an approach flap angle of $\delta_{f_{APP}}$ =65°, only with a MA flap angle of $\delta_{f_{MAOEI}}$ =35° can sufficient climb angles for MA with OEI be achieved (Figure 70). However, an approach flap angle of $\delta_{f_{APP}}$ =65° is not a suitable solution, as the climb angle for MA with AEO γ_{MA} is below the one required (Figure 71).

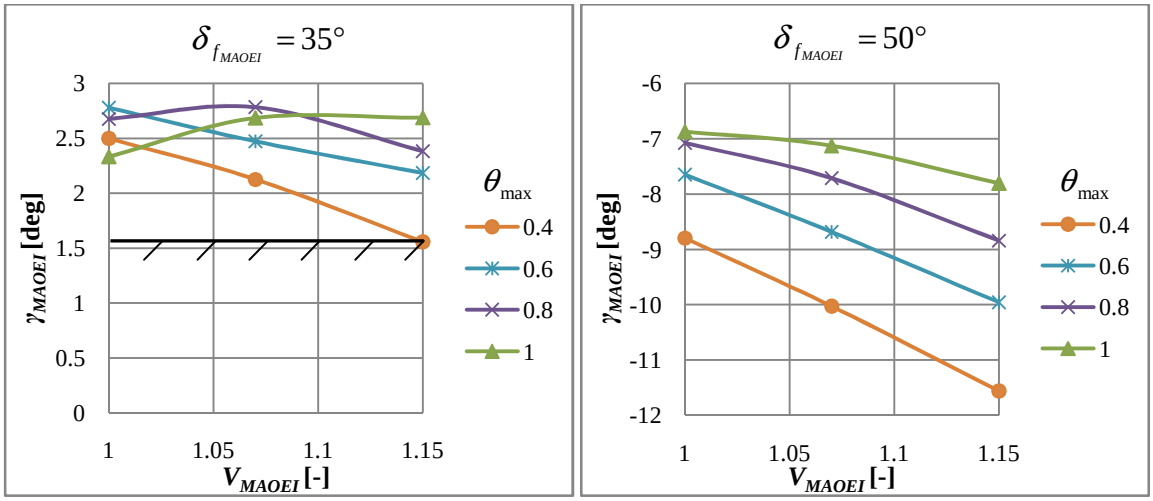

Figure 70. Climb angle for MA with OEI over V_{MAOEI} and θ_{max} ($\delta_{f_{APP}}$ =65°)

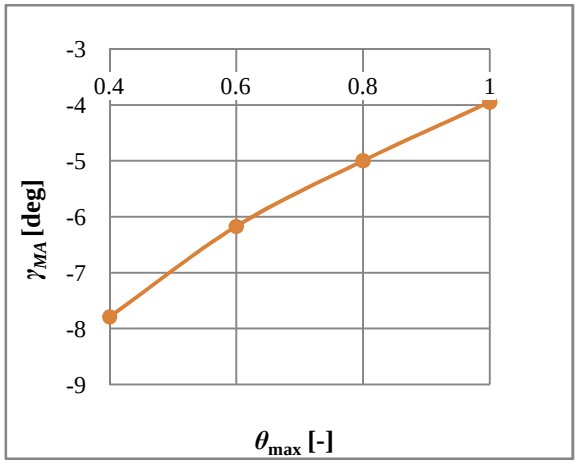

Figure 71. Climb angle for MA with AEO ($\delta_{f_{APP}}$ =65°)

D. Conclusion

For this exemplary concept, an approach flap angle of $\delta_{f_{APP}}$ =50° and a MA flap angle of $\delta_{f_{MAOEI}}$ =35° give the landing flap angle combination with the minimum approach speed that satisfies all requirements. It has been shown that decreasing the approach thrust does not improve the climb performance, neither for MA with OEI nor for MA with AEO. Decreasing approach thrust increases the approach speed, which in total reduces the jet momentum coefficient, which reduces the climb angles. Increasing the MA speed does not improve the climb performance, as again the jet momentum coefficient is decreased.

In summary, the determination of a suitable combination of the approach flap angle $\delta_{f_{APP}}$ and the missed approach flap angle with OEI $\delta_{f_{MAOEI}}$ is the best measure to meet the required climb performance for MA with OEI and AEO.

6.2.2 Matching Charts

In this section, the matching charts for the investigated blown-flaps aircraft are presented. For each aircraft, the combination of $\delta_{f_{MAOEI}}$ and $\delta_{f_{APP}}$ was determined with the procedure documented in the previous section.

A. EBF

Figure 72 to Figure 74 show the matching charts for the EBF aircraft for different BPRs. Thereby, the approach flap angles derived in the previous section are applied. The flap angle for take-off is $\delta_{f_{TO}}$ =35°, which cannot be optimized for the EBF aircraft, as lower flap angles are not available from the wind-tunnel tests.

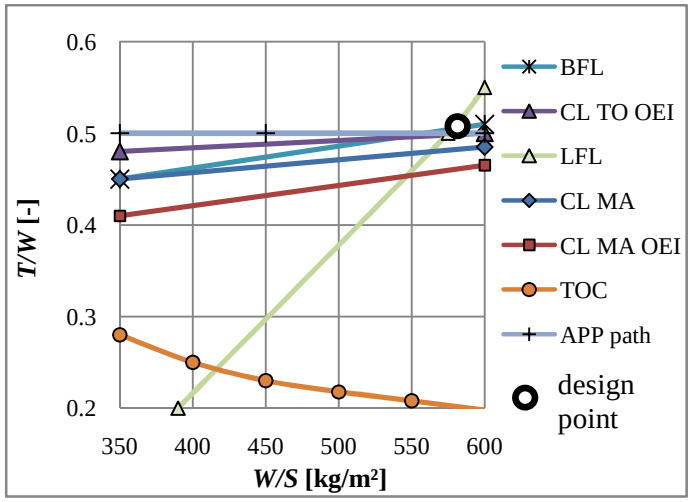

Figure 72. Matching chart of EBF aircraft, *BPR*=6.2

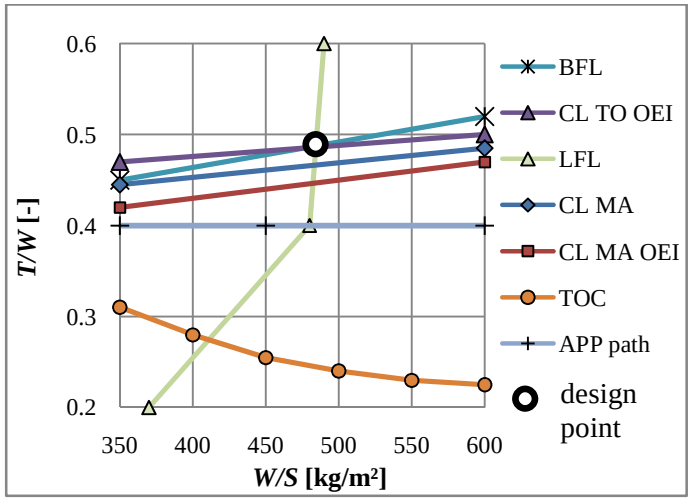

Figure 73. Matching chart of EBF aircraft, *BPR*=8

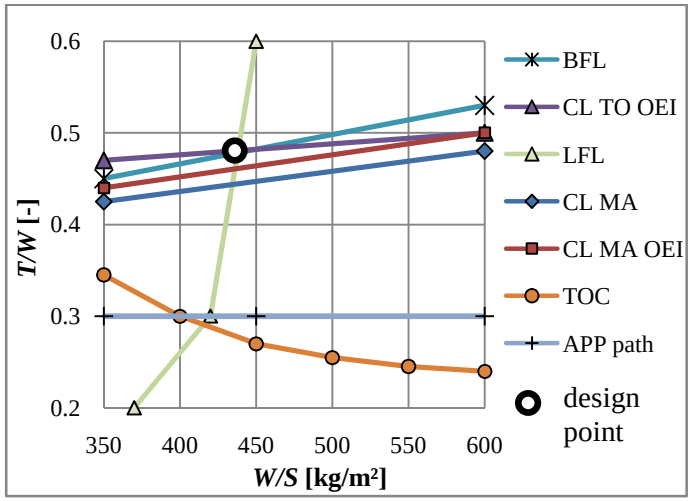

Figure 74. Matching chart of EBF aircraft, *BPR*=10

For aircraft with mechanical high-lift devices, the landing constraint is a vertical line, as the landing field length is only a function of the wing loading. For the EBF aircraft, the landing field length constraint is a function of the wing loading and the thrust-to-weight ratio, as the approach speed is a function of the wing area and the installed thrust (see Figure 59, p. 83).

The landing constraint has a break at the thrust-to-weight ratio, where the approach path constraint is active. Above this thrust-to-weight ratio, the available thrust has to be reduced to achieve the -6° approach path. Below this thrust-to-weight ratio, the -6° approach angle cannot be maintained and the entire thrust is used during landing, which causes a higher dependency of the installed thrust on the landing constraint. This characteristic can also be observed for all other blown-flaps systems.

With increasing BPR, the wing loading required to meet the required landing field length decreases. The reason is that, with increasing BPR, less air blows on the flaps (see also section 4.1.6), which has the following effects:

- The super-circulation is reduced, which reduces the lift coefficient (Figure 32)
- More forward thrust is produced, which forces a reduction in the thrust rating during approach to meet the required approach angle (Figure 75 left). This again decreases the lift coefficient due to the lower jet momentum coefficient available (Figure 75 right).

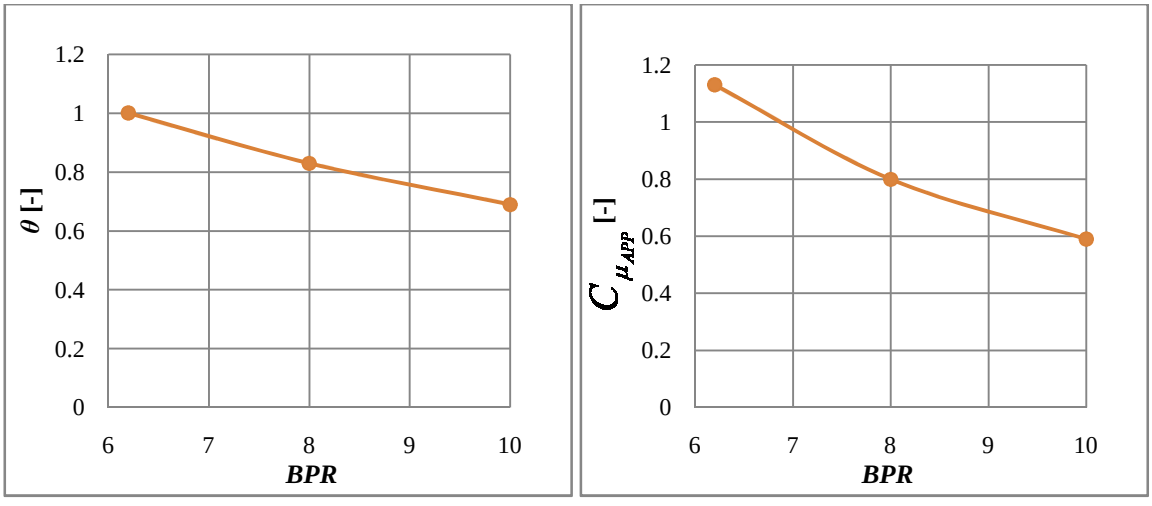

Figure 75. Approach thrust rating (left) and jet momentum coefficient (right) over *BPR* for EBF aircraft

For a given reference area, these effects cause an increase in the approach speed. If a certain LFL is required, the reference area has to be increased to meet the required LFL and the related approach speed, which results in lower wing loadings.

Due to the increasing approach speed with increasing BPR, the jet momentum coefficient during MA with OEI decreases, resulting in lower climb performance during this segment, which is the reason, why the climb constraint for MA with OEI moves upwards in the matching chart with increasing BPR.

Due to decreasing thrust rating during approach with increasing BPR, the wing area has more impact on the landing field length compared to the aircraft with lower BPRs, where more thrust is used for landing. This explains that, with increasing BPR, the landing field length constraint moves more towards a vertical line.

For aircraft with mechanical high-lift devices, the climb constraints are horizontal lines (see Figure 23, p. 26), as the thrust required to meet a certain climb angle required is calculated assuming constant lift-to-drag ratio. Here, for every point within the design space, the take-off and approach speed and lift coefficients are different. Due to slightly lower lift coefficients required for the lower wing loadings, the climb performance is better, resulting in lower thrust requirements compared to aircraft with higher wing loadings.

The impact of the BPR on the balanced field length and climb during take-off with OEI constraints is negligible. The take-off constraint moves only slightly upwards with increasing BPR. On the one hand, the increased BPR increases the take-off speed, as less thrust is used for lift generation. On the other hand, more forward thrust is available, which increases the acceleration and improves the climb performance.

The thrust required to meet the minimum climb rate at top of climb increases with increasing BPR, as the thrust available at cruise altitude is decreasing with increasing BPR. However, the thrust required for the different requirements related to take-off and landing is significantly higher compared with the thrust required for the top of climb requirement.

The climb constraints for the MA segments are close to the design point which is a result of the flap angle selection documented in the previous section. The flap angles for approach are chosen so as to deliver the required performance.

Table 17 shows the different design points for the different BPRs and the design mission fuel burn for the design mission relative to the fuel burn of the aircraft with the BPR of 6.2. The decreased wing loading with increasing BPR decreases the lift-to-drag ratio and increases the wing weight. However, due to the better SFC of the aircraft with the higher BPRs the total mission fuel burn is only slightly higher compared with the aircraft with *BPR*=6.2 for the investigated design mission.

Table 17. Design points for EBF aircraft with different BPRs

		T/W [-]	*W/S* [kg/m²]	$\overline{m}_{BF}$ [-]
BPR	6.2	0.51	580	1
	8	0.49	480	1.01
	10	0.48	440	1.02

Due to the slightly better mission fuel burn, the aircraft with *BPR*=6.2 is selected for the further comparison with the other blown-flaps aircraft. The design point for this BPR is *T/W*=0.51 and *W/S*=580 kg/m².

B. USB

For the USB aircraft, an approach flap angle of $\delta_{f_{APP}}$=60° and a MA flap angle of $\delta_{f_{MAOEI}} = 40°$ result in the minimum approach speed and meet the climb angle and safety margin requirements.

The impact of the BPR on the aerodynamic characteristics of the USB aircraft is not modeled as wind-tunnel data for different BPRs are not available. However, due to the different engine characteristics, the USB aircraft has an increasing wing loading with increasing BPR for the required landing field length (see Figure 76 to Figure 78). With increasing BPR, the ram drag and the gross thrust are increasing (see Figure 38, p. 54), which increase the jet momentum coefficient during approach (see Table 18). Therefore, the approach speed is decreasing with increasing BPR. For a required approach speed the wing loading increases with increasing BPR.

The thrust required for top of climb is very high compared to the EBF aircraft, which results from the drag penalty due to the engine installation on the upper side of the wing (see section 4.6.1). Again, with increasing BPR the thrust required for top of climb is increasing. The thrust required for top of climb is higher than the thrust required for the take-off requirements or the MA requirements.

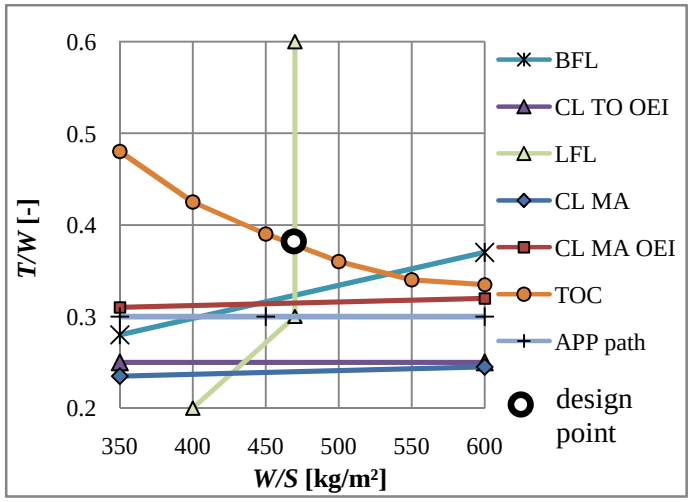

Figure 76. Matching chart for USB aircraft, *BPR*=5

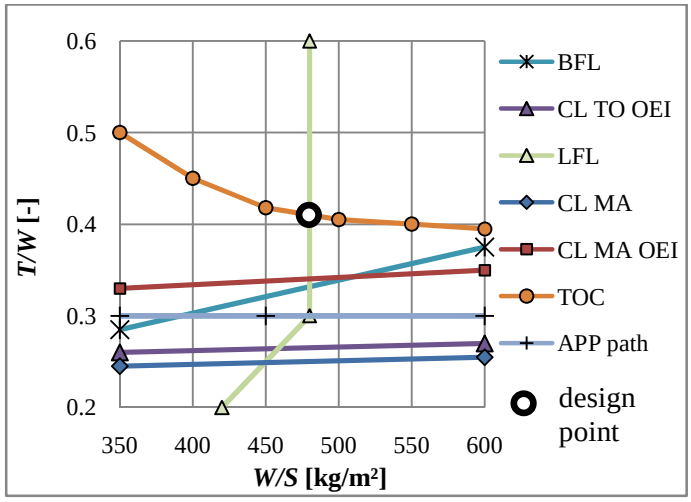

Figure 77. Matching chart for USB aircraft, *BPR*=7.5

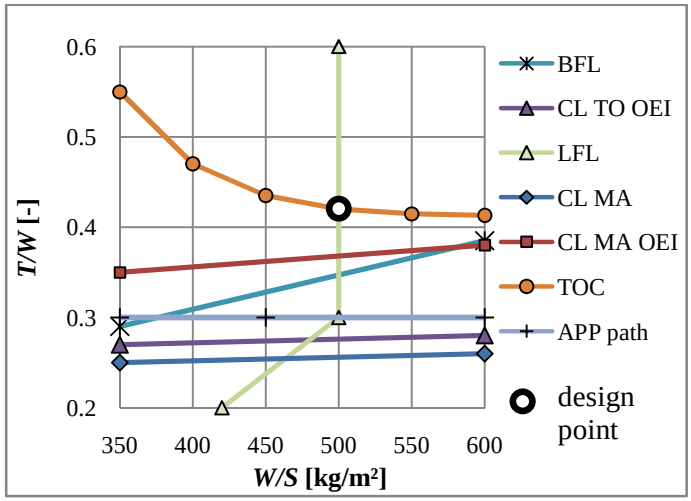

Figure 78. Matching chart for USB aircraft, *BPR*=10

Table 18 shows that the aircraft with *BPR*=10 has the lowest overall mission fuel burn and is therefore selected for comparison with the other aircraft. The lower fuel burn results from the higher wing loading and better SFC with increasing BPR. The design point has a thrust-to-weight ratio of *T/W*=0.42 and a wing loading of *W/S*=500 kg/m².

Table 18. Design points for USB aircraft with different BPRs

		T/W [-]	*W/S* [kg/m²]	$\overline{m}_{BF}$ [-]	$C_{D_{RD}}$ [-]	$C_{\mu_{APP}}$ [-]
BPR	5	0.38	470	1.2	0.08	0.49
	7.5	0.41	480	1.09	0.1	0.55
	10	0.42	500	1.0	0.12	0.6

C. AIBF

For the AIBF aircraft, only the engine with a BPR of 10 was considered feasible, due to the suitable fan pressure ratio (see section 4.3). An approach flap angle of $\delta_{f_{APP}}$ =60° and a MA flap angle of $\delta_{f_{MAOEI}}$ =45° result in the minimum approach speed and meet the climb angle and safety margin requirements. For take-off, only a flap angle of $\delta_{f_{TO}}$ =30° is available.

The wing loading for the design point is *W/S*=550 kg/m² determined by the landing field length constraint, which for the AIBF aircraft is a vertical line above *T/W*=0.3. Above *T/W*=0.3, there is more thrust available than necessary to achieve the required approach speed and the required approach angle. A higher installed thrust does not improve the landing performance, as the thrust during approach would anyway have to be reduced to meet the required approach angle. Therefore, the LFL is not a function of the thrust-to-weight ratio installed. Below *T/W*=0.3, the entire installed thrust can be used during landing, with the result that the landing constraint is a function of the installed thrust.

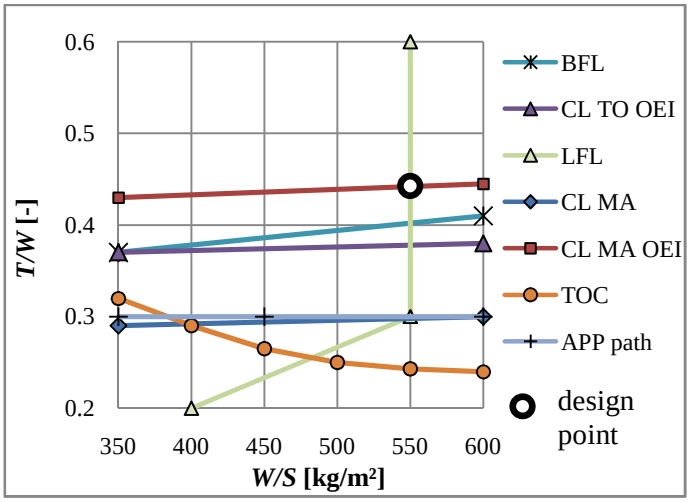

Figure 79. Matching chart for AIBF aircraft, *BPR*=10

The thrust-to-weight ratio for the design point is *T/W*=0.44, determined by the MA with OEI constraint. A lower flap angle for MA OEI could reduce the thrust required, but would result in a safety margin that is below the one required (see Figure 137, appendix E).

D. IBF with Exhaust Offtake

For the IBF aircraft with exhaust offtake as well as with bypass offtake, only the engine with a BPR of 5 is feasible, due to the suitable fan pressure ratio (see section 4.3). For the IBF aircraft with exhaust offtake, a flap angle of $\delta_{f_{APP}}$=60° and a MA flap angle of $\delta_{f_{MAOEI}} = 45°$ result in the minimum approach speed and meet the climb angle and safety margin requirements. Thereby, the best value for τ is 0.6 (60 % of the total mass flow). A higher value would further decrease the approach speed but also reduce the safety margin for MA with OEI (see Figure 138, appendix E).

For the take-off segment, the lower BFL is achieved with a flap angle of $\delta_{f_{TO}}$=15° compared with a flap angle of $\delta_{f_{TO}}$=30°, while at this flap angle the offtake-ratio has almost no impact on the BFL (Figure 139, appendix E). The same value of τ=0.6 as for landing is selected.

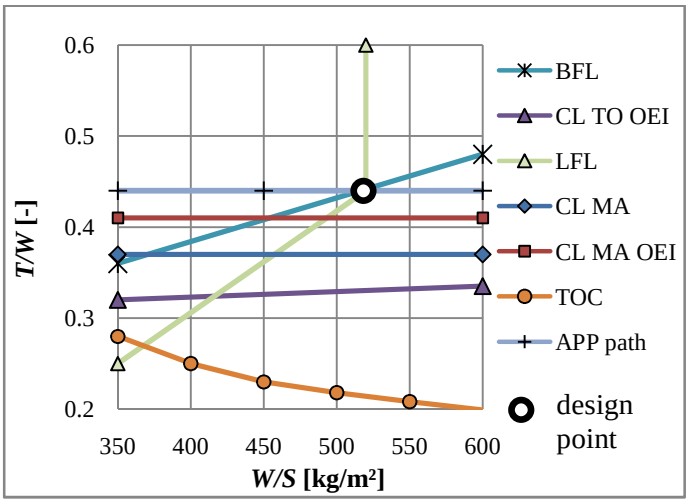

Figure 80. Matching chart for IBF aircraft with exhaust offtake, *BPR*=5

The design point for the IBF aircraft with exhaust offtake is *T/W*=0.44 and *W/S*=520 kg/m², determined by the landing constraint, BFL constraint and the approach angle required.

E. IBF with Bypass Offtake

An approach flap angle of $\delta_{f_{APP}}$=55° and a MA flap angle of $\delta_{f_{MAOEI}}$=45° result in the minimum approach speed and meet the climb angle and safety margin requirements.

Compared with the IBF aircraft with the exhaust offtake a slightly lower approach flap angle is necessary to meet the required approach angle. For the IBF aircraft with bypass offtake, only around 20 % of the thrust is produced by the core and acting in forward direction. With the approach flap angle of 60°, the total forward force is not enough to maintain the -6° approach angle. The IBF aircraft with exhaust offtake has 40 % of the gross thrust produced in a forward direction, which allows for a higher approach flap angle which produces more lift and less thrust with the jet momentum that goes through the flaps compared to the lower flap angle.

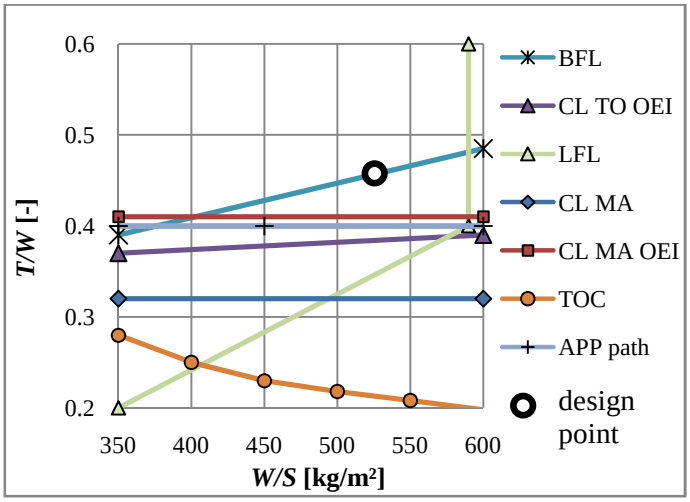

Figure 81. Matching chart for IBF aircraft with bypass offtake, *BPR*=5

With increasing wing loading along the BFL constraint, the thrust-to-weight ratio required increases, which has opposed trends with respect to mission fuel burn. For this reason, for the determination of the best design point, the design mission fuel burn has to be considered.

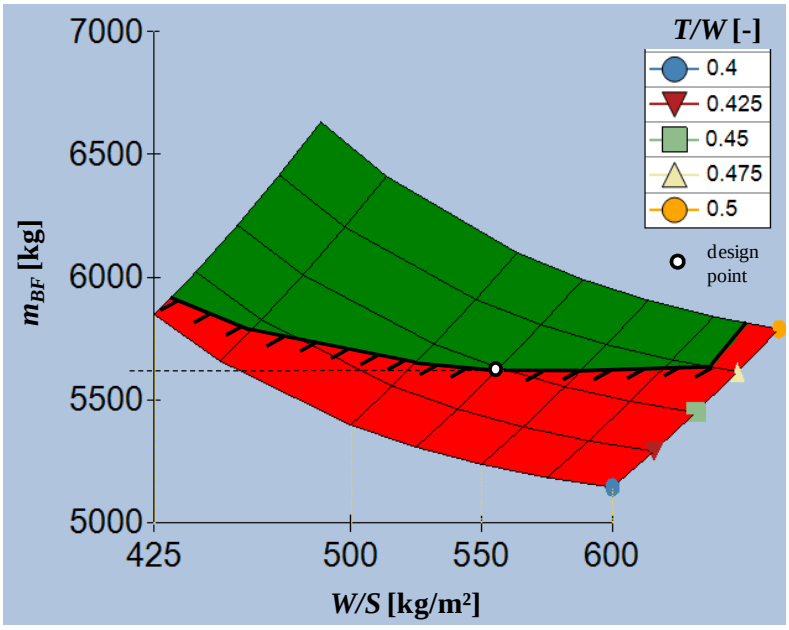

Figure 82. Block fuel over *T/W* and *W/S* for IBF aircraft with bypass offtake

Figure 82 shows the design mission fuel burn over *T/W* and *W/S* in a carpet plot including the considered constraints. The green area represents the combinations of *T/W* and *W/S* that meet all requirements. Between a wing loading of *W/S*=525 kg/m² and *W/S*=575 kg/m² almost no difference is observable. The combination of *T/W*=0.45 and *W/S*=525 kg/m² is selected as the design point for the IBF aircraft with bypass offtake.

F. Comparison of Design Points

Table 19 compares the design points for the different blown-flaps aircraft and their absolute values for BFL and LFL. The tail volumes determined in the next section are, thereby, applied. The design of the reference aircraft is documented in a previous study (Gologan, Stagliano et al. 2009).

Table 19. Comparison of design points for blown-flaps aircraft

	Unit	Reference	USB	EBF	AIBF	IBF-by	IBF-ex
T/W	-	0.27	0.42	0.51	0.44	0.45	0.44
W/S	kg/m²	510	500	580	550	525	520
BFL	m	1,900	750	1,000	880	1,000	1,000
LFL	m	1,450	1,000	1,000	1,000	920	1,000

The USB aircraft has the lowest required thrust-to-weight ratio compared with the other blown-flaps aircraft, but also the lowest wing loading. The LFL is exactly 1,000 m, as the design point lies exactly at the landing constraints. The BFL is 750 m and shorter than the one required, as the thrust-to-weight ratio at the required wing loading is determined by the top of climb constraint; the thrust-to-weight ratio required for the BFL constraint is lower than the thrust required for top of climb condition. The EBF aircraft has the highest *T/W* required, but also the highest wing loading. The BFL and LFL are exactly 1,000 m, as the design point is determined by the take-off and landing constraints. The AIBF aircraft has a LFL of 1,000 m, as the wing loading (550 kg/m²) is determined by the landing constraint. The BFL is 880 m, which is shorter than that required, as more thrust is installed due to the missed approach with OEI segment than required for the 1,000 m BFL. The IBF aircraft have similar design points. The IBF aircraft with bypass offtake has a LFL of 920 m, as a lower wing loading than the one required was selected for the design point. While the wing loadings of the blown-flaps aircraft are comparable or even higher compared with the reference aircraft, the thrust-to-weight ratio is significantly higher.

Table 20 compares the take-off with OEI of the different blown-flaps aircraft. The USB, EBF and AIBF aircraft have similar flap deflections and take-off speeds, while the IBF

aircraft have a smaller flap angle and, therefore, higher take-off speeds. Due to the higher take-off speed, the lift coefficients are lower (between 2.15 and 2.51), while the USB, EBF and AIBF aircraft have higher lift coefficients (around 3.0). All lift coefficients are above typical values for aircraft with mechanical high-lift devices; the reference aircraft has a take-off lift coefficient of 1.67 and a take-off speed of 135 kts. The EBF aircraft has the highest jet momentum coefficient (C_μ=1.38), while the USB and AIBF aircraft have jet momentum coefficients approximately 1.0. The IBF aircraft with the bypass offtake has a jet momentum coefficient of 0.71, while the IBF aircraft with the exhaust offtake has a jet momentum coefficient of 0.44. The low jet momentum and lift coefficients of the IBF aircraft with the exhaust offtake is explained by the comparably low amount of engine jet momentum that goes through the jet flaps (60 % of the total engine mass flow).

Table 20. Comparison of take-off with OEI

	Unit	USB	EBF	AIBF	IBF by	IBF ex
C_μ	-	1.04	1.38	0.99	0.71	0.44
C_L	-	2.87	3.18	3.22	2.51	2.15
C_D^*	-	-0.28	-0.10	-0.21	-0.15	-0.19
γ	deg	5.6	1.8	3.7	3.5	5.0
δ_f	deg	30	35	30	15	15
v_{TO}	kts	103	105	102	113	121
v_1	kts	93	105	96	105	109
v_{mc}	kts	94	96	93	103	111

The lift coefficients and the jet momentum coefficient for take-off are below the maximum lift coefficients measured in wind-tunnel for blown flaps. The reasons are the limitations that occur if applying blown flaps to a real aircraft. Figure 83 shows how the lift (left) and lift coefficient (right) change during the iteration of the take-off speed for the USB aircraft. The algorithm starts at the minimum speed $v_{\min}$, where wind-tunnel data is available (30.5 m/s). At this point, C_μ equals 3.06 and the lift coefficient that satisfies the safety margin is 4.85, but the lift that is produced by the aircraft (280 kN) is not enough to lift the aircraft MTOW (540 kN). Therefore, the aircraft cannot take off and the speed has to be increased, which decreases the jet momentum coefficient and thus the lift coefficient. The speed is increased until the lift equals *MTOW*. An additional reduction of the total lift coefficient results from the lift coefficient required to trim the aircraft (compare lift of the wing-fuselage configuration and the total aircraft lift in Figure 83).

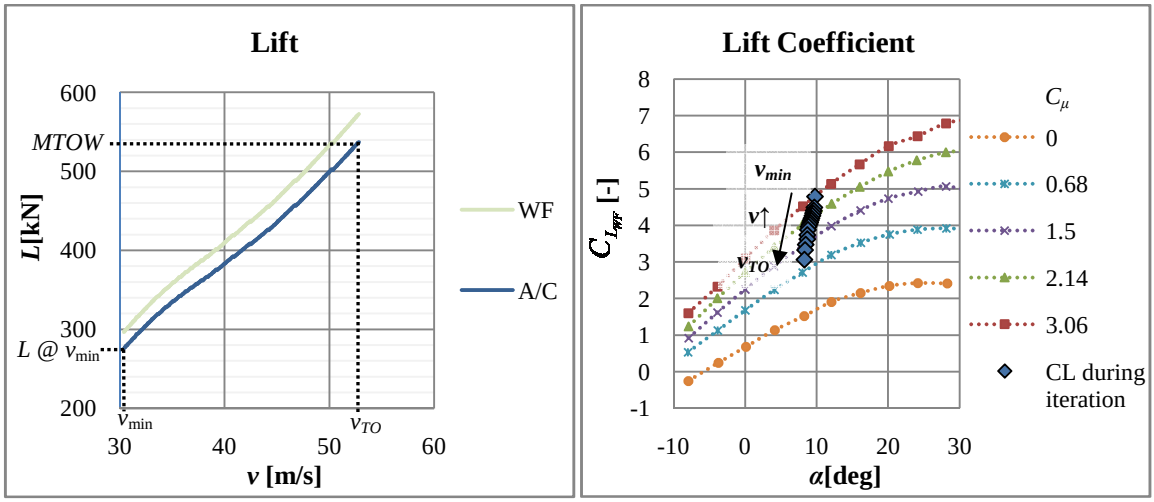

Figure 83. Lift and lift coefficient during take-off speed iteration

The take-off with AEO has the same lift coefficients as the OEI take-off, as it occurs at the same speed as the take-off with OEI. The same trends compared to the OEI take-off apply to the jet momentum coefficients, while the absolute values are higher, as the thrust of all engines is available. As a consequence of the higher available thrust, the climb angles are higher compared to the OEI take-off (see Table 21).

Table 21. Comparison of take-off with AEO

	Unit	USB	EBF	AIBF	IBF-by	IBF-ex
C_μ	-	1.26	1.67	1.20	0.86	0.53
C_L	-	2.87	3.18	3.22	2.51	2.15
C_D^*	-	-0.64	-0.49	-0.55	-0.39	-0.39
γ	deg	12.6	8.7	9.8	8.8	10.2

Table 22 compares the approach with OEI of the different aircraft. The EBF aircraft has the highest jet momentum coefficient and makes use of the entire available OEI thrust during approach (θ=1), while the other aircraft have to reduce their thrust to achieve the required approach angle. The lift coefficients are between 2.34 (USB) and 2.81 (AIBF) and, thus, in the same range as the take-off lift coefficients or even lower. The reason for the relatively low lift coefficients are that the full potential of the blown flaps cannot be used. Reasons are the limitations the required approach path, the required climb performance during missed approach and due to the lift coefficient safety margin. The approach speeds are between 103 kts and 110 kts and lower than for the reference aircraft with mechanical high-lift devices, which has an approach speed of v_{APP}=130 kts at a lift coefficient of C_L=1.67.

Table 22. Comparison of final approach

	Unit	USB	EBF	AIBF	IBF-by	IBF-ex
C_μ	-	0.63	1.14	0.60	0.64	0.47
θ	-	0.74	1.0	0.7	0.83	0.97
C_L	-	2.34	2.64	2.81	2.78	2.40
C_D^*	-	0.25	0.30	0.30	0.30	0.26
C_m	-	-0.49	-0.58	-1.24	-0.71	-0.58
δ_f	deg	60	50	60	55	60
v_{APP}	kts	108	110	104	103	110

6.2.3 Tail and Aileron Sizing

In this section, the trade-studies performed to size the tail are discussed for the USB aircraft and the IBF aircraft with bypass offtake, as examples. The trade studies performed to determine the tail volumes of the other blown-flaps aircraft are given in appendix F. Figure 84 compares the side force coefficient required to trim the aircraft in the case of OEI at v_1 and v_{mc} over the vertical tail volume coefficient, calculated according to section 4.2.3. The side force coefficient required at v_1 is higher, as the dynamic pressure is lower at this lower speed. For both aircraft, $C_{Y_{v\,\mathrm{req}}}$ decreases with increasing vertical tail (VT) volume coefficient c_v. The maximum side force coefficient defined in section 6.1.2 is $C_{Y\,\max_v}$=0.5. The USB aircraft requires a larger vertical tail volume coefficient of c_v=0.155 compared to the IBF aircraft with bypass offtake, which requires a vertical tail volume coefficient of c_v=0.09. The reasons are the following: The IBF aircraft has a lower BPR engine, which has a lower wind-milling drag, and has a lower lever-arm, because the bypass of the engine is spread over the entire flapped section. Additionally, the IBF aircraft takes-off at a higher speed compared with the USB aircraft (see Table 20), which results in higher v_1 and v_{mc}.

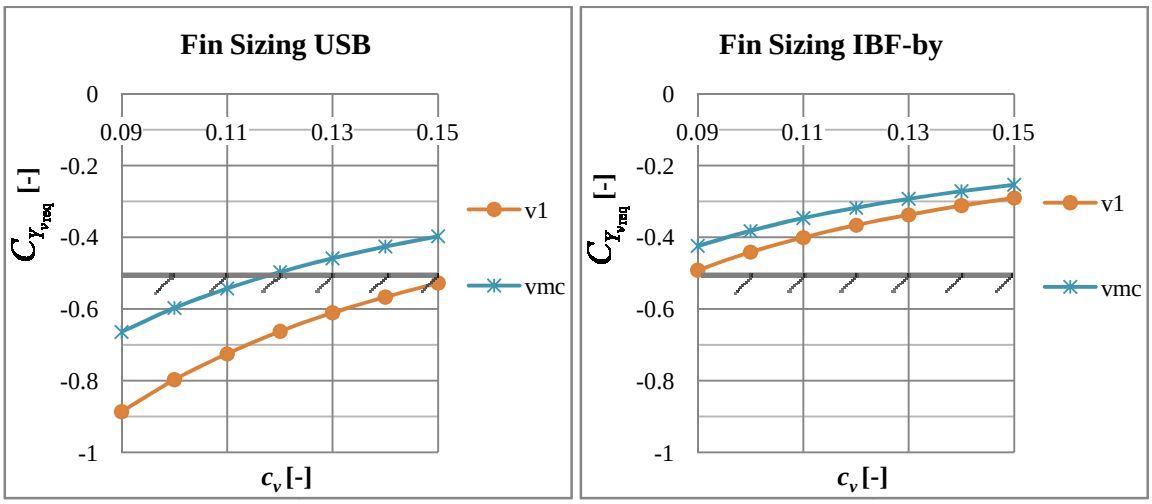

Figure 84. VT sizing for USB (left) and IBF with bypass offtake (right)

Figure 85 compares the HT lift coefficient required to trim the aircraft longitudinally over the HT volume coefficient for the different segments documented in section 4.2.5. The maximum HT lift coefficient available for trim defined in section 6.1.2 is $C_{L\max_h}$=1.3. The HT volume required for the USB aircraft is c_h=1.2 and for the IBF aircraft with bypass offtake c_h=1.6. For both aircraft, the MA segment results in the highest lift coefficient required, since during this segment the jet momentum and the flap deflection are very high. Both increase the nose-down pitching moment coefficient (Figure 5 and Figure 6, p. 10).

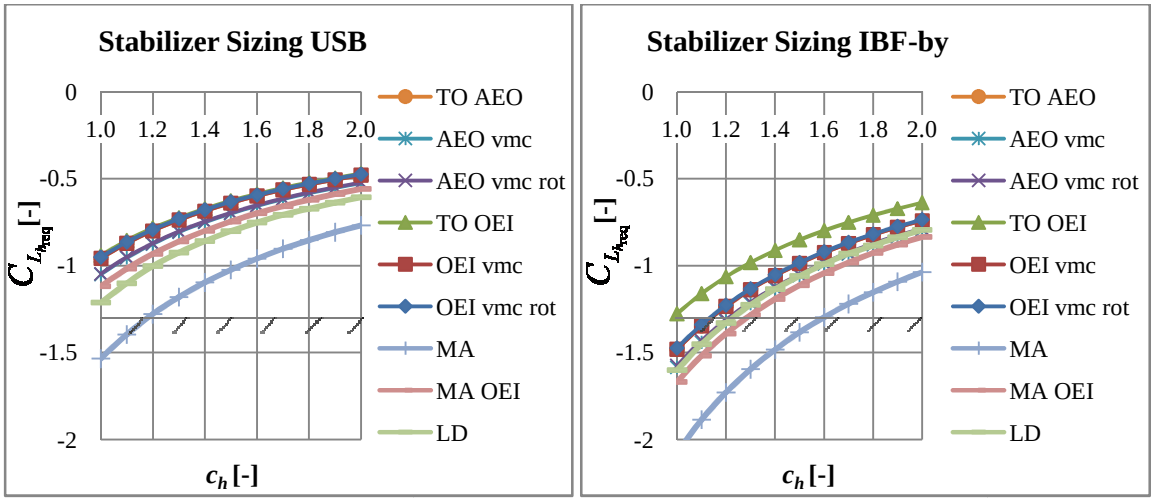

Figure 85. HT sizing for longitudinal trim; USB (left) and IBF with bypass offtake (right)

Figure 86 compares the longitudinal stability margin over the HT volume coefficient for the take-off (TO) and landing (LD) condition of the USB and IBF aircraft, calculated according to section 4.2.4. The USB aircraft requires a HT volume coefficient of 1.55 to achieve a stability margin of 10 %, while the IBF aircraft needs a volume coefficient of 1.1 only.

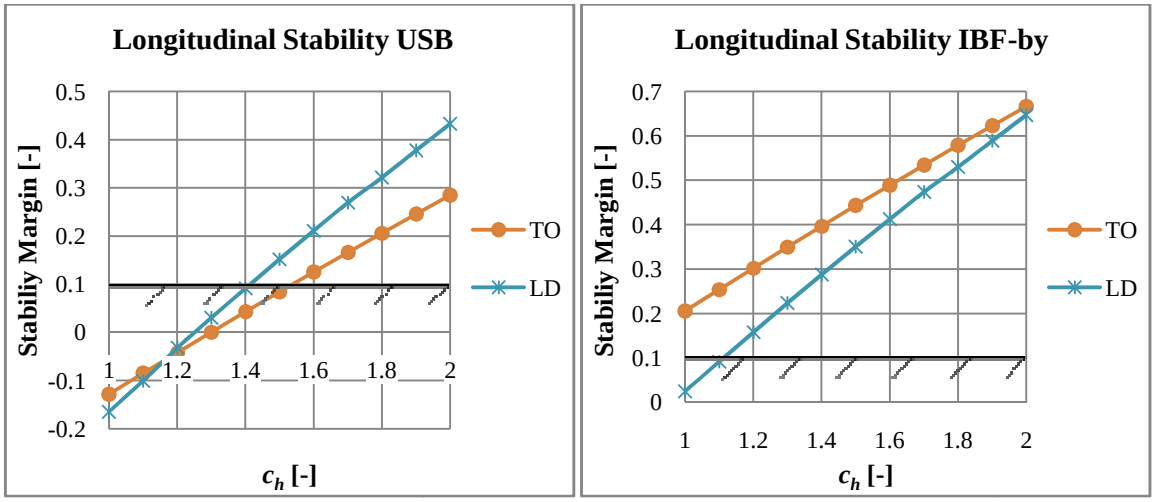

Figure 86. HT sizing for longitudinal static stability; USB (left) and IBF with bypass (right)

In total, both aircraft require a similar value for the HT volume coefficient. For the USB aircraft, the stability constraint determines the volume coefficient; for the IBF aircraft the longitudinal trim condition determines the HT volume coefficient. The reason lies in the different characteristics of the pitching moment coefficient for the wing-fuselage configuration (Figure 87): The IBF aircraft has higher values for the nose-down pitching moment coefficient at comparable jet momentum coefficients, which requires higher lift coefficients to trim the aircraft longitudinally. At the same time, the gradient of the pitching moment slope is lower compared with the USB aircraft, which requires a smaller HT to achieve the required stability margin.

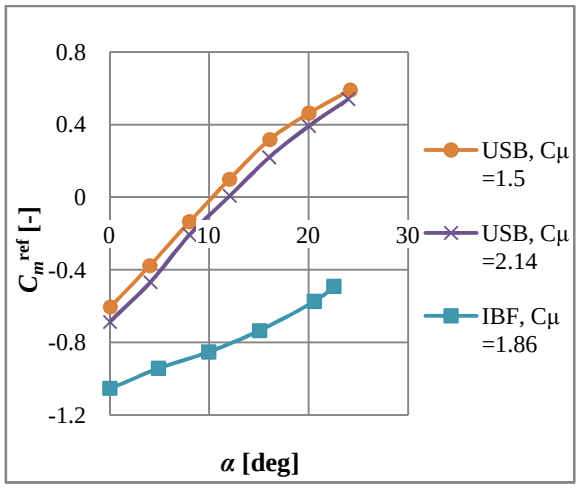

Figure 87. Comparison of pitching moment coefficient for USB and IBF wing-fuselage configuration, δ_f=30°

Table 23 shows a comparison of the tail volumes required for the different aircraft. The aircraft with the internally blown-flaps systems have smaller VT volume coefficients due to lower wind-milling drag, lower lever arms and higher take-off speeds.

The lower pitching moment coefficient for MA with AEO (Table 29) and OEI (Table 30, appendix G) and the higher approach speed are the reasons why the IBF aircraft with exhaust offtake has the lower HT volume coefficient compared to the IBF aircraft with bypass offtake.

Table 23. Comparison of tail volume coefficients required

	Unit	USB	EBF	AIBF	IBF-by	IBF-ex
c_v	-	0.155	0.135	0.125	0.09	0.09
c_h	-	1.55	1.66	1.8	1.6	1.25

Table 24 shows the aileron rolling moment coefficient required to trim the aircraft in the case of OEI at v_{mc}.

Table 24. Comparison of rolling moment coefficient required

	Unit	USB	EBF	AIBF	IBF-by	IBF-ex
$C_{l_{\text{ail}_{\text{req}}}}$	-	0.13	0.13	0.08	0.08	0.07

The EBF and USB aircraft have higher rolling moment coefficients required compared to the aircraft with internally blown flaps. The USB and EBF aircraft have higher lever arms in the case of OEI, as the lift loss acts in the region of the outer engine, while the for the internally blown-flaps aircraft the lever arm is smaller, as the engine jet is spread in spanwise direction. For the aileron layout selected in section 6.1.2 ($C_{l\max}$=0.13), all aircraft are able to trim the engine out rolling moment without special layouts or blowing devices.

6.3 Overall Mission Comparison

In this section, the design mission performance of the blown-flaps aircraft is compared with a conventional take-off and landing regional jet with mechanical high-lift devices and sensitivity studies are performed.

6.3.1 Design Mission

Based on the selected design point for each aircraft, the overall mission performance of the reference aircraft and the blown-flaps aircraft is calculated. Table 25 shows the design points of the different blown-flaps aircraft and the related absolute values for installed thrust and wing area as well as the tail areas. All blown-flaps aircraft have significantly higher thrust installed compared to the reference aircraft. The values range between 84 % for the AIBF to 228 % for the EBF aircraft. The difference in absolute wing area is lower, since most STOL aircraft have higher wing loadings than the reference aircraft. All STOL aircraft have larger tail areas, while the USB aircraft has by far the largest tail due to the large wing area. These differences compared to the reference aircraft are visualized in Figure 88 where the top-views of the blown flaps aircraft are compared with the dimensions of the reference aircraft (black contour line).

Table 25. Comparison of main design parameters

	Unit	Reference	USB	EBF	AIBF	IBF-by	IBF-ex
T/W	-	0.27	0.42	0.51	0.44	0.45	0.44
W/S	kg/m²	510	500	580	550	525	520
T_0	kN	109.0	222.5	248.0	201.0	213.0	205.0
S	m²	81	109.5	85.5	84.8	92.0	91.4
S_h	m²	13.9	34.3	24.7	26.5	26.3	20.5
S_v	m²	12	38.3	20.6	18.9	15.0	14.7

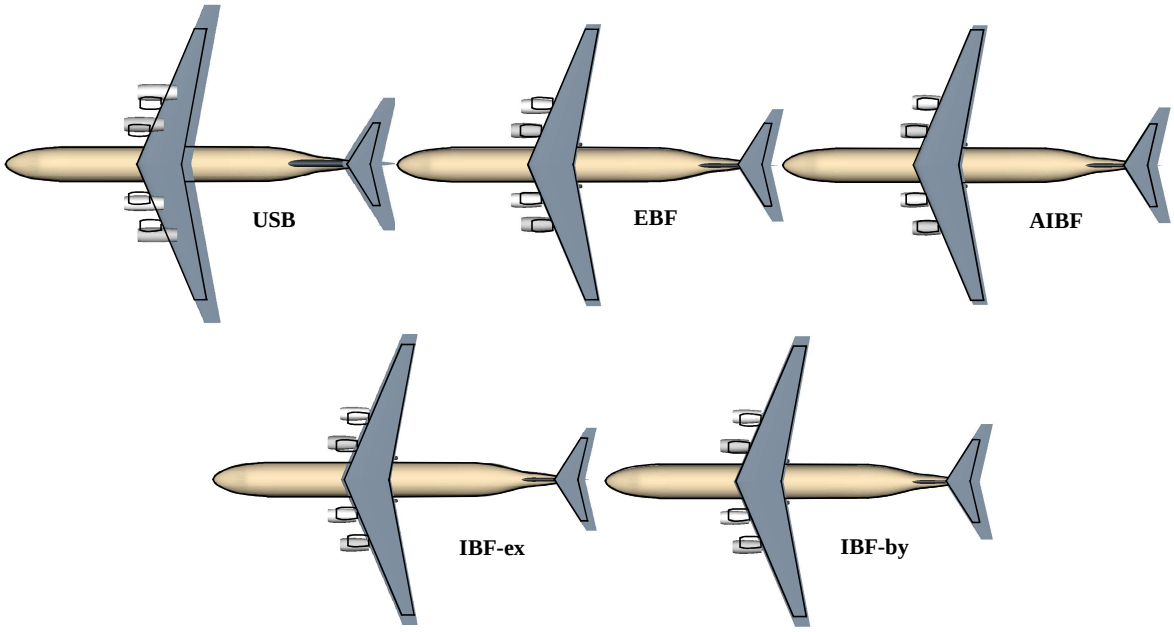

Figure 88. Top-views of investigated aircraft

Table 26 summarizes the main overall mission performance, which quantifies the impact of the STOL capability on the overall mission performance for the requirements investigated. Figure 89 shows the field length and the mission penalties of the blown-flaps aircraft relative to the reference aircraft. The block fuel consumption for the USB aircraft is 106 % and for the EBF 35 % higher compared to the reference aircraft, while the fuel burn penalty for the AIBF aircraft is 19 %. The IBF aircraft with the bypass offtake has a fuel burn penalty of 31 %, while the fuel burn penalty of the IBF aircraft with exhaust offtake is 27 %.

Table 26. Main design mission results

	Unit	Reference	USB	EBF	AIBF	IBF-by	IBF-ex
Payload	kg	11,220	11,220	11,220	11,220	11,220	11,220
OEW	kg	24,075	31,311	30,356	28,369	29,316	28,787
Reserve Fuel	kg	1,633	3,314	2,167	1,912	2,095	2,043
Block Fuel	kg	4,313	8,903	5,838	5,131	5,644	5,494
MTOW	kg	41,241	54,748	49,581	46,632	48,275	47,544

MTOW is increased by 33 % for the USB, by 20 % higher for the EBF aircraft and by 13 % for the AIBF aircraft. The IBF aircraft with bypass offtake has a 17 % higher MTOW and the IBF aircraft with exhaust offtake has a 15 % higher MTOW. The penalties for OEW are between 18 % for the AIBF and 30 % for the USB aircraft.

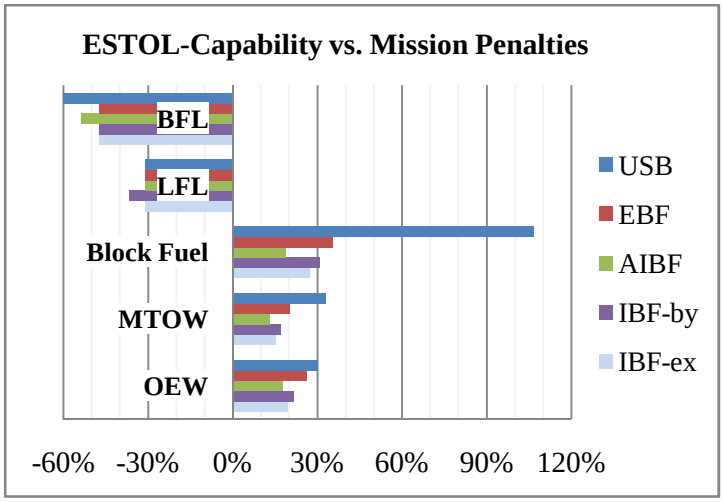

Figure 89. Design mission penalties relative to reference aircraft

Table 27 shows the cruise performance of the investigated aircraft. The higher values for SFC for the IBF and EBF aircraft (13 %) compared with the reference aircraft are a result of the lower BPR. The AIBF aircraft has the same BPR as the reference aircraft but 4 % higher SFC, as the engines are over-designed for cruise and therefore run in part load. The USB has the same SFC compared with the reference aircraft, because, the USB aircraft uses the entire thrust during cruise and does not suffer from a part load penalty.

The lift-to-drag ratio at mid-point cruise (L/D_{Cr}) of the EBF and IBF aircraft is slightly higher compared to the reference aircraft (Table 27) which results from the slightly higher wing loading. The AIBF aircraft has the same lift-to-drag ratio as the reference aircraft. The lift-to-drag ratio for the USB aircraft is significantly lower (10.8) which results from the high cruise drag penalty (see section 4.6.1). The value for USB lies roughly in the same range as the lift-to-drag ratio of the YC-14 (12.3) given for Mach 0.68 (Wimpress and Newberry 1998) and the values given in a concept study of Braden et al. (Braden, Hancock et al. 1980b) (12.1 at Mach 0.75) or van Toor (11.0 at Mach 0.74) (Toor 1979). The low lift-to-drag ratio is the main reason, why the USB aircraft has the highest fuel consumption.

Table 27. Cruise performance

	Unit	Reference	USB	EBF	AIBF	IBF-by	IBF-ex
L/D_{Cr}	-	16.7	10.8	17.2	16.7	17.0	17.1
SFC_{Cr}	kg/N/s	1.65E-05	1.65E-05	1.88E-05	1.71E-05	1.87E-05	1.87E-05

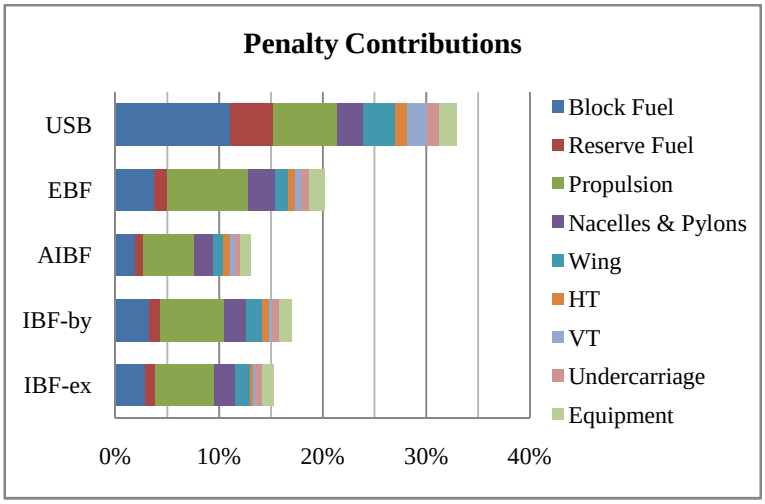

Figure 90. Contributions to MTOW penalty

Figure 90 compares the contributions to the MTOW penalty of the different aircraft. For all aircraft, the highest contribution is from the additional propulsion group weight (propulsion including nacelles and pylon) and from the additional fuel burn (block fuel and reserve fuel). The penalty contributions of the wing and tail are comparably low. Additional penalties result from the additional weight of the undercarriage and equipment due to scaling effects. The detailed component weight breakdowns are given in absolute values in appendix H.

The results presented in this section show that for the investigated design mission the AIBF aircraft has the lowest fuel burn penalty followed by the IBF aircraft and the EBF aircraft. The USB aircraft has the highest fuel burn penalties of all blown-flaps aircraft. These results show that a comparison of the low-speed aerodynamic characteristics only is not sufficient for the selection of the preferred blown-flaps system. The USB aircraft, for example, has better low-speed aerodynamic performance compared to the EBF aircraft (section 2.4), but the overall mission performance comparison showed that the EBF aircraft has a significantly lower fuel consumption due to better aerodynamic performance in cruise.

6.3.2 Sensitivity Studies

In this section, sensitivity studies are performed to show the impact of a potential variation of some parameters of interest. The results are given relative to the results for the respective aircraft documented in the previous sections.

For the IBF and AIBF aircraft, the method is based on assumptions for the duct pressure losses. The engine data were given for different pressure losses to allow for sensitivity studies. For this application example the duct pressure loss assumptions were based on experimental data for a realized duct design. However, as duct pressure losses can vary

compared to the available experimental data depending on the detailed duct design, the impact of the duct pressure losses on the take-off and landing performance is analyzed.

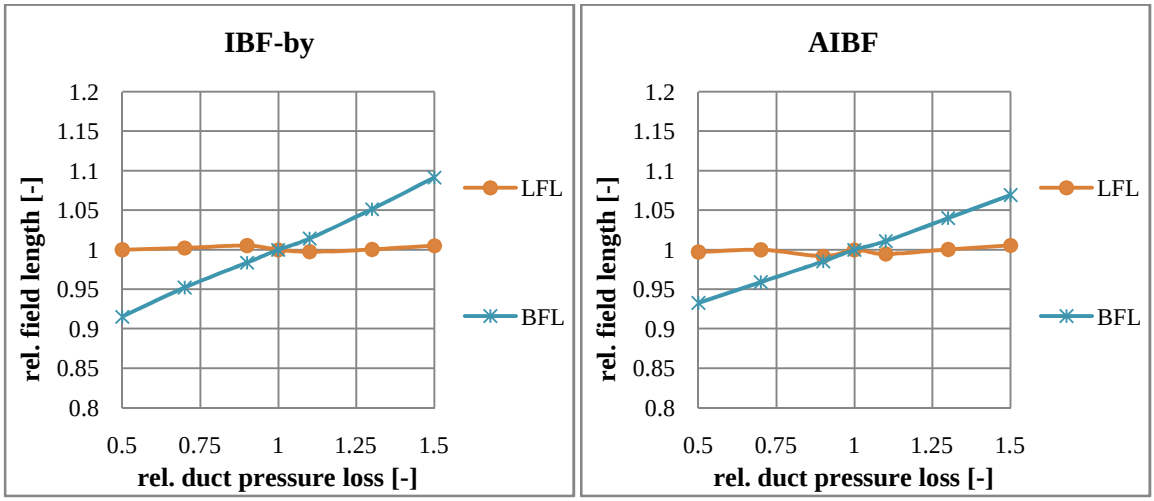

Figure 91. Sensitivity study for duct pressure losses for IBF aircraft with bypass offtake and AIBF aircraft

Figure 91 shows the relative BFL and LFL over a relative deviation from the pressure losses that were assumed for the IBF (σ =5 %) aircraft with bypass offtake and for the AIBF (σ =10 %) aircraft. For the IBF aircraft, a pressure ratio of half of the reference value would result in around 9 % shorter field length; a pressure ratio of 1.5 times the reference value would result in a 9 % longer field length. For the AIBF aircraft the difference in field length is 7 % for the same relative deviation from the reference pressure loss.

The pressure loss has no impact on the landing performance. A pressure loss lower than the reference value results in a higher jet momentum, and, as a consequence, the aircraft has to reduce the approach thrust to maintain the required approach path. A pressure loss higher than the reference value is compensated for by the engine by an increase in the thrust during approach (see Figure 92).

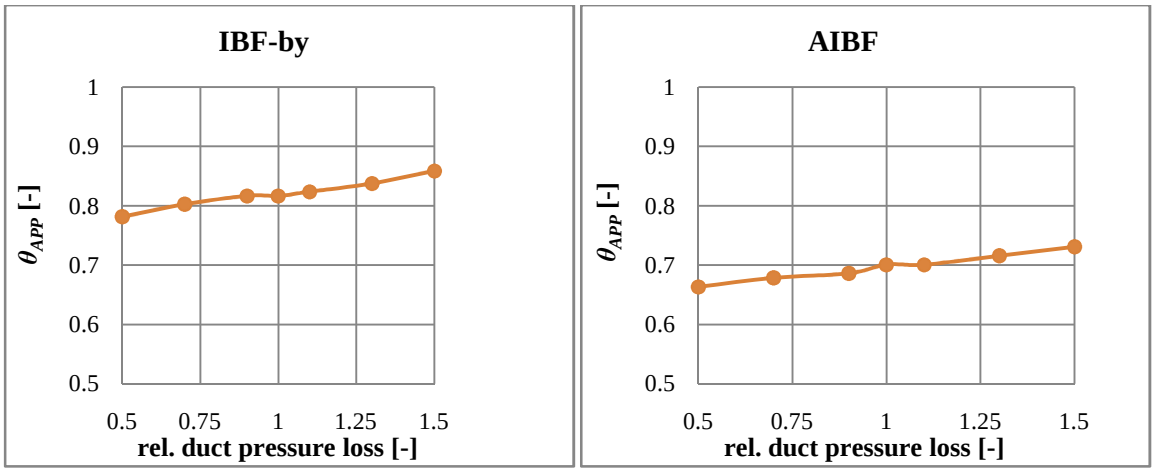

Figure 92. Approach thrust over relative pressure loss deviation

Figure 93 shows the impact of a wing drag penalty (represented by the calibration factor *d*) due to engine installation on the mission fuel burn. If the engine installation would increase the wing drag by 50 %, the additional mission fuel burn would be between 8 % and 9.5 %. Cruise drag due to engine installation for blown-flaps aircraft has not been a focus of previous research except for the USB engine installation. However, this may be an important issue for future research because of the direct impact on the mission fuel burn.

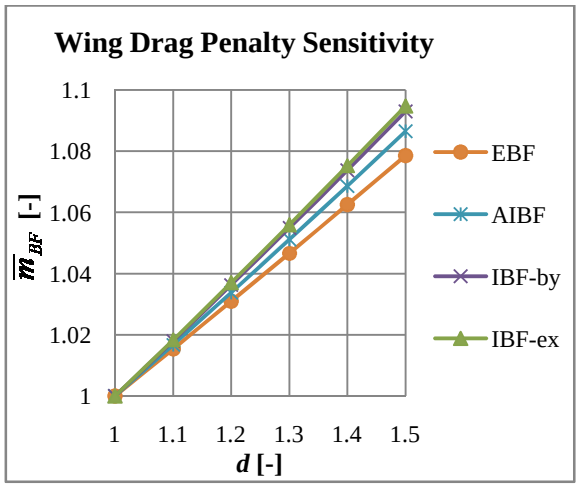

Figure 93. Impact of wing drag penalty on mission fuel burn

The impact of the weight penalty of the control surfaces on the mission fuel burn was studied in a previous paper (Gologan, Stagliano et al. 2009) showing that the control surface weight penalty has only little impact on the mission fuel burn.

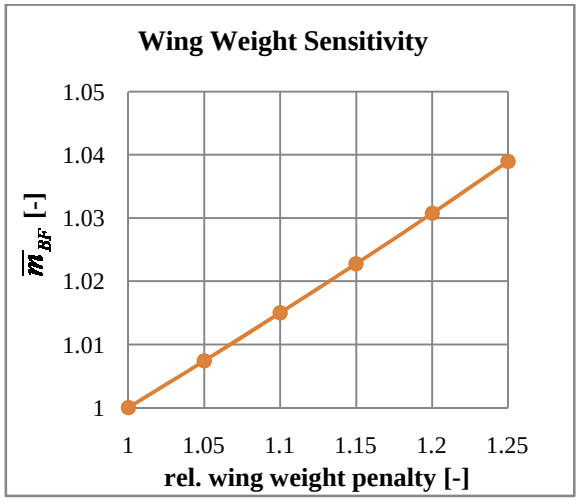

Figure 94. Impact of wing weight penalty on mission fuel burn for IBF aircraft with exhaust offtake

Figure 94 shows a potential relative wing weight penalty that could result from the ducting and heat insulation of the IBF system with exhaust offtake. An additional wing weight of 25 % causes a fuel burn increase of 4 % relative to the reference fuel burn for the design mission of

the IBF aircraft with exhaust offtake. The fuel burn penalty compared to the reference CTOL aircraft is increased from 27 % to 32 %. For a wing weight penalty of 50 %, the IBF aircraft with exhaust offtake would reach a fuel burn penalty which is equal to the EBF aircraft.

6.4 Mission Fuel Burn vs. Field Length

The previous section presented overall mission penalties for a field length requirement of 1,000 m. In this section, the mission fuel burn penalty is presented for even more challenging field length requirements down to 700 m and the same transport mission of 110 passengers and 1,200 nm. The respective design points that were determined with the methodology presented are given in appendix I. Each point in Figure 95 represents one designed aircraft.

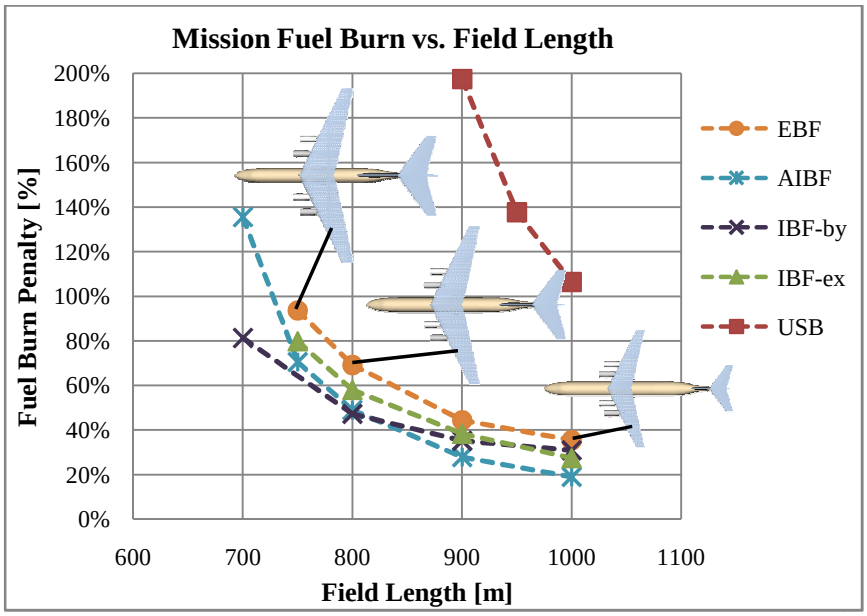

Figure 95. Mission fuel burn vs. field length for different blown-flaps aircraft

Down to 800 m field length the AIBF aircraft have the best mission performance. For a field length below 800 m the IBF aircraft with bypass offtake have the lowest fuel burn penalty.

Figure 96 (see also Table 35 and Table 36 in appendix I) shows the design points over the field length requirement. The IBF aircraft with bypass offtake have the highest wing loadings between field length requirements of 700 m and 900 m. A slightly increased thrust requirement at the 900-m field length is the reason for the higher fuel burn of the IBF aircraft with bypass offtake, even with the higher wing-loading, compared to the AIBF aircraft. The IBF aircraft with the exhaust offtake have lower wing loadings compared to the AIBF and IBF aircraft with bypass offtake and, therefore, higher fuel burn penalties. The EBF aircraft have comparable wing loadings to the AIBF aircraft, but significantly

higher installed thrust, which results in higher fuel burn penalties. The USB aircraft have by far the highest fuel burn penalties due to the low aerodynamic performance in cruise. The penalties range between 105 % and 300 % which are all not acceptable for commercial application.

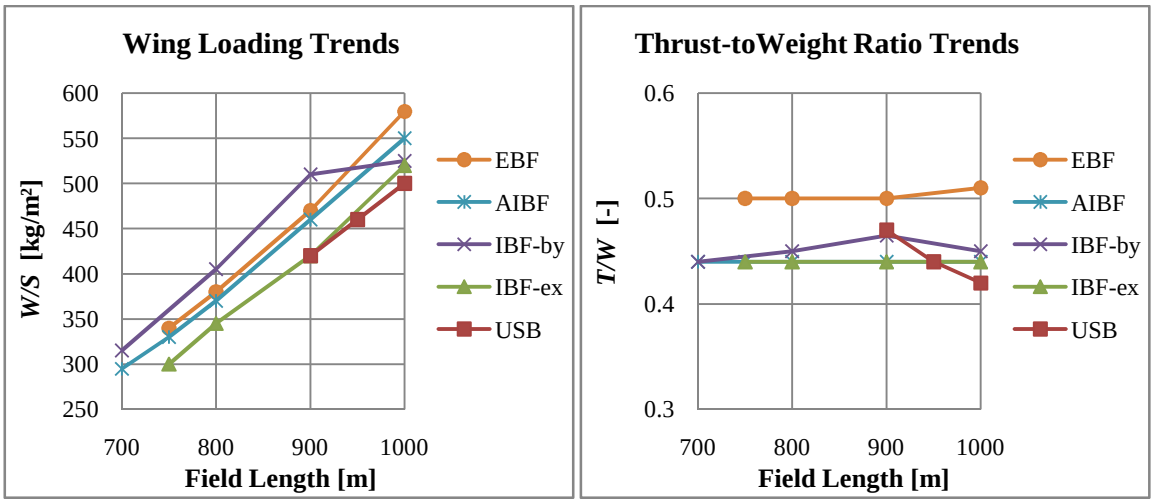

Figure 96. Design points over field length requirement

Included in Figure 95 are top views of the EBF aircraft for different field length requirements that show how the aircraft scale with a decreasing field length requirement. The wing loading decreases, which increases the tail areas and at constant MTOW increases the wing area. As the MTOW increases to meet the 1,200 nm range requirement due to the higher wing weight and drag, the wing area again increases. These scaling effects are the reason, why the fuel penalties increase reciprocally.

7 Conclusion and Outlook

The objective of this thesis is the development of a method that enables the conceptual design and comparison of STOL turbo-fan aircraft with different blown-flaps systems, taking the implications on the overall mission performance into consideration as well as certification requirements as far as applicable to blown flaps.

A literature survey on the current state in blown-flaps research summarizes the functionality of the blown-flaps systems investigated showing that the dependence of the aerodynamic coefficients on the engine jet momentum is the main difference between blown-flaps aircraft and aircraft with mechanical high-lift devices. An overview of the publicly available wind-tunnel data of blown-flaps aircraft configurations is given, showing that there are a large number of wind-tunnel data publicly available, which can be used for the conceptual design and comparison of blown-flaps aircraft. A review of previous comparison studies shows the need for a better consideration of certification aspects for the calculation of the field length and the need for more detailed engine models in conceptual design. A comparison of different blown-flaps systems for current transport aircraft application is not possible based on the realized aircraft with blown flaps, as only few data are available. Furthermore, too few blown-flaps aircraft have been built to generate a useful empirical database.

The approach chosen for the comparison of the different blown-flaps aircraft is the development of methods for the calculation of the take-off and landing performance of blown-flaps aircraft and their integration into a parametric aircraft model. Therein, the aircraft is sized for the required performance by a design space exploration. The performance for each relevant mission segment is, thereby, calculated and checked against the required performance to find the best design point that meets all mission segment requirements.

The main focus of the thesis is on the development and the documentation of the adapted methods for the take-off and landing of blown-flaps aircraft, since during these segments, the physics of blown-flaps aircraft is different from aircraft with mechanical high-lift devices due to the coupling of thrust and lift. Related to this, the main issues considered are:

- Low-speed aerodynamics
- Low-speed control
- Low-speed engine modeling
- Calculation of take-off and landing performance

Publicly available wind-tunnel data are shown to be utilizable for the determination of the low speed aerodynamic coefficients of blown-flaps aircraft. Various corrections of the wind-tunnel data required are discussed with respect to the comparability of the different data for the different blown-flaps systems.

Low-speed control is important for blown-flaps aircraft as they typically take-off and land at lower speeds compared with conventional aircraft. The calculation of the one engine inoperative (OEI) rolling and yawing moments and the static longitudinal stability made directly from the low-speed aerodynamic data is explained. It is documented, how these results can be used to size the tails and the aileron of blown-flaps aircraft.

The low-speed engine model developed provides scalable characteristics of the engine jet momentum which is required for the calculation of the aerodynamic coefficients. Thereby, different bleed air offtake options are considered and quantified. It is shown that the offtake of engine core bleed is not a suitable method for blown flaps application.

For the calculation of the balanced field length it is shown that the stall speed decreases with increasing speed, which requires an iterative calculation of take-off speed and an interpretation of the speed safety margin from certification requirements as a lift coefficient safety margin. The calculation of the different segments required for balanced field length calculation can be made from the low-speed engine characteristics and the low-speed aerodynamic data, as demonstrated in the text.

The landing field length calculation is more complex than the balanced field length calculation as, in addition to the approach speed, the thrust rating during landing has to be iterated to meet the required approach path. Additionally, the missed approach climb angles with all engines operative (AEO) as well as OEI have to be calculated.

Subsequently, the level of detail required for a parametric aircraft model, to model the impact of the short take-off and landing (STOL) capability provided by blown flaps on the overall mission performance is discussed. Component-based handbook methods from the literature are briefly presented and their use in accounting for penalties due to blown-flaps installations is explained.

The methods developed for take-off and landing are validated with available flight test data, showing good agreement of calculation and flight tests. The methods are checked for plausibility where flight test data is not available.

In an application example, the following blown-flaps systems are compared at the aircraft system level for a 1,200 nm mission and 110 passengers:

- Upper Surface Blown Flaps (USB)
- Externally Blown Flaps (EBF)
- Internally Blown Flaps (IBF) with bypass air offtake
- Internally Blown Flaps with exhaust air offtake
- Advanced Internally Blown Flaps (AIBF)

The trade studies required to find a suitable design point that meets all mission segment requirements are discussed for the EBF aircraft, as example. The matching charts for all aircraft are presented, discussed and the resulting design points are compared with each other. The trade studies performed for the sizing of the tails are presented. The overall mission performance calculation shows fuel burn penalties between 19 % for the AIBF aircraft and 106 % for the USB aircraft compared with a conventional take-off and landing regional jet with mechanical high-lift devices. The IBF aircraft with exhaust offtake has a fuel burn penalty of 27 % and the IBF aircraft with bypass offtake of 31 %, while the EBF aircraft has a fuel burn penalty of 35 %. The main reasons for the fuel burn penalties are the higher thrust installed and the larger wings and tails, which increase the aircraft weight and drag, and their associated scaling effects. The very high fuel burn penalty of the USB aircraft results from a cruise drag penalty due to the engine installation over the wings. A tradeoff between field length and fuel burn shows that with decreasing field length the fuel burn penalty increases reciprocally.

With the methodology developed, the overall mission penalties of the different blown-flaps aircraft can be determined for different design missions, such as, for example design range, payload, speed or altitude. The outcomes of these studies can directly be used for cost calculation to determine the additional costs that have to be expected due to the STOL capability. These costs can then be compared to potential benefits due to STOL operation that, for example, can be lower delay costs or higher profit for the airline. However, additional aspects have, thereby, to be considered as for example noise or maintenance.

In the application example, aircraft with state of the art blown flaps technologies have been compared with each other based on available wind-tunnel data. With today’s Computational Fluid Dynamics methods, the different blown-flaps systems can be optimized and new aerodynamic data sets can be generated. These optimized data can be

compared at the aircraft system level with the method developed, giving the overall mission penalties for advanced blown-flaps systems.

The documented method can be extended to account for other powered lift systems as, for example, propeller driven systems (e. g. deflected slipstream), lift-fans, or cross-flow fans. Other extensions can be the mapping of circulation control devices, such as, for example, rotating cylinders. For this purpose, the specific low-speed aerodynamic characteristics have to be analyzed and new low-speed engine models have to be generated to provide the power characteristics required for the calculation of the aerodynamic coefficients. The different characteristics of the low-speed aerodynamic behavior may require an adaption of the algorithms developed for the iteration of take-off and approach speed and mass models may be required, for example, for the modeling of additional components, such as lift-fans or cross-flow fans.

References

Aiken, T. N., K. Aoyagi and M. D. Falarski (1973). Aerodynamic Characteristics of a Large-Scale Model with a Swept Wing and a Jet Flap Having an Expandable Duct. Moffet Field, California, NASA Ames Research Center, NASA TM X-62281.

Antonov. (2004). "Start>Products and services>Aircraft>Freighters>AN-74T>Photos." Retrieved 5th December, 2009, from http://www.antonov.com/products/air/transport/AN-74t/photos.xml.

Aoyagi, K., M. D. Falarski and D. G. Koenig (1973). Wind Tunnel Investigation of a Large-Scale 25° Swept-Wing Jet Transport Model with an External Blowing Triple-Slotted Flap. Moffet Field, California, NASA Ames Research Center, NASA TM X-62197.

Aoyagi, K., M. D. Falarski and D. G. Koenig (1975). Wind Tunnel Investigation of a Large-Scale Upper Surface Blown-Flap Model Having Four Engines. NASA Ames Research Center, NASA TM X-62419.

Ball, T., S. Turner and D. D. Marshall (2008). Short Takeoff Performance using Circulation Control. 46th AIAA Aerospace Sciences Meeting and Exhibit, Reno, Nevada.

Bertsch, L., G. Looye, T. Otten and M. Lummer (2009). Integration and Application of a Tool Chain for Environmental Analysis of Aircraft Flight Trajectories. 9th AIAA Aviation Technology, Integration, and Operations Conference (ATIO), Hilton Head, South Carolina, AIAA 2009-6954.

Birckelbaw, L. (1992). High Speed Aerodynamics of Upper Surface Blowing Aircraft Configurations. 10th AIAA Applied Aerodynamics Conference, Palo Alto, CA, AIAA-1992-2611.

Bobbitt, P. and R. Margason (2007). Analysis of the Take-Off and Landing of Powered-Lift Aircraft. 45th AIAA Aerospace Sciences Meeting and Exhibit, Reno, Nevada, AIAA-2007-1256.

Böck and C. Kelders (2009). Simulation of the Theoretical Capacity Potential of ESTOL Operations on an Intersecting Runway at Hub Airports. 9th AIAA Aviation Technology, Integration, and Operations Conference (ATIO), Hilton Head, South Carolina, AIAA 2009-6988.

Boeing. (2009a). "Boeing: Multimedia -- Image Gallery -- C-17 Globemaster III." Retrieved 5th December, 2009, from http://www.boeing.com/defense-space/military/c17/slf08-00386-082.html.

Boeing. (2009b). "Current Market Outlook 2009-2028." Retrieved 05th December, 2009, from http://www.boeing.com/commercial/cmo/.

Bombardier. (2009). "Aerospace>Products>Commercial Aircraft>CSeries>CS100." Retrieved 05th December, 2009, from http://www.bombardier.com/en/aerospace/products/commercial-aircraft/cseries/cs100.

Braden, J. A., J. P. Hancock, J. E. Hackett, K. P. Burdges and V. Lyman (1980a). Exploratory Studies of the Cruise Performance of Upper Surface Blown Configurations. NASA Langley Research Center, NASA CR-3193.

Braden, J. A., J. P. Hancock, J. E. Hackett, K. P. Burdges and V. Lyman (1980b). Exploratory Studies of the Cruise Performance of Upper Surface Blown Configurations. NASA Langely Research Center, NASA-CR-3193.

Brandt, S. A. (2004). Intorduction to aeronautics: a design perspective. Blacksburg (Virginia, USA), AIAA.

Chambers, J. R. (2005). Innovation in Flight. NASA Langley Research Center, NASA SP-2005-4539.

Chin, Y.-T., T. N. Aiken and G. S. Oates (1975). "Evaluation of a New Jet Flap Propulsive-Lift System." Journal of Aircraft **12**(7): 605-610.

Cochrane, J. A., D. W. Riddle and Y. S. (1982). Application of Advaced Upper Surface Blowing Propulsive-Lift Technology. SAE Paper 820,956.

Couluris, G. J., C. E. Hange, D. A. Wardwell, D. Signor and J. Phillips (2007). A Potential Impact Analysis of ESTOL Aircraft on Newark Airport Operations. AIAA Modeling and Simulation Technologies Conference and Exhibit, Hilton Head, South Carolina, AIAA 2007-6700.

Dorsch, R. G. and M. Reshotko (1972). EBF Noise Tests with Engine Under-the-Wing and Over-the-Wing Configurations. Conference on STOL Technology, Moffett Field, California, NASA SP-320, Paper 32, pp. 455-73.

Englar, R. J. and R. A. Hemmerly (1981). "Design of the Circulation Control Wing STOL Domonstrator Aircraft." Journal of Aircraft **18**(1): 51-58.

Eurocontrol (2008). Challenges of Growth 2008.

FAA (2007). Capacity Needs in the National Airspace System 2007-2025. Washington, Federal Aviation Administration.

FAA. (2009). "Electronic Code of Federal Regulation." Retrieved 5th December, 2009, from http://ecfr.gpoaccess.gov.

Farbridge, J. E. (1987). A review of the de Havilland Augmentor-Wing Powered-Lift Concept and its Future Applications. SAE-Paper 872313.

Finck, R. D. (1978). USAF Stability and Control Datcom. Ohio, AFWAL-TR-83-3048.

Fujino, M. (2003). "Wave-Drag Characteristics of an Over-the-Wing Nacelle Business-Jet Configuration " Journal of Aircraft **40**(6): 1177-1184.

Galloway, T. L. (1972). Future Short-Field Aircraft. Conference on STOL Technology, Moffet Field, California, NASA SP-320, Paper 2, pp. 9-21.

Gologan, C., K. Broichhausen and J. Seifert (2009). "A Calculation Method for Parametric Design Studies of V/STOL Aircraft." The Aeronautical Journal **113**(1143): 309-317.

Gologan, C., C. Kelders, A. Kuhlmann and J. Seifert (2009). "Extreme Short Take-Off and Landing Regional Jets – Economic Motivation and Technological Challenges." The Aeronautical Journal **113**(1147): 563-574.

Gologan, C., S. Stagliano and D. Schmitt (2009). Impact of ESTOL Capability on the Mission Fuel Burn of Regional Jets. 9th AIAA Aviation Technology, Integration, and Operations Conference (ATIO), Hilton Head, South Carolina, AIAA 2009-7096.

Hange, C. (2003). Trajectory Kinematics of a Simultaneous Non-Interfering Landing Approach, and the Impact on ESTOL Regional Transport Performance and Flight Control. 3rd Annual Aviation Technology, Integration, and Operations (ATIO) Forum, Denver, Colorado, AIAA 2003-6857.

Hange, C. (2008). Overview of the CESTOL Partnership in NASA's Subsonic Fixed Wing Project. International Powered Lift Conference, London, UK, Royal Aeronautical Society.

Hoad, D. R. (1972). Comparison of Aerodynamic Performance of Several STOL Concepts. Conference on STOL Technology, NASA SP-320, Paper 10, pp. 111-119.

Hunting (1963). "Hunting H.126 Jet-Flap Research Aircraft: Details of the British Aircraft Corporation Research Aircraft Designed to a Ministry of Aviation Specification Which Recently Made its First Flight." Aircraft Engineering and Aerospace Technology **35**(6): 166-167.

Jane's (1977). Jane's All The World Aircraft 1977-1978. Coulsdon, Surrey, Jane's Information Group Inc.

Jane's (1979). Jane's All The World Aircraft 1979-1980. Coulsdon, Surrey, Jane's Information Group Inc.

Jane's (1989). Jane's All The World Aircraft 1989-1990. Coulsdon, Surrey, Jane's Information Group Inc.

Jane's (2000). Jane's All The World Aircraft 2000-2001. Coulsdon, Surrey, Jane's Information Group Inc.

Jenkinson, L., P. Simpkin and D. Rhodes (1999). Civil Jet Aircraft Design. Oxford, Butterworth-Heinemann Ltd.

Johnson, W. G. J. (1972). Aerodynamic and Performance Characteristics of Externally Blown Flap Configurations. Conference on STOL Technology, NASA SP-320, Paper 5, pp. 43-54.

Johnson, W. G. J. (1975). Aerodynamic Characteristics of a Powered, Externally Blown Flap STOL Transport Model with Two Engine Simulator Sizes. Hampton, VA, NASA Langley Research Center, NASA TN D-8057.

Kehse, T. (2008). Gesamtentwurf von Flugzeugen mit Hochauftriebshilfen nach dem Prinzip des Upper Surface Blowing. Deutscher Luft-und Raumfahrt Kongress, Darmstadt, DGLR.

Kurzke, J. (2007a). GasTurb - Gas Turbine Performance Program. Dachau.

Kurzke, J. (2007b). GasTurb Manual. Dachau.

Loftin, L. K. (1980). Subsonic Aircraft: Evolution and the Matching of Size to Performance. NASA Langley Research Center, NASA Reference Publication 1060.

Margason, R. (2002). Comparison of Five STOL Concepts for Runway Independent Aircraft. 2002 Biennial International Powered Lift Conference and Exhibit, Williamsburg, Virginia, AIAA 2002-6025.

Mentral, A. and F. Zerner (1948). The Coanda Effect. Publication Scientifiques et Technique du Ministere de l'Air.

NASA. (2009). "Phtographer: King C-8A (NASA-716) Buffalo Augmentor Wing Jet STOL Research Aircraft at Crows." Retrieved 05th December, 2009, from http://ntrs.nasa.gov.

Nicolai, L. M. (1975). Fundamentals of Aircraft Design. San Jose, CA, METS, Inc.

PACE. (2007). "Pacelab APD." Retrieved 08th December, 2009, from http://www.pace.de.

Parlett, L. P. (1972). Stability and Control of Externally Blown Flap Configurations. Conference on STOL Technology, NASA SP-320, Paper 6, pp. 55-69.

Peperak, M. (2008). Economic Impact of the Hybrid Wing Cruise Efficient Short Take-Off and Landing (CESTOL) Commercial Aircraft. International Powered Lift Conference 2008, London, UK, Royal Aeronautical Society.

Phelps, A. E. (1972). Aerodynamics of the Upper Surface Blown Flap. Conference on STOL Technology, NASA SP-320, Paper 9, pp. 97-110.

RAF-Museum. (2009a). "Hunting H126 airplane pictures & aircraft photos." Retrieved 5th December, 2009, from http://www.rafmuseum.org.uk/cosford/collections/aircraft/hunting-h126.cfm.

RAF-Museum (2009b). Personal communication with Department of Research & Information Services of the RAF-Museum. 2009.

Raymer, D. P. (2006). Aircraft Design: A Conceptual Approach. Reston, Virginia, AIAA.

Riddle, D. W., R. C. Innis, J. L. Martin and J. A. Cochrane (1981). Powered-Lift Takeoff Performnace Chracteristics Determined from Flight Test of the Quiet Short-Haul Research Aircraft (QSRA). 1st Flight Testing Conference, Las Vegas, Nevada, AIAA-81-2409, AIAA / SETP / SFTE / SAE / ITEA / IEEE.

Roskam, J. (1985a). Airplane Design Part I. Ottawa, Kansas.

Roskam, J. (1985b). Airplane Design Part II. Ottawa, Kansas.

Roskam, J. (1985c). Airplane Design Part VI. Ottawa, Kansas.

Schlichting, H. and E. Truckenbrodt (2001). Aerodynamik des Flugzeugs II. Berlin Heidelberg New York, Springer-Verlag.

Schmitt, D. (2005). Flugzeugentwurf. Garching, Technische Universität München, Lehrstuhl für Luftfahrttechnik.

Schmitt, D. (2009). Skript zur Vorlesung Flugzeugentwurf. Garching, Technische Universität München, Lehrstuhl für Luftfahrttechnik.

Scholz, D. (1999). Skript zur Vorlesung Flugzeugentwurf. Hamburg, Universitiy of Applied Sciences.

Schwanke, S. (2009). Entwicklung eines Versuchsdesigns zur Validierung von An- und Abflugverfahren für ein neuartiges STOL-Luftfahrzeug mittels Echtzeitsimulation mit Fluglotsenbeteiligung. Deutscher Luft- und Raumfahrt Kongress, Aachen, DGLR.

Sleeman, W. J., W. Hohlweg and N. L. R. Center (1975). Low-speed wind-tunnel investigation of a four-engine upper surface blown model having a swept wing and rectangular and d-shaped exhaust nozzles. NASA Langley Research Center, NASA TN D-8061.

Stinton, D. (1988). The Anatomy of the Airplane. Reston, Virginia, AIAA.

Toor, J. B. H. v. (1979). Voorontwerp von een korte-afstands verkeersvliegtuig met Upper Surface Blowing. Delft, Delft University. Diploma Thesis.

Torenbeek, E. (1982). Synthesis of Subsonic Airplane Design. Delft, Delft University Press.

Vogler, R. D. (1976). Wind-Tunnel Investigation of Internally Blown Jet-Flap STOL Airplane Model. NASA Langley Research Center, NASA TN D-8309.

Waters, M., C. Anthony, G. McKenzie and D. D. Marshall (2009). Propulsion System Modelling and Takeoff Distance Calculation for a Powered-Lift Aircraft with Circulation-Contorl Wing Aerodynamics. 47th AIAA Aerospace Sciences Meeting and Exhibit, Orlando, Florida, AIAA 2009-1258.

Whittley, D. C. (1971). Some aspects of propulsion for the augmentor-wing concept. AGARD Inlets and Nozzles for Aerospace Eng. 14 p, SEE N72-16685 07-28.

Williams, J., S. F. J. Butler and M. N. Wood (1963). The Aerodynamics of Jet Flaps. Ministry of Aviation, R. & M. No. 3304.

Wimpress, J. K. and C. F. Newberry (1998). The YC-14 STOL Prototype: Its Design, Development, and Flight Test. Reston, Virginia, AIAA.

Zuk, J. and D. Wardwell (2005). Summary of NASA's Extreme Short Take-Off and Landing (ESTOL) Vehicle Sector Activities. AeroTech Congress and Exibition, Grapevine, Texas, SAE-Paper 2005-01-3145, SAE International.

Appendix

A. Low-Speed Control

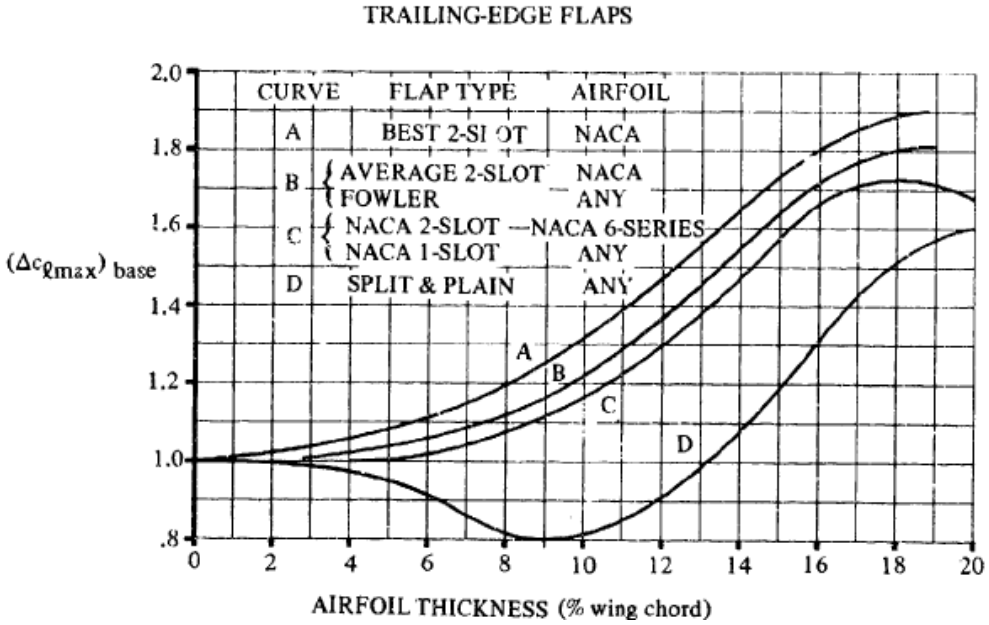

Figure 97. Maximum lift increments for 25%-chord flaps (Finck 1978, p. 6.1.1.3-12)

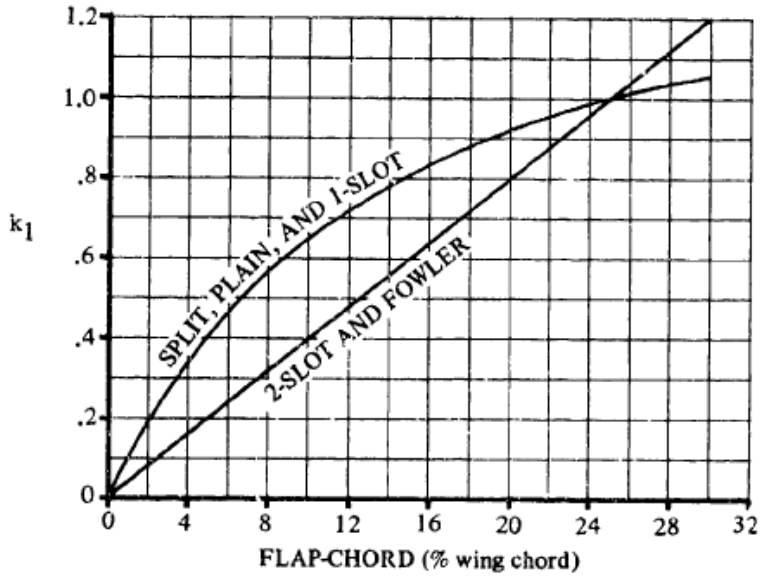

Figure 98. Flap-chord correction factor (Finck 1978, p. 6.1.1.3-12)

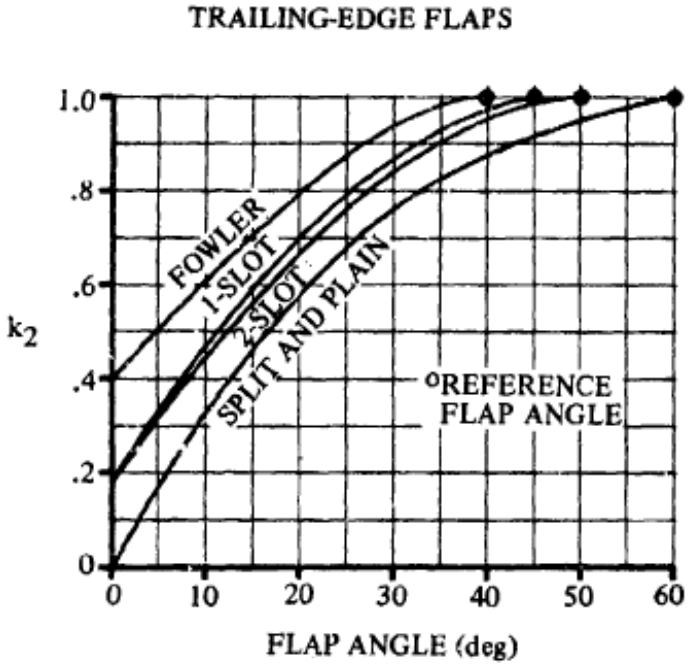

Figure 99. Flap-angle correction factor (Finck 1978, p. 6.1.1.3-13)

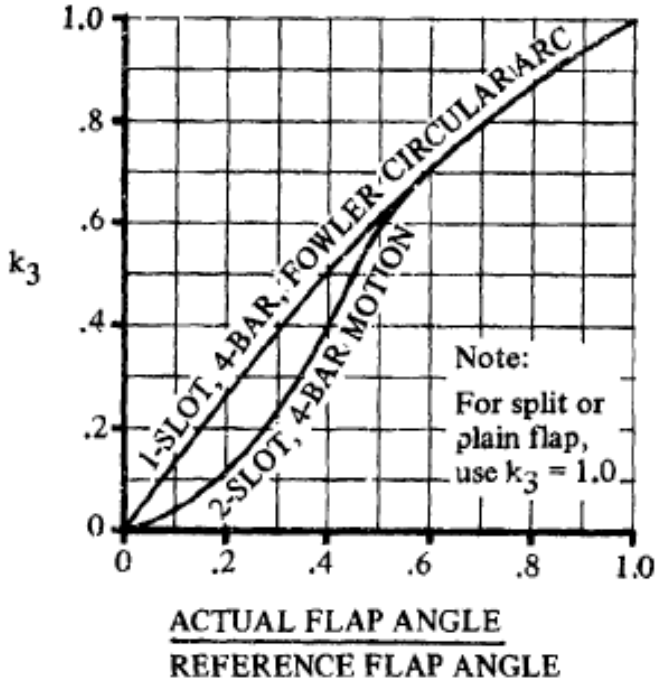

Figure 100. Flap-motion correction factor (Finck 1978, p. 6.1.1.3-13)

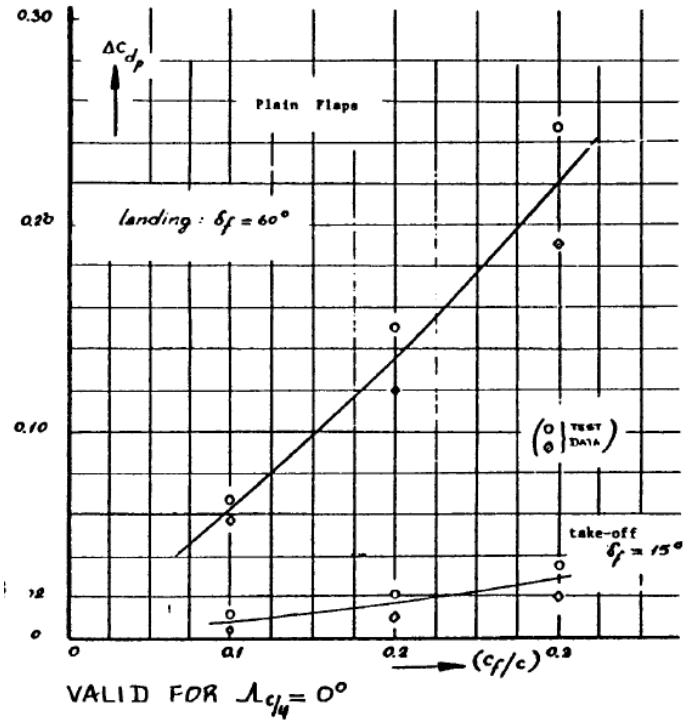

Figure 101. 2-dimensional drag increment due to plain flaps, (Roskam 1985c, p. 83)

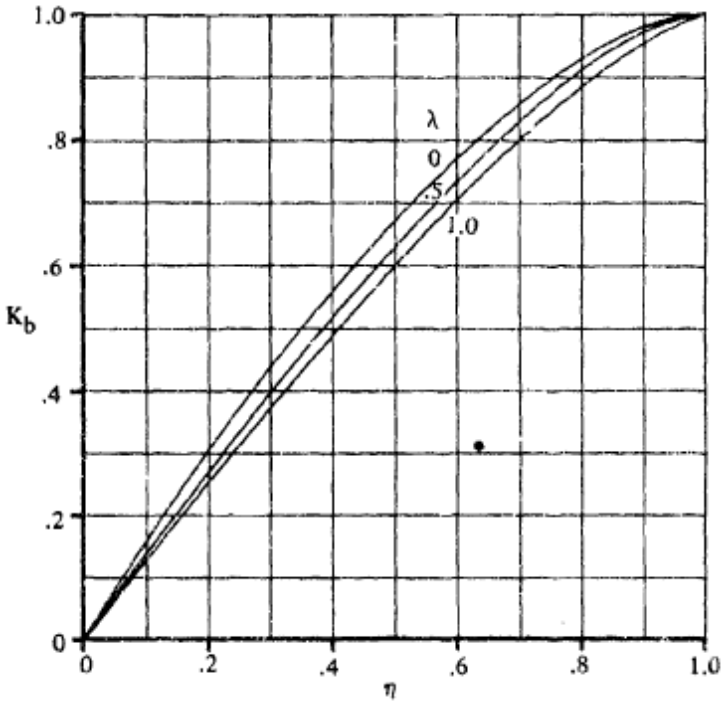

Figure 102. Span factor for inboard flaps, (Finck 1978, p. 6.1.4.1-15)

B. Low-Speed Engine Models

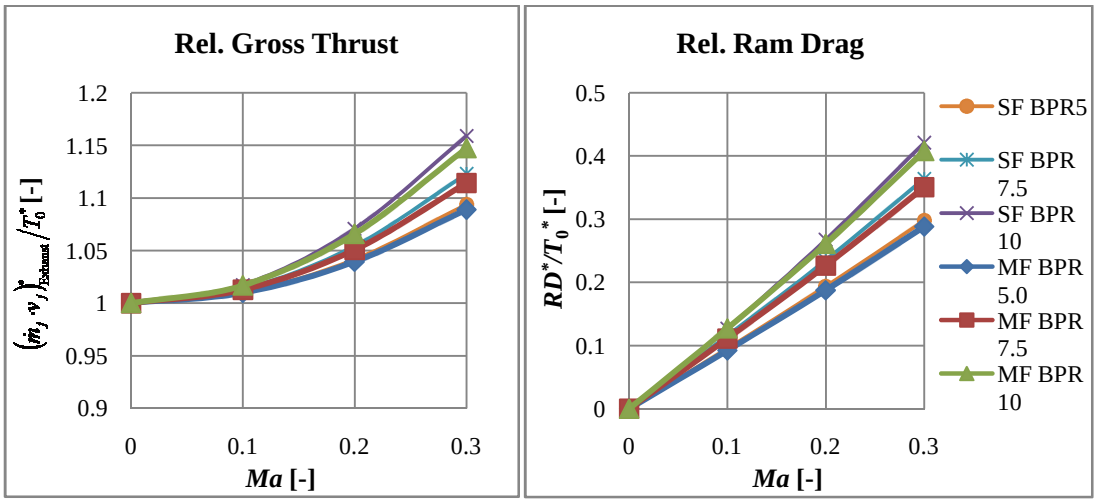

Figure 103. Comparison of relative gross thrust and relative ram drag, separate-flow (SF) and mixed-flow (MF) engines

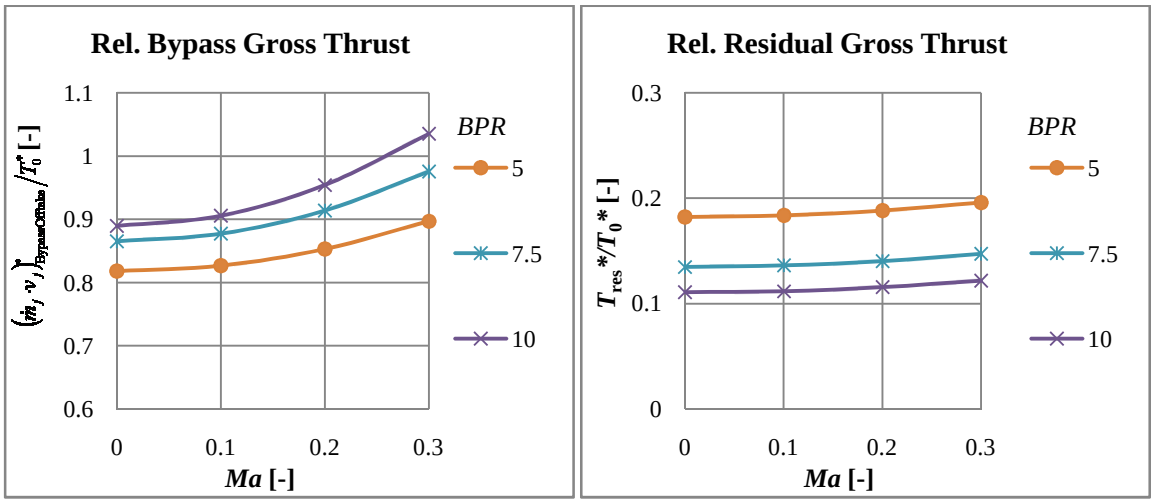

Figure 104. Relative bypass and residual gross thrust, separate-flow engines with bypass offtake, σ=-0 %

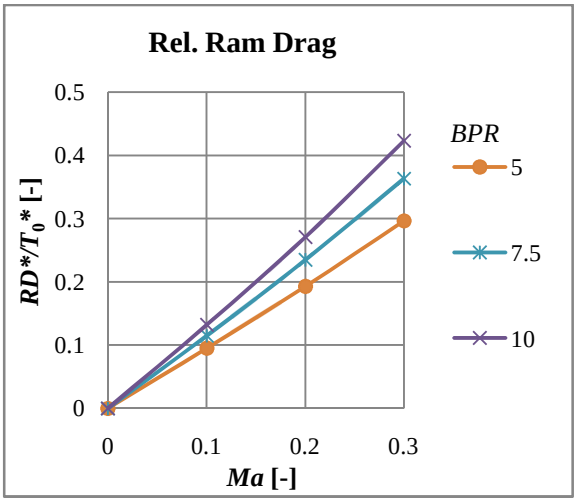

Figure 105. Relative ram drag, separate-flow engines with bypass offtake, σ=-0 %

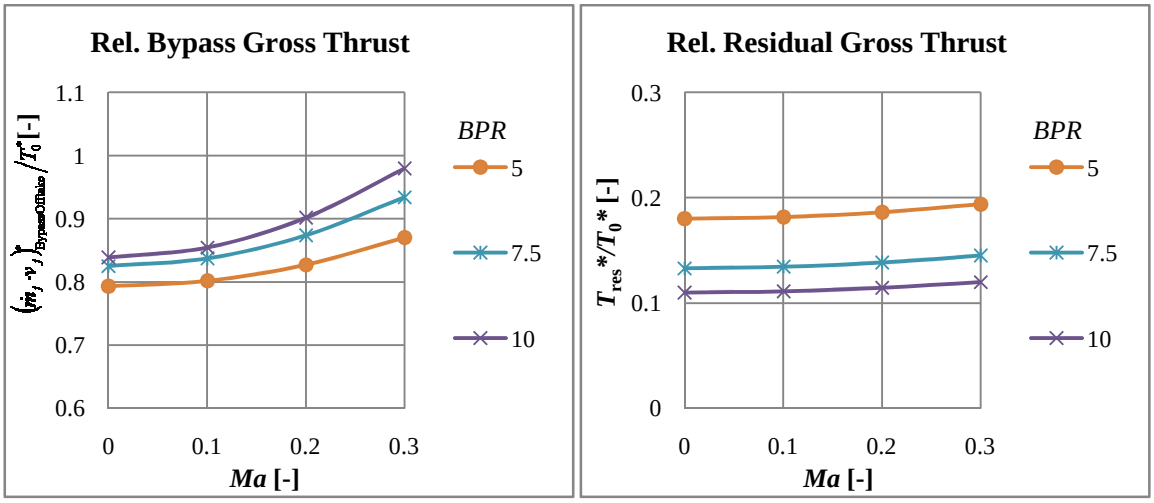

Figure 106. Relative bypass and residual gross thrust, separate-flow engines with bypass offtake, σ=-3 %

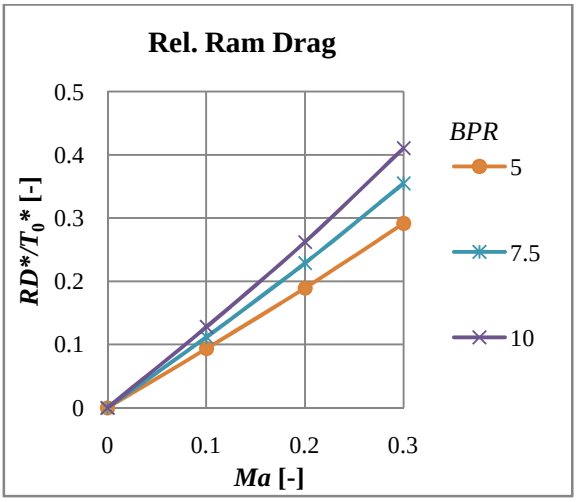

Figure 107. Relative ram drag, separate-flow engines with bypass offtake, σ=-3 %

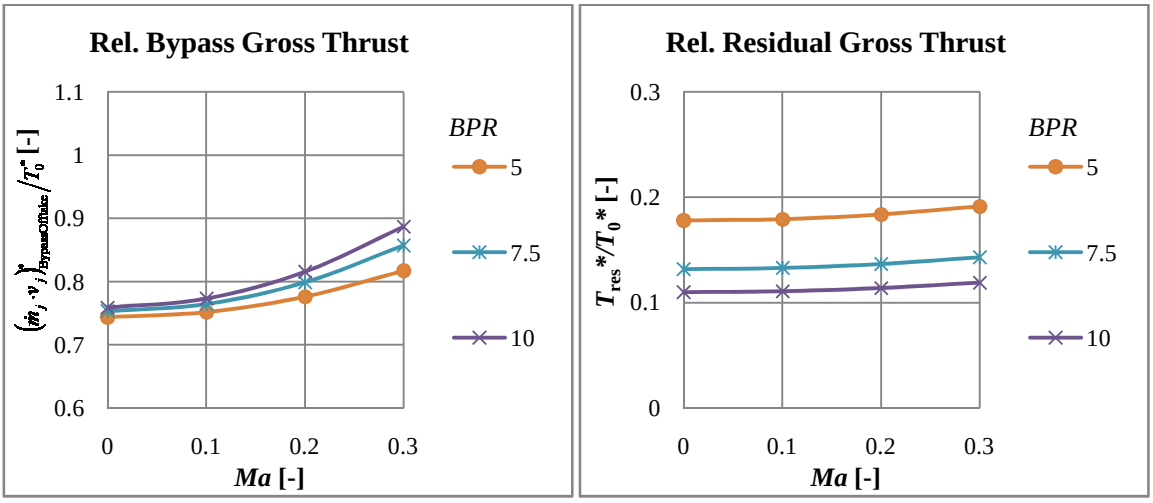

Figure 108. Relative bypass and residual gross thrust, separate-flow engines with bypass offtake, σ=-9 %

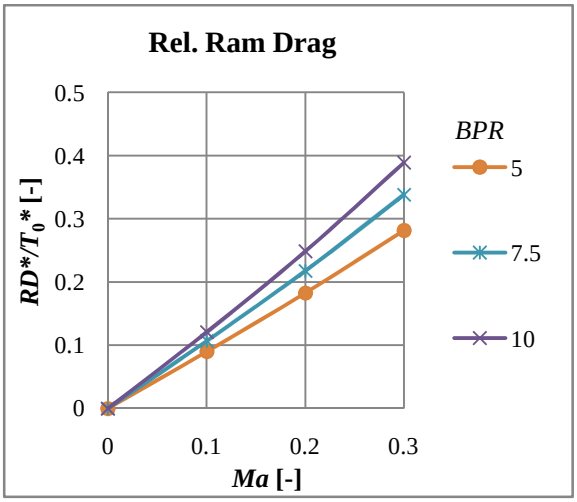

Figure 109. Relative ram drag, separate-flow engines with bypass offtake, σ=-9 %

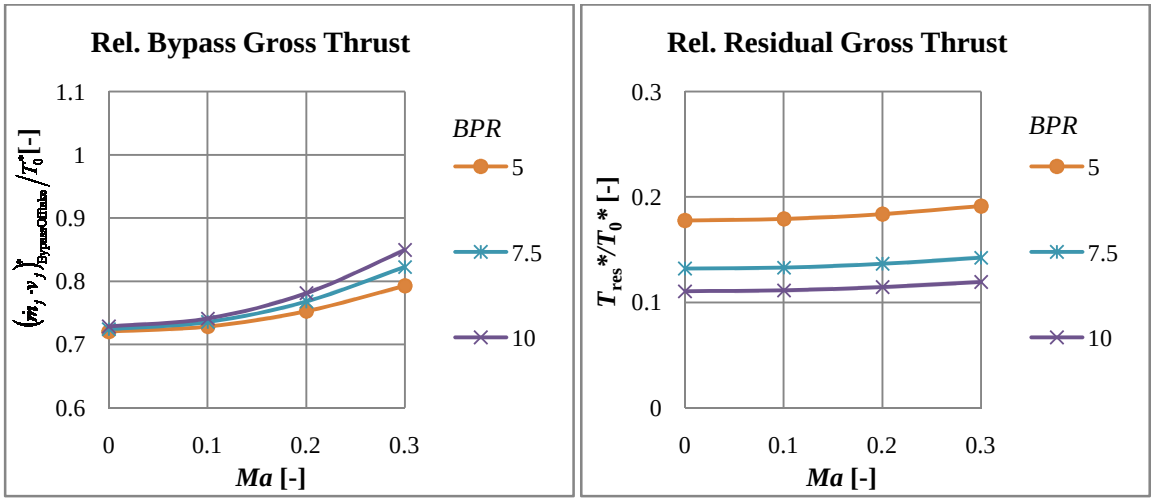

Figure 110. Relative bypass and residual gross thrust, separate-flow engines with bypass offtake, σ=-12 %

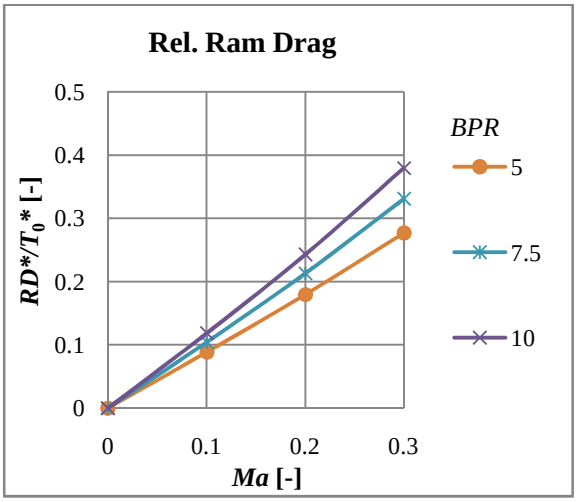

Figure 111. Relative ram drag of the separate-flow engine with bypass offtake, σ=-12 %

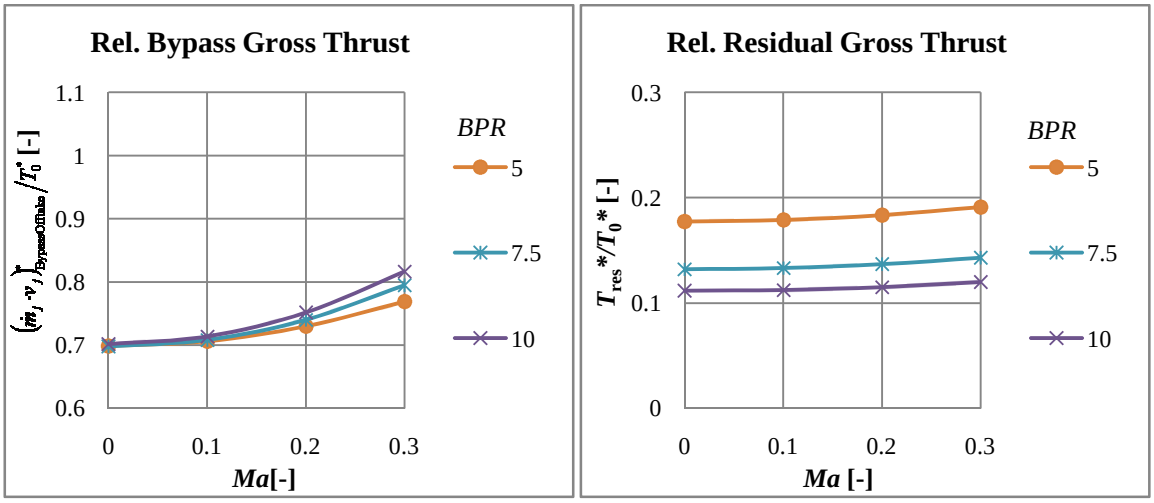

Figure 112. Relative bypass and residual gross thrust, separate-flow engines with bypass offtake, σ=-15 %

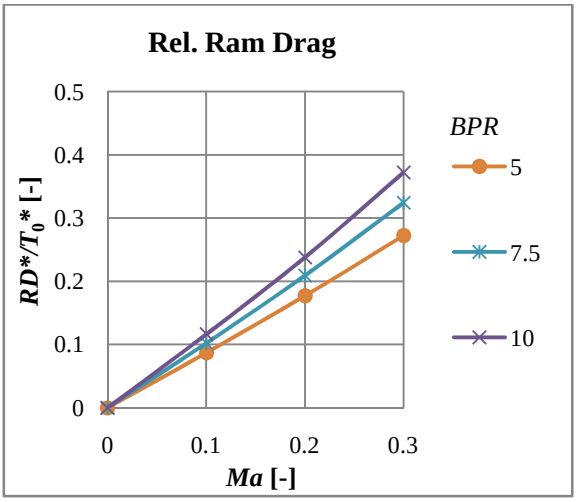

Figure 113. Relative ram drag, separate-flow engines with bypass offtake, σ=-15 %

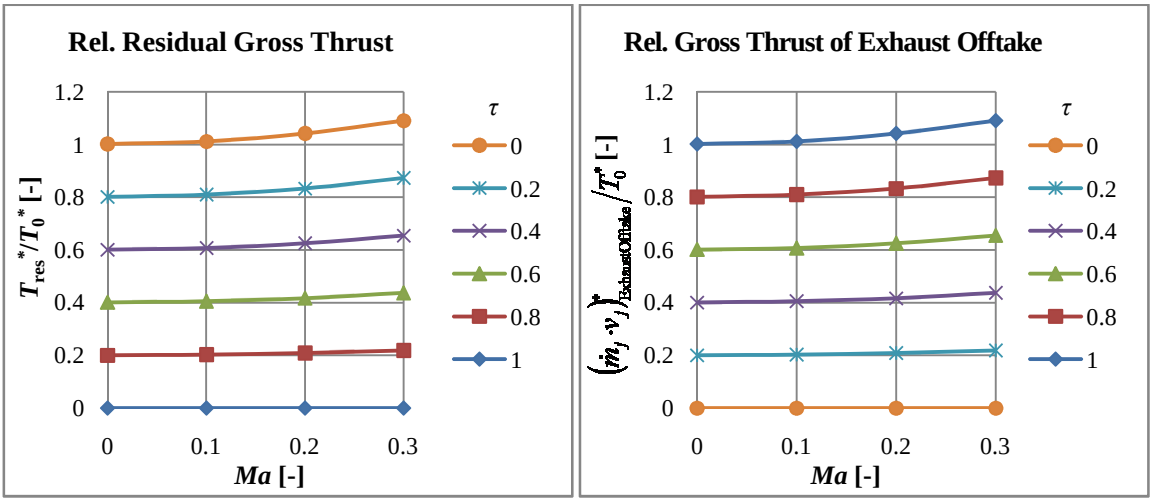

Figure 114. Relative residual and exhaust offtake gross thrust, mixed-flow engine, BPR=5, σ=-0 %

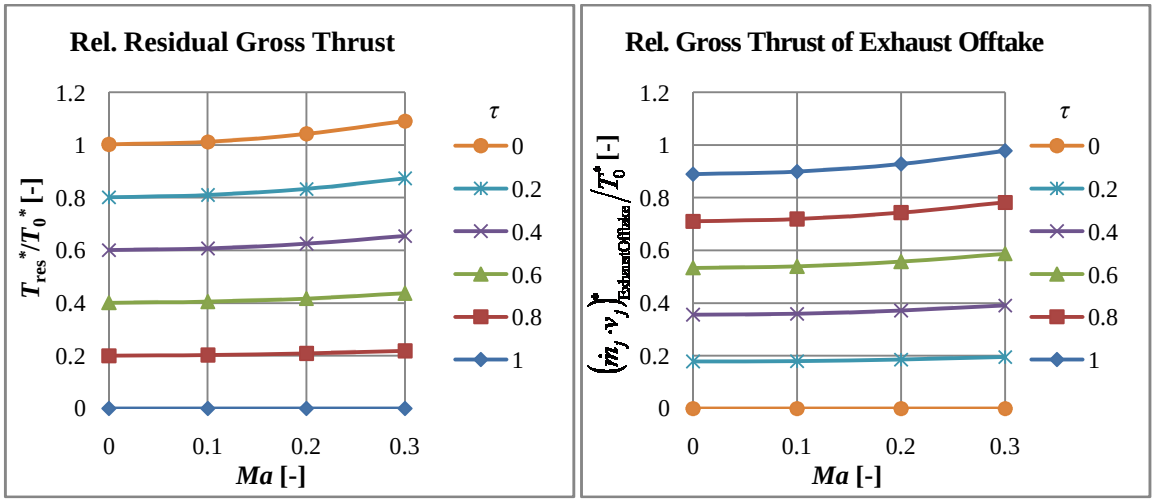

Figure 115. Relative residual and exhaust offtake gross thrust, mixed-flow engine, BPR=5, σ=-12 %

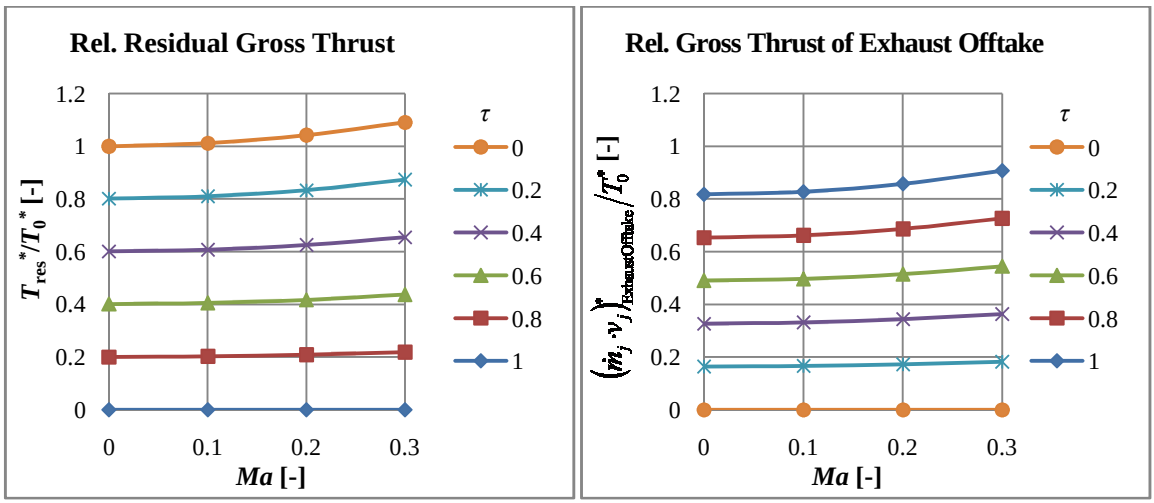

Figure 116. Relative residual and exhaust offtake gross thrust, mixed-flow engine, BPR=5, σ=-18 %

C. High-Speed Aerodynamics

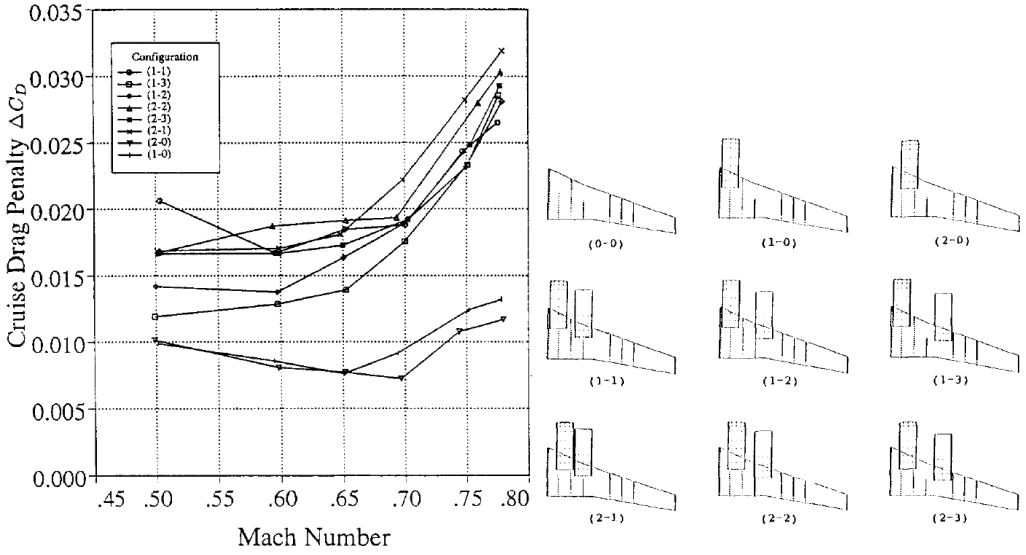

Figure 117. USB cruise drag penalty (left) for different engine installation configurations (right)

D. Wind-Tunnel Polars Selected for the Application Example

Table 28. Important operational conditions measured in wind-tunnel experiments

	Report No.	Sub-models	AEO TO-Flaps	AEO LD-Flaps	AEO Tail	OEI TO-Flaps	OEI LD-Flaps	OEI Tail	Static Turning Data	*RD*	*BPR*
USB	TN D-8061	split flaps	0°, 35°	50°, 65°	tail off	n.a.	limited*	n.a.	0°, 35°, 50°, 65°	ES	n.a.
		radius flaps	45°	60°, 75°, 90°	tail off	n.a.	limited*	n.a.	?	ES	n.a.
	TM X-62419		0°, 30°	75°, 90°	tail off	30°	90°	tail off	30°, 75°, 90°	not corrected	3
	TM X-62296		30°	55°, 75°	tail off	n.a.	75°	tail off	30°, 55°, 75°, 90°	not corrected	3
IBF AW	TN D-8309		0°, 15° 30°	45°, 60° 70°	tail off and on	n.a.	n.a.	n.a.	n.a.	n.a.	n.a.
	TM X-62145		30° 40°	60°, 70°	tail off and on	n.a.	n.a.	n.a.	n.a.	corrected	n.a.
	TM X-62029†		30° 40°	60°, 70°	tail off and on	n.a.	n.a.	n.a.	n.a.	corrected	n.a.
AIBF	TM X-62281		30°	60°	tail off	n.a.	n.a.	n.a.	n.a.	corrected	n.a.
EBF	TN D-8057	*BPR* 6.2	35°	55°	tail off	35°	55°	tail on	35°, 65°	ES	6.2
		BPR 10	0°, 35°	55°	tail off	35°	55°	tail off and on	35°, 65°	ES	10
	TM X-62197		0°, 30°	55°	tail off	30°	55°	tail on	20°,30°, 40°,45°, 55°	not corrected	3

* No polars, only few conditions available at two engines inoperative

† TM X-62029 is the continuation of the experiments documented in TM X-62145

IBF

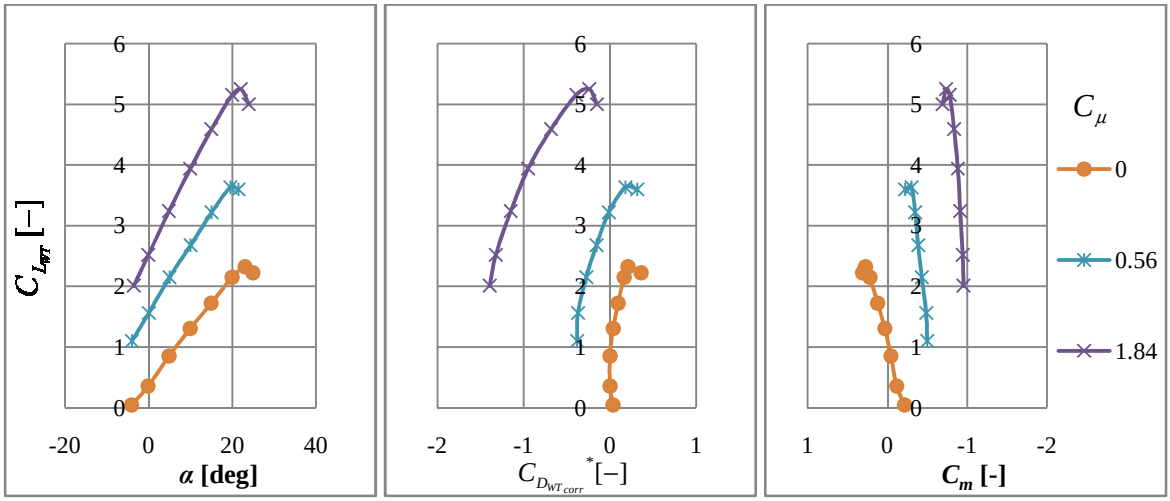

Figure 118. Corrected wind-tunnel polar for IBF, δ_f =15°

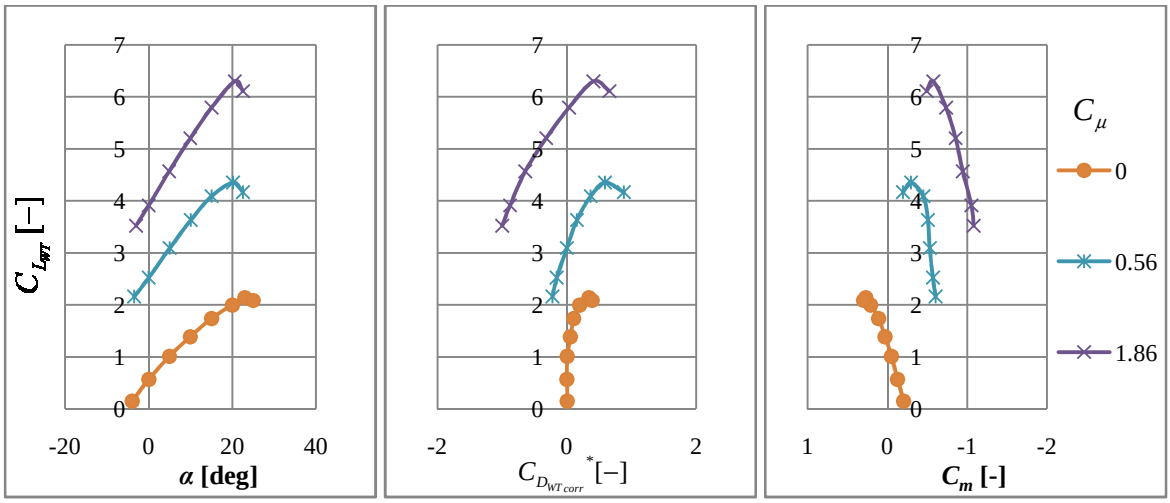

Figure 119. Corrected wind-tunnel polar for IBF, δ_f =30°

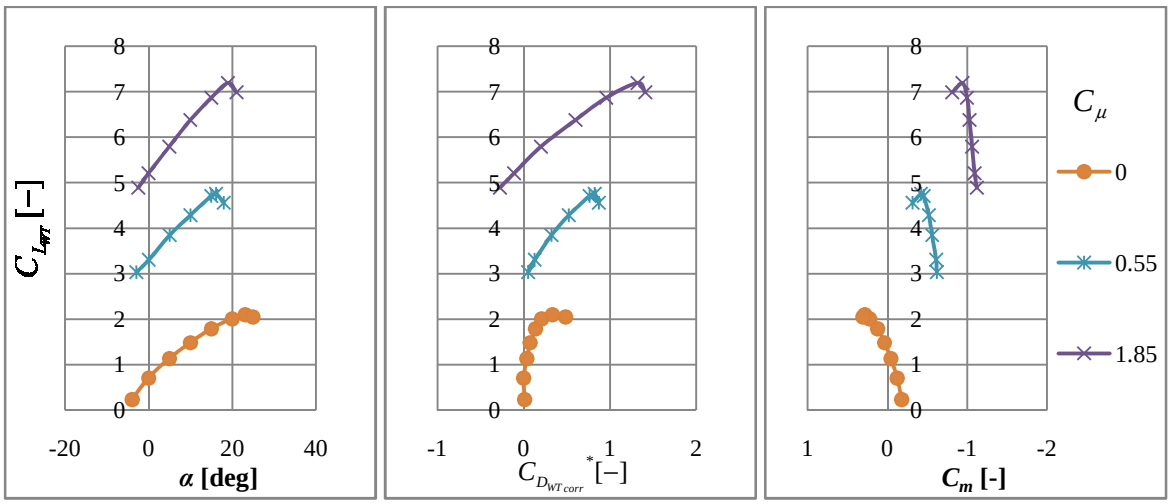

Figure 120. Corrected wind-tunnel polar for IBF, δ_f =45°

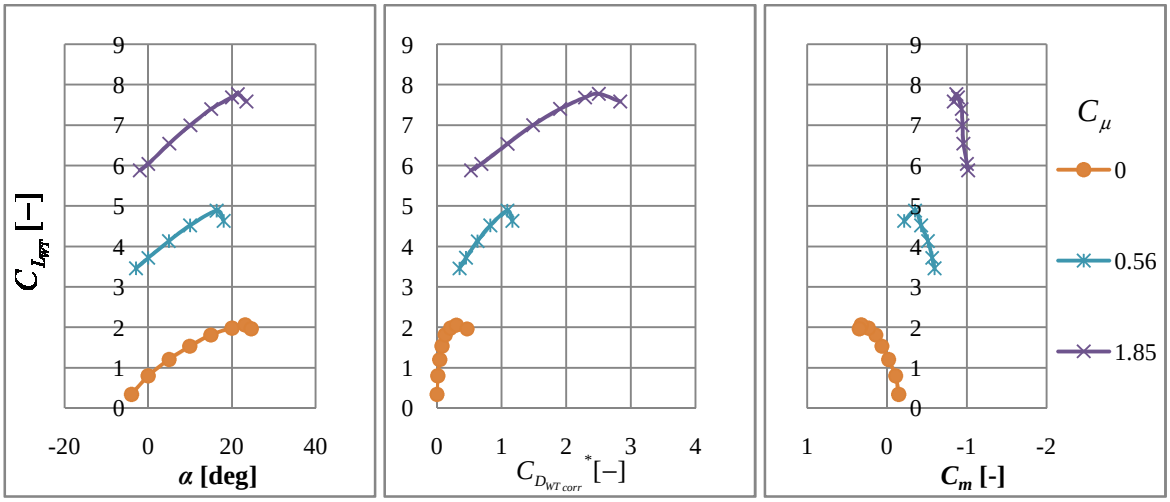

Figure 121. Corrected wind-tunnel polar for IBF, δ_f =60°

AIBF

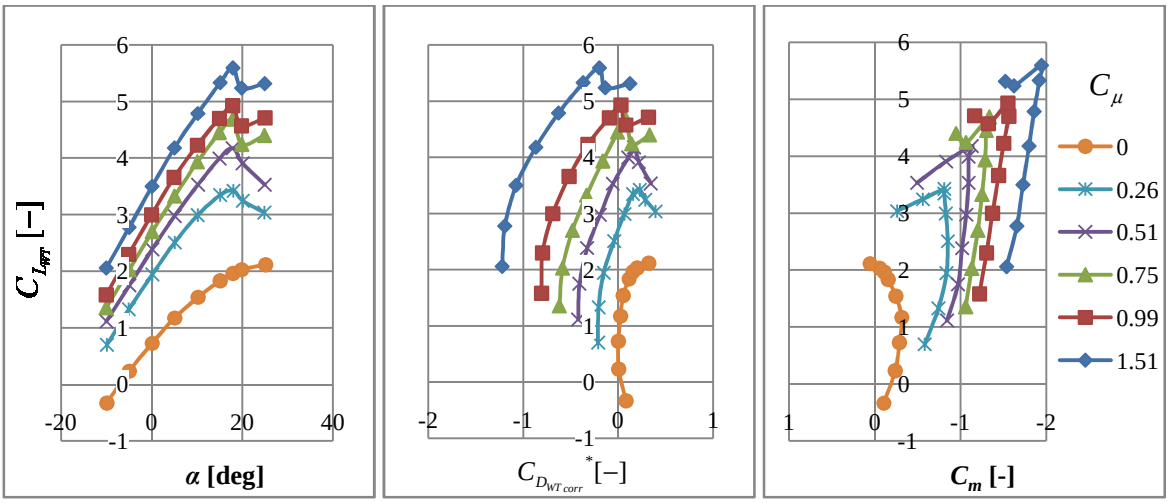

Figure 122. Corrected wind-tunnel polar for AIBF, δ_f=30°

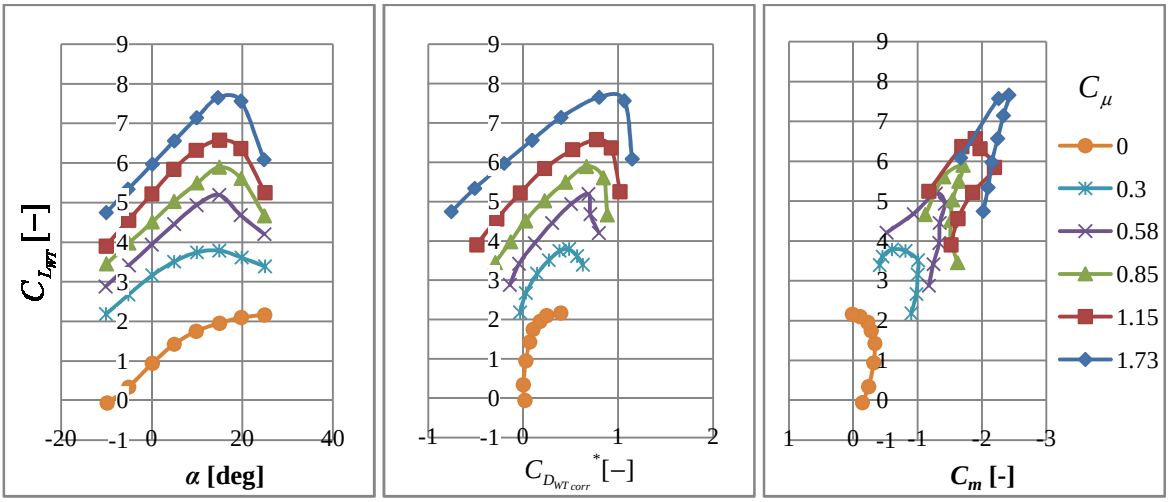

Figure 123. Corrected wind-tunnel polar for AIBF, δ_f =60°

USB

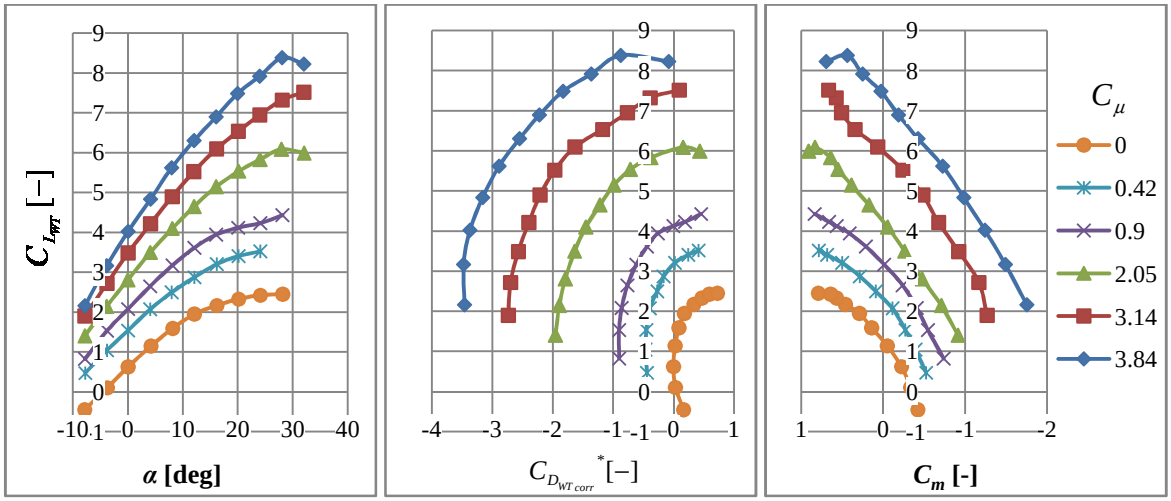

Figure 124. Corrected wind-tunnel polar for USB with AEO, δ_f =30°

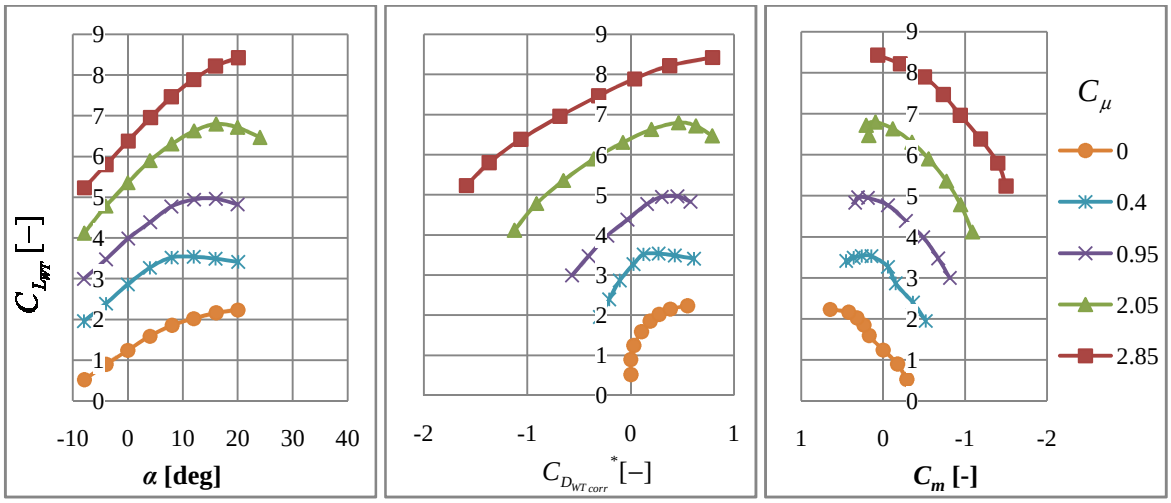

Figure 125. Corrected wind-tunnel polar for USB with AEO, δ_f =75°

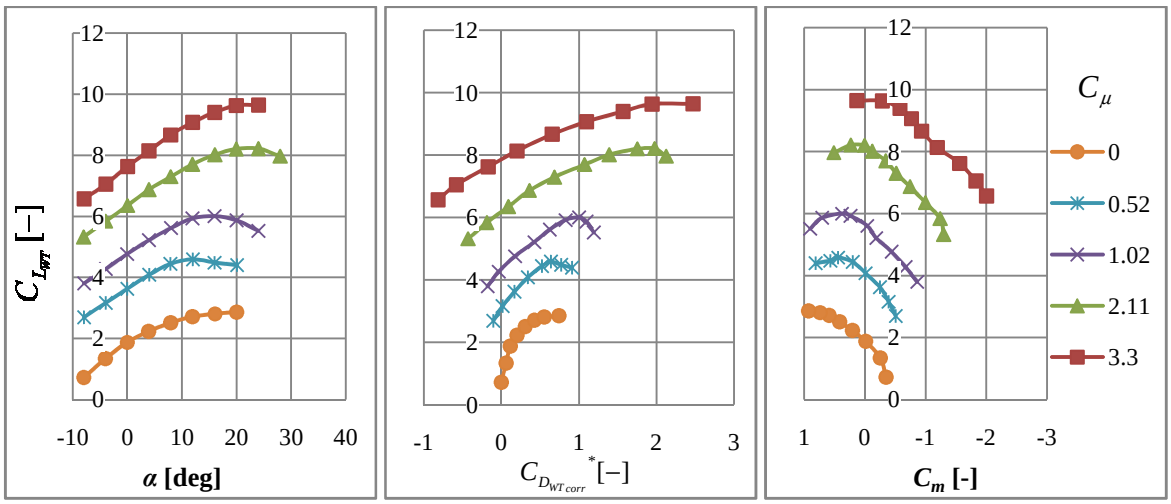

Figure 126. Corrected wind-tunnel polar for USB with AEO, δ_f =90°

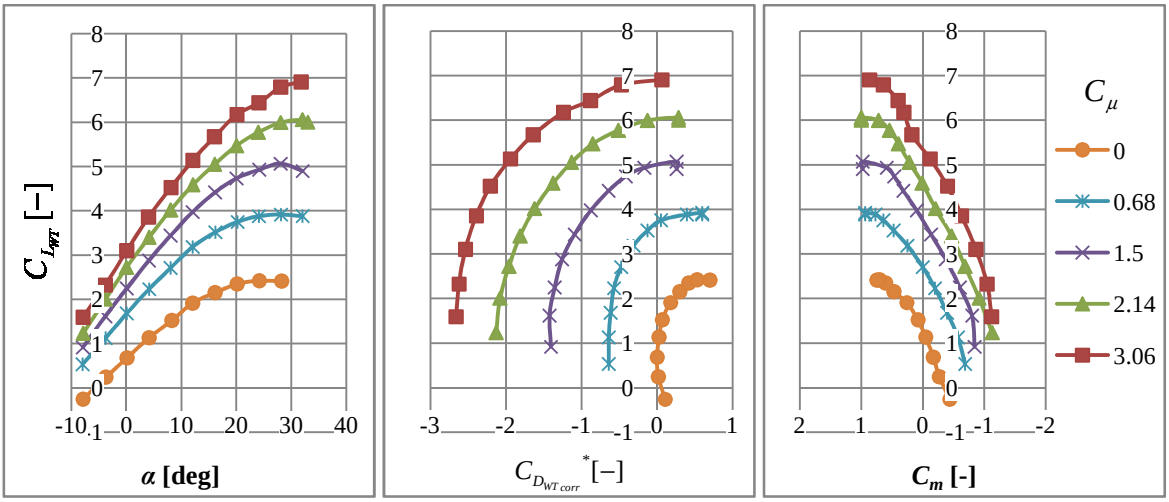

Figure 127. Corrected wind-tunnel polar for USB with OEI, δ_f =30°

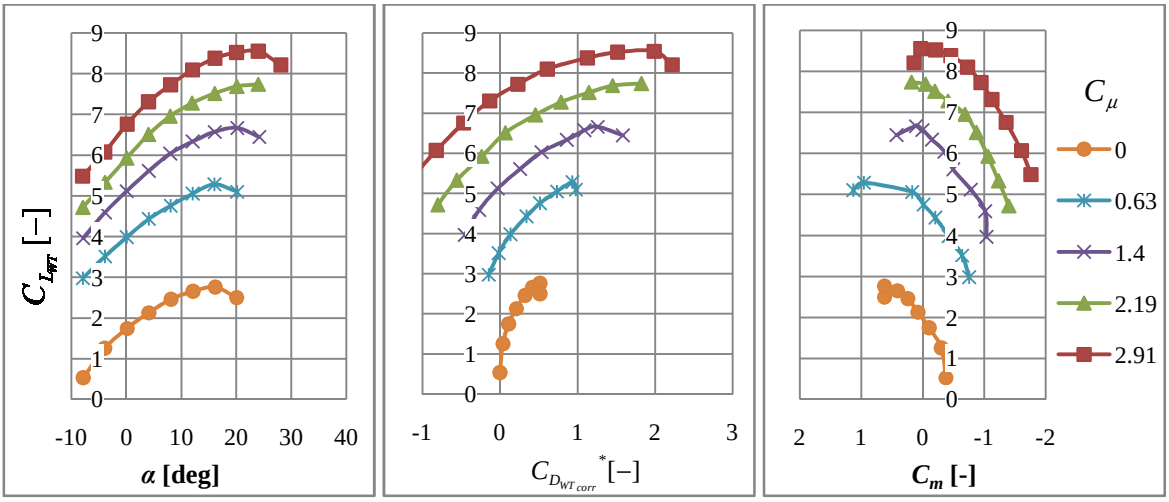

Figure 128. Corrected wind-tunnel polar for USB with OEI, δ_f =90°

EBF

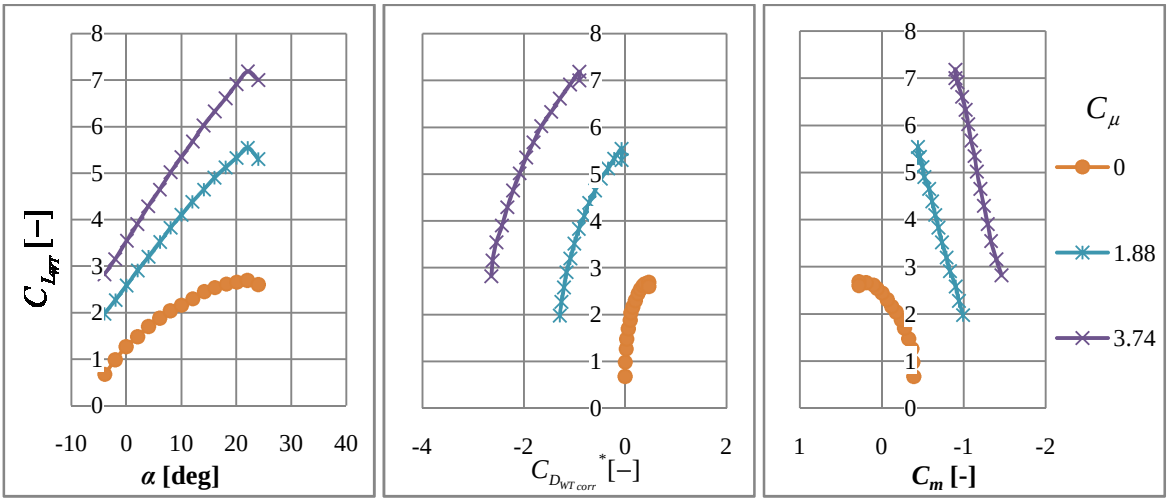

Figure 129. Corrected wind-tunnel polar for EBF with AEO, *BPR*=6.2, δ_f =35°

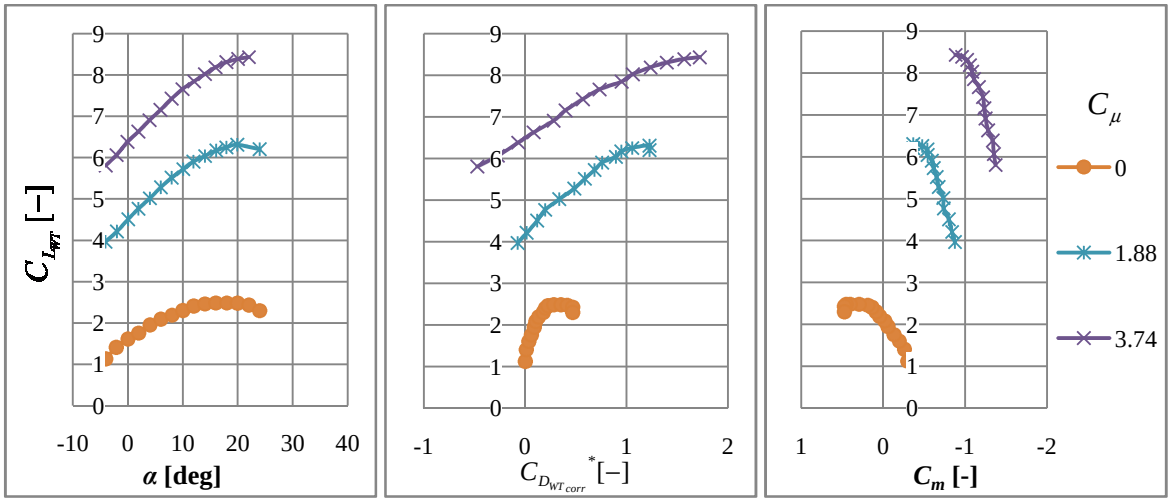

Figure 130. Corrected wind-tunnel polar for EBF with AEO, *BPR*=6.2, δ_f =65°

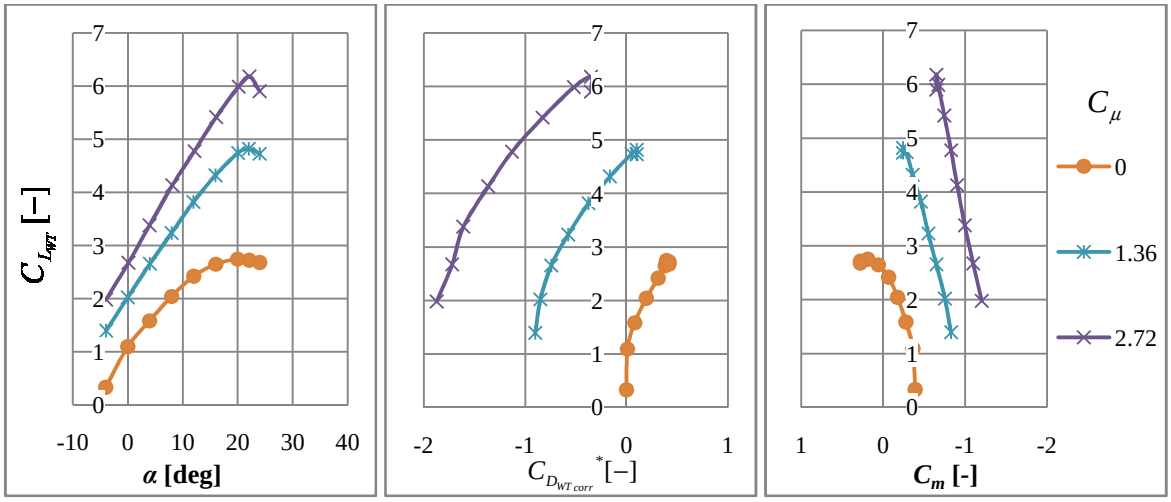

Figure 131. Corrected wind-tunnel polar for EBF with OEI, *BPR*=6.2, δ_f =35°

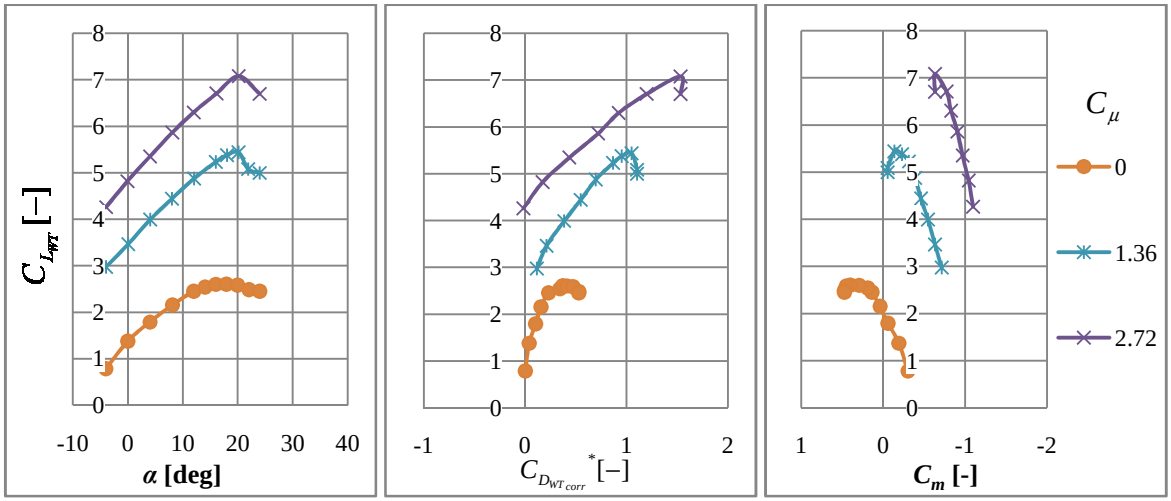

Figure 132. Corrected wind-tunnel polar for EBF with OEI, *BPR*=6.2, δ_f =65°

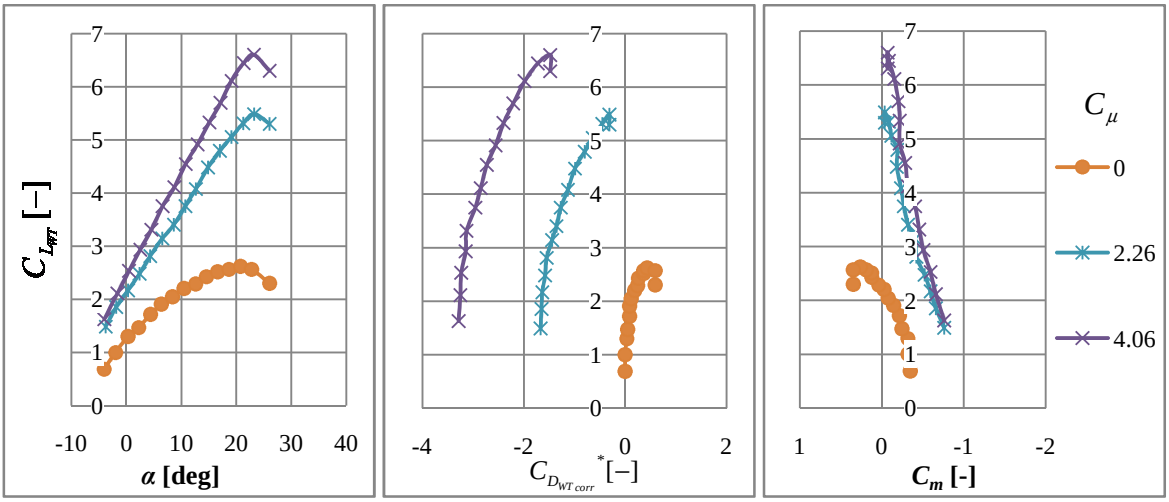

Figure 133. Corrected wind-tunnel polar for EBF with AEO, *BPR*=10, δ_f =35°

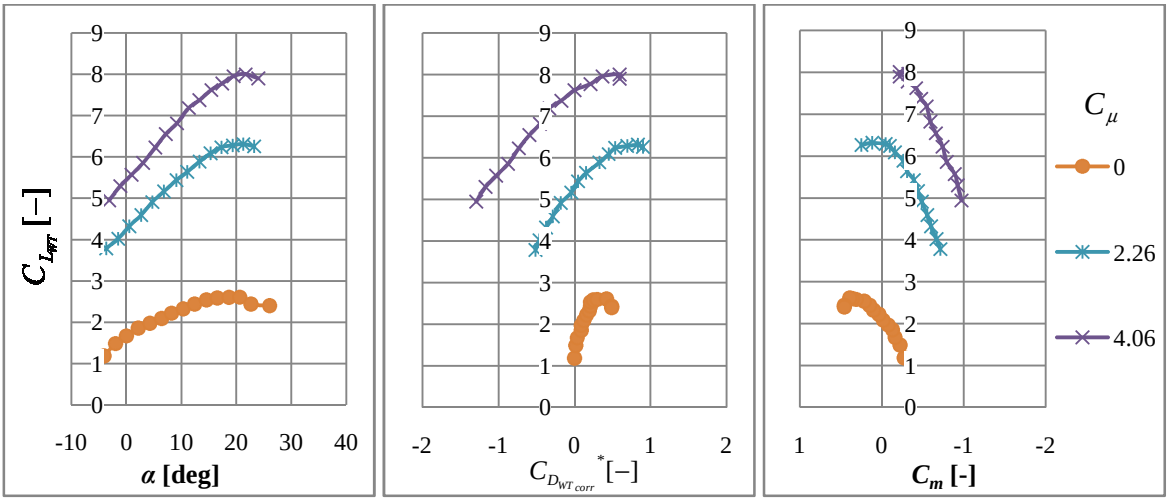

Figure 134. Corrected wind-tunnel polar for EBF with AEO, *BPR*=10, δ_f =65°

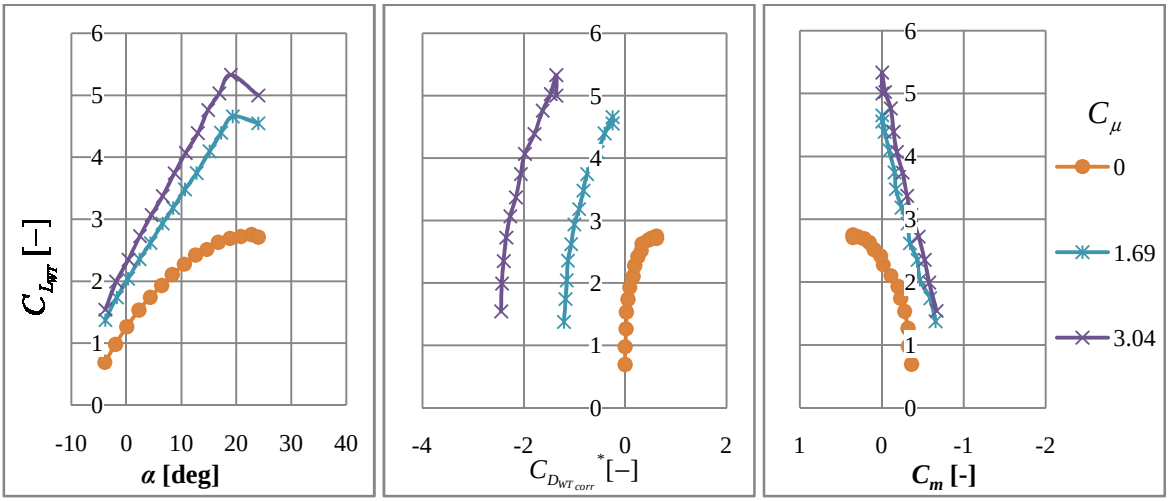

Figure 135. Corrected wind-tunnel polar for EBF with OEI, *BPR*=10, δ_f =35°

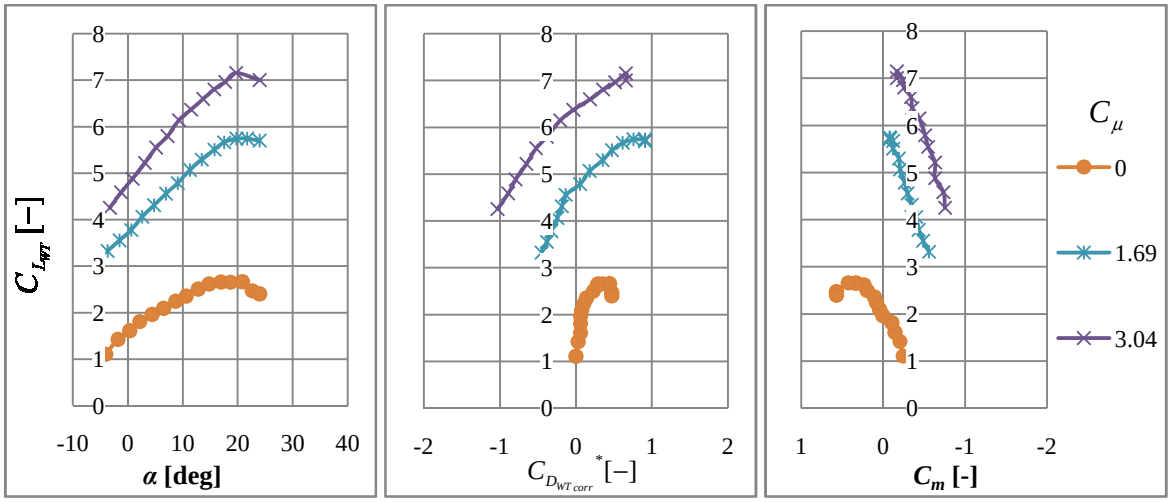

Figure 136. Corrected wind-tunnel polar for EBF with OEI, *BPR*=10, δ_f =65°

E. Sizing for Performance

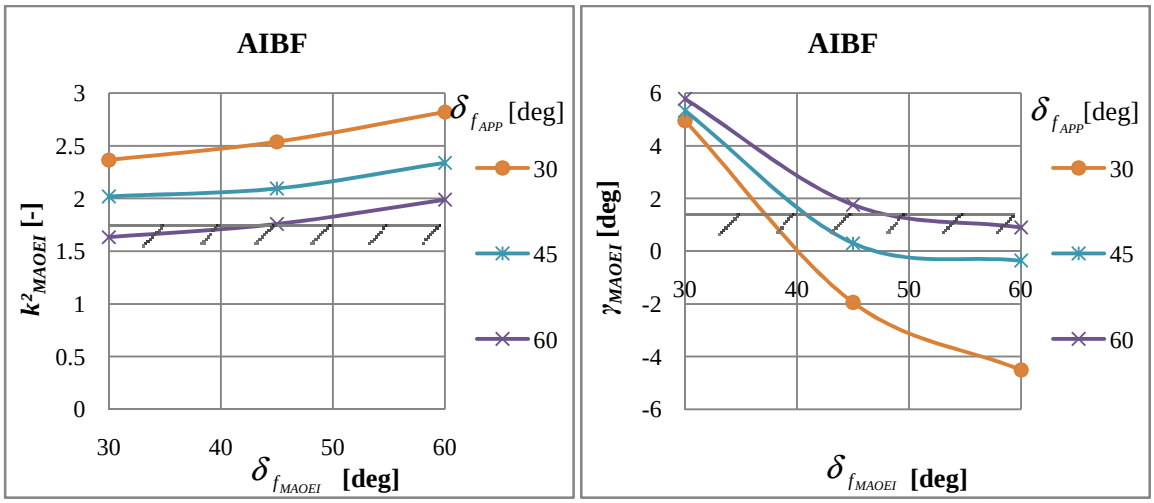

Figure 137. Safety margin (left) and climb angle for MA with OEI (right) for AIBF aircraft

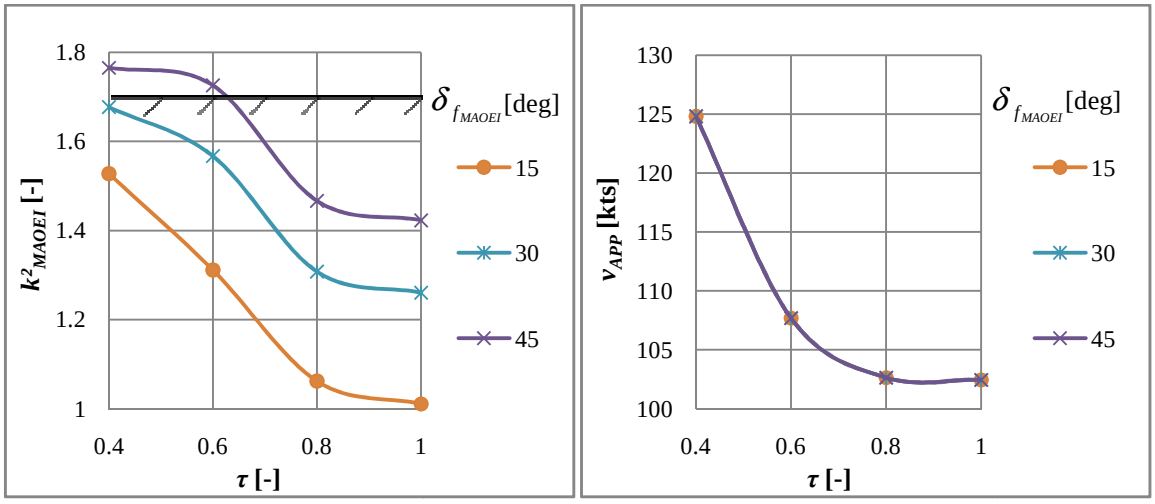

Figure 138. Safety margin (left) and approach speed (right) over τ for different values of $\delta_{f_{MAOEI}}$ for IBF aircraft with exhaust offtake

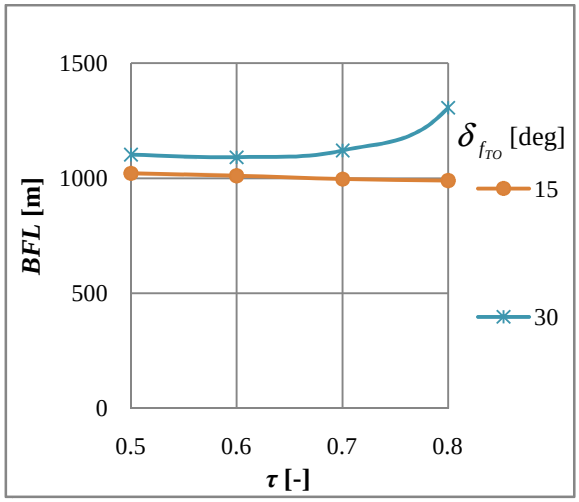

Figure 139. Balanced field length over exhaust mass flow offtake and take-off flap angle for IBF aircraft with exhaust offtake

F. Tail Sizing

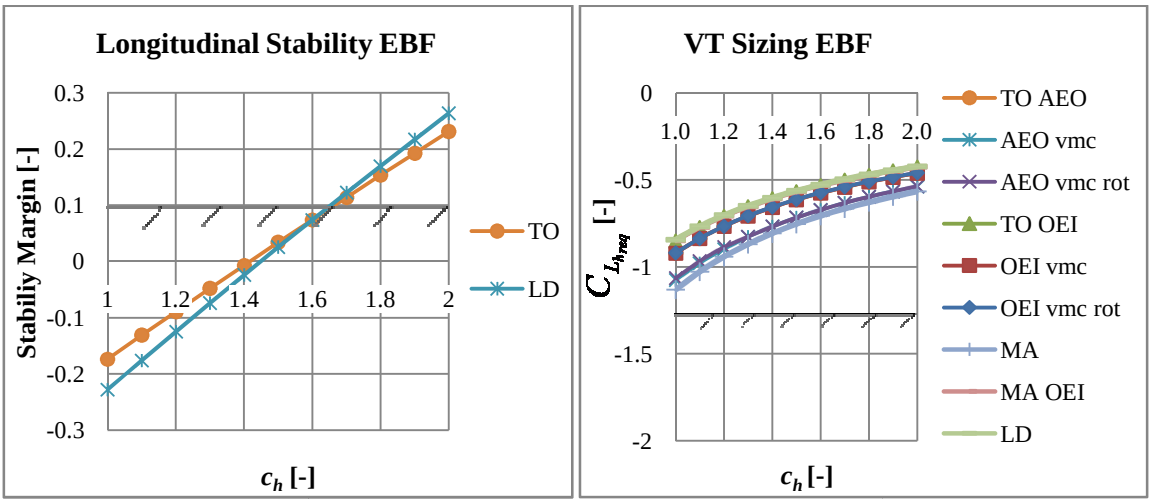

Figure 140. HT sizing for EBF aircraft

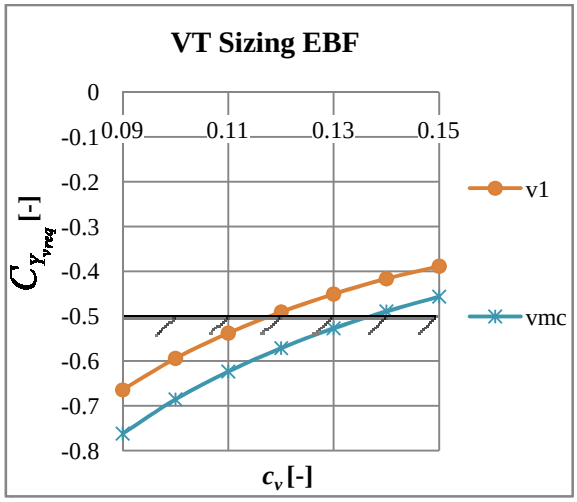

Figure 141. VT sizing for EBF aircraft

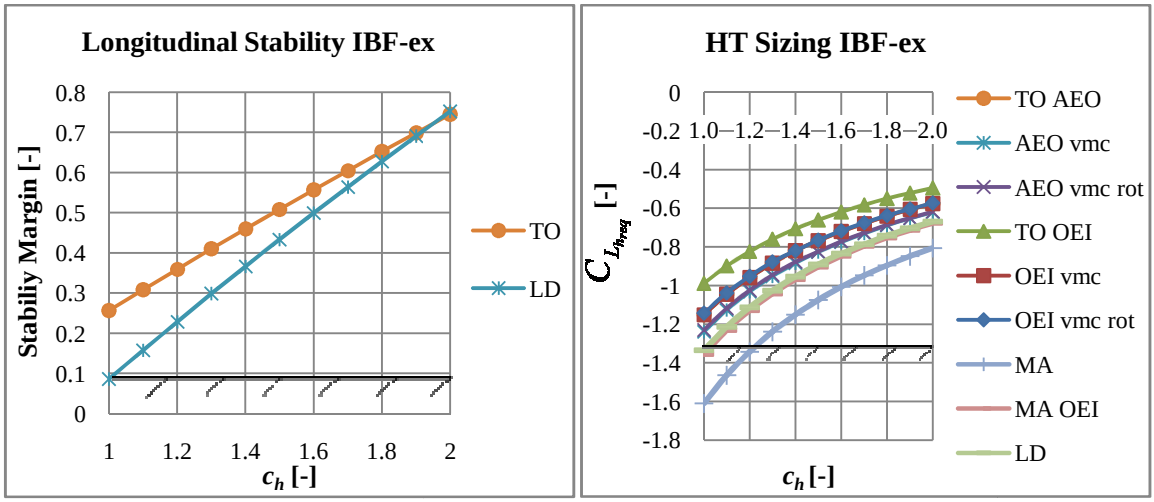

Figure 142. HT sizing for IBF aircraft with exhaust offtake

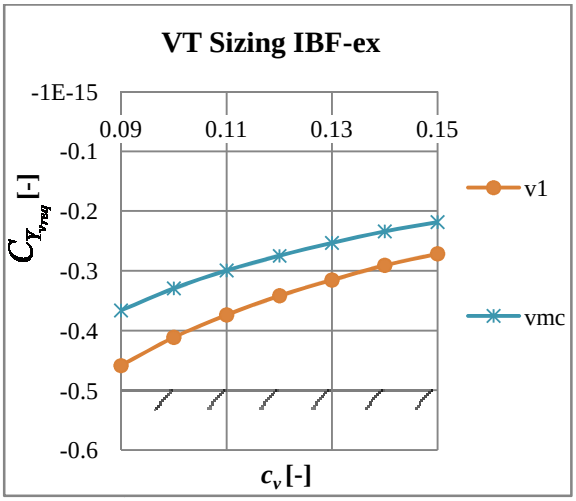

Figure 143. VT sizing for IBF aircraft with exhaust offtake

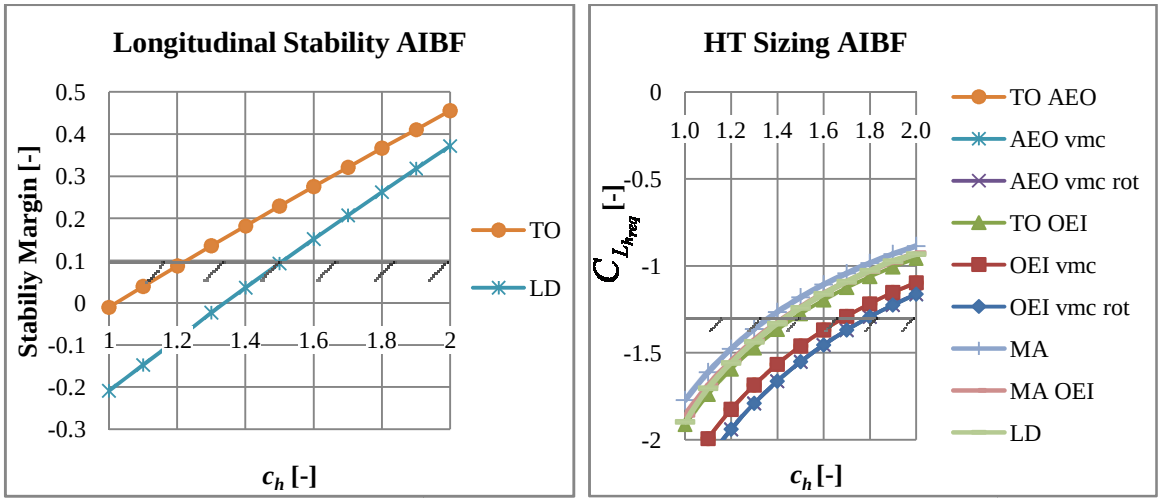

Figure 144. HT sizing for AIBF aircraft

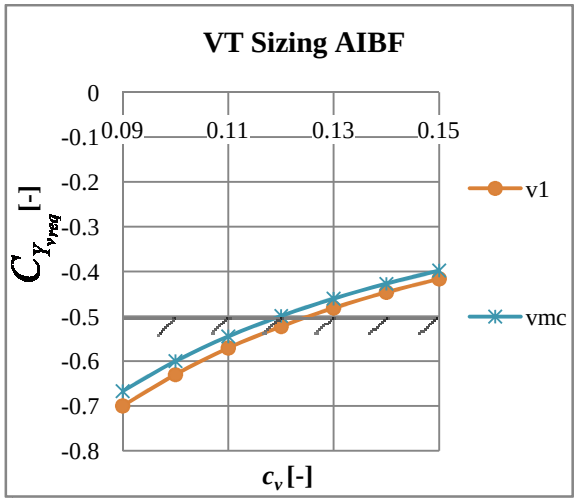

Figure 145. VT sizing for AIBF aircraft

G. Discussion of Take-Off and Landing

Table 29. Comparison of MA with AEO

	Unit	USB	EBF	AIBF	IBF-by	IBF-ex
C_μ	-	1.25	1.70	1.27	1.13	0.71
C_D^*	-	-0.36	-0.12	-0.53	-0.46	-0.39
C_m	-	-0.79	-0.87	-1.32	-1.02	-0.86

Table 30. Comparison of MA with OEI

	Unit	USB	EBF	AIBF	IBF-by	IBF-ex
C_μ	-	0.94	1.27	0.95	0.85	0.53
C_D^*	-	-0.11	-0.12	-0.06	-0.20	-0.14
C_m	-	-0.39	-0.59	-1.40	-0.81	-0.62
δ_f	deg	40	35	45	45	45

H. Overall Mission Comparison

Table 31. OEW breakdown

	Unit	Reference	USB	EBF	AIBF	IBF-by	IBF-ex
Structure	kg	13,369	17,357	15,824	15,238	15,582	15,285
Propulsion	kg	2,817	5,375	6,035	4,825	5,341	5,159
Equipment	kg	6,099	6,801	6,709	6,518	6,609	6,558
Operational Items	kg	1,790	1,778	1,787	1,788	1,784	1,784
OEW	kg	24,075	31,311	30,355	28,369	29,316	28,786

Table 32. Structure weight breakdown

	Unit	Reference	USB	EBF	AIBF	IBF-by	IBF-ex
Fuselage	kg	6,284	6,208	6,284	6,271	6,316	6,314
Wing	kg	3,417	4,657	3,931	3,789	4,047	3,998
HT	kg	227	730	481	527	522	380
VT	kg	248	1,022	496	455	353	331
Nacelles & Pylons	kg	1,404	2,461	2,511	2,202	2,295	2,240
Undercarriage	kg	1,789	2,279	2,121	1,994	2,049	2,022
Total	kg	13,369	17,357	15,824	15,238	15,582	15,285

I. Fuel Burn vs. Field Length

Table 33. Design points of EBF aircraft for different field length requirements, *BPR*=6.2

		T/W [-]	*W/S* [kg/m²]
Field length required	1000	0.51	580
	900	0.5	470
	800	0.5	380
	750	0.5	340

Table 34. Design points of USB aircraft for different field length requirements, *BPR*=10

		T/W [-]	*W/S* [kg/m²]
Field length required	1000	0.42	500
	950	0.44	460
	900	0.47	420

Table 35. Design points of AIBF aircraft for different field length requirements

		T/W [-]	*W/S* [kg/m²]
Field length required	1000	0.44	550
	900	0.44	460
	800	0.44	370
	750	0.44	330
	700	0.44	295

Table 36. Design points of IBF aircraft with bypass offtake for different field length requirements

		T/W [-]	*W/S* [kg/m²]
Field length required	1000	0.45	525
	900	0.465	510
	800	0.45	405
	700	0.44	315

Table 37. Design points of IBF aircraft with exhaust offtake for different field length requirements

		T/W [-]	*W/S* [kg/m²]
Field length required	1000	0.44	520
	900	0.44	420
	800	0.44	345
	750	0.44	300